# University of Alberta

Study of solute-solvent interactions with vibrational CD spectroscopy and DFT calculations

by

Mohammad Reza Poopari

A thesis submitted to the Faculty of Graduate Studies and Research

in partial fulfillment of the requirements for the degree of

Doctor of Philosophy

Department of Chemistry



Spring 2014
Edmonton, Alberta

# Dedicated to:

To the inspiring support of both my parents

&

To my sisters and brothers

&

To my loving wife, Zahra, for her kindness and devotion

## Abstract

My PhD thesis work is centered on developing a suitable approach to account for solvent effects in solution spectroscopic measurements and on providing significant insights into the intermolecular interactions between chiral solute and solvent, in particular water, molecules. Vibrational absorption (VA) and vibrational circular dichroism (VCD) spectroscopic techniques have been used as the main experimental tools to study conformational distributions and most importantly solute-solvent interactions of a number of prototype chiral molecules in several common solvents. The spectral window from 800 $cm^{-1}$ to 1800 $cm^{-1}$ was used for data acquisition. Aqueous solutions, both normal and deuterated water, and organic solvents such as methanol, dimethyl sulfoxide, and chloroform were used. Complementary optical rotatory dispersion measurements have also been carried out. Density functional theory has been employed to perform all calculations for conformational searches, geometry optimizations, VA, VCD, UV, and ECD intensities, and spectral simulations. To account for effects of water solvent, a clusters-in-a-liquid approach has been proposed. Molecular dynamics simulations and radial distribution function calculations have also been carried out to identify the representative hydration clusters, i.e. chiral solute-$(water)_N$. Initial conformational analyses have been done using small basis set like 6-31G(d), which is a compromise between accuracy and computational cost. For final calculations, several larger basis set like 6-31++G(d,p), 6-311++G(d,p), cc-pVTZ, and aug-cc-pVTZ, have been used and the specific choices depend on the size and complexity of systems under the investigation.

Geometries of the molecular systems of interest have been evaluated in the gas phase and in bulk solvent using the implicit solvation polarization continuum model, while the related geometries of the explicit hydration clusters of the targeted chiral molecules have been similarly evaluated. My thesis work shows that inclusion of both explicit and implicit solvent effects simultaneously is essential to interpret the experimental VA and VCD spectra whenever strong hydrogen-bonding interactions are expected between chiral solute and solvent molecules. When no strong solvent–solute hydrogen-bonding interactions are expected, it was found that the gas phase monomer model is adequate but not optimal for spectral interpretations and the inclusion of the implicit bulk water environment is highly recommended.

## Acknowledgments

I owe a debt to gratitude to many people who have helped and supported me during the course of my PhD program since the PhD work is hardly the accomplishment of single individual, and mine is also no exception. I wish to express my sincerest gratitude to my supervisor Prof. Yunjie Xu for her support and guidance over the last five years. She has given me many opportunities to learn and grow as an independent researcher and for that, I am really grateful. I would like to thank my colleagues in the Xu group, both past and present, namely Fumie, Christian, Javix, Shawn, and Connie. I would like to thank Prof. Wolfgang Jäger for his invaluable advice during the course of my research and for bringing up stimulating discussions. I also wish to thank my friends in Jäger group, Steve, Elijah, Chrissy, and Jen.

The course of my research was substantially enhanced by the support of many individuals. I would like to acknowledge all of my advisory committee members who have accepted generously to be part of my PhD journey, Prof. Todd Lowary, Dr. Alex Brown, and Dr. Gabe Hanna. I also wish to gratitude my external examining committee member, Prof. Prasad Polavarapu from Vanderbilt University. I am so grateful to my teaching assistant coordinators, Dr. Norman Gee (10X general chemistry course) and Dr. Anna Jordan (37X physical chemistry course) for their support and advice on many difficult occasions.

I would like to thank the inspiring support of my family members especially my parents for their endless love throughout of my life. Finally, I would like to express my gratitude to my lovely wife, Zahra, for being with me ALWAYS. Doctoral work has a lot of ups and downs and I could not have finished my PhD research without her support and devotion.

# Table of contents

# List of Tables (Chapters)

# List of Tables (Appendices)

# List of Figures (Chapters)

# List of Figures (Appendices)

# 1 Chapter Introduction

## 1.1 Chirality and the related nomenclature

The word *chirality* is derived from the Greek word for hand. A molecule is "**chiral**" if it is non-superposable onto its mirror image, whereas a molecule is "**achiral**" when it is identical to its mirror image. A pair of human hands is the most common chiral objects we encounter in our daily life since the right hand are not superposable onto the left one. From the molecular symmetry point of view, a molecule is chiral if it does not possess an *improper rotation* (rotation-reflection) axis, i.e. the combination of a rotation along an axis followed by a reflection in a plane which is perpendicular to the axis of rotation. The term "*enantiomers"* is used to describe a pair of mirror images of a chiral molecule.

Chiral molecules can exhibit several types of chirality. The first and the most common one is point chirality where an atom, such as a carbon atom, takes on four different substituents. By definition, the point is called a *stereogenic* center. For example, bromo, chloro, fluoro-methane, CHBrClF (Figure 1.1) is a chiral molecule in which three hydrogen atoms of methane are replaced by the Br, Cl, and F atoms.

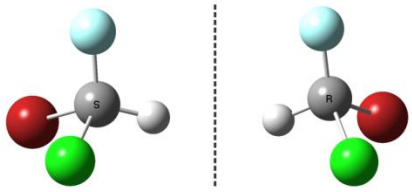


Figure 1.1. The pair of mirror images of CHBrClF molecule, a prototype chiral molecule.

A molecule can still be chiral even though there is no stereogenic center available. The two most common types are *axial* and *spiral* chirality. The 1,1'-bi-

2-naphthol (BINOL) and 1,3-substituted-allene are two examples of axial chirality. In systems with axial chirality, four groups sit in a non-planar arrangement about a chiral axis about which the rotation is restricted due to steric hindrance. The spiral chirality can be found frequently in nature; for instance, the double strand A-DNA is a right-handed structure.

The 3D spatial arrangements of chiral molecules can be described using different nomenclature conventions. It was recognized early on that a pair of enantiomers can rotate the plane of polarization of a linearly polarized light either clockwise or counterclockwise, i.e. dextrorotation and levorotation, respectively.[1] The optical isomer with dextrorotation is called dextrorotatory or (+)-isomer, while the mirror image with levorotation is called levorotatory or (-)-isomer. Figure 1.2 illustrates how the plane of polarization turns when a linearly polarized light passes through a chiral medium. This and other special properties which chiral molecules exhibit when they interacting with polarized light are generally termed optical activities.

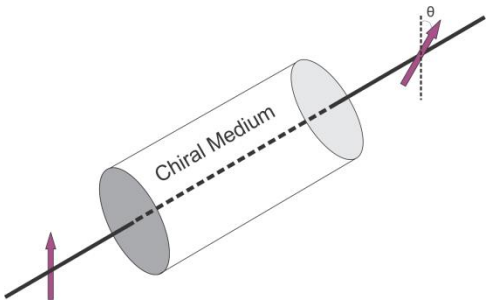


Figure 1.2: Rotation of the plane of polarization when linearly polarized light passes through a chiral medium.

The *absolute configuration* of a chiral molecule refers to the precise spatial arrangement of substituents at a stereogenic center or at a chiral axis.

These are identified by letters R and S based on Cahn-Ingold-Prelog (CIP)[2] priority rules. The CIP rules contain two simple parts. First, an atom with higher atomic number takes higher priority, i.e. O > N > C > H. Second, if the first atom is the same for two or more groups, the second atom will be considered and treated the same way as the first atom, i.e. $OCH_3$ > OH. As a consequence, a group with higher total weights might get lower priority in the group ordering regime, i.e. OH > C-$(CH_3)_3$. Figure 1.3 shows the R- and S-configurations based on such priority rules.

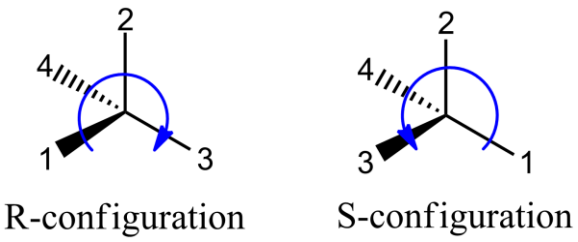


Figure 1.3: R and S absolute configuration labels based on the CIP priority rules.

Since most important biological molecules are chiral, chirality plays an incredibly important role in the fields of pharmaceutical and medicinal chemistry. A few examples of well-known chiral drugs are provided in Figure 1.4. Thalidomide was sold in the fifties and sixties as an over the counter drug to alleviate morning sickness in pregnant women. While its R-enantiomer has a sedative effect, the S-enantiomer causes severe birth defects.[3] It was later recognized that thalidomide racemizes *in vivo*. This drug disaster prompted much stricter drug regulations in many countries. In 1992, the Food and Drug Administration (FDA) in the USA issued guidelines regarding new stereoisomeric drugs and required their toxicity be tested separately. Another well-known drug,

Ibuprofen, which is nowadays marketed under different brand names like Advil, also racemizes in the body, although the S-enantiomer is a better pain reliever.[4] Lastly, Cialis, a drug used for treating impotence, has two stereogenic centers. It can adopt RR, RS, SR, and SS configurations. Experimentally, it was found that the RR-isomer is much more effective than the others, so the RR-isomer is synthesized and marketed today.[5]

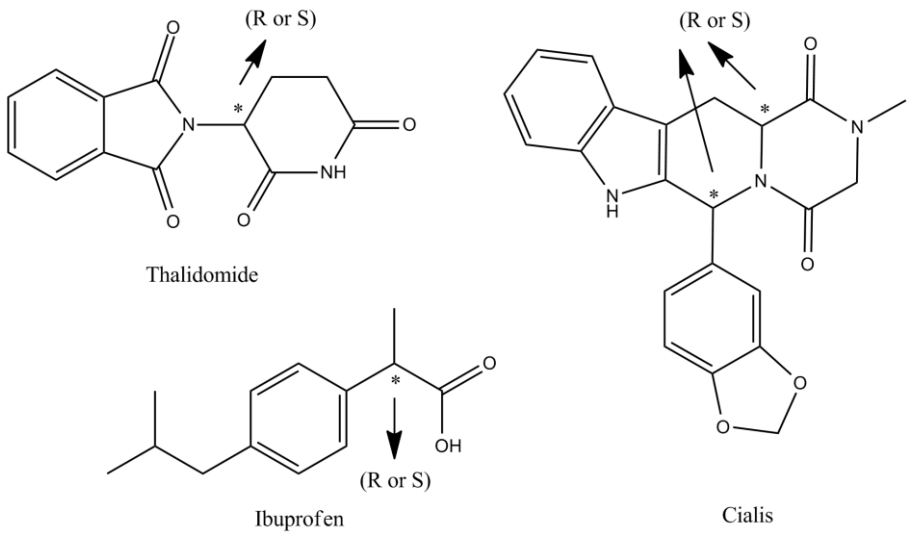


Figure 1.4. Structural representations of three chiral drugs, namely Thalidomide, Ibuprofen, and Cialis.

## 1.2 Vibrational circular dichroism spectroscopy for absolute configuration determination and conformational analyses

To comply with the guidelines set out by the regulatory bodies such as the FDA and the European Agency for the Evaluation of Medicinal Products (EMEA), it is necessary to know the absolute configurations of the drug candidates. Several methods have been used for three-dimensional structural

determination. One of the oldest methods is stereoselective synthesis. This consists of a series of well-understood synthetic steps to arrive at a final chiral product with known absolute stereochemistry. This is tedious and may not be applicable in all cases. Spectroscopic tools such as NMR, X-ray, electronic circular dichroism (ECD), vibrational CD and Raman optical activity (ROA), as well as optical rotatory dispersion (ORD) spectroscopy have all been used for such a purpose in certain occasions and each comes with its own pros and cons. For example, NMR technique needs a chiral shift reagent.[6] A single good quality crystal is required for X-ray analysis.[7] High-level ab initio calculations are needed for ECD interpretation and even so the broad nature of the spectral contours often prevents a well-defined assignment.[8] It takes time to achieve good signal-to-noise ratio for VCD and ROA measurements because their intensities are generally very small. Consequently, full structural characterizations, including absolute configuration and conformational diversity determination may benefit from or even require usage of more than one technique.[9] Below I briefly summarize the advantages of VCD and the challenges one may face in utilizing this technique for absolute configuration and conformational landscape determinations.

VCD is the differential absorbance of left versus right circularly polarized light of a molecular vibrational transition in the mid-infrared spectral region. In the last decades, VCD spectroscopy has experienced significant developments in both experimental and theoretical sides.[10] It is now possible to obtain excellent quality VCD spectra with a commercial VCD spectrometer offered by a number of companies such as BioTools and Bruker. Density functional theory (DFT)

calculations of VCD signs and intensities have been implemented into the popular electronic structure packages such as Gaussian suite of programs[24,25] and Amsterdam DF (ADF).[11] Chapter 2 of my thesis provides a brief overview of the theoretical and experimental aspects of the IR and VCD spectroscopy. A concise historical background and theoretical developments of VCD and its implementation into the computational software like Gaussian are also highlighted in the chapter.

VCD has several significant advantages over other techniques mentioned above. First, the experiment can be performed directly in solution. Second, as an optical spectroscopic method, it can register signals from individual conformers in contrast to X-ray and NMR which have intrinsic slow response to structural changes. Third, VCD spectra show distinct spectral responses from different functional groups and with much narrow bandwidth in contrast to ECD. Finally, VCD calculations involve only the ground electronic state and are quite reliable compared to others such as ECD and ORD where information about the excited electronic states are needed. For these reasons, this technique has matured into a very successful spectroscopic technique for determinations of absolute configurations and conformational distributions of a wide range of mid-sized chiral molecules in solution. There are some remaining challenges in VCD application with respect to the structural determination. The most significant one is how to properly account for solvent effects, especially those related to water. This is the main topic of this thesis. Another one is conformational flexibility. The latter is discussed in connection to solvent effects in this thesis.

## 1.3 Goals and VCD spectroscopy as a novel tool for studying intermolecular interactions in solution

Interactions between solute and solvent molecules, particularly water, are of significant importance in chemistry and in life in general. Considerable amounts of research have been focused on this topic. For example, chemical reaction outcomes and stability of reactive intermediates in aqueous solution can be strongly influenced by the ability of water molecule to dissipate energy through ultra-fast vibrational relaxations.[12] This ability of water is governed by the related vibrational couplings. Using two-dimensional infrared and transient absorption spectroscopy, Tokmakoff and co-workers characterized the vibrational couplings by examining the response in the whole mid-infrared region after exciting the OH stetching transition.[12] Panman et al. found a "lubrication" effect of water in hydrogen-bonded molecular machines using time-resolved vibrational spectroscopy and NMR lines-shape analysis.[13] Wester and co-workers demonstrated that the interaction with just one water molecule is enough to affect the outcome of the nucleophilic substitution reaction of $CH_3I + OH^-$.[14] This study highlights in particular the significance of such explicit hydrogen-bonding interaction with even just one water molecule.

The significant advantges of VCD spectroscopy discussed above make it a highly suitable spectroscopic technique to investigate hydrogen-bonding interactions between chiral solute and achiral solvents, such as water, directly in solution.[15] In contrast, in nonpolar solvents, such as $CCl_4$ and $CDCl_3$, one may

obtain satisfactory agreement between experimental and theoretical VCD spectra without consideration of the existence of solvent, i.e. gas phase VCD simulations.[16,17] There are many exceptions to this general observation. In Chapter 3, I examined how VCD signatures of methyl mandelate alter in different solvents such as chloroform ($CHCl_3$), dimethyl sulfoxide (DMSO), and methanol (MeOH). The goal is to evalute how the solute-solvent interaction is affected by variation of solvent polarity and their hydrogen bonding formation capability.[17]

Evaluation of water solvent effects is significantly more complicated because of the tendency of water to form extensive hydrogen-bonding networks in aqueous solution. In 1996, for the first time, Jalkanen et al. attempted to include the explicit hydrogen-bonding interaction between water molecules and N-acetyl-L-alanine N'-methylamide in their interpretation of the observed VCD spectrum.[18] There have been questions concerning the existence of these chiral solute-water clusters in solution because of the dynamic nature of the water solvent. Our research group has been working on finding a systematic approach to account for water solvent effects using the 'cluster-in-a-liquid' model. Basically, we try to build explicit chiral solute-water hydrogen bonded clusters and solvate such clusters in bulk water using an implicit solvent model, for example integral equation formalism polarizable continuum model (IEF-PCM).[19] It is, however, significantly challenging to know what hydration clusters to build, i.e. how many water molecules are needed and where to attach them. One major focus of my thesis is to find a solution to these problems.

In chpaters 4 to 6, I applied VCD spectrosocpy to probe water solvent effects of several amino acids, i.e. Acetyl-L-Cysteine Methyl Ester (NALCME),[20] acetylated form of Cysteine (NALC),[21] and Leucine (Leu)[22] in water under different pH conditions. To understand the nature of solute-solvent interactions, I also applied Fourier transform infrared (FT-IR), ECD and ORD spectroscopies, complemented with DFT[23] calculations implemented in Gaussian03[24] and Gaussian09[25] and molecular dynamics simulations using the Amber suite of programs.[26] In these studies, I recognized the importance of both explicit chiral solute-water hydrogen-bonding interactions and the surrounding bulk water and developed a suitable approach to account for them systematically.

In chapter 4, the VCD signatures of two vibrational modes, carboxylic and amide I, have been investigated using implicit solvent model to search for possible conformations in aqueous solution. The signs of those two modes are rationalized to be quite sensitive to the conformational changes. However, as it is shown in the following chapters, the gas phase and implicit solvent models are not sufficient to account for the experimental features precisely. Therefore, the explicit solvent-solute hydrogen-bonding interctions are taken into consideration accordingly. Significant improvements in agreement with the experimental data have been achieved for the simulated VA and VCD spectra when the 'cluster-in-a-liquid' approach is compared to the individual gas phase and PCM approaches.

The final chapter of my thesis gives the general conclusions of this thesis and proposes future work to further explore and evaluate the solvation approach developed in this thesis work. I also include a number of appendices at

the end of my thesis which include the supporting information associated with each research chapter and several publications I have also been involved in during my PhD study.

## References


[1] (a). D.F. Arago, *Mem. de L'Inst.*, 1811, 12, part1, 93. (b). J. B. Biot, *Bull. Soc. Philomath.*, 1815, 190.

[2] (a). R. S. Cahn, C. K. Ingold, V. Prelog, *Angew. Chem. Int. Ed*., 1966, 5, 385. (b). J. March. Advanced Organic Chemistry 3Ed. 2007, John Wiley & Sons. ISBN 0-471-85472-7.

[3] T. Eriksson, S. Bjourkman, B. Roth, A. Fyge, and P. Houglund, *Chirality.*, 2004, 7, 44–52.

[4] J. Caldwell, A. J. Hutt, Y. Fasnel-Gigleux, *Biochem. Pharmacol*., 1988, 37, 105–114.

[5] A. Daugan, P. Grondin, C. Ruault, A.-C. Le Monnier de Gouville, H. Coste, J. M. Linget, J. Kirilovsky, F. Hyafil, and R. Labaudiniere, *J. Med. Chem.*, 2003, 46, 4533–4542.

[6] (a). T. R. Hoye, A.-S.S. Hamad, D.O. Koltun, M. A. Tennakoon, *Tetrahedron Lett*., 2000, 41, 2289–2293. (b). T.R. Hoye, D. O. Koltun, *J. Am. Chem. Soc*., 1998, 120, 4638–4643.

[7] H. D. Flack, Bernardinelli, G., *Acta Crystallogr. Sect. A*, 1999, 55, 908–915.

[8] G. Pescitelli, S. Gabriel, Y. Wang, J. Fleischhauer, R. W. Woody, N. Berova,, *J. Am. Chem. Soc*., 2003, 125, 7613–7628.

[9] (a). P. Polavarapu, *Chirality.*, 2008, 20, 664–672. (b). P. Polavarapu, *Chirality.*, 2012, 24, 909–920.

[10] (a). X. Qu, E. Lee, G.-S. Yu, T. B. Freedman, L.A. Nafie, *Appl. Spectrosc*., 1996, 50, 649-657. (b). T. B. Freedman, X. Cao, Rina K. Dukor, L. A. Nafie, *Chirality*., 2003, 15, 743–758. (c). A. Lakhani, P. Malon, T. A. Keiderling, *Appl. Spectrosc.* 2009, 63, 775-785. (d). L. A. Nafie, *Appl. Spectrosc*., 2000, 54, 1634-1645. (e). P. Malon, T. A. Keiderling, *Appl. Spectrosc.*, 1988, 42, 32-38. (f). P. L. Polavarapu, *Appl. Spectrosc.*, 1989, 43, 1295-1297. (g). Z. Dezhahang, M. R. Poopari, Y. Xu, *Chemistry: An Asian Journal*., 2013, 8, 1205-1212. (h). Z. Dezhahang, C. Merten, M. R. Poopari, Y. Xu, *Dalton Transactions*, 2012, 41, 10817-10824. (i). G. Yang, Y. Xu, *Top. Curr. Chem*., 2011, 298, 189-236.

[11] Amsterdam Density Functional Program; Vrije Universiteit: Amsterdam, The Netherlands; http://www.scm.com. E.J. Baerends, T. Ziegler, J. Autschbach, D. Bashford, A. Bérces, F.M. Bickelhaupt, C. Bo, P.M. Boerrigter, L. Cavallo, D.P. Chong, L. Deng, R.M. Dickson, D.E. Ellis, M. van Faassen, L. Fan, T.H. Fischer, C. Fonseca Guerra, M. Franchini, A. Ghysels, A. Giammona, S.J.A. van Gisbergen, A.W. Götz, J.A. Groeneveld, O.V. Gritsenko, M. Grüning, S. Gusarov, F.E. Harris, P. van den Hoek, C.R. Jacob, H. Jacobsen, L. Jensen, J.W. Kaminski, G. van Kessel, F. Kootstra, A. Kovalenko, M.V. Krykunov, E. van Lenthe, D.A. McCormack, A. Michalak, M. Mitoraj, S.M. Morton, J. Neugebauer, V.P. Nicu, L. Noodleman, V.P. Osinga, S. Patchkovskii, M. Pavanello, P.H.T. Philipsen, D. Post, C.C. Pye, W. Ravenek, J.I. Rodríguez, P. Ros, P.R.T. Schipper, G. Schreckenbach, J.S. Seldenthuis, M. Seth, J.G. Snijders, M. Solà, M. Swart, D. Swerhone, G. te Velde, P. Vernooijs, L. Versluis, L. Visscher, O. Visser, F. Wang, T.A. Wesolowski, E.M. van Wezenbeek, G. Wiesenekker, S.K. Wolff, T.K. Woo, A.L. Yakovlev.

[12] K. Ramasesha, L. De Marco, A. Mandal, A. Tokmakoff, *Nature Chem.,*, 2013, 5, 935–940.

[13] M. R. Panman, B. H. Bakker, D. den Uyl, E. R. Kay, D. A. Leigh, W. Jan Buma, A. M. Brouwer, J. A. J. Geenevasen, S. Woutersen, *Nature Chem.*, 2013, 5, 929–934.

[14] R. Otto, J. Brox, S. Trippel, M. Stei, T. Best, R. Wester, *Nature Chemistry., 2012*, 4, 534–538.

[15] (a). S. Gobi, E. Vass, G. Magyarfalvi, G. Tarczay, *Phys. Chem. Chem. Phys*., 2011,13, 13972–13984. (b). J. Sadlej J. Cz. Dobrowolski, J. E. Rode, *Chem. Soc. Rev*., 2010, 39, 1478–1488. (c). J. Sadlej, J. Cz. Dobrowolski, J. E. Rodec, M. H. Jamroz, *Phys. Chem. Chem. Phys*., 2006, 8, 101–113.

[16] (a). T. Kuppens, P Bultinck, W. Langenaeker., *Drug Discovery Today: Technologies*, 2004, 1, 269-275.

[17] M. R. Poopari, Z. Dezhahang, and Y. Xu, *Phys. Chem. Chem. Phys*., 2013, 15(5), 1655-1665.

[18] K. Jalkanen and S. Suhai, *Chem. Phys*., 1996, 208, 81.

[19] (a) J. Tomasi, J , M. Persico, *Chem. Rev*., 1994, 94, 2027; (b) C. Cramer, D. Truhlar, *Chem. Rev*., 1999, 99, 2161.

[20] M. Reza Poopari, Z. Dezhahang, Y. Xu, *Spectrochimica Acta Part A: Mol. Bio. Spectrosc*, 2013, http://dx.doi.org/10.1016/j.saa.2013.08.118.

[21] M. R. Poopari, Z. Dezhahang, G. Yang, and Y. Xu, *ChemPhysChem.*, 2012, 13, 2310-2321.

[22] M. R. Poopari, P. Zhu, Z. Dezhahang, and Y. Xu, *J. Chem. Phys*., 2012, 137, 194308.

[23] (a) Honhenber, P. D.; Kohn, W. *J. Phys. Rev*. 1964. 135, B864. (b) W. Kohn, L. Sham, *J. Phys. Rev*., 1965.140, A1133.

[24] Gaussian 03, Revision E.01, M. J. Frisch, G. W. Trucks, H. B. Schlegel, G. E. Scuseria, M. A. Robb, J. R. Cheeseman, J. A. Montgomery, Jr., T. Vreven, K. N. Kudin, J. C. Burant, J. M. Millam, S. S. Iyengar, J. Tomasi, V. Barone, B. Mennucci, M. Cossi, G. Scalmani, N. Rega, G. A. Petersson, H. Nakatsuji, M. Hada, M. Ehara, K. Toyota, R. Fukuda, J. Hasegawa, M. Ishida, T. Nakajima, Y. Honda, O. Kitao, H. Nakai, M. Klene, X. Li, J. E. Knox, H. P. Hratchian, J. B. Cross, V. Bakken, C. Adamo, J. Jaramillo, R. Gomperts, R. E. Stratmann, O. Yazyev, A. J. Austin, R. Cammi, C. Pomelli, J. W. Ochterski, P. Y. Ayala, K. Morokuma, G. A. Voth, P. Salvador, J. J. Dannenberg, V. G. Zakrzewski, S. Dapprich, A. D. Daniels, M. C. Strain, O. Farkas, D. K. Malick, A. D. Rabuck, K. Raghavachari, J. B. Foresman, J. V. Ortiz, Q. Cui, A. G. Baboul, S. Clifford, J. Cioslowski, B. B. Stefanov, G. Liu, A. Liashenko, P. Piskorz, I. Komaromi, R. L. Martin, D. J. Fox, T. Keith, M. A. Al-Laham, C. Y. Peng, A. Nanayakkara, M. Challacombe, P. M. W. Gill, B. Johnson, W. Chen, M. W. Wong, C. Gonzalez, and J. A. Pople, Gaussian, Inc., Wallingford CT, 2004.

[25] Gaussian 09, Revision **C.01**, M. J. Frisch, G. W. Trucks, H. B. Schlegel, G. E. Scuseria, M. A. Robb, J. R. Cheeseman, G. Scalmani, V. Barone, B. Mennucci, G. A. Petersson, H. Nakatsuji, M. Caricato, X. Li, H. P. Hratchian, A. F. Izmaylov, J. Bloino, G. Zheng, J. L. Sonnenberg, M. Hada, M. Ehara, K. Toyota, R. Fukuda, J. Hasegawa, M. Ishida, T. Nakajima, Y. Honda, O. Kitao, H. Nakai, T. Vreven, J. A. Montgomery, Jr., J. E. Peralta, F. Ogliaro, M. Bearpark, J. J. Heyd, E. Brothers, K. N. Kudin, V. N. Staroverov, R. Kobayashi, J. Normand, K. Raghavachari, A. Rendell, J. C. Burant, S. S. Iyengar, J. Tomasi, M. Cossi, N. Rega, J. M. Millam, M. Klene, J. E. Knox, J. B. Cross, V. Bakken, C. Adamo, J. Jaramillo, R. Gomperts, R. E. Stratmann, O. Yazyev, A. J. Austin, R. Cammi, C. Pomelli, J. W. Ochterski, R. L. Martin, K. Morokuma, V. G. Zakrzewski, G. A. Voth, P. Salvador, J. J. Dannenberg, S. Dapprich, A. D. Daniels, Ö. Farkas, J. B. Foresman, J. V. Ortiz, J. Cioslowski, and D. J. Fox, Gaussian, Inc., Wallingford CT, 2009.

[26] D.A. Case, T.A. Darden, T.E. Cheatham, III, C.L. Simmerling, J. Wang, R.E. Duke, R. Luo, R.C. Walker, W. Zhang, K.M. Merz, B. Roberts, S. Hayik, A. Roitberg, G. Seabra, J. Swails, A.W. Goetz, I. Kolossváry, K.F. Wong, F. Paesani, J. Vanicek, R.M. Wolf, J. Liu, X. Wu, S.R. Brozell, T. Steinbrecher, H. Gohlke, Q. Cai, X. Ye, J. Wang, M.-J. Hsieh, G. Cui, D.R. Roe, D.H. Mathews, M.G. Seetin, R. Salomon-Ferrer, C. Sagui, V. Babin, T. Luchko, S. Gusarov, A. Kovalenko, and P.A. Kollman (2012), AMBER 12, University of California, San Francisco.

# 2 Chapter
# Theory and Experiment

## 2.1. Introduction

For my thesis research, I have utilized a number of optical spectroscopic techniques like VA, VCD, ECD, and ORD spectroscopies. VCD spectroscopy shows unique sensitivity to the chirality and is also highly sensitive to conformational changes and environmental variations. In comparison, the conventional IR spectroscopy is insensitive to chirality information, i.e. a pair of enantiomers produces identical IR absorption spectra, but mirror image VCD spectra. Like any other chiroptical spectroscopic measurements, information about the absolute configuration cannot be obtained directly through the experiment. One needs to simulate the theoretical VCD spectrum of a targeted molecule and compare that to the experimental data in order to assign the absolute configuration of a sample.

## 2.2. Brief review on the historic developments of VCD experiment and theory

The first VCD spectrum was measured by Holzwarth in 1974 using 2,2,2-trifluoromethyl-1-phenylethanol sample and it was also confirmed in 1975 by Nafie et al.[1] The dispersive scanning instruments were the first instruments constructed for measuring VCD spectra by Osborne et al in 1973.[2] The first Fourier transform (FT) based VCD spectrum was recorded a few years later in 1978 by Nafie and his co-workers using a photoelastic modulator (PEM) and a lock-in amplifier (LIA).[3] The commercialization of VCD instrumentation was started by two companies namely BioRad (Digilab) and Nicolet (Thermo Nicolet) in the 1980s adopting the FT-IR spectrometer for VCD measurements. Later, in

the mid 1990s, the Bruker Company, with the advent of step-scan FT-IR instrumentation, started commercializing the VCD spectrometer. The first stand-alone VCD spectrometer, Chiral*IR* FT-VCD, was marketed jointly by Bomem and BioTools companies. More recently, a single-platform VCD spectrometer is marketed by Jasco Company in Japan. Over the decades, the FT-IR manufacturers have been improving the VCD accessories and data processing software. The new generation of VCD spectrometer, Chiral*IR-2X*, is now offered by BioTools.

It was recognized in the early days of VCD theoretical development that both electric and magnetic dipole transition moments, i.e. EDTM and MDTM, respectively, are needed for the calculations of VCD intensities and signs.[4,6] One hurdle encountered in the early development was how to calculate the vibrational magnetic dipole transition moment.[5] Within the Born-Oppenheimer (BO) approximation, the electronic contribution to the vibrational magnetic dipole transition moment vanishes.[6] A few theoretical models like localized molecular orbitals[7], vibronic coupling[8], and nuclear electric shielding tensor[9] were proposed to better evaluate MDTM, but the results were not satisfactory. To include corrections to the BO approximation, Buckingham[10] and Stephens[6,11] proposed the magnetic field perturbation (MFP) approach. In their approach, the first derivatives of the ground state wave-function with respect to the nuclear displacements and the applied magnetic field are evaluated and used for the calculations of MDTM.

While calculations of the harmonic force field (HFF) and atomic polar tensor (APT)[12] had long been implemented into several electronic structure

calculation packages, such as Gaussian, to obtain the normal mode frequencies and band intensities, the corresponding calculations for VCD were not possible in the early days. The MFP method was implemented into Gaussian electronic structure calculation package by Stephens and collaborators using density functional theory in the 1990s.[13] To calculate a harmonic VCD spectrum, the analytical derivatives (AD) method was used to evaluate the three terms needed, i.e. HFF, APT, and the atomic axial tensor (AAT).[10] The resulting VCD spectral calculations were found to compare favorably to the experimental data.[14] Similar approaches have since been implemented into other electronic structure calculation packages such as ADF, DALTON, and CADPAC.

## 2.3. Some basics of IR and VCD spectroscopies

For a simple diatomic harmonic oscillator, the vibrational potential energy is proportional to the square of the displacement from equilibrium, i.e. $V = 1/2kx^2$. Here the system is viewed as two masses connected by a spring and obeys Hooke's Law ($F = -kx$). Therefore, the vibrational frequency of a diatomic molecule is classically expressed as:

$$v = \frac{1}{2\pi}\sqrt{\frac{k}{\mu}} \qquad (2.2)$$

where υ is the fundamental vibrational frequency, μ is the reduced mass of the system, and $k$ is the force constant. The energy levels of a quantum harmonic oscillator are quantized and equally spaced, and can be expressed as the following:

$$E_n = \left(n + \frac{1}{2}\right)\hbar\omega \qquad (2.3)$$

where n is the vibrational quantum number, ħ is Planck's constant (ħ = h/2$\pi$), and ω is the angular frequency (ω = 2$\pi\upsilon$). Figure 2.1 represents the simple harmonic vibrational energy levels of a diatomic molecule:

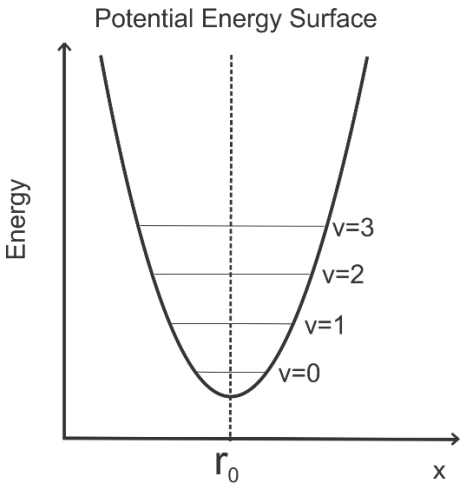


Figure 2.1: Vibrational levels in a diatomic harmonic oscillator.

As defined in Chapter 1, VCD is the preferential absorption of the left versus right circularly polarized light by a chiral molecule accompanying a vibrational transition. This can be written as following:

$$\Delta A = A_L - A_R \qquad (2.1)$$

If $A_L > A_R$, the VCD signal is positive, and vice versa. For an achiral molecule, interaction with the left and right circularly polarized light gives rise to identical vibrational spectra and therefore ΔA = 0. For a chiral molecule, interaction with the left and right circularly polarized light can be viewed in a similar way to a

diastereomeric interaction. Consequently, $\Delta A \neq 0$ in the case of chiral molecules. For a pair of enantiomers, the mirror image VCD spectra are expected.

Considering a transition from the ground vibrational state, ψ*g*, to the excited vibrational state, ψ*e*, ($g \rightarrow e$), the IR band intensity is proportional to a quantity called dipole strength, while the VCD sign and intensity is determined by a term named rotational strength, as shown in the following:

Dipole strength: $$D_{ge} = \langle \Psi_g | \hat{\mu} | \Psi_e \rangle . \langle \Psi_e | \hat{\mu} | \Psi_g \rangle \quad (2.4)$$

Rotational strength: $$R_{ge} = -Im \langle \Psi_g | \hat{\mu} | \Psi_e \rangle . \langle \Psi_e | \hat{m} | \Psi_g \rangle \quad (2.5)$$

Where $\hat{\mu}$ and $\hat{m}$ are the electric and the magnetic dipole operators, respectively. The dipole strength is related to the extinction coefficient using [15]

$$D_{ge} = 9.184 \times 10^{-39} \int_{band} \varepsilon \frac{\partial \bar{\nu}}{\bar{\nu}} \quad (2.6)$$

where ε is extinction coefficient ($M^{-1}$ $cm^{-1}$) and $\bar{\nu}$ is the transition frequency in wavenumber ($cm^{-1}$). The unit of dipole strength, *D*, is $esu^2$ $cm^2$. The rotational strength, R (in unit of $esu^2$ $cm^2$), is linked to the differential molar absorptivity, Δε, as following:

$$R_{ge} = 2.296 \times 10^{-39} \int_{band} \Delta\varepsilon \frac{\partial \bar{\nu}}{\bar{\nu}} \quad (2.7)$$

Rotational strength can also be written as $R = |\mu| \cdot |m| \cdot \cos\theta$, where |μ| and |m| are the magnitude of the electric and magnetic dipole transition moments vectors, respectively, and θ is the angle between these two vectors. If $-90° < \theta < 90°$, then cosθ is positive and if $90° < \theta < 270°$, then cosθ is negative. R=0 when θ is exactly

90° or 270°. As an example, for any vibrational mode whose VCD signal is negative, the angle between the two aforementioned vectors falls between 90° to 270°.

## 2.4. FT-VCD Instrumentation

As illustrated in Figure 2.2, infrared radiation covers the wavelength region from 10 $cm^{-1}$ to 14000 $cm^{-1}$. This region is further divided into three distinctive sub-regions namely: Far-Infrared (FIR), 10 - 400 $cm^{-1}$, Mid-Infrared (MIR), 400 – 4000 $cm^{-1}$, and Near-Infrared (NIR), 4000 – 14000 $cm^{-1}$. From 500 - 1500 $cm^{-1}$ of the MIR region is also called the finger print region where distinct vibrational bands associated with various functional groups of a compound appear. These bands typically consist of a series of bending and stretching vibrations, and are mostly fundamental transitions which are generally stronger than the overtone and hot-band transitions.

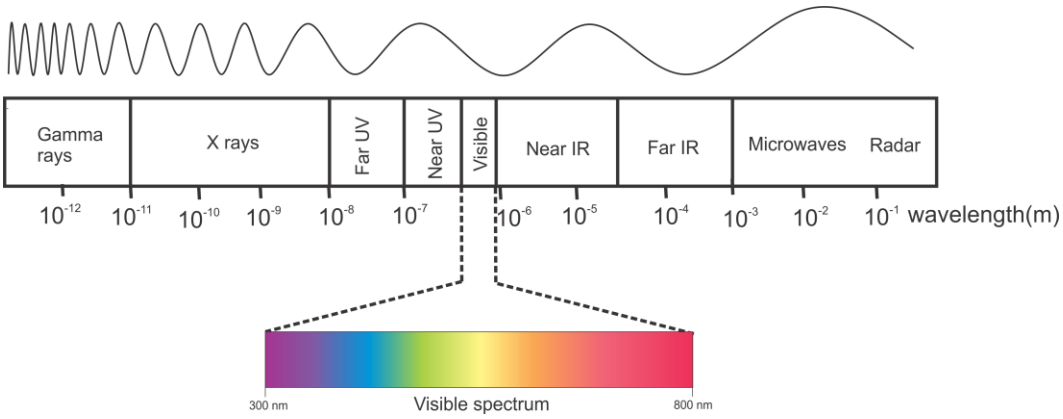


Figure 2.2. Electromagnetic Spectrum

For all VA and VCD measurements in my thesis, an FTIR-VCD module which consists of a FTIR spectrometer (Vertex 70, Bruker) and a VCD module (PMA 50, Bruker) was used. Figure 2.3 shows a schematic diagram of the FTIR-VCD instrumentation. In the following, I will discuss briefly the common main components shared by both the FTIR and FT-VCD spectrometers (Section 2.4.1) and then the special components used for VCD measurements (Section 2.4.2).

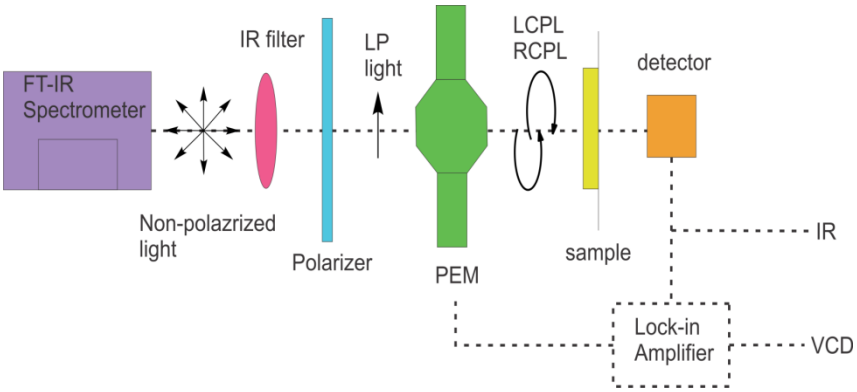


Figure 2.3. A schematic diagram of an FTIR-VCD instrumentation.

### 2.4.1. Some main components of the FTIR spectrometer

**Light source**: Figure 2.4 shows the comparison of a variety of broadband light sources available for several spectroscopic regions, courtesy of Bruker Optic Corporation. The most commonly used light source for the mid-IR region is a globar. Toward the UV-Vis region, the desirable light sources to use are Tungsten for NIR and Deuterium for UV-Vis regions.

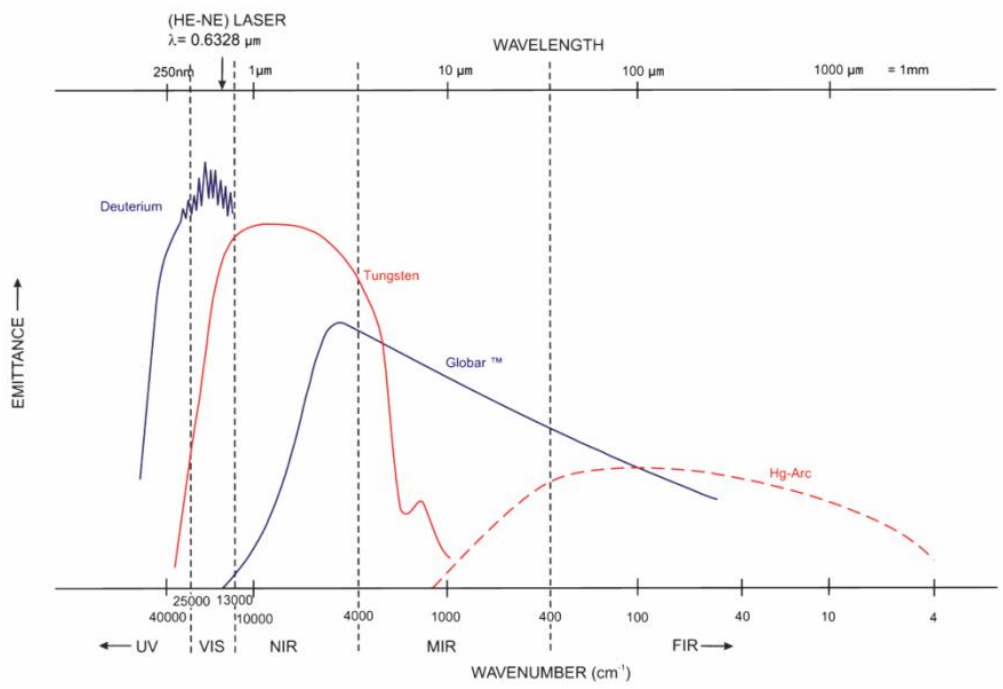


Figure 2.4. Emittance vs. wavenumber for a series of light sources used for different spectroscopic regions, taken from "Guide for Infrared Spectroscopy" manual, courtesy of Bruker Corporation, (www.bruker.com), permission to use the marketing literature including component specifications in this thesis.[16]

**Interferometer**: Both IR and VCD measurements utilize the advantages of the Fourier transform technique. A Michelson interferometer is at the heart of the FTIR spectrometer. Figure 2.5 shows a general scheme of a typical Michelson interferometer. A collimating mirror is positioned right after the infrared source to generate parallel light rays and transmit them to a beam-splitter at the center of the interferometer. After the light rays hit the beam-splitter, some are transmitted to a fixed mirror and others are reflected toward a moving mirror. The light beams reflected from both the fixed and moving mirrors are recombined at the beamsplitter. Depending on their phase differences, one will obtain constructive interference (in-phase light beams), or destructive interference. The combined

light beams then pass through a sample and are collected by a mid-IR detector eventually.

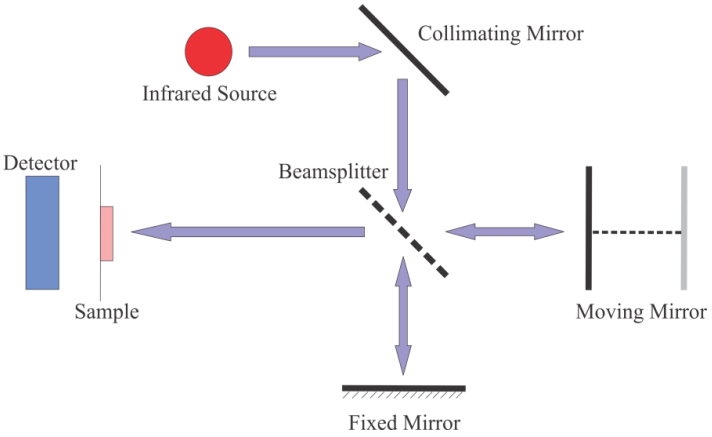


Figure 2.5. Interior design of a typical Michelson interferometer used for FTIR-VCD techniques

If the light beams are in phase, i.e. experience constructive interference, then the following equation is applied:

$$\delta = n\,\lambda \qquad (2.8)$$

where $\delta$ is the optical path difference, $\lambda$ is the wavelength, and n is an integer number. The zero path difference (ZPD) is obtained when n=0. Another terminology uses the mirror displacement ($\Delta$) which indicates the distance by which the moving mirror travels upon each scan. As the moving mirror goes forward and backward at each scan, $\delta = 2\Delta$ applies. In the case of destructive interference, the following formula is used:

$$\delta = (n+1/2)\,\lambda \qquad (2.9)$$

For example, for a single wavelength with the magnitude of $\lambda$=5 micron, the constructive interference occurs at optical differences of $\delta$=0, 5, 10, … micron

whereas the destructive interference happens at δ=2.5, 7.5, 12.5, … micron,. The resultant interferogram is a cosine function with the light intensity as the vertical axis and the δ value, the distance travelled by the moving mirror, as the horizontal axis. FT is applied afterward to extract the frequency domain signal for that specific wavelength. In reality, the infrared light source produces a broad range of wavelengths, and all of them travel together and hit the beam-splitter simultaneously. Therefore, the resulting interferogram contains all the frequencies and appears with a large burst at δ=0 (called center-burst) since all wavelengths interfere constructively at ZPD. The intensity (vertical axis) falls off rapidly as δ increases.

**Beam splitter**: Figure 2.6 shows the efficiency versus spectral ranges for a series of beam splitters, courtesy of Bruker Optics Corporation. For example, Cesium Iodide, CsI, and Potassium Bromide, KBr, are widely used for the fingerprint region and are also highly efficient nearly for the whole region from 400 - 4000 $cm^{-1}$. On the other hand, their efficiencies drop rapidly in the NIR region. For the NIR this region, different materials like Calcium Fluoride, $CaF_2$, can be used.

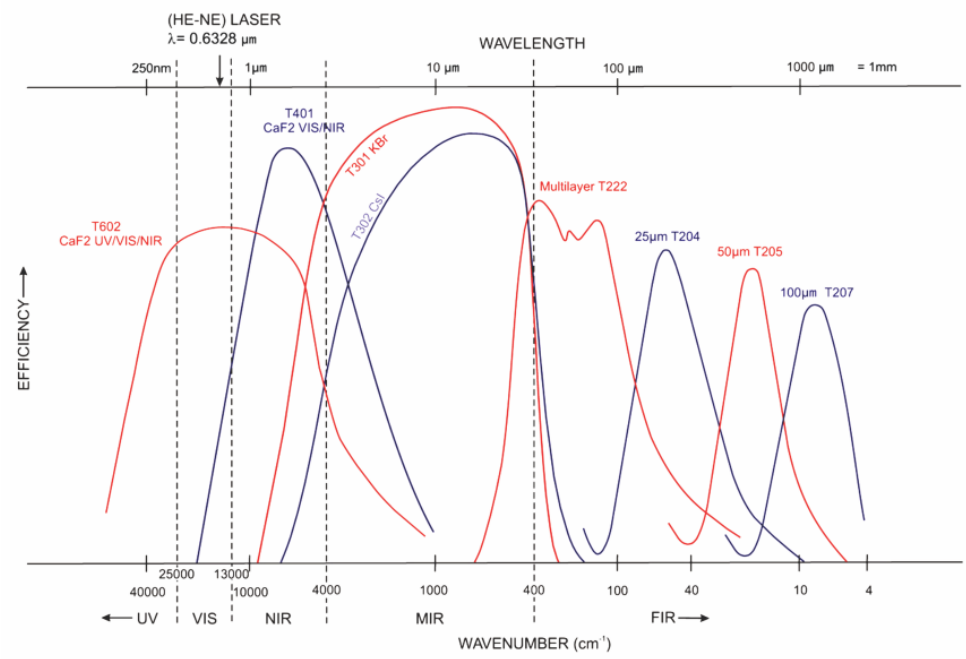


Figure 2.6. Comparison of efficiency curves of different beam-splitters over a wide spectral range from IR to UV-Vis, taken from "Guide for Infrared Spectroscopy" manual, courtesy of Bruker Corporation, (www.bruker.com), permission to use the marketing literature including component specifications in this thesis.[16]

**Detectors:** Figure 2.7 shows the sensitivity vs. wavenumber for a series of detectors applicable for different spectral regions, courtesy of Bruker Optics Corporation. The HgCdTe (MCT) detectors which require cryo-cooling are amongst the most frequently used detectors in the mid-IR region. DLaTGS type detector is less sensitive but operates at room temperature.

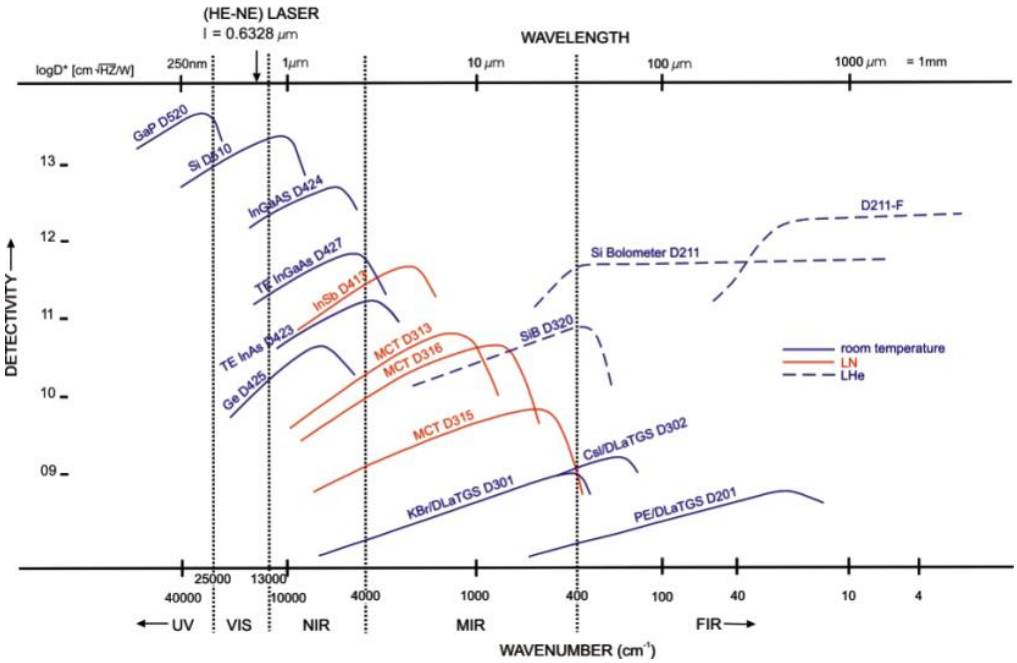


Figure 2.7. The detectivity vs. wavenumber for a series of detectors ranging from far-IR to UV, taken from "Guide for Infrared Spectroscopy" manual, courtesy of Bruker Corporation, (www.bruker.com), permission to use the marketing literature including component specifications in this thesis.[16]

### 2.4.2. Main components of the VCD module

**Photoelastic Modulator (PEM)**: The IR light source from the FTIR spectrometer is directed to the VCD compartment by means of several mirrors. To cut off the undesired ranges of frequencies, optical filters with different wavenumber coverage, for example up to 1800 $cm^{-1}$ or up 3800 $cm^{-1}$ can be used. A wire grid linear polarizer is used right after the IR filter to convert the randomly unpolarized light to the linearly polarized light polarized at a particular direction. The PEM, commonly made of ZnSe, is used to generate right or left circularly polarized light with a specific modulation frequency. The use of the modulation helps to obtain better quality VCD signals, which are typically 4 to 6 orders of

magnitude smaller than the normal IR absorption. The PEM consists of a piezoelectric transducer material fused to a transparent bar of silica, which produces the left and right circularly polarized light, LCPL and RCPL, respectively, at a modulation frequency of 50 kHz, see Figure 2.8.

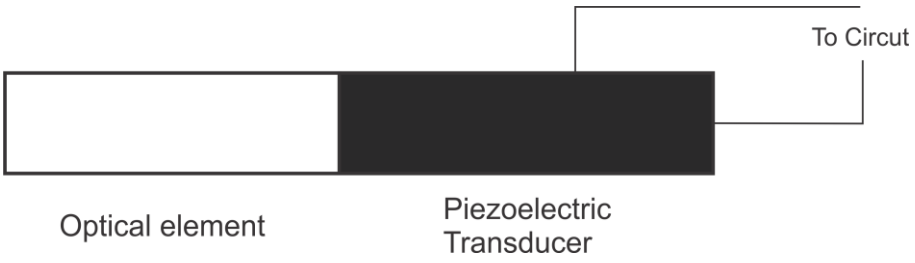


Figure 2.8. Representation of the block of piezoelectric transducer fused to a transparent bar of silica used in PEM.

The modulator axis of the PEM is aligned 45 degree to the incoming linearly polarized light. The linear polarized light can be viewed as two orthogonal components; one parallel and the other is perpendicular to the axis of the PEM. The birefringence of the transducer material changes as a current is applied to stretch or compress the material. The current is modulated at 50 kHz. Consequently, the speeds of the parallel and perpendicular components through the material are different and the light exit phases would be retarded accordingly. On the compress cycle, the perpendicular component of light is being retarded and the parallel one is left unaffected. When the optical device is in the stretch cycle, the parallel component is retarded while the perpendicular one is unaffected. The phase differences of 90 and 270 degrees will give rise to RCP and LCP light, respectively. The production of RCP and LCP light when linearly polarized light passes through a quarter-wave plate is illustrated in Figure 2.9. As

the phase difference of the two orthogonal components of linearly polarized light becomes larger and approaches 90 degrees, the spiral-propagating wave becomes elliptical and approaches circular. When the phase retardation is exactly 90 degrees, a perfect RCP is produced. In the next quarter cycle, as the phase difference becomes much larger than 90 degrees and reaches 180º, a linearly polarized light emerges right after the PEM. Then, in the stretch cycle, LCP is similarly generated. After passing through the chiral sample placed in a sample holder, the RCP and LCP lights are focused onto a liquid nitrogen cooled MCT detector.

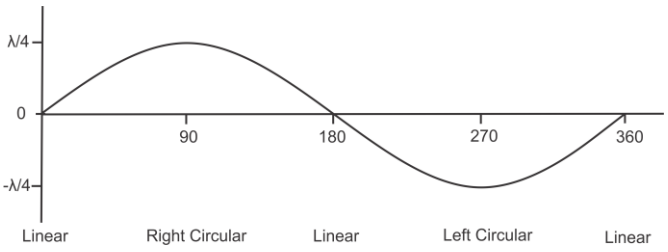


Figure 2.9. Production of the RCP and LCP lights as a linearly polarized light passes through a PEM. See text for details.

**Lock-in amplifier (LIA):** As indicated before, the VCD signal is the differential absorbance of the left and right circularly polarized light accompanying a vibrational transition, i.e. $\Delta A = A_L - A_R$. This difference is typically only about $10^{-4}$ to $10^{-6}$ of the magnitude of the parent IR band. To extract such a small signal, a LIA is utilized. In an FT-VCD experiment, the signal from the MCT detector is filtered using a low pass filter to obtain the dc signal which is then sent to the

usual FTIR electronics and computer software to provide the regular IR spectrum. For the VCD signal, the signal from the MCT detector is first filtered using a high pass filter. The reason for this step is to attenuate the modulation due to the interferometer. The treated signal is then sent to the LIA which is referenced to the PEM modulation frequency of 50 kHz to obtain the demodulated ac signal. The demodulated signal is then sent to the standard FTIR electronics. Finally, the VCD spectrum is generated by taking the ratio of the FT spectrum of the ac signal with respect to the related IR spectrum.

## 2.5. Running an experimental VCD measurement

There are several sample preparation techniques that can be used for IR and VCD measurements. Depending on the chemical properties, solubility, and the quantity available, one can choose the right method. Most commonly, the chemical is dissolved in a proper solvent, which hopefully does not have any significant vibrational absorption in the finger-print region, and injected between a pair of IR transparent windows. Care should be taken to adjust the concentration and path-length to get the absorbance of most bands between 0.2-0.9. The IR windows used are typically KBr, ZnSe, CsI, $CaF_2$, and $BaF_2$. Although, KBr and CsI windows provide cut-off down to 400 and 200 $cm^{-1}$, respectively, they are water soluble. The ZnSe window goes to down 700 $cm^{-1}$, but it is expensive and less transmissive than for example $BaF_2$. $BaF_2$ and $CaF_2$ are two commonly used mid-IR window materials, but the former is brittle and the latter cuts off around 1100 $cm^{-1}$.

For solid state and powder analyses, other techniques like KBr and KCl pellets, mull, and casting film can be used. The pellet technique is inexpensive and works with many solids, but the salt is hygroscopic and may react with the sample. The main problems with the mull technique are opacity and interference of the oil bands with sample spectra. For the purpose of my thesis, I have mainly used the solution technique with a pair of $BaF_2$ windows. Figure 2.10 shows the three sample holders, courtesy of Pike technologies Company.

To obtain a good quality VCD spectrum with high signal-to-noise ratio, the scan time needs to increase significantly compared to that for a standard IR spectrum. While 32 scans, which take less than a minute, are more than enough to obtain a reasonably good IR spectrum of a sample, 3 to 6 hours of measurements, i.e. 15000 to 25000 scans, are routinely used for a VCD experiment.

## 2.6. Computational strategies for spectral simulations

To interpret the experimental observation, the related spectral simulations are necessary. Both molecular dynamic (MD) simulations using AMBER (Assisted Model Building and Energy Refinement) suite of programs[17] and quantum chemistry methods using commercial software like Gaussian03[18] and Gaussian09[19] can be used for conformational searches and structural analyses. Less-expensive methods, such as universal force field (UFF)[20] molecular

mechanics (MM) or semi-empirical (SE) methods, such as AM1[21], PM3[22], PM6[23] Hamiltonians, are often used for initial conformational searches and provide reasonably good starting geometries. These initial geometries are then further investigated by means of high-level quantum chemistry. Density functional theory (DFT)[24] has been used for all theoretical modeling and spectral simulations in my thesis. The popular hybrid functional B3LYP, Becke three-parameter Lee-Yang-Parr,[25] is used for most of the calculations. This hybrid functional is pretty reliable in describing systems with strong hydrogen bonding tendency and in predicting VA and VCD intensities and frequencies.[26] If more than one conformer is present in solution for a typical molecule, a population-weighted spectrum needs to be calculated. The contribution of each conformer is weighted by their Boltzmann factors based on their relative energies.

A series of basis sets have been employed, such as 6-31G (d), 6-31++G (d, p), 6-311++G (d, p), cc-pVTZ, and aug-cc-pVTZ. Typically, I optimized the initial geometries in the gas phase or with PCM solvent model with the smallest basis set, i.e. 6-31G (d). This basis set is known as the best compromise of accuracy, speed, and computational cost. Further studies, depending on the size of the systems under investigation, have been carried out with larger basis sets in which more polarization and diffuse functions are employed.

To account for bulk solvent effects, the implicit solvation model such as PCM has been used. If strong hydrogen bonding interactions are present between solute and solvent molecules, it is necessary to consider explicit solute-solvent hydrogen-bonding clusters. Initial guesses of these solute-solvent clusters have

been generated by means of molecular dynamics simulations. In the case of water solvent, the combinatory implicit + explicit solvent models have been employed.

## References


[1] (a). G. Holzwarth, E. C. Hsu, H. S. Mosher, T. R. Faulkner, A. Moscowitz, *J. Am. Chem. Soc*., 1974, 96 (1), 251–252. (b). L. A. Nafie, J. C. Cheng, P. J. Stephens, *J. Am. Chem. Soc*., 1975, 97 (13), 3842–3843.

[2] G. A. Osborne, J. C. Cheng, P. J. Stephens, *Rev. Sci. Instrum*., 1973, 44, 10.

[3] (a). L. A. Nafie, M. Diem, *Appl. Spectrosc.*, 1979, *33*, 130. (b). L. A. Nafie, M. Diem, D. W. Vidrine, *J. Am. Chem. Soc.*, 1979, 101, 496. (c). E. D. Lipp, C. G. Zimba, L. A. Nafie, *Chem. Phys. Lett.*, 1982, 90, 1.

[4] M. A. Lowe, G. A. Segal, P. J. Stephens, *J. Am. Chem. Soc*., 1986, 108, 248-256.

[5] P. J. Stephens, M. A. Lowe, *Ann. Rev. Phys. Chem*., 1985, 36, 213-41.

[6] P. J. Stephens, *J. Phys. Chem.*, 1985, *89*, 148-752.

[7] (a) L. A. Nafie, T. H. Walnut, *Chem. Phys. Lett*., 1977, 49, 441. (b) T. H. Walnut, L. A. Nafie, *Chem. Phys*., 1977, 67, 1501.

[8] (a) L. A. Nafie, T. B. Freedman, *J. Phys. Chem*., 1983, 78, 7108. (b) R. Dutler, A. Rauk, *J. Am. Chem. Soc*., 1989, 111, 6957. (c) D. Yang, A. Rauk, *J. Chem. Phys*., 1992, 97, 6517.

[9] (a) K. L. C. Hunt, R. A. Harris, *J. Chem. Phys.*, 1991, 94, 6995. (b) P. Lazzeretti, M. Malagoli, R. Zanasi, *Chem. Phys. Lett.*, 1991, 179, 297.

[10] A. D. Buckingham, P. W. Fowler, P.A. Galwas, *Chem. phys*., 1987, 112, 1-14.

[11] P.J. Stephens, *J. Phys. Chem*. 1987, 91, 1712-1715.

[12] W. B. Person, J. H. Newton, *J. Chem. Phys*., 1974, 61, 1040.

[13] F. J. Delvin, P. J. Stephens, J. R. Cheesman, M. J. Frisch, J. Am. Chem. Soc, 1996, 118, 6327-6328.

[14] P. J. Stephens, *J. Phys. Chem.*, 1985, 89,748.

[15] J. He, A. Petrovich, P. L. Polavarapu, *J. Phys. Chem. A*, 2004, 108, 1671-1680.

[16] Guide for Infrared Spectroscopy manual, Bruker Corporation, Bruker Optics Inc. 19 Fortune Drive Billerica MA 01821.

[17] D.A. Case, T.A. Darden, T.E. Cheatham, III, C.L. Simmerling, J. Wang, R.E. Duke, R. Luo, R.C. Walker, W. Zhang, K.M. Merz, B. Roberts, S. Hayik, A. Roitberg, G. Seabra, J. Swails, A.W. Goetz, I. Kolossváry, K.F. Wong, F. Paesani, J. Vanicek, R.M. Wolf, J. Liu, X. Wu, S.R. Brozell, T. Steinbrecher, H. Gohlke, Q. Cai, X. Ye, J. Wang, M.-J. Hsieh, G. Cui, D.R. Roe, D.H. Mathews, M.G. Seetin, R. Salomon-Ferrer, C. Sagui, V. Babin, T. Luchko, S. Gusarov, A. Kovalenko, and P.A. Kollman, 2012, AMBER 12, University of California, San Francisco.

[18] Gaussian 03, Revision E.01, M. J. Frisch, G. W. Trucks, H. B. Schlegel, G. E. Scuseria, M. A. Robb, J. R. Cheeseman, J. A. Montgomery, Jr., T. Vreven, K. N. Kudin, J. C. Burant, J. M. Millam, S. S. Iyengar, J. Tomasi, V. Barone, B. Mennucci, M. Cossi, G. Scalmani, N.

Rega, G. A. Petersson, H. Nakatsuji, M. Hada, M. Ehara, K. Toyota, R. Fukuda, J. Hasegawa, M. Ishida, T. Nakajima, Y. Honda, O. Kitao, H. Nakai, M. Klene, X. Li, J. E. Knox, H. P. Hratchian, J. B. Cross, V. Bakken, C. Adamo, J. Jaramillo, R. Gomperts, R. E. Stratmann, O. Yazyev, A. J. Austin, R. Cammi, C. Pomelli, J. W. Ochterski, P. Y. Ayala, K. Morokuma, G. A. Voth, P. Salvador, J. J. Dannenberg, V. G. Zakrzewski, S. Dapprich, A. D. Daniels, M. C. Strain, O. Farkas, D. K. Malick, A. D. Rabuck, K. Raghavachari, J. B. Foresman, J. V. Ortiz, Q. Cui, A. G. Baboul, S. Clifford, J. Cioslowski, B. B. Stefanov, G. Liu, A. Liashenko, P. Piskorz, I. Komaromi, R. L. Martin, D. J. Fox, T. Keith, M. A. Al-Laham, C. Y. Peng, A. Nanayakkara, M. Challacombe, P. M. W. Gill, B. Johnson, W. Chen, M. W. Wong, C. Gonzalez, and J. A. Pople, Gaussian, Inc., Wallingford CT, 2004.

[19] Gaussian 09, Revision C.01, M. J. Frisch, G. W. Trucks, H. B. Schlegel, G. E. Scuseria, M. A. Robb, J. R. Cheeseman, G. Scalmani, V. Barone, B. Mennucci, G. A. Petersson, H. Nakatsuji, M. Caricato, X. Li, H. P. Hratchian, A. F. Izmaylov, J. Bloino, G. Zheng, J. L. Sonnenberg, M. Hada, M. Ehara, K. Toyota, R. Fukuda, J. Hasegawa, M. Ishida, T. Nakajima, Y. Honda, O. Kitao, H. Nakai, T. Vreven, J. A. Montgomery, Jr., J. E. Peralta, F. Ogliaro, M. Bearpark, J. J. Heyd, E. Brothers, K. N. Kudin, V. N. Staroverov, R. Kobayashi, J. Normand, K. Raghavachari, A. Rendell, J. C. Burant, S. S. Iyengar, J. Tomasi, M. Cossi, N. Rega, J. M. Millam, M. Klene, J. E. Knox, J. B. Cross, V. Bakken, C. Adamo, J. Jaramillo, R. Gomperts, R. E. Stratmann, O. Yazyev, A. J. Austin, R. Cammi, C. Pomelli, J. W. Ochterski, R. L. Martin, K. Morokuma, V. G. Zakrzewski, G. A. Voth, P. Salvador, J. J. Dannenberg, S. Dapprich, A. D. Daniels, Ö. Farkas, J. B. Foresman, J. V. Ortiz, J. Cioslowski, and D. J. Fox, Gaussian, Inc., Wallingford CT, 2009.

[20] A. K. Rappé, C. J. Casewit, K. S. Colwell, W. A. Goddard III, and W. M. Skiff, *J. Am. Chem. Soc*., 1992, 114 10024-35.

[21] M. J. S. Dewar, E. G. Zoebisch, and E. F. Healy, *J. Am. Chem. Soc*.,1985, 107, 3902-09.

[22] J. J. P. Stewart, *J. Comp. Chem*., 1989, 10, 209-20.

[23] J. J. P. Stewart, *J. Mol. Model*., 2007, 13, 1173-213.

[24] (a). P. Hohenberg and W. Kohn, *Phys. Rev*., 1964, 136, B864-B71. (b). W. Kohn and L. J. Sham, *Phys. Rev*., 1965, 140, A1133-A38. (c). J. K. Labanowski, J. W. Andzelm, Density functional Methods in Chemistry, Springer-Verlag: New York, 1991.

[25] (a) A. D. Becke, *J. Chem. Phys*., 1993, 98, 5648. (b) C. T. Lee, W. T. Yang, R. G. Parr, *Phys. Rev. B-Condens. Matter*., 1988, 37, 785.

[26] (a) P. J. Stephens, F. J. Devlin, C. F. Chabalowski, M. J. Frisch, *J. Phys. Chem*., 1994, 98, 11623. (b) T. Kuppens, W. Langenaeker, J. P. Tollenaere, P. Bultinck, *J. Phys. Chem. A*, 2003, 107, 542. (c) T. Kuppens, K. van der Vandyck, J. Eycken, W. Herrebout, B. J. van der Veken, P. Bultinck, *J. Org. Chem*., 2005, 70, 9103. (d) T. Kuppens, W. Herrebout, B. van der Veken, P. Bultinck, *J. Phys. Chem. A*, 2006, 110, 10191. (e) Ducasse, F. Castet, A. Fritsch, I. Huc, T. Buffeteau, *J. Phys. Chem. A*, 2007, 111, 5092. T. Brotin, D. Cavagnat, J.- P. Dutasta, T. Buffeteau, *J. Am. Chem. Soc*., 2006, 128, 5533.

# 3 Chapter

## A comparative VCD study of methyl mandelate in methanol, dimethyl sulfoxide, and chloroform: explicit and implicit solvation models

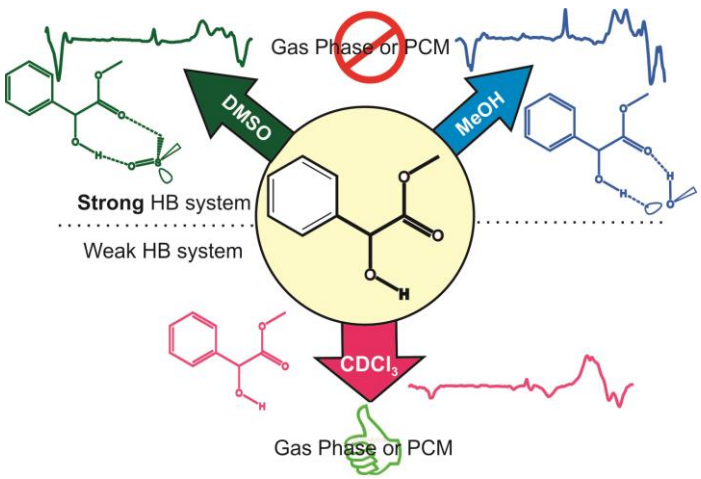


**This chapter is directly copied from the published paper:**

M. R. Poopari, Z. Dezhahang, Y. Xu, "A comparative VCD study of methyl mandelate in methanol, dimethyl sulfoxide, and chloroform: explicit and implicit solvation models", Phys. Chem. Chem. Phys., 15, 2013, 1655-1665.

## 3.1. Introduction

Chiroptical spectroscopy, such as vibrational circular dichroism (VCD) spectroscopy, in combination with density functional theory (DFT) calculations, has emerged in recent years as a powerful new tool to probe absolute configurations and conformations of chiral molecules in solution.[1,2] To achieve a reliable interpretation, it is often necessary to consider effects of solvents since solvents can have significant and non-intuitive effects on the corresponding chiroptical measurements.[3-5] It had been demonstrated experimentally that the water bending vibrational mode can gain markedly VCD intensity in chiral aqueous solutions[6-9] and such chirality transfer VCD signatures are highly sensitive to the hydrogen-bonding network consisting of the chiral solute and the surrounding water molecules.[10,11] For example, chirality transfer effects and effects of solvent in general in VCD spectra of methyl lactate, a simple chiral α-hydroxyester, in water[6] and in methanol,[12] had been investigated.

Methyl mandelate (MM), methyl 2-hydroxy-2-phenylacetate (IUPAC), is a relatively small chiral α-hydroxyester with multi-functional groups, including a phenyl ring. It was chosen as the model chiral molecule for investigation of solvent effects because it has a few interesting features. First, it has a number of electronegative atoms and a hydroxyl hydrogen atom, thus offering a range of intermolecular hydrogen-bonding options with suitable solvent molecules in solution. Second, as an α-hydroxyester, it has an intramolecular OH···O=C hydrogen bond, providing the opportunity to

examine the competition between intra- and intermolecular hydrogen bonding interactions. Third, the presence of a phenyl ring with delocalized electrons may give rise to different chemistry compared to methyl lactate and influence the closeness and orientation of solvent molecules that are hydrogen-bonded to MM. Indeed, the solubility of MM in aqueous solution is much lower than methyl lactate because of the replacement of its methyl group by a bulky phenyl group. On the other hand, MM is highly soluble in organic solvents such as methanol, dimethyl sulfoxide (DMSO), and chloroform. While vibrational absorption (VA) spectra of MM in carbon tetrachloride were investigated before,[13] its VCD spectra in the CH and OH stretching regions were also reported previously.[14] Kuppens et al. used MM as an example to showcase VCD spectroscopy as a powerful tool to determine absolute configurations of chiral molecules in solution.[15] More recently, Albrecht et al. studied the self-aggregation pattern of MM and unravelled the influence of relative chirality of the aggregating monomers by means of several spectroscopic techniques, such as matrix-Fourier transform infrared (FTIR) and jet-FTIR spectroscopy.[16] Finally, MM and its associated free mandelic acid are also of practical importance in the field of enantioselective chemistry for their usage in separation of racemates.[17]

In the current study, VA and VCD spectra of MM in a series of organic solvents, namely methanol, dimethyl sulfoxide, and chloroform have been measured to unveil the effects of MM-solvent interactions. The main focus is on how different degrees of hydrogen-bonding capability of solvents influence

the outcome of VCD measurements and on developing a strategy to model the solvent effects adequately in all cases. Molecular dynamic (MD) simulation and the corresponding radial distribution functions (RDFs) have been utilized to examine how MM molecules behave in methanol solution. To properly account for solvation effects, both the implicit polarizable continuum model (PCM) and the explicit solvation models have been considered separately and jointly. As pointed out by Polavarapu and co-workers, a combination of different chiroptical techniques usually gives rise to more reliable interpretations of chiroptical measurements.[18] This is because different chiroptical techniques, such as VCD spectroscopy and optical rotation dispersion (ORD) spectroscopy, are all sensitive to environmental perturbations but with various degrees of sensitivity to specific chemical and physical properties. We have therefore further carried out experimental ORD measurements and theoretical modeling to verify if the conclusions reached with the VA and VCD investigations are also supported by the ORD studies.

## 3.2. Experimental and theoretical details

### 3.2.1. FTIR VA and VCD measurements.

(S)-(+)-MM (99%), (R)-(-)-MM (99%), and the racemic MM were purchased from Alfa Aesar and used without further purification. Three different solvents, i.e. MeOH-$d_4$, DMSO-$d_6$, and $CDCl_3$, all fully-deuterated, were purchased from Sigma Aldrich and used for the VA and VCD

measurements. The corresponding spectra of MM in carbon tetrachloride which had been reported before[15] were re-measured to provide comparison with those obtained in the other three solvents. The experimental VA and VCD spectra were obtained using an FTIR spectrometer (Vertex 70, Bruker) equipped with a VCD module (PMA50, Bruker) at room temperature.[6] To obtain reproducible and good quality VCD spectra, the concentration and path length were optimized to ensure that the VA absorbance for the most VA bands in the frequency region of interest is between 0.2 and 0.8. Since the absorption strength of the carbonyl stretching band is about a factor of two or more larger than the other vibrational bands, separated VCD measurements were carried out for the region above and below 1650 $cm^{-1}$. The upper frequency region was measured with a 0.1 mm PTFE spacer (International Crystal laboratory) and a concentration of 0.30 M. The region below 1650 $cm^{-1}$ was measured with twice the concentration and the same path length. All VCD spectra were measured with a total time duration of 3 h (3 x 1h), or about ~13000 scans, and with a resolution of 4 $cm^{-1}$, except in the case of methanol where we used 6 x 0.5h because of the much higher volatility of methanol than the other solvents at room temperature. For baseline correction, the final VCD spectra were obtained by subtracting the corresponding spectra of racemic MM in the respective solvents measured under identical condition.

### 3.2.2. ORD measurements.

Solutions with 0.06, 0.30, and 0.60 M of MM in methanol and chloroform, and 0.06, 0.30, 0.60, and 1.20 M of MM in dimethyl sulfoxide were prepared. The ORD data were collected at a series of wavelengths at 589 nm of sodium D line, and at 578, 546, 436, and 365 nm of mercury lamp, by means of a Perkin-Elmer 240 polarimeter.

### 3.2.3. DFT calculations.

The Gaussian 03[19] and 09[20] program packages were used for all the geometry optimizations, harmonic frequency calculations, and the calculations of the VA and VCD intensities at the B3LYP/cc-pVTZ level. For the calculations of ORD spectra, time-dependent (TD) DFT at the B3LYP/cc-pVTZ level of theory was utilized. A Lorentzian line shape with a half-width at half-height (HWHH) of 4 $cm^{-1}$ was used for simulations of VA and VCD spectra. For MM in methanol (MeOH-$d_4$), there is D/H exchange and the hydroxyl hydrogen atom of MM is replaced by D in all the calculations. In the other two solvents, no D/H exchanges are expected. The integral equation formalism (IEF) version of PCM[21] using universal force field (UFF) radii was applied in order to account for the effects of solvent molecules implicitly. For this purpose, the dielectric constants of 32.61, 46.82, and 4.71 were used for methanol, dimethyl sulfoxide, and chloroform, respectively. For the ORD calculations, excitation wavelengths, λ, at 589, 578, 546, 436, and 365 nm

were used. No scaling factor was applied for the comparisons of the simulated results with the experimental ones.

### 3.2.4. MD simulation.

The Amber 11 suite of programs[22] was utilized to perform MD calculations of MM in a specific solvent using the PMEMD module. The goal here was to locate the sites for strong hydrogen-bonding interactions between the solute and solvent molecules and to estimate the number of solvent molecules which are explicitly hydrogen-bonded to MM. The AMBER ff99 force field based on molecular mechanics approximation was used. A rectangular periodic box with 888 pre-equilibrated methanol molecules with a cut-off of 16.0 Å was used to solvate the MM molecule. A four-step MD simulation was carried out in this study. First, the system was minimized using 1000 steps of steepest descent algorithm, followed by 1000 steps of conjugate gradient algorithm. Then, a 200 ps heating from 0 K to 300 K under NVT ensemble was conducted. After that, the whole system was equilibrated for a duration of 400 ps at 300 K. Lastly, a 5 ns production MD was done under NPT condition. RDFs were calculated to estimate the number of solvent molecules directly hydrogen-bonded to MM within the first shell of solvation.

## 3.3. Results and Discussions

### 3.3.1. Comments on the experimental VA and VCD spectra in different solvents

Figure 3.1 shows the comparison of the experimental VA and VCD spectra of MM in MeOH-$d_4$, DMSO-$d_6$, and $CDCl_3$ in the region of 1800-1150 $cm^{-1}$. Despite an overall similarity among the three VA spectra and among the three VCD spectra, there are noticeable differences in the VCD spectra among these three solvents. At the highest wavenumber region, i.e. the carbonyl stretching region, while MM in $CDCl_3$ shows a more or less symmetric peak, the corresponding band in DMSO has a noticeable shoulder and the main peak is blue shifted, whereas the band in methanol is substantially broader and is also blue shifted compared to that in $CDCl_3$. In the middle section of 1700-1350 $cm^{-1}$, the VA spectra of all three look similar, whereas the VCD features are somewhat different. The most noticeable difference is the negative VCD band at ~1392 $cm^{-1}$ in $CDCl_3$ which is missing in the other two solvents. In the lowest wavenumber region of 1350-1150 $cm^{-1}$, vibrational bands show severe overlapping and the resulting VA and VCD spectra appear quite different among the three solvents. For example, the VCD features show the +/+/-/- pattern in the chloroform solution, which turn into the +/+/+/- sequence in DMSO and methanol. Compared to the VA spectra, the differences among the three solvents are generally more distinctive in the VCD spectra since VCD signatures are often considerably more sensitive than VA patterns to the conformational distribution and the solvent environments. For completion, the

corresponding VA and VCD spectra of MM in $CCl_4$ are also compared with the corresponding spectra in $CDCl_3$ in Figure A1, supporting information, Appendix A. The spectra obtained in $CCl_4$ are essentially the same as those published previously.[15] It is also noted that the VA and VCD spectra of MM in $CDCl_3$ and $CCl_4$ look essentially identical, suggesting that the dominant species in these two solvents are the same.

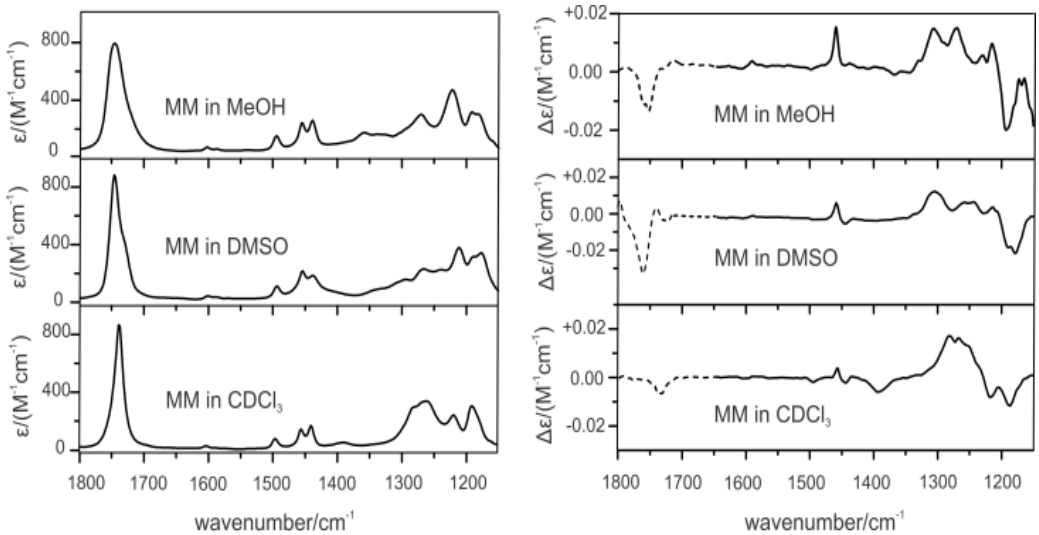


Figure 3.1. Experimental VA (left) and VCD (right) spectra of MM in three different organic solvents. The VCD carbonyl stretching sections marked with dotted lines were measured with half of the concentration used for the rest of the spectra to avoid saturation (see experimental section for details).

### 3.3.2. Different approaches to simulate VA and VCD spectra of MM in solution

Several approaches have been undertaken in order to adequately account for the experimental features observed, to gain insights into the solute-solvent interactions, and to establish some general rules in dealing with

solvents with different degrees of hydrogen-bonding capability. The first step is to establish the lowest energy conformers of MM and simulate its gas phase VA and VCD spectra. This is described in the next section. Next, to account for the different VA and VCD spectral features observed, one needs to systematically investigate and compare the effects of these three very different solvents. For example, they have very different dielectric constants, with Ɛ=32.613, 46.826, and 4.7113, for methanol, dimethyl sulfoxide, and chloroform, respectively. Their ability in making hydrogen-bonds with MM also varies. Methanol solvent is considered as a polar protic solvent and has an acidic proton capable of hydrogen-bonding interaction. Chloroform is a nearly non-polar solvent with three withdrawing atoms attached to a carbon atom, thus its hydrogen atom is more acidic compared to those of methane. Lastly, dimethyl sulfoxide is a polar aprotic solvent with no acidic hydrogen atoms capable of hydrogen-bonding interaction. Rather, it acts as a hydrogen-bond acceptor agent. Since the approaches used for the solvents capable or not capable of hydrogen-bonding interactions will be different, the simulated VA and VCD spectra of MM in methanol and in DMSO are discussed in s*trongly solute-solvent hydrogen-bonded systems* section, whereas those of MM are in chloroform in *systems with no strong solute-solvent hydrogen-bonds* section.

### 3.3.3. Search for the lowest energy conformers of MM

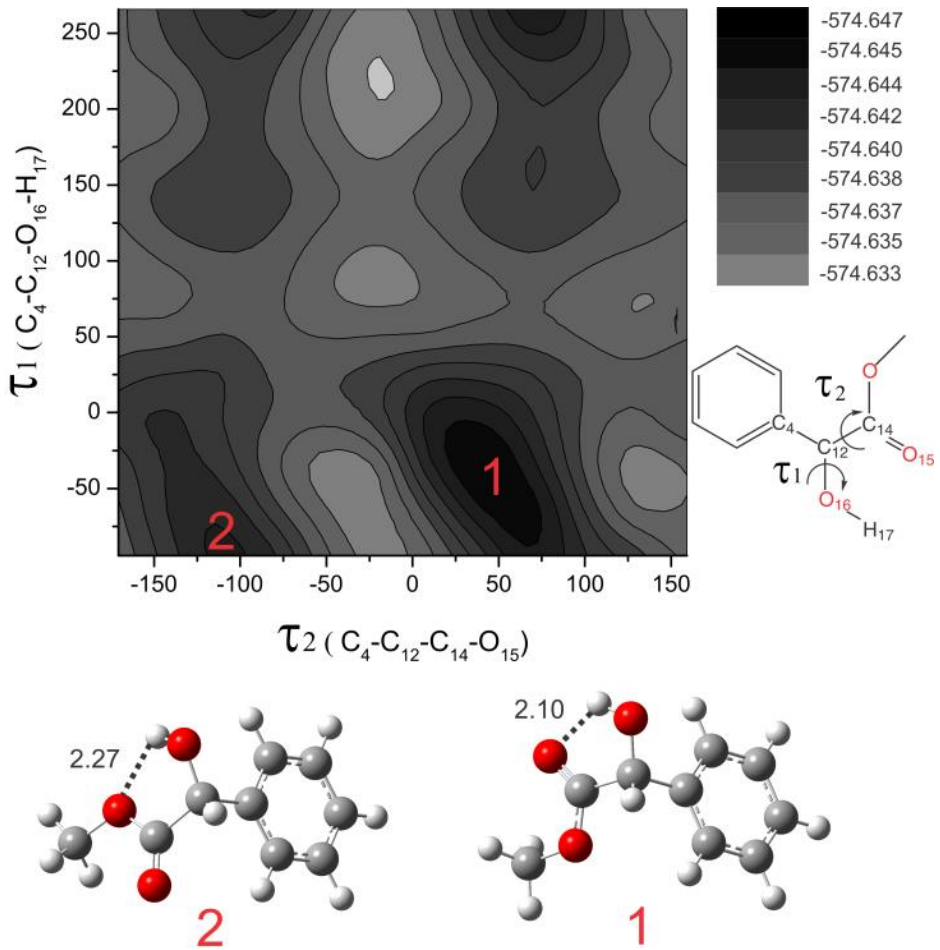


Figure 3.2. Two-dimensional PES plot of MM at the B3LYP/6-31G(d) level, scanned along its two dihedral angles, $\tau_1$ and $\tau_2$ (in degree). The atom labelling of MM and the motions associated with these two dihedral angles are provided at the side bar. See text for the detailed definitions of these two dihedral angles. The energy unit is in Hartree. The optimized geometries of the two most stable MM conformers are also shown at the bottom. The hydrogen-bonding distances (in Å) are also indicated.

The MM molecule has a number of rotatable single bonds which can bring about new conformations. Two dihedral angles, namely $\tau_1$ ($C_4$-$C_{12}$-$O_{16}$-$H_{17}$) and $\tau_2$ ($C_4$-$C_{12}$-$C_{14}$-$O_{15}$), corresponding to rotation around the $C_{12}$-$O_{16}$ and $C_{12}$-$C_{14}$ bonds, (see Figure 3.2 for atom labelling) are the most effective dihedral angles in generating new conformations. A potential energy surface

(PES) scan along these two dihedral angles was carried out at the B3LYP/6-31G(d) level. The level of theory was chosen because it offers a good combination of accuracy and computational efficiency. The two-dimensional plot of the PES scan along those two aforementioned dihedral angles is depicted in Figure 3.2. As one can see, the deepest minimum detected is related to the most stable structure of MM with $\tau_1$ = -64.2˚and $\tau_2$ = 69.2˚ where the hydroxyl hydrogen atom points at the O atom of the carbonyl group to form an intramolecular hydrogen-bonded ring. Based on the PES plot, there is a second minimum at $\tau_1$ = -64.2˚and $\tau_2$ = -110.7˚where the intramolecular hydrogen-bond acceptor is the ester O atom rather than the carbonyl O atom in the most stable structure. These two structures were optimized at the B3LYP/cc-pVTZ level and the resulting geometries are also included in Figure 3.2. We also performed a transition state calculation to estimate the conversion barrier between these two minima at the B3LYP/cc-pVTZ level of theory. The result is provided in Figure A2, supporting information, Appendix A. The relative free energy difference between these two conformers is about 10 kJ/mol and the conversion barrier is ~34 kJ/mol from the most stable conformer to the second most stable one. Consequently, the most stable conformer is the only conformer which contributes significantly at room temperature and is therefore the only one considered in the following treatments of solvent effects.

### 3.3.4. Strongly solute-solvent hydrogen-bonded systems

**Methanol.** The simulated VA and VCD spectra of the MM monomer in the gas phase and with PCM of methanol are shown in Figure 3.3. The simulated gas phase VA and VCD spectra are very different from the experimental ones, making it not possible to assign the spectra accordingly. The inclusion of the bulk methanol with PCM has improved the agreement between theory and experiment noticeably. In particular, the relative intensities of the VA bands in the 1350-1150 $cm^{-1}$ region are in better agreement with the experimental one, so are the VCD features in the same region. However, there are still considerable differences which make the assignments somewhat ambiguous. For example, the relative intensities of the VCD features in the 1350-1150 $cm^{-1}$ region are still not in accord with the experiment. While only one relatively weak negative VCD band at the lowest wavenumber end was predicted with the implicit methanol solvation model, two strong negative VCD bands were detected experimentally. The band width of the carbonyl stretch is substantially broader compared to that in $CDCl_3$ or $CCl_4$, suggesting hydrogen-bonding interactions with methanol. Therefore, explicit solvation of MM by methanol was considered in the following.

To facilitate the construction of the MM-methanol clusters, RDF calculations were performed for MM in methanol. The RDFs of MM in methanol are provided in Figure A3, supporting information, Appendix A.

Each RDF represents the probability of finding an atom of methanol molecules at a distance (r) from a center atom of MM.

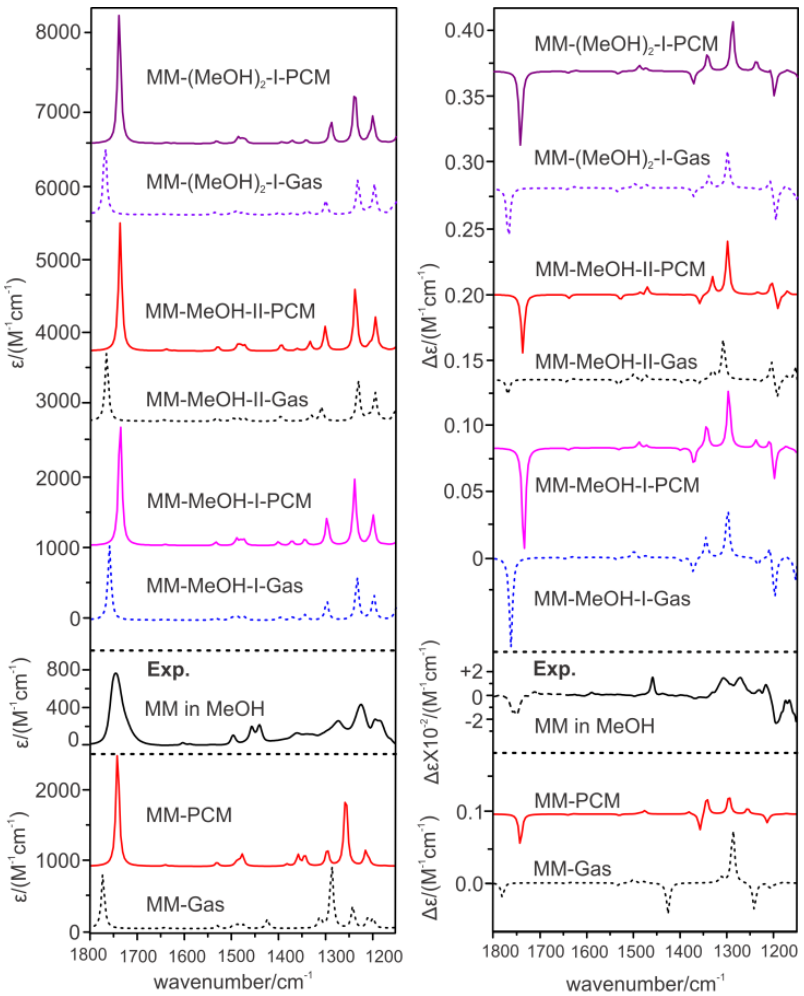


Figure 3.3. Comparisons of the experimental VA/VCD spectra of MM in MeOH (middle) with the corresponding spectra of the MM monomer in the gas phase and with PCM (bottom) and of the two most stable 1:1 MM-MeOH conformers and the most dominant 1:2 MM-$(MeOH)_2$ conformer in the gas phase and with PCM (top) calculated at the B3LYP/cc-pVTZ level at room temperature.

For example, g(r)O1Hm shows the probability of finding the hydrogen atom of methanol molecules at a distance r from the carbonyl oxygen atom of MM. Om and Hm refer to the O and H atoms of methanol. The particular RDF

has a well-defined sharp first maximum at ~1.89 Å, indicating hydrogen-bonding nature of the interaction. The integration to the first minimum provides a number of 1.57 which implies that on average, about one or two methanol molecules are directly hydrogen-bonded to MM at this site. On the other hand, the RDF corresponding to the intermolecular interaction between the ester O atom of MM with the H atom of methanol, shows no well- defined peaks. This indicates no strong hydrogen-bonding interaction with methanol at this site of MM on average.

Based on the RDF results, MM is most likely hydrogen-bonding to methanol through O2H1¨Om and (C=)O1¨Hm interactions. The integrated values to the first minimum suggest that on average there can be one or two methanol molecules directly hydrogen-bonded to MM. Therefore, several explicit 1:1 and 1:2 MM-methanol binding models were proposed accordingly. The first one is where one methanol molecule is inserted into the existing intramolecular hydrogen-bonding ring and is hydrogen bonded respectively to $O_1$ and $H_1$ as a proton donor and acceptor. This results in two 1:1 conformers, i.e. MM-MeOH-I and MM-MeOH-II, where the methyl group of methanol and the phenyl ring are at the opposite or the same side of the intramolecular hydrogen-bonded ring, respectively. Such insertion conformers [6,7,23] are much more stable than the addition conformers where the methanol molecule is associated through intermolecular hydrogen-bonding to the O atom of the carbonyl or hydroxyl group, without breaking the existing intramolecular hydrogen-bond of MM. The more subtle preference for MM-MeOH-I versus

II is due to the repulsion between the phenyl ring and the methyl group. MM-MeOH-I is considerably more favourable than II since its phenyl group is further away from the methyl group of methanol.

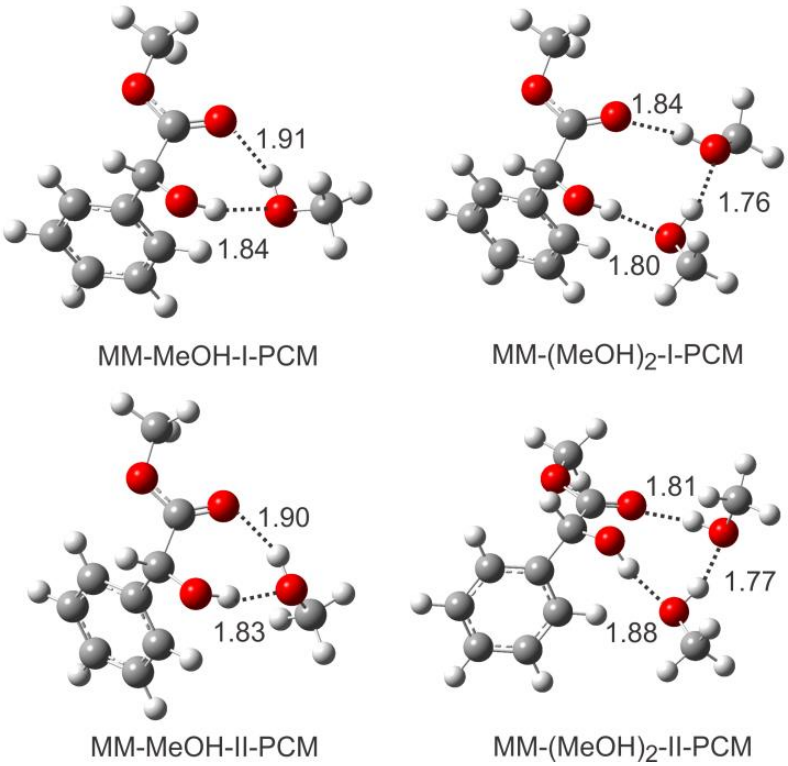


Figure 3.4. Optimized geometries of the most stable conformers of the 1:1 MM-MeOH and 1:2 MM-$(MeOH)_2$ complexes at the B3LYP/cc-pVTZ level with the PCM of methanol. The intermolecular hydrogen-bond lengths (in Å) are indicated.

**Table 3.1.** The relative free energies of the most stable 1:1 and some 1:2 MM-solvent complexes

| Solvent | Complexes | ΔG (kcal/mol)[a] | pop%[a] |
|---|---|---|---|
| Methanol | MM-MeOH-I | 0.00 (0.00) | 80.4 (75.6) |
| | MM-MeOH-II | 0.84 (0.67) | 19.6 (24.4) |
| | MM-$(MeOH)_2$-I | 0.00 (0.00) | 70.40 (93.4)[b] |
| | MM-$(MeOH)_2$-II | 0.73 (1.57) | 20.44 (6.5) |
| | MM-$(MeOH)_2$-III | 1.34 | 7.28 |
| DMSO | MM-DMSO-I | 0.00 (0.00) | 99.0(94.7) |
| | MM-DMSO-II | 2.70 (1.64) | 1.0(5.9) |
| $CDCl_3$ | MM-$CDCl_3$-I | 0.00 | 94.3 |
| | MM-$CDCl_3$-II | 1.72 | 5.1 |
| | MM-$CDCl_3$-III | 2.99 | 0.6 |

[a] The gas phase values obtained at the DFT/B3LYP/cc-pVTZ level. The corresponding values with the PCM of the respective solvents are in brackets. [b]Only the two most stable 1:2 conformers were calculated with the PCM of methanol.

We also evaluated the 1:2 MM-$(MeOH)_2$ clusters. The second methanol molecule can be inserted into the existing intermolecular hydrogen-bonded ring to form a larger concerted hydrogen-bonded ring, resulting in an insertion complex. Or it can be hydrogen-bonded to the oxygen atom of the carbonyl or hydroxyl group, leaving the existing intermolecular hydrogen-bonded ring in the 1:1 complex intact. It was shown in a number of previous studies[6,12] that the so-called insertion complexes of the type of MM-$(MeOH)_2$-I and II are substantially more stable than the purely association or mixed insertion and association complexes such as MM-$(MeOH)_2$-III and IV, Figure A4, Appendix A. The association of the hydrogen atom of methanol to the lone pair of the ester O atom was found to be much less favorable compared to the O2H1···Om and (C=)O1···Hm interactions, consistent with the previous finding.[24-26] This observation was also supported by the RDF results reported

here, showing no well-defined sharp peaks, thus no hydrogen-bonding interaction at the ester O site.

How about the effects of the rest of methanol molecules? It was shown in a few previous studies that the addition of even just one more solvent molecule may significantly influence the prefer binding sites at the solute molecules[27,28] and also alter the appearance of the VCD spectrum.[6,8,12,29] On the other hand, to build up several explicit solvation layers of methanol molecules surrounding a MM molecule would be prohibitively expensive computationally. To this end, we have taken the approach to apply the continuum solvation model, i.e. PCM, around the explicitly solvated 1:1 and 1:2 MM-methanol clusters to account for the effects of surrounding bulk methanol molecules. Such combined explicit and implicit solvation approach was used recently to account for the solvation effects of an amino acid in aqueous solution.[30] It would be of considerable interest to verify if this approach is generally applicable for the cases when strong solute-solvent hydrogen-bonding interactions are expected.

The equilibrium geometries obtained for the 1:1 and 1:2 complexes were re-optimized with the PCM of methanol. The final optimized geometries of the dominant 1:1 and 1:2 conformers with PCM of methanol are given in Figure 3.4, together with the important hydrogen-bonding distances. The corresponding gas phase structures are provided in Figure A4, supporting information, Appendix A. Only relatively small changes in geometries were observed with the inclusion of PCM. It seems that the addition of bulk

methanol by PCM in general strengthens the strongest intermolecular hydrogen-bond in the complex, and weakens the other intermolecular hydrogen-bonding interactions slightly. These are evidenced by the shortening or lengthening of the respective hydrogen-bond lengths in Figure 3.4 and Figure A4, Appendix A. The relative free energies of the most stable 1:1 and 1:2 MM-methanol conformers in the gas phase and with PCM are summarized in Table 3.1, together with their Boltzmann population factors at room temperature. The numbers I, II, and etc. in the names indicate the most stable, the second most stable, and etc. conformers of each class of the complexes, respectively. It is noted that the relative stability ordering of these conformers does not alter with the addition of PCM.

The simulated VA and VCD spectra of the dominant 1:1 and 1:2 MM-methanol conformers in the gas phase and with PCM of methanol are also depicted in Figure 3.3, together with the experimental VA and VCD spectra of MM in methanol. For completion, the corresponding VA and VCD spectra of the minor 1:2 conformers, which contribute in total less than 7% are given in Figure A5, supporting information, Appendix A. From Figure 3.3, one can see that the VA spectrum of the dominant MM-MeOH-I conformer (~80%) with PCM shows better agreement in terms of relative VA band intensities in the 1350-1150 $cm^{-1}$ region with experiment. More importantly, the VCD features of MM-MeOH-I with PCM in the same region agree much better with the experimental ones than the implicit solvation model alone. Not only their signs and their amplitudes, but also their frequency positions are better predicted.

The importance of the further inclusion of the PCM model with the explicit solvation model can be appreciated by comparison between MM-MeOH-I in the gas phase and with PCM. First, the predicted band frequencies moved closer to their experimental values with PCM. Second, the negative VCD band of MM-MeOH-I at ~1234 $cm^{-1}$ changed its sign with the inclusion of PCM and is now in agreement with the experiment. It is interesting to note that the VA and VCD spectra of the 1:2 MM-$(MeOH)_2$-I conformer with PCM which has over 93% population at room temperature, are essentially the same as those of MM-MeOH-I with PCM. Overall, the combined explicit and implicit solvation model provides satisfactory interpretation of the observed VA and VCD spectra of MM in methanol and gives better performance than either models alone.

**Dimethyl sulfoxide.** Compared to methanol, dimethyl sulfoxide does not have any acidic hydrogen atom and consequently the solute-solvent hydrogen-bonding interaction occurs only when the oxygen atom of a dimethyl sulfoxide molecule is placed in close proximity of the hydrogen atom of the hydroxyl group of MM.

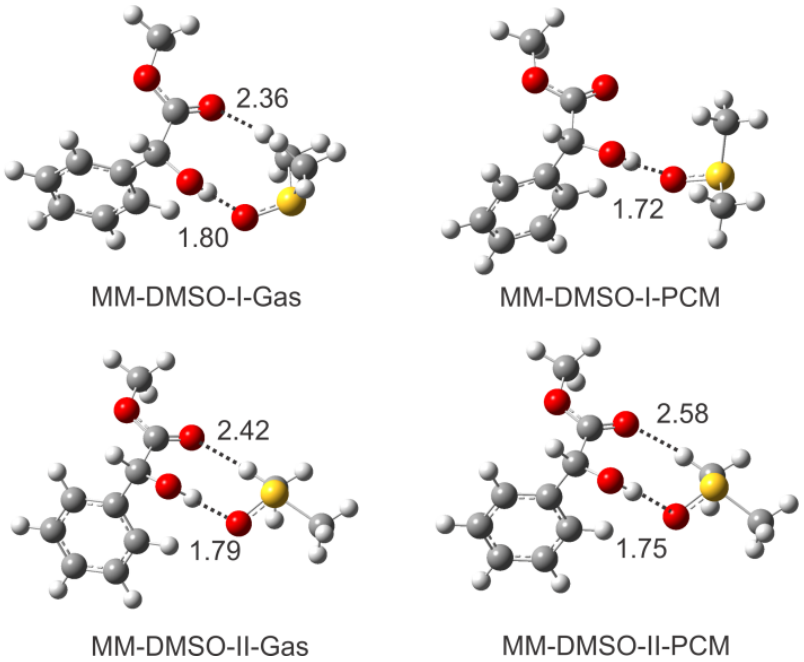


Figure 3.5. Optimized geometries of the two most stable 1:1 conformers of MM-DMSO at the B3LYP/cc-pVTZ level in the gas phase and PCM. The important intermolecular distances less than 3.0 Å are indicated.

For this reason, only the 1:1 MM-DMSO complex was considered for the explicit solvation of MM in dimethyl sulfoxide. Two lowest energy conformers, MM-DMSO-I and II were identified. These two conformers are related to whether the phenyl ring and the methyl group of DMSO are at the opposite or the same side of the intermolecular hydrogen-bonded ring, as shown in Figure 3.5. MM-DMSO-I where the methyl group points further away from the phenyl ring of MM is much more stable than MM-DMSO-II where the distance between these two groups is closer. In the gas phase, a secondary hydrogen-bond between the hydrogen atom of the methyl group of DMSO and the O atom of the carbonyl group of MM is noted for both conformers, evidenced by their 2.36 Å and 2.42 Å intermolecular bond lengths

in Figure 3.5. These two conformers were re-optimized with PCM of DMSO and the corresponding geometries are also provided in Figure 3.5. It is interesting to note that the bulk DMSO seems to strengthen the primary hydrogen-bond, and on the other hand, weaken the secondary hydrogen-bonding interaction. While the primary hydrogen-bond (S=O···H) length is shortened by about 0.08 to 0.04 Å in these two conformers, the secondary hydrogen-bond length increased significantly from 2.36 to 3.72 Å in MM-DMSO-I and from 2.42 to 2.58 Å in MM-DMSO-II when the PCM of DMSO was applied. Similar phenomena but to a lesser degree have also been observed for the methanol case when the PCM of solvent was applied to the explicit solvation models. Nevertheless, MM-DMSO-I remains the dominant one in solution. The relative free energies and the Boltzmann factors at room temperature of these two conformers in the gas phase and with PCM of DMSO at the B3LYP/cc-pVTZ level of theory are summarized in Table 3.1.

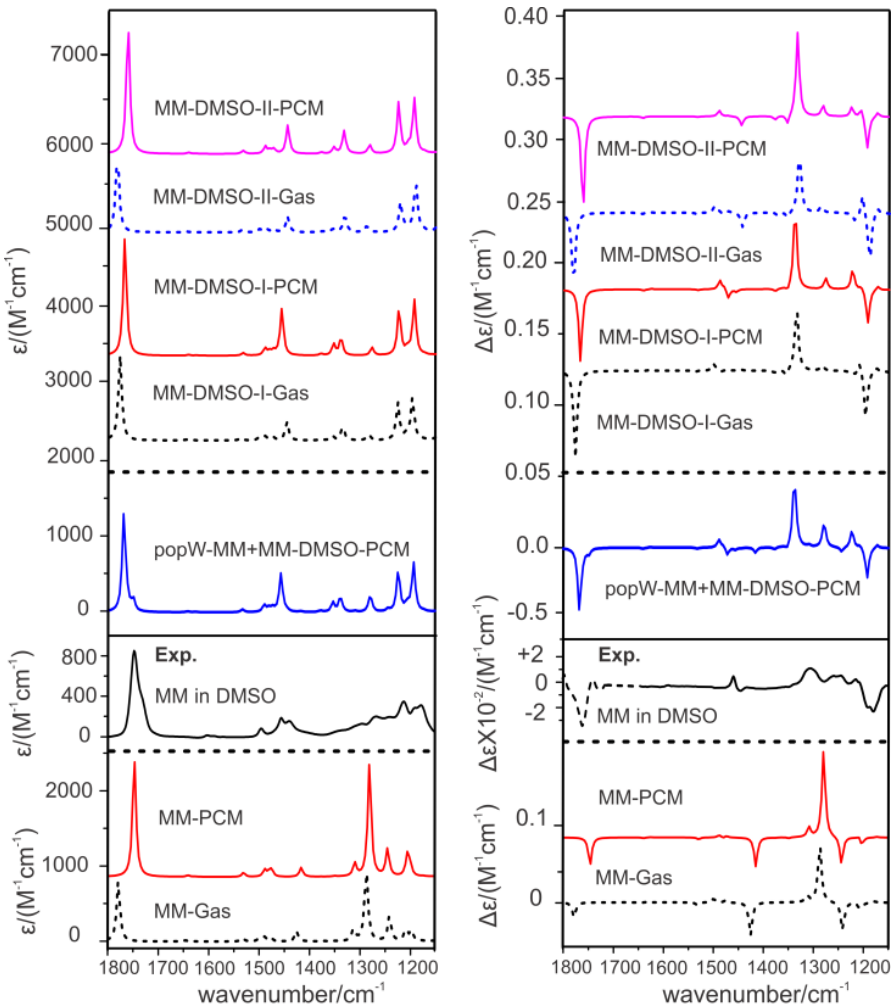


Figure 3.6. Comparisons of the experimental VA and VCD spectra of MM in DMSO (middle) with the corresponding simulated spectra of the gas phase and PCM of the MM monomer (bottom) and of the two most stable 1:1 MM-DMSO clusters in the gas phase and with PCM (top) calculated at the B3LYP/cc-pVTZ level. The empirically population weighted VA and VCD spectra of MM and MM-DMSO at room temperature are also presented (see text for details).

In Figure 3.6, the simulated VA and VCD spectra of the MM monomer and the 1:1 MM-DMSO complex in the gas phase and with PCM are compared with the experimental spectra obtained in DMSO. Both the VA and VCD spectra of the MM monomer in the gas phase and with PCM show noticeable disagreement in the 1350-1150 $cm^{-1}$ region with the respective

experimental data. From Figure 3.6, it is obvious that neither the gas phase nor the PCM model of the MM monomer alone can bring out all the main experimental features observed. In particular, the VA intensity pattern of the bands in the 1350-1150 $cm^{-1}$ region is clearly in disagreement with the experimental spectrum. At the same time, the experimental VCD signatures in the same region show the +/+/+/- pattern from higher to lower frequencies and this pattern was not at all predicted with the gas phase and the PCM of MM models. The strong negative VCD feature predicted with MM in the gas phase and with PCM at about 1424 $cm^{-1}$ is obviously absent in the corresponding experimental VCD spectrum. The explicit solvation model, i.e. MM-DMSO-I and II in the gas phase, on the other hand, generated considerable pattern changes in both the simulated VA and VCD spectra. It is also noted that MM-DMSO-I and II show quite similar overall VA and VCD patterns, although the former one carries ~99% of population at room temperature based on the relative free energies calculated. Clearly, the experimental VA intensity pattern of the bands in the low wavenumber region is now much better captured with the explicit solvation model. Even more importantly, the experimental +/+/+/- VCD pattern in the same low wavenumber region is now reproduced. Furthermore, the strong negative VCD band at ~1420 $cm^{-1}$ which is absent in the experiment is also no longer visible in the calculation. Finally, the experimental +/- bisignate VCD feature at ~1460 $cm^{-1}$ is correctly predicted with the explicit solvated MM-DMSO-I. The inclusion of the implicit bulk DMSO molecules surrounding the explicit solvated DMSO has

brought the predicted frequencies closer to the experimental ones and modified the relative intensity of a few VA and VCD bands to better agreement with the experiment, but generated no drastic pattern changes.

With the much better overall agreement between experimental and theoretical VA and VCD spectra provided by the combined implicit and explicit solvation model, it is possible to examine some finer spectral details. For example, the C=O stretching band shows a shoulder at the lower frequency side. The corresponding VCD spectrum also has a second weak, negative VCD feature at the lower frequency side of the main C=O band. A possible explanation is that these are due to the co-existence of a small amount of the MM monomer which is not hydrogen-bonded to DMSO in solution. Indeed, both the shoulder and the small additional VCD feature at the C=O region can be explained well by the simulated VA and VCD spectra of the MM monomer with PCM. The second strongest VA feature predicted at ~1283 $cm^{-1}$ for the MM monomer is visible in the same region in the observed experimental spectrum. The related strongest VCD feature of the MM monomer is also visible as a slightly split peak in the same region. These comparisons are highlighted in Figure 3.6 with the inclusion of the empirically population weighted VA and VCD spectra of MM (10%) and MM-DMSO (90%). We also noted that the carbonyl stretching frequency of MM-DMSO was predicted to be blue-shifted by about 13 $cm^{-1}$ from the MM monomer, similar to the experimental shift of 13 $cm^{-1}$ observed for the main C=O band in DMSO versus in $CDCl_3$.

Overall, it is satisfying that the combined implicit and explicit solvation model reproduced all the main VA and VCD spectral features in the experimental ones in methanol and in DMSO. One important point is that it is essential to consider the hydrogen-bonding interactions between methanol and MM and between DMSO and MM using the explicit solvation model in order to interpret the VA and VCD experimental data reliably. Although the further inclusion of PCM of bulk DMSO has improved the agreement only slightly in the DMSO case, the effects of bulk solvent molecules in the case of methanol are more severe. It is therefore advisable to include both models simultaneously in treating solvents that are capable of intermolecular hydrogen-bonding interactions with solutes.

### 3.3.5. Systems with no strong solute-solvent hydrogen-bonds

**Chloroform.** The chloroform solvent can be categorized as a non-polar solvent with no acidic proton capable of hydrogen-bonding interaction. It is very different from methanol and DMSO discussed above. Therefore, one may expect that it is sufficient to account for the solvent effects using just the implicit solvent model. On the other hand, chloroform has three withdrawing chlorine atoms attached to a carbon atom to pull off the electron density from the hydrogen atom, making it accessible for the CH···O type secondary hydrogen-bonding interaction. The MM molecule has three oxygen atoms which may be involved in such interaction with the chloroform molecule. For

completion, we also constructed the 1:1 MM-$CDCl_3$ and 1:2 MM-$(CDCl_3)_2$ complexes to examine the VA and VCD features of these somewhat weakly bound systems. For the 1:1 complex, the hydrogen and chlorine atoms of $CDCl_3$ can be inserted into the existing intramolecular hydrogen-bonded ring of MM or the hydrogen atom can be attached to the carbonyl or ester O atom while leaving the intramolecular hydrogen-bonded ring of MM intact. The association of the deuterium atom of $CDCl_3$ to the carbonyl O atom while maintaining the intramolecular hydrogen-bonded ring of MM did not result in a stable conformer. The association at the hydroxyl O atom resulted in the most stable conformer, while the association at the ester O atom produced the least stable conformer. This is of no surprise since the ester O atom is highly unlikely site for hydrogen-bonding based on our RDF analysis. It is interesting to see that the insertion type conformer is only the second most stable conformer in this case, in contrast to the previous findings with methanol and DMSO. This is because the CH¨O type secondary hydrogen-bonding interaction is weaker than the existing intramolecular OH¨O=C bond. Consequently, in the competition of intra- and intermolecular interactions, the latter wins. Figure 3.7 shows the optimized geometries of these explicitly solvated clusters in the gas phase. The relative free energies of these 1:1 clusters at room temperature at the B3LYP/cc-pVTZ level are also summarized in Table 3.1. Similar searching strategies were applied to construct the 1:2 MM-$(CDCl_3)_2$ clusters as well. The associated results of the 1:2 conformers are summarized in Figure A6, supporting information,

Appendix A.

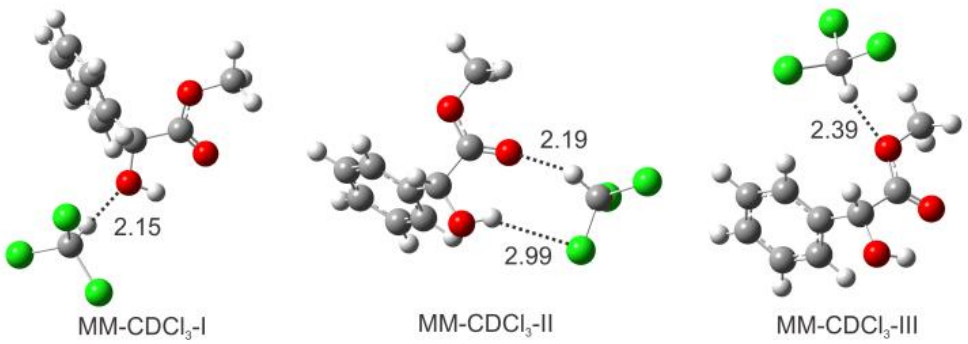


Figure 3.7. Optimized geometries of the three most stable conformers of the 1:1 MM-$CDCl_3$ complex at the B3LYP/cc-pVTZ level in the gas phase. The intermolecular interaction bond lengths (in Å) are indicated.

The simulated VA and VCD spectra of the MM monomer in the gas phase and with PCM are compared with the experimental data in Figure 3.8, together with the respective spectra of the 1:1 explicit solvated MM conformers. The corresponding comparison for the 1:2 explicit solvated MM complex is provided in Figure A7, supporting information, Appendix A.

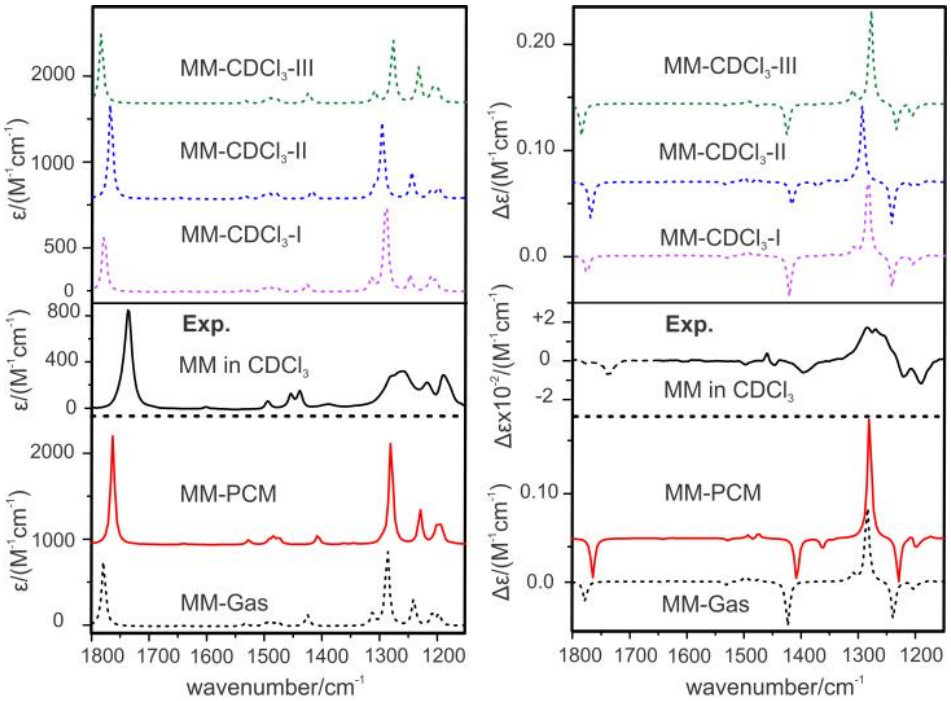


Figure 3.8. Comparisons of the experimental VA and VCD spectra of MM in $CDCl_3$ (middle) with the corresponding simulated spectra of the gas phase and PCM of the MM monomer (bottom) and of the three most stable 1:1 MM-($CDCl_3$) clusters in the gas phase (top) calculated at the B3LYP/cc-pVTZ level.

In contrast to the cases of methanol and DMSO, it is already possible to interpret the observed VA and VCD spectra based on just the isolated spectra of the MM monomer. The main VA spectral features, for example the overall relative VA band intensities and wavenumber positions, were largely reproduced with the gas phase MM. So were all the main VCD features, such as the negative C=O band, all the weak bands in the 1520-1420 $cm^{-1}$ region, the medium strength VCD band at 1392 $cm^{-1}$ which is missing in the methanol and DMSO experimental spectra, and the +/+/-/- pattern in the 1350-1150 $cm^{-1}$ region. The inclusion of the PCM again brought about a better frequency

agreement with the experimental data, but did not alter either the VA or VCD features substantially. It appears that for $CDCl_3$, the implicit solvation model or even just the gas phase monomer models are accurate enough to interpret the experimental features. Having said that, we were also interested to see how the explicit solvation model alters the appearance of the VA and VCD spectra. It is interesting to see that all of the 1:1 MM-$CDCl_3$ conformers show general similar VA and VCD features. The most dominant one, with about 94% population, exhibits VA and VCD spectral features which are essentially identical to those of the MM monomer. It appears that the weak explicit intermolecular interaction between MM and $CDCl_3$ does not alter the VA and VCD spectra of MM noticeably. Although one does not expect substantial amount of the 1:2 explicit solvated MM-$(CDCl_3)_2$ in solution at room temperature, we nevertheless compare their simulated VA and VCD spectra in Figure S7, Appendix A, with the experimental data. Again, the overall main features are similar to those obtained with just MM, supporting the above statement. In a recent VCD study of some very different molecular systems, i.e. chiral binaphthyl diphosphine ligands and their palladium complexes, it was found: similar to the present case, the addition of the solvent PCM had not changed the conformational distribution; but unlike the current case, the addition of the PCM of solvent has noticeably effects on the appearance of VCD spectra.[31] It is therefore advisable to include PCM of solvents in VCD simulations. In the case of MM in $CCl_4$, one can expect that the observed VA and VCD spectra to be explained by those of the MM monomer. This is

indeed the case since the spectra obtained in $CCl_4$ are essentially the same as those in $CDCl_3$.

### 3.3.6. Experimental and simulated ORD comparison

Figure 3.9 shows the experimental specific ORD curves of MM measured in methanol, chloroform, and dimethyl sulfoxide at a series of concentrations over five excitation wavelengths using sodium D line and mercury lamps. The specific ORD measurements are generally concentration independent in the concentration range from 0.06 M to 1.2 M, meaning that the specific optical rotation value at a certain wavelength in a specific solvent does not change noticeably with respect to concentration. This observation suggests that generally the nature of solute-solvent interactions is kept more or less the same from the very dilute solution to the more concentrated one. The observation may also suggest that there is no drastic change in the dominant MM conformer in the three different organic solvents employed here. Both statements are supported by the vibrational studies discussed above. The theoretical ORD values of MM in methanol, chloroform, and DMSO at the five experimental excitation wavelengths have been calculated by using TDDFT at the B3LYP/cc-pVTZ level. All the proposed solvation models have been used in the calculations. For conciseness, the calculated ORD results of the most relevant species derived from the VA and VCD studies are summarized in Figure 3.9 for comparison with the experimental ones, while the rest of ORD theoretical results of methanol are collected in Figure A8,

supporting information, Appendix A.

It has been recognized that the TDDFT method utilized for ORD calculations has certain deficiency in obtaining the key excitation energy and the related rotational strength adequately.[32] For example, the ORD values calculated by the B3LYP method tend to be too large in magnitude because the key excitation energy is usually underestimated and the related rotational strength overestimated.[31,33] Indeed, the ORD values calculated for the MM monomer in the gas phase and with PCM are much larger negative numbers than the corresponding measurements, for example in $CDCl_3$. Although the accuracy of the current ab initio calculations of ORD values may not allow a meaningful quantitative comparison with the experimental ones, one can nevertheless check if the general trends observed can be reproduced theoretically and if consistent conclusions can be reached with the dominant species derived from the VA and VCD studies discussed above.

From Figure 3.9, one can see that the ORD values predicted for the MM monomer with and without PCM are more or less the same, and similar observation can be made for the 1:1 MM-DMSO complex. For this reason, we omitted the plots of the 1:1 MM-MeOH and MM-$CDCl_3$ complexes with PCM to avoid overcrowded in Figure 3.9. At first glance, one may wonder if the 1:1 MM-$CDCl_3$-I conformer, which has ~94% of the 1:1 cluster population at room temperature, provides better agreement with the experimental data since smaller specific ORD values were predicted for it at the wavelengths measured. However, in order to compare the specific ORD values of the 1:1

complex with the experimental data one needs to multiply the theoretical values by a scaling factor equivalent to the mass ratio of the 1:1 complex with respective to the MM monomer or about 1.8. This is because the experimental specific ORD values were determined using the concentration of MM itself in g/mol, whereas the calculated specific ORD values of the 1:1 complex were computed with respect to the complex. This resulted in even larger negative ORD values than the MM monomer, thus indirectly supporting the conclusion reached with the vibrational studies that in $CDCl_3$, the dominant species is the MM monomer. In the cases of methanol and DMSO, the experimental ORD values are noticeably smaller than those in $CDCl_3$. On the other hand, the theoretical ORD values of MM itself in the three solvents were predicted to be quite similar. These observations indirectly suggest that the dominant species in these two solutions are different from in $CDCl_3$. Indeed, the most abundant 1:1 MM-DMSO conformer (~99%) exhibits much smaller ORD values with a correction factor of 1.5 implemented. Similarly, the population weighted 1:1 MM-MeOH clusters provide smaller negative ORD values with a correction factor of 1.2 than the MM itself. Overall, the ORD investigations presented support the conclusions drawn from the VA and VCD studies despite the less desirable accuracy of the current ORD calculations.

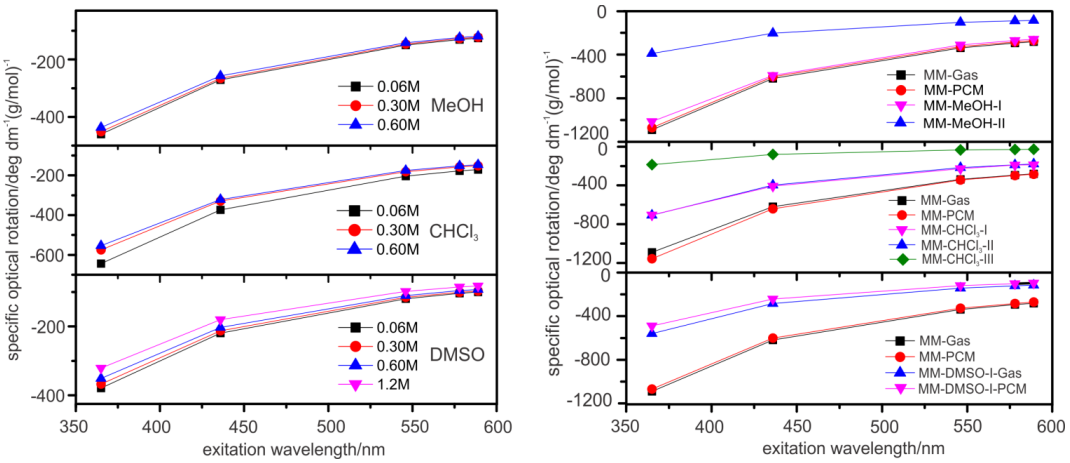


Figure 3.9 Comparison of the experimental and calculated specific ORD values of MM in methanol, $CDCl_3$, and DMSO solvents

## 3.4. Conclusions

VA and VCD spectra of MM in three different organic solvents, namely, methanol, dimethyl sulfoxide, and chloroform have been measured and compared. The experimental observed differences among these three solvents highlight the conformational sensitivity of VA and in particular VCD spectroscopy and the severity of the effects of solvents. By applying DFT and MD simulations, a general approach of using the combined explicit and implicit solvation model has been developed to account for the observed differences in both VA and VCD spectra among these three solvents. It was found that in the case of strongly hydrogen-bonding systems, such as MM in methanol and in DMSO, the application of explicit solvent model is highly

recommended. The first shell of solvation can be achieved by hydrogen-bonding interaction between solvent and solute at the important sites suggested by MD simulations. The further inclusion of the implicit solvation model is beneficial and can rectify some persistent mismatches when the explicit solvation model alone is applied. For the non-hydrogen bonding systems, such as MM in $CDCl_3$ and in $CCl_4$, the gas phase MM monomer or the MM monomer with PCM are sufficient to simulate the VA and VCD spectra for comparison against experiment. It is nevertheless advisable to include the PCM of solvents since more drastic changes in VCD spectra with the inclusion of PCM had been reported before.[31] Finally, the related ORD experiments and simulations also support the conclusions reached with the vibrational studies.

## 3.5. Acknowledgements

This research was funded by the University of Alberta, the Natural Sciences and Engineering Research Council of Canada, and the Canada Research Chairs Program. We also gratefully acknowledge access to the computing facilities provided by the Academic Information and Communication Technology group at the University of Alberta and by the Western Canada Research Grid (Westgrid).

## References


[1] L. A. Nafie, *Vibrational Optical Activity: Principles and Applications*, John Wiley & Sons, Ltd., Chichester, 2011.

[2] Y. He, B. Wang, R. K. Dukor, L. A., Nafie, *Appl. Spectrosc*., 2011, **65**(7), 699-723.

[3] E. L. Eliel, S. Wilen, M. P. Doyle, *Basic Organic Stereochemistry*, Wiley-Interscience: New York, 2001.

[4] S. M. Wilson, K. B. Wiberg, J. R. Cheeseman, M. J. Frisch, and P. H. Vaccaro, *J. Phys. Chem. A*., 2005, **109**, 11752-11764.

[5] P.L. Polavarapu, *Chirality*, 2012, DOI: 10.1002/chir.22015.

[6] M. Losada and Y. Xu, *Phys. Chem. Chem. Phys.*, 2007, **9**, 3127-3135.

[7] M. Losada, H. Tran, and Y. Xu, *J. Chem. Phys.*, 2008, **128**, 014508/1-11.

[8] M. Losada, P. Nguyen, and Y. Xu, *J. Phys. Chem. A*, 2008, **112**, 5621–5627.

[9] G. Yang and Y. Xu, *J. Chem. Phys.*, 2009, **130**, 164506-164515.

[10] J. Sadlej, J. C. Dobrowolski, J. E. Rode, *Chem. Soc. Rev.*, 2010, **39**,1478-1488.

[11] G. Yang and Y. Xu, *Vibrational Circular Dichroism Spectroscopy of Chiral Molecules*, in *Top. Curr. Chem*., Volume: Electronic and Magnetic Properties of Chiral Molecules and Supramolecular Architectures, Eds R. Naaman, D.N.Beratan, D.H.Waldeck, Springer-Verlag Berlin Heidelberg, 2011, 298, 189-236.

[12] Y. Liu, G. Yang, M. Losada, and Y. Xu, *J. Chem. Phys.*, 2010, **132**, 234513 -234524.

[13] R. J. Piffath and S. Sass, *Applyied Spectroscopy*, 1972, **26**, 92-95.

[14] D. M. P. Gigante, F. Long, L. A. Bodack, J. M. Evans, J. Kallmerten, L. A. Nafie, T. B. Freedman, *Journal of Physical Chemistry A*, 1999, **103**, 1523-1537.

[15] T. Kuppens, P. Bultinck, and W. Langenaeker, *Drug Discovery Today: Technology*, 2004, **1**, No 3, 269-275.

[16] M. Albrecht, A. Borba, K. L. Barbu-Debus, B. Dittrich, R. Fausto, S. Grimme, A. Mahjoub, M. Nedić , U. Schmitt, L. Schrader, M. A. Suhm, A. Zehnacker-Rentien, and J. Zischang, *New Journal of Chemistry*, 2010, **34**, 1266-1288.

[17] G. D. Yadav, A. D. Sajgure and S. B. Dhoot, *J. Chem. Technol. Biotechnol*., 2008, **83**, 1145–1153.

[18] P. Polavarapu, *Chirality*, 2008, **20**, 664-672.

[19] M. J. Frisch, G. W. Trucks, H. B. Schlegel, G. E. Scuseria, M. A. Robb, J. R. Cheeseman, J. A. Montgomery Jr., T. Vreven, K. N. Kudin, J. C. Burant, J. M. Millam, S. S. Iyengar, J. Tomasi, V. Barone, B. Mennucci, M. Cossi, G. Scalmani, N. Rega, G. A. Petersson, H. Nakatsuji, M. Hada, M. Ehara, K. Toyota, R. Fukuda, J. Hasegawa, M. Ishida, T. Nakajima, Y. Honda, O. Kitao, H. Nakai, M. Klene, X. Li, J. E. Knox, H. P. Hratchian, J. B. Cross, V. Bakken, C. Adamo, J. Jaramillo, R. Gomperts, R. E. Stratmann, O. Yazyev, A. J. Austin, R. Cammi, C. Pomelli, J. W. Ochterski, P. Y. Ayala, K. Morokuma, G. A. Voth, P. Salvador, J. J. Dannenberg, V. G. Zakrzewski, S. Dapprich, A. D. Daniels, M. C. Strain, O. Farkas, D. K. Malick, A. D. Rabuck, K. Raghavachari, J. B. Foresman, J. V. Ortiz, Q. Cui, A. G. Baboul, S. Clifford, J. Cioslowski, B. B. Stefanov, G. Liu, A. Liashenko, P. Piskorz, I. Komaromi, R. L. Martin, D. J. Fox, T. Keith, M. A. Al-Laham, C. Y. Peng, A. Nanayakkara, M. Challacombe, P. M. W. Gill, B. Johnson, W. Chen, M. W. Wong, C. Gonzalez and J. A. Pople, Gaussian 03, Revision E.01, Gaussian, Inc., Wallingford, CT, 2004.

[20] M. J. Frisch, G. W. Trucks, H. B. Schlegel, G. E. Scuseria, M. A. Robb, J. R. Cheeseman, G. Scalmani, V. Barone, B. Mennucci, G. A. Petersson, H. Nakatsuji, M. Caricato, X. Li, H. P. Hratchian, A. F. Izmaylov, J. Bloino, G. Zheng, J. L. Sonnenberg, M. Hada, M. Ehara, K. Toyota, R. Fukuda, J. Hasegawa, M. Ishida, T. Nakajima, Y. Honda, O. Kitao, H. Nakai, T. Vreven, J. A. Montgomery, Jr., J. E. Peralta, F. Ogliaro, M. Bearpark, J. J. Heyd, E. Brothers, K. N. Kudin, V. N. Staroverov, R. Kobayashi, J. Normand, K. Raghavachari, A. Rendell, J. C. Burant, S. S. Iyengar, J. Tomasi, M. Cossi, N. Rega, J. M. Millam, M. Klene, J. E. Knox, J. B. Cross, V. Bakken, C. Adamo, J. Jaramillo, R. Gomperts, R. E. Stratmann, O. Yazyev, A. J. Austin, R. Cammi, C. Pomelli, J. W. Ochterski, R. L. Martin, K. Morokuma, V. G. Zakrzewski, G. A. Voth, P. Salvador, J. J. Dannenberg, S. Dapprich, A. D. Daniels, Ö. Farkas, J. B. Foresman, J. V. Ortiz, J. Cioslowski, and D. J. Fox, Gaussian 09, Revision B.01, Gaussian, Inc., Wallingford CT, 2009.

[21] J. Tomasi, B. Mennucci, R. Cammi, *Chemical Review*, 2005, **105**, 2999-3093.

[22] D. A. Case, T. A. Darden, T. E. Cheatham, III, C. L. Simmerling, J. Wang, R. E. Duke, R. Luo, R. C. Walker, W. Zhang, K. M. Merz, B. P. Roberts, B. Wang, S. Hayik, A. Roitberg, G. Seabra, I. Kolossváry, K. F. Wong, F. Paesani, J. Vanicek, J. Liu, X. Wu, S. R. Brozell, T. Steinbrecher, H. Gohlke, Q. Cai, X. Ye, J. Wang, M.-J. Hsieh, G. Cui, D. R. Roe, D. H. Mathews, M. G. Seetin, C. Sagui, V. Babin, T. Luchko, S. Gusarov, A. Kovalenko, and P. A. Kollman (2010), *AMBER 11*, University of California, San Francisco.

[23] N. Borho, M. A. Suhm, K. Le Barbu-Debusb, and A. Zehnacker, *Phys. Chem. Chem. Phys.*, 2006, **8**, 4449–4460.

[24] M. Urbanova, V. Setnicka, F. J. Devlin, and P. J. Stephens, *J. Am. Chem. Soc*. ,2005, **127**, 6700-6711.

[25] J. Sadlej, J. Cz. Dobrowolski, J. E. Rode, and M. H. Jamroz, *J. Phys. Chem. A.*, 2007,**111**, 10703-10711.

[26] N. Seurre, K. Le Barbu-Debus, F. Lahmani, A. Zehnacker, N. Borho and M. A. Suhm, *Phys. Chem. Chem. Phys*., 2006, **8**, 1007–1016.

[27] Z. Su, Q. Wen, and Y. Xu, *J. Am. Chem. Soc.*, 2006, **128**, 6755-6760.

[28] Z. Su and Y. Xu, *Angew. Chem.*, 2007, **119**, 6275 – 6278; *Angew. Chem. Int. Ed.*, 2007, **46**, 6163-6166.

[29] P. Zhu, G. Yang, M. R. Poopari, Z. Bie, Y. Xu, *ChemPhysChem*, 2012, **13**, 1272 –1281.

[30] M. R. Poopari, Z. Dezhahang, G. Yang, and Y. Xu, *ChemPhysChem*, 2012, **13**, 2310-2321.

[31] Z. Dezhahang, C. Merten , M. R. Poopari and Y. Xu, *Dalton Trans.*, 2012, DOI: 10.1039/C2DT31184D.

[32] T. D. Crawford in *Comprehensive Chiroptical Spectroscopy*: *Methodologies and Theoretical Simulations*, ed. N. Berova, P. L. Polavarapu, K. Nakanishi, and R. W. Woody, John Wiley & Sons, Inc. 1st edn. 2012, vol. 1, ch. 23, pp. 675-697.

[33] J. Autschbach, S. Patchkovskii, T. Ziegler, S. J. A. van Gisbergen, E. J. Baerends, *J. Chem. Phys.*, 2002, **117**, 581-592.

# 4 Chapter

# Identifying dominant conformations of N-acetyl-L-cysteine methyl ester and N-acetyl-L-cysteine in water: VCD signatures of the amide I and the C=O stretching bands

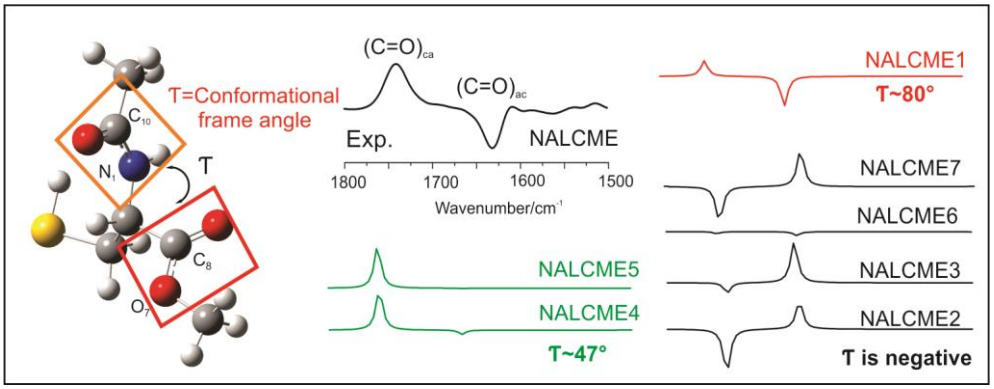


**This chapter is directly copied from the published paper:**

M. R. Poopari, Z. Dezhahang, Y. Xu, "Identifying dominant conformations of N-acetyl-L-cysteine methyl ester and N-acetyl-L-cysteine in water: VCD signatures of the amide I and the C=O stretching bands", Spectrochimica Acta - Part A Molecular and Biomolecular Spectroscopy, 2013, DOI: 10.1016/ j.saa.2013.08.118.

## 4.1. Introduction

Infrared (IR) spectroscopy and the related vibrational circular dichroism (VCD) spectroscopy[1,2] have been used to provide information about conformational distributions of amino acids[3,4] and polypeptides, as well as secondary structures of proteins[5] in film or in solution. VCD spectroscopy measures the differential absorbance of the left versus the right circularly polarized lights accompanying a vibrational transition. As a result, VCD spectroscopy exhibits unique sensitivity to chirality and is also highly sensitive to structural deformations due to environmental perturbations in comparison to regular IR spectroscopy.[6,7] To extract the rich structural information encoded in the VCD spectral patterns measured, one needs to carry out extensive density functional theory (DFT) calculations in order to identify the possible conformations of the targeted systems and to simulate their VCD spectra. This approach has been utilized successfully in a significant number of studies reported.[1,2,8-10] In highly polar solvents such as water, however, less satisfactory agreements between the experimental and theoretical simulated spectra result because the solvent effects can be drastic.[11,12] For example, the inclusion of bulk solvent using models such as the polarizable continuum model (PCM) is critical in some cases.[12] Yet in some other cases, the VCD features observed can only be reproduced by further considering explicit hydrogen-bonding interactions between chiral solute and water molecules.[4,13-16] Since it may be too expensive to include explicit water molecules in the simulations of larger biomolecules in aqueous solution, it is of significant interest to investigate in details why the PCM approaches are able to adequately interpret the observed IR and VCD spectra at

one time and not at another. It is well known that the final simulated spectral features rely on both the spectral signatures of individual conformers and their Boltzmann population contributions. We therefore focus our attention on evaluating these two factors for two model chiral molecular systems, namely N-Acetyl-L-Cysteine Methyl Ester (NALCME) and N-Acetyl-L-Cysteine (NALC) in water under different pHs. Both NALCME and NALC are used for example, as mucolytic agents to reduce the viscosity of mucus secretions, while NALC is also used in the management of paracetamol overdose.[17,18]

These two model systems are chosen for two main reasons. First, standard amino acids and their derivatives are chemically highly versatile molecules with a wide range of applications in pharmacy, biology, and chemistry. Their specific functions in water depend strongly on the pH of the solution and the particular conformations they adopt under such conditions. It is therefore highly desirable to obtain information about their dominant conformations in water under different pH conditions. Second, NALCME has fewer hydrogen-bonding sites compared to NALC. In comparison to NALC, its ability to form intramolecular hydrogen-bonds and intermolecular hydrogen-bonds with water molecules is significantly reduced. This allows one to evaluate how methyl substitution of the carboxylic group influences the dominant conformations in aqueous solution and how the related IR and VCD spectral features change. Although the VCD spectrum of NALC under neutral pH=7 was reported previously,[15] we include the VCD spectra of NALC under acidic conditions of pH=2.5 and 3.1 in this study since the dominant species are different under the neutral and acidic conditions. In

particular, we focus on the amide I band and the C=O stretching bands associated with the –COOH and –COOMe (Me=–$CH_3$) groups in the region of 1800-1500 $cm^{-1}$ which have strong IR and VCD intensities. We examine the dominant conformations predicted and how their geometries and relative stabilities change from the gas phase calculations to those with the PCM of water solvent. We aim to establish empirical structural-spectral relationships which one may utilize to extract conformational structural information for larger and related chiral molecular systems.

## 4.2. Experimental and theoretical details

### 4.2.1. Experimental IR and VCD measurements

NALC (99% purity), NALCME (90%, purity) and $D_2O$ (99.9%, purity) were obtained from Aldrich and were used without further purification. $D_2O$ was used as solvent for all the IR and VCD measurements reported. The experimental IR and VCD spectra were recorded using an Fourier transform IR spectrometer (VERTEX 70, Bruker) equipped with a VCD module (PMA50, Bruker) at room temperature.[13] The spectral range of 1800-1500 $cm^{-1}$ was selected for the current study where the solvent does not show any strong interference. In order to obtain VCD spectra with good quality, the concentration and path-length were optimized so that the experimental absorbance is in the range of 0.2 to 0.8 for the relevant IR bands. Solutions with a concentration of ~0.6 M and a path-length of 0.05 mm were used. All VCD spectra were obtained with a resolution of 4 $cm^{-1}$ and with a

total measurement time of 3 h (3 x 1 hour), roughly ~4300 scans per hour. Upon dissolving of NALC sample in water, a solution with a pH value of ~2.5 is obtained. The NALC solutions with higher pH values were prepared by adding a small amount of 6 M NaOD dropwise. Upon dissolving of NALCME sample in water, a solution with a pH value of ~6.6 is made. Please note that the pH values reported are the direct read out values in a $D_2O$ solution using a $H_2O$-calibrated pH-meter. Please see Ref. 19 for the detailed differences between pH and pD. The final reported VCD spectra were baseline corrected using the solvent spectra obtained under the same condition.

### 4.2.2. Theoretical

The Gaussian 09[20] suite of programs was used in all the geometry optimization calculations, potential energy surface scans, and harmonic vibrational frequencies calculations, as well as the IR and VCD intensities predictions. DFT[21] calculations were performed with the Becke, three-parameter, Lee-Yang-Parr (B3LYP)[22-24] hybrid functional and the augmented correlation-consistent triple zeta basis sets with added diffuse functions, i.e. aug-cc-pVTZ[25] for all conformational searches and spectral simulations. A Lorentzian line shape with a half-width at half-height (HWHH) of 4 $cm^{-1}$ was used for the simulations of IR and VCD spectra. The integral equation formalism of polarization continuum model (IEF-PCM)[26] using the universal force field (UFF) radii was used to account for the effects of solvent molecules implicitly. A dielectric constant of 78.3553 was used for $D_2O$. It was established previously[15] that the

H/D exchange happens at the three possible hydrogen-bonding sites, namely the –COOH, –SH and –NH sites, under the current experimental conditions. Consequently, in all the spectral simulation performed in this study, all these possible sites are fully D substituted whenever it is appropriate. Please note that we use *R*-enantiomers throughout this study.

## 4.3. Results and discussions

### 4.3.1. The experimental IR and VCD spectra

Figure 4.1 shows the experimental IR and VCD spectra of NALCME at pH= 6.6 and NALC at pH=7, 3.1, and 2.5. Comparing to NALC, NALCME has no acidic proton and the dominant species is expected to be the same in the pH range from 2.5 to 7.0. Therefore, only one pH result is reported here. Different spectral features are noted for NALC under different pHs. It is known from the previous study that the carboxylic group exists essentially as –COOH at a pH value of 2.5, and as $COO^-$ at pH=7.0, whereas both species coexist at pH=3.1.[15] While IR spectra at pH values ranging from 0.65 to 13 and VCD spectrum at pH=7.0 of NALC were reported in Ref. 15, the VCD spectra of NALC at pH=2.5 and 3.1 are reported here for the first time. At pH=2.5, two IR bands are observed for NALC at ~1720 and ~1630 $cm^{-1}$. These corresponds to the C=O stretch of the –COOH group, i.e. $\nu(C=O)_{ca}$ where 'ca" stands for carboxylic acid', and the amide I mode, i.e. $\nu(C=O)_{ac}$ where 'ac' stands for acetyl. At pH=3.1 and 7, a new band corresponding to the asymmetric stretch of $–COO^-$, i.e. $\nu_{as}(COO^-)$, appears at 1599 $cm^{-1}$. For NALCME, two IR bands are observed, corresponding to the C=O

stretch of the –COOME group, i.e. $\nu(C=O)_{ester}$, and the amide I band, $\nu(C=O)_{ac}$, from high to low wavenumber. In the case of NALCME, the amide I band occurs at essentially the same wavenumber position as the NALC molecule, whereas $\nu(C=O)_{ester}$ emerges at ~1735 $cm^{-1}$ which is blue shifted by ~15 $cm^{-1}$ compared to $\nu(C=O)_{ca}$ of NALC. The experimental VA and VCD spectra extended down to 1300 $cm^{-1}$ are provided in Figure B1, Supporting Information Appendix B.

Another interesting observation highlighted in Figure 4.1 is the sign reversal of the VCD amide I mode. For neutral NALC and NALCME, this band exhibits a negative VCD sign, whereas for the deprotonated NALC species, i.e. depNALC, the sign of this VCD band changes to positive. In addition, the VCD signs of the $\nu(C=O)_{ca}$ of neutral NALC and of $\nu(C=O)_{ester}$ of NALCME remain positive.

In the following, we use theoretical modeling to explain these observations. In particular, we focus on the comparison of the experimental and theoretical VCD patterns of the most stable conformers of the NALCME, NALC, and depNALC species predicted. Our goals are to establish useful empirical structural-spectra relationships and to explore a suitable approach to interpret the experimental VCD spectra in water adequately and efficiently.

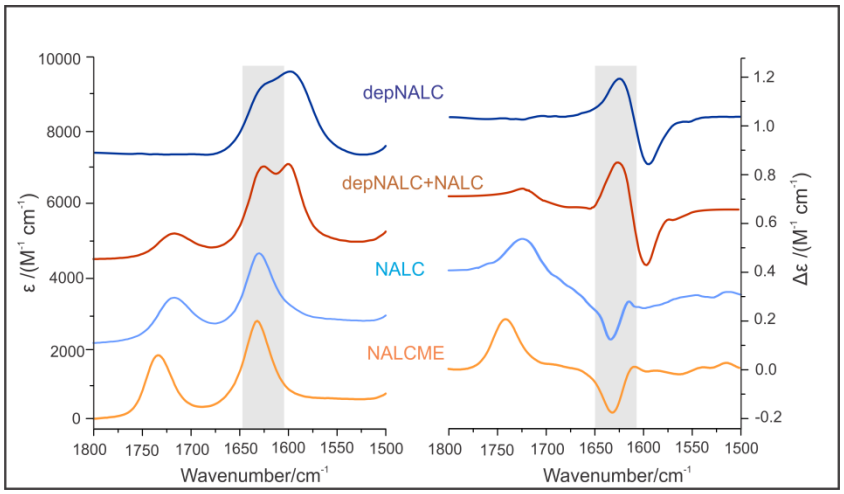


Figure 4.1. Experimental IR (left) and VCD (right) spectra of NALC in water at pH=7, 3.1, 2.5 and of NALCME in water at pH=6.6, from the top to the bottom, respectively. The dominant species under each pH are also indicated.

### 4.3.2. Conformational searches

The conformational search of depNALC is discussed first since NALC and NALCME also contain similar molecular fragments. A preliminary two-dimensional energy plot of depNALC at the B3LYP/6-31G(d) level in the gas phase, scanned along two of its most important rotational angles about the C3-C5 and C3-N1 bonds (See Figure 4.2 for atom labeling), was reported previously.[15] It was recognized that the lone electron pairs of the N atom is involved in a resonance structure with the adjacent –C=O group, and the –NH group forms an intramolecular hydrogen-bond with the $–COO^-$ group. As a result, this part of molecule is fairly rigid. Therefore, the main conformational freedom involves the rotation of the –SH group about the C3-C5 bond. We further carried out the potential energy scan along this angle at the B3LYP/aug-cc-pVTZ level in the gas phase and with the PCM of water solvent. The scanned results obtained in the gas phase and with PCM are provided in Figure B2, Supporting Information,

Appendix B. Altogether; five most stable conformers of depNALC with the PCM of water solvent were optimized and proved to be true minima with no imaginary frequencies. Their geometries with the PCM of water solvent are provided in Figure 4.3, while the corresponding gas phase geometries are given in Figure B3, Supporting Information, Appendix B. To facilitate easy differentiation of the conformers, all intramolecular hydrogen-bond lengths or van der Waals bond lengths less than 3 Å are indicated in the related figures. Their relative energies and the associated Boltzmann population factors at room temperature of these five conformers are summarized in Table 1. We note that the most stable conformers identified are similar to those obtained with the 6-311++G(d,p) basis set,[15] although with a somewhat different stability order.

For the next species, i.e. neutral NALC, its conformational landscape had been studied extensively before both in the gas phase and with the PCM of water solvent.[15-28] Therefore, only the six most stable NALC conformers re-optimized at the B3LYP/aug-cc-pVTZ are reported here. Their geometries with the PCM of water solvent are shown in Figure 4.3, while the corresponding gas phase geometries are depicted in Figure B4, Supporting Information, Appendix B. Their relative energies and the associated Boltzmann population factors at room temperature are provided in Table 4.1.

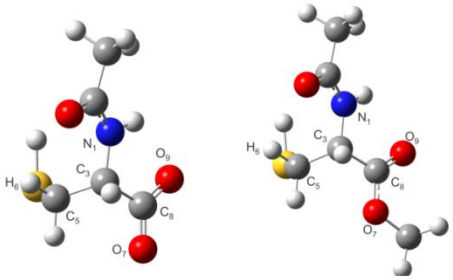


Figure 4.2. Atom labelling for the depNALC (left) and NALCME (right) molecules.

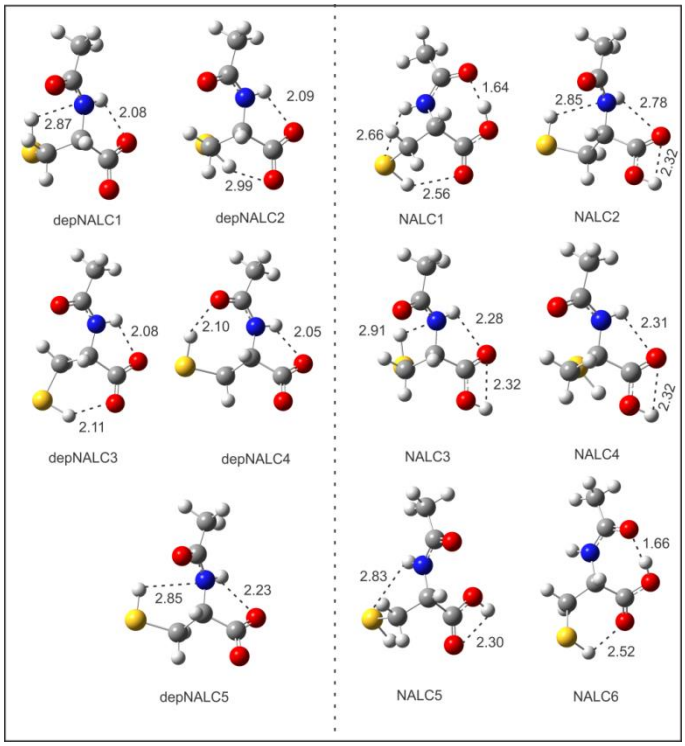


Figure 4.3. Geometries of the most stable conformers of depNALC and the neutral NALC at the PCM/B3LYP/aug-cc-pVTZ level. All relevant intramolecular bonds with a bond length less than 3 Å are indicated.

Table 4.1. Values of the relative free energy ΔG (in kcal/mol) in the gas phase and with PCM, and the relative zero-point-corrected energy ΔE (kcal/mol) with PCM, as well as the corresponding Boltzmann population percentage factors at room temperature of the most stable conformers of depNALC, neutral NALC and NALCME at the B3LYP/aug-cc-pVTZ level.

| | PCM | | Gas Phase | | PCM | |
|---|---|---|---|---|---|---|
| Conformers | ΔG [rank][a] | pop%ΔG | ΔG [rank][b] | pop%- ΔG | ΔE [rank][c] | pop%- ΔE |
| Deprotonated NALC | | | | | | |
| depNALC1 | 0.00 [1] | 39.68 | 0.42 [2] | 29. 97 | 0.01 [2] | 37.72 |
| depNALC2 | 0.04 [2] | 36.54 | 1.95 [4] | 2.29 | 0.00 [1] | 38.49 |
| depNALC3 | 0.60 [3] | 14.34 | 0.00 [1] | 61.48 | 0.50 [3] | 16.33 |
| depNALC4 | 1.05 [4] | 6.74 | 1.35 [3] | 6.25 | 1.21 [4] | 4.92 |
| depNALC5 | 1.59 [5] | 2.70 | N/A[d] | | 1.61 [5] | 2.53 |
| Neutral-NALC | | | | | | |
| NALC1 | 0.00 [1] | 25.82 | 0.22 [3] | 20.15 | 0.00 [1] | 70.50 |
| NALC2 | 0.08 [2] | 22.45 | 0.65 [5] | 9.70 | 2.10 [5] | 2.03 |
| NALC3 | 0.16 [3] | 19.42 | 0.00 [1] | 29.05 | 1.47 [3] | 5.90 |
| NALC4 | 0.34 [4] | 14.49 | 0.06 [2] | 26.33 | 1.83 [4] | 3.21 |
| NALC5 | 0.48 [5] | 11.35 | 0.43 [4] | 13.95 | 2.33 [6] | 1.37 |
| NALC6 | 0.82 [6] | 6.74 | 2.11 [6] | 0.82 | 0.84 [2] | 17.00 |
| Methyl ester-NALC | | | | | | |
| NALCME1 | 0.00 [1] | 21.53 | 2.24 [6] | 0.97 | 0.61 [3] | 13.92 |
| NALCME2 | 0.05 [2] | 19.70 | 0.71 [3] | 2.80 | 0.88 [4] | 8.95 |
| NALCME3 | 0.09 [3] | 18.37 | 2.81 [7] | 0.37 | 1.19 [6] | 5.21 |
| NALCME4 | 0.23 [4] | 14.52 | 0.00 [1] | 42.44 | 0.00 [1] | 39.43 |
| NALCME5 | 0.32 [5] | 12.50 | 0.21 [2] | 29.80 | 0.35 [2] | 21.64 |
| NALCME6 | 0.56 [6] | 8.36 | 0.80 [4] | 10.90 | 1.23 [7] | 4.91 |
| NALCME7 | 0.86 [7] | 5.04 | 1.63 [5] | 2.73 | 1.12 [5] | 5.93 |

[a] Relative stability based on ΔG obtained with the PCM of water.
[b] Relative stability based on ΔG obtained in the gas phase.
[c] Relative stability based on the zero-point-energy corrected ΔE obtained with the PCM of water solvent.
[d] This optimized structure in the gas phase turns to depNALC4 (see Figure B3).

For NALCME, because of the methyl substitution at the carboxylic site of NALC, its ability to form hydrogen-bonds is reduced and the conformational landscape for NALCME is less-complicated compared to that of neutral NALC. In fact, methyl esterification was used before as a method to eliminate or

minimize the inter- and intramolecular hydrogen-bonding interactions in the related chiral systems, such as 2-(2-chlorophenoxy) propanoic acid and 2-(3-chlorophenoxy) propanoic acid, in order to identify their absolute configurations.[27] Building on the results obtained for neutral NALC,[15,28] potential energy scans along the two dihedral angles namely, $O_9$-$C_8$-$C_3$-$N_1$ and $H_6$-$C_5$-$C_3$-$N_1$ (See Figure 4.2 for atom labelling) were performed. Such scans allow the –$CH_2SH$ group to make an intramolecular hydrogen-bond with either the –NH or the –COOMe group. Furthermore, such hydrogen-bonding interaction can happen either with the carbonyl or the ester oxygen atom of the –COOMe group. Overall, seven most stable conformers were identified. The optimized geometries of these seven conformers at the PCM/B3LYP/aug-cc-pVTZ level are shown in Figure 4.4, while the corresponding gas phase geometries are summarized in Figure B5, Supporting Information, Appendix B. Their relative energies and the related Boltzmann population factors at room temperature obtained with the PCM of water solvent and in the gas phase are also summarized in Table 1.

The energy spread is relatively small among these conformers. For example, NALCME1 and NALCME3 differ only in one main aspect: –NH points to the ester oxygen atom in NALCME3 instead of the carboxylate oxygen atom as in NALCME1. It is known from both the solution[13,15] and the gas phase[29,30] experimental studies that the –NH$^{\cdots}O_{ester}$ or –OH$^{\cdots}O_{ester}$ interactions contribute less to the stabilization energy compared to the –NH$^{\cdots}$O=C or –OH$^{\cdots}$O=C interactions. Indeed, the intramolecular hydrogen-bonding distance of –NH$^{\cdots}$O=C in

NALCME1 is 2.26 Å, whereas that distance of –NH···$O_{ester}$ in NALCME3 is 2.78 Å.

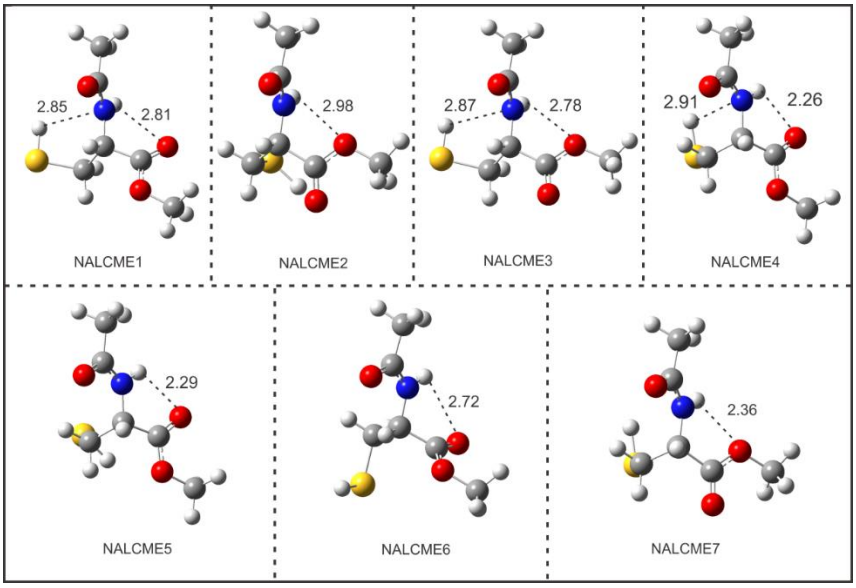


Figure 4.4. Geometries of the seven most stable conformers of NALCME at the PCM/B3LYP/aug-cc-pVTZ level. All relevant intramolecular bonds with a bond length less than 3 Å are indicated.

### 4.3.3 Changes in the conformational geometries and their relative stability ordering in the gas phase and with the PCM of water solvent

To appreciate the effects of bulk solvent, it is interesting to highlight some changes in the geometries and the relative stability of the most stable conformers from the gas phase and to the presence of an implicit solvent. For consistency, the following discussions are based on the relative free energies at room temperature (See Table 4.1). Comments about the differences in the ΔG- and ΔE-based stability orderings are provided at the end of the section.

The most stable conformer of depNALC in the gas phase exhibits an –$NH^{\cdots}OCO^{-}$ intramolecular hydrogen-bond, and at the same time the H atom of the –SH group points toward the oxygen atom of $OCO^{-}$ (See Figure B3). The corresponding PCM conformer has a similar geometrical arrangement with the same intramolecular hydrogen-bonds. The exception is that the intramolecular hydrogen-bond lengths become noticeably longer: from about 1.8 Å in the gas phase to about 2.1 Å with the PCM of water solvent. The two aforementioned cyclic hydrogen-bond formations deliver significant stability to the particular structure in the gas phase. While this most stable conformer of depNALC in the gas phase carries about 60% of the total population, its corresponding structure optimized with the PCM of water solvent contributes only about 14%. In general, the intramolecular hydrogen-bond or van der Waals bond lengths associated with the –SH group are in the range of 2.10~2.99 Å in the conformers obtained with the PCM of water, while their values vary from 1.88 to 2.88 Å in the gas phase. As a result of these geometric changes, the relative stability ordering of the depNALC conformers also changes going from the gas phase to the PCM of water solvent.

For the NALC species, a number of dihedral angles are important in generating the low energy conformations. This flexibility brings about a more complex conformational landscape. It is interesting to note that all six conformers identified in the gas phase have the one-to-one corresponding PCM conformers. Similarly, for the NALCME, the inclusion of the implicit solvent model tends to alter some dihedral angles for those involved in the intramolecular hydrogen-

bonds, such as the –NH and –SH groups. While the first five conformers with PCM contribute about 10% to 26% each to the total population, i.e. contribute fairly evenly, this trend is not seen with those in the gas phase where two main conformers contribute over 70% to the total population.

Overall, the bulk solvent environment plays two important roles here, namely to modify both the relative stability ordering of the conformers and their geometries. Generally speaking, the gas phase structures are more compact than those obtained with the PCM of water solvent. This is not surprising since without the interference of water solvent, the solute molecule is free to optimize the possible intramolecular hydrogen-bonds, resulting in more compact geometries.

The relative stability orderings based on ΔG and on ΔE are more or less the same for the depNALC species, with the first two most stable conformers having essentially the same stability. For NALC, although the most stable conformer is strongly favored with about 70% of the total population based on ΔE, the contributions of the five lowest energy conformers are fairly evenly distributed based on ΔG. Related observation can also be made for NALCME. Overall, stability orderings based on the ΔG and ΔE values differ slightly for depNALC, and more drastically for NALC and NALCME, as can be seen from Table 1. Since the amount of order or disorder is directly associated with the entropy term which makes the two terms, ΔG and ΔE, different, one can expect different stability ordering based on these two terms. In fact, a strong temperature dependence of the ΔG values for different conformers in other systems had been clearly demonstrated in a number of previous studies.[31] Consequently, it is not

surprising that the stability ordering of the conformers based on ΔG can differ noticeably from that based on ΔE. For the solution measurements considered here, it is logical to use ΔG rather than ΔE for population weighed spectral simulations.

### 4.3.4 Comparison of the experimental and simulated IR and VCD spectra

**NALCME:** The experimental IR and VCD spectra of NALCME are compared with the corresponding spectra of individual conformer in Figure 4.5 to facilitate detailed comparison. It is noted that the peak frequencies of the $\nu(C=O)_{ester}$ stretch mode for all seven conformers show only a small spread, i.e. from 1755 $cm^{-1}$ to 1740 $cm^{-1}$. For the amide I bands, this spread is even smaller, i.e. from ~1675 $cm^{-1}$ to 1666 $cm^{-1}$. Therefore, based on the comparison of the calculated and observed IR spectral features, one cannot tell apart of these possible conformers. The VCD spectral features, on the other hand, differ drastically for the different conformers of NALCME. While NALCME1 shows a positive-negative couplet in accord with the experimental observation, NALCME2, NALCME3, and NALCME7 all show a negative-positive couplet, in contrary to the experiment. Furthermore, NALCME4 and NALCME5 have both very low and diminishing amide I VCD intensity, whereas two negatives VCD bands with low intensities are predicted for NALCME6.

It is clear from Figure 4.5 that the population weighted VCD spectrum based on the ΔG-Boltzmann factors in Table 4.1 would be in poor agreement with the experiment. While the room temperature Boltzmann factors suggest similar amount of NALCME1, 2, and 3 in solution, the spectral signatures observed

indicate that NALCME1 should dominate over NALCME2 and 3 in order to obtain the experimental observed features. One may argue that the DFT energies predicted are off. There are, however, a substantial body of literature, where such predictions serve their purposes well.[2,32,33] In general, it appears that the relative free energy predictions tend to deviate more when water is the solvent and the targeted chiral molecules have multiple hydrogen-bonding sites. It is therefore desirable to probe this phenomenon further by examining the related systems which have stronger hydrogen-bonding capability. In the following sections, we look at the cases of depNALC and neutral NALC.

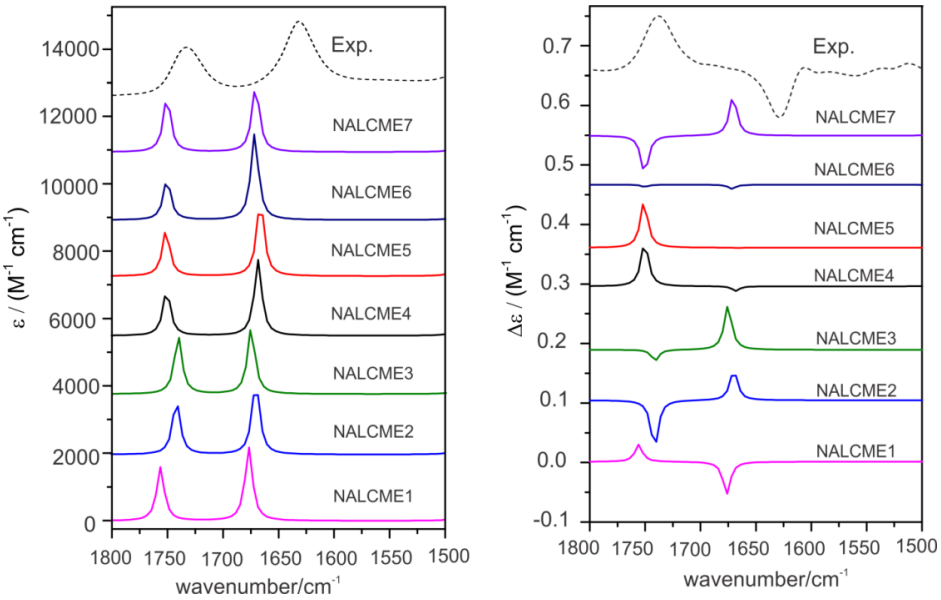


Figure 4.5. Comparison of the experimental IR (left) and VCD (right) spectra of NALCME with the related theoretical spectra of the seven conformers of NALCME at the PCM/B3LYP/aug-cc-pVTZ level.

**depNALC:** The dominant species of NALC in water at pH=7.0 is depNALC. The corresponding experimental IR and VCD spectra were reported before and both implicit and explicit solvation models at the B3LYP/6-311++G

(d,p) level were utilized to interpret the experimental data.[15] For completion, the comparison of the experimental and simulated IR and VCD spectra with the new basis set, aug-cc-pVTZ, is presented in Figure 4.6. It is interesting to note that all five most stable conformers exhibit two closely spacing IR bands, corresponding to the amide I and $\nu_{as}(COO^-)$ bands, from high to low wavenumber. They also all show a positive-negative VCD couplet. The spacing between the amide I and the carboxylate bands differ slightly among conformers. This spacing depends mainly on the relative orientation of the –SH group with respect to the rest of the molecule where it can make an intramolecular hydrogen-bond with either –NH, $–(O=C)_{ac}$ or $–COO^-$. Since both experimental IR and VCD bands appear quite broad in the spectra, it is likely that all these conformers contribute to the observed spectra. In the previous study, it was found that the significant hydrogen-bonding interactions with water molecules influence mostly the VCD features in the 1500-1300 $cm^{-1}$ region.[15] Nevertheless, the most stable conformers identified with the joint implicit and explicit solvent approach[15] are consistent with those predicted with the PCM model. On the other hand, since all the conformers show very similar IR and VCD patterns, it is not possible to discriminate one against another. This is in contrast to the case of NALCME.

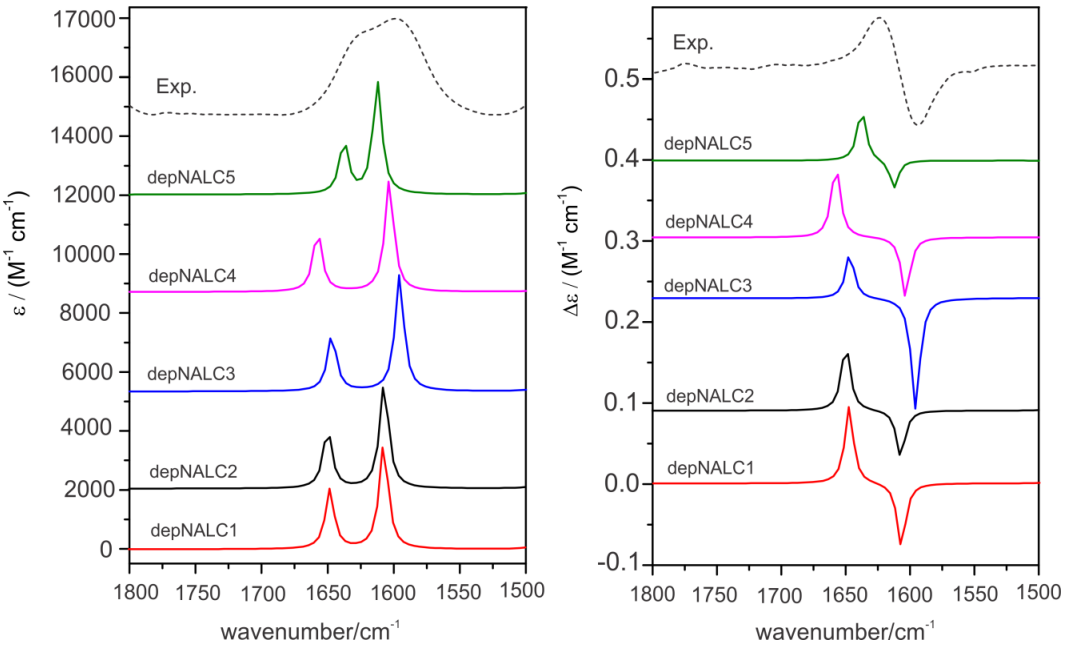


Figure 4.6. Comparison of the experimental IR (left) and VCD (right) spectra of depNALC with the related theoretical spectra of the five conformers of depNALC at the PCM/B3LYP/aug-cc-pVTZ level.

**Neutral NALC:** In Figure 4.7, the experimental IR and VCD spectra of NALC in water at pH=~2.5 are compared with the simulated spectra of the six most stable conformers of the neutral NALC which is the dominant species at such a low pH value. While the $\nu(C=O)_{ca}$ bands are predicted to have very similar peak wavenumbers for all six conformers, the amide I bands spread widely. In particular, the $\nu(C=O)_{ac}$ bands of NALC1 and NALC6 are red shifted by ~65 $cm^{-1}$ compared to NALC2. This is because in these two conformers, the $-(OH)_{ca}$ group points toward the $-(C=O)_{ac}$ group to make an intramolecular hydrogen-bond, whereas the $-(C=O)_{ac}$ groups in the other conformers are free. Since the experimental $\nu(C=O)_{ac}$ band of NALC appears at essentially the same peak position as for NALCME, and NALCME does not have the $-(OH)_{ca}$ group to form such an intramolecular hydrogen-bond, we conclude that NALC1 and

NALC6 do not contribute significantly in solution. At the same time, their corresponding $\nu(C=O)_{ac}$ VCD signals are positive, in contrary to the sign of the corresponding experimental VCD band at ~1630 $cm^{-1}$. A closer examination reveals that this strongest experimental IR band has a tail at the lower frequency side. Correspondingly, there is a small positive VCD bump at ~1615 $cm^{-1}$. These observations suggest that there may be a small amount of NALC1 in solution.

The other four conformers have very similar IR patterns and one cannot tell them apart based on the IR spectral features observed. On the other hand, the VCD features predicted for these four conformers are quite different. NALC5 shows the VCD couplet with the opposite sign of the experiment. While the $\nu(C=O)_{ca}$ bands of NALC3 and NALC4 have the same positive sign as the experiment, their VCD bands at the amide I band have diminishing intensity, in contrast to the experiment. The only remaining conformer, namely NALC2, shows consistent VCD signatures as the experiment. We therefore conclude that overall, NALC2 contributes dominantly to the observed spectra, while some small contributions from other conformers may also be present as discussed above.

As can be seen from Table 4.1, the first three conformers of NALC were predicted to have very similar stability, whereas the experimental data clearly suggest that only one of them, i.e. NALC2, is the dominant conformer. This conclusion echoes the result obtained with NALCME: it is possible to utilize the rich VCD spectral patterns to identify the dominant conformers even though the calculated abundance of these conformers may not support the same conclusion. The latter point will be further discussed in section 4.3.6

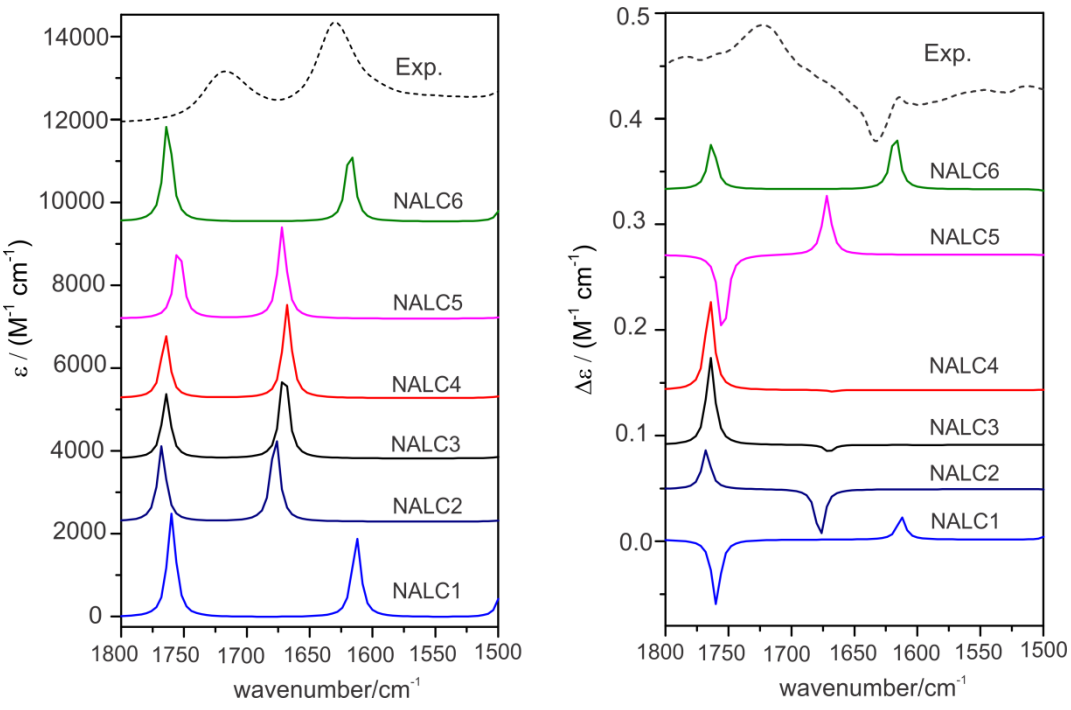


Figure 4.7. Experimental IR (left) and VCD (right) spectra of NALC at pH=2.5 where the dominant species is the neutral form of NALC. The corresponding simulated spectra of the six most stable NALC conformers at the PCM/B3LYP/aug-cc-pVTZ level are also presented.

### 4.3.5 The conformational structure markers

It is known that the sign and the intensity of a VCD band are associated with its rotational strength R. R can be expressed as the imaginary part of the dot product of the electric and magnetic transition dipole moment vectors, i.e. R = $|\boldsymbol{\mu}|\cdot|\mathbf{m}|\cdot\cos\theta$,[1] where $|\boldsymbol{\mu}|$ and $|\mathbf{m}|$ are the magnitudes of the electric and magnetic transition dipole moment vectors, respectively, and θ is the angle between these two vectors. Clearly, the sign of a particular VCD band is determined by the angle θ. On the other hand, such θ values do not provide one with the intuitive structural information. We therefore set out to seek a more direct, empirical correlation

between the observed VCD signatures and the corresponding conformational structures. The four atoms involved in the amide bonds are essentially in one plane due to the resonance structure of the with the –NH group with the adjacent –C=O group. Here, we define a *conformational frame angle*, τ, which is the dihedral angle between this amide plane and the –COO plane. This angle characterizes the most important conformational arrangement of the three targeted species, except the orientation of the –SH group. For depNALC, τ can in principle take on values ranging from -90º to +90º where "+" means clockwise rotation viewing from the amide plane to the –COO plane and "-" the opposite. For neutral NALC and NALCME, this range expands to -180º to +180º since there are either an H atom or a methyl group attached to the –COO group, respectively. The values of this conformational frame angle for all conformers studied here are summarized in Figure 4.8. The τ values are color coded. Red indicates that the conformer with this specific τ value has both VCD signatures in agreement with the experiment. Black means that one or both VCD signature bands show opposite signs to those observed or both bands have diminishing intensities. Green indicates that while the C=O stretching band shows consistent sign as the experiment, the amide I band has very weak or diminishing intensity.

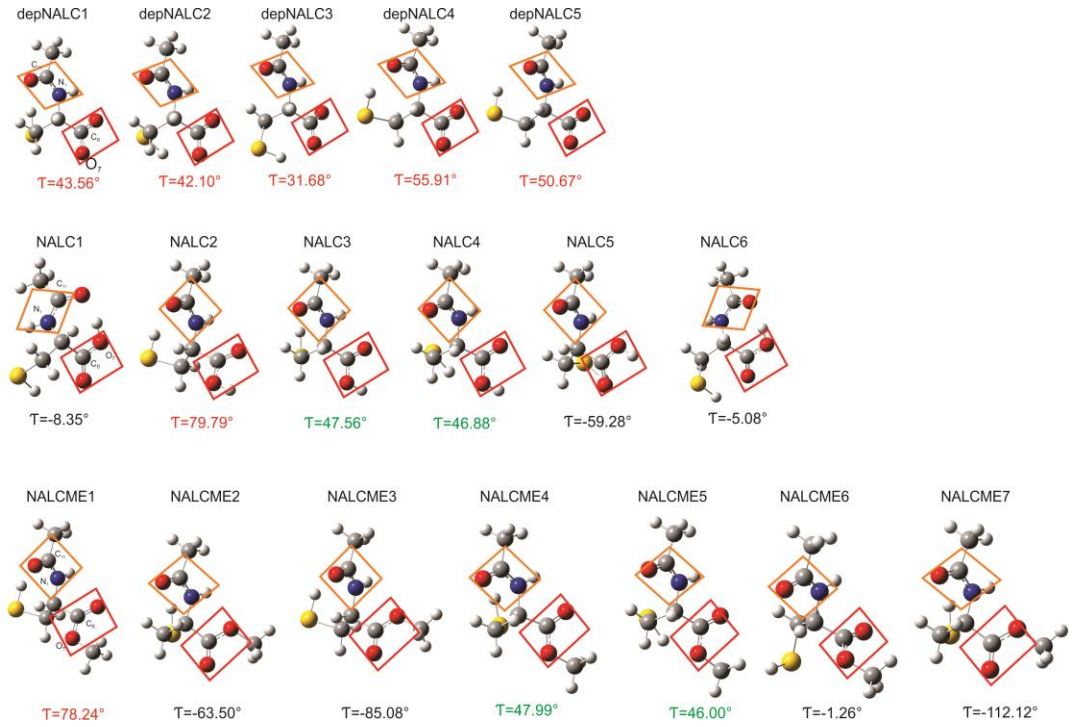


Figure 4.8. Conformational frame angle τ (in degree) for all the conformers reported in Table 4.1. The τ values are color coded. See text for the detailed discussions.

As one can see, all five conformers of depNALC have a positive τ value ranging from about 32 to 51 degrees. All of them show the positive amide I VCD bands and the negative $\nu_{as}(COO^-)$ VCD bands, in according with the experimental observed spectral features. For the neutral NALC conformers, those with the *negative* τ values all show the *opposite* amide I VCD sign compared to the experiment, whereas NALC2 with a positive τ value of about 80 degree has both of its amide I and carboxylic bands agree well with the experiment. NALC3 and 4 have the τ values of about 47 degree and both have very weak VCD amide I band. The same parallel observation can be made for NALCME conformers as for the NALC conformers. In particular, the dominant conformers identified for NALC

and NALCME in water, i.e. NALC2 and NALCME1, have essentially the same conformational frame angle of about 80 degree. Of course, $\tau$ does not have a simple one-to-one relationship to $\theta$s. Nevertheless, as shown here, the VCD signatures observed for the amide I band and the C=O stretching bands can be used as markers to identify such conformational preference in water.

For depNALC, the conformational frame as defined above is fairly rigid. It is not surprising that all five conformers show very much the same VCD signatures in the 1800-1500 $cm^{-1}$ region. Furthermore, it appears that these two VCD bands are not sensitive to the relative orientation of the –SH group in the molecule since this is precisely how the five conformers are generated. On the other hand, one may expect different VCD signatures for the –SH stretching band. Indeed, the simulated VCD features of the –SH mode for these five conformers are very different (See Figure B6, Supporting Information, Appendix B). Unfortunately, this mode is too weak to be measured experimentally.

### 4.3.6 The solute-water hydrogen-bonding interactions and DFT conformational stabilities

It is recognized in the current study that the dominant conformers identified are not necessarily those predicted theoretically. Although DFT population factors have been used successfully in many cases, their applications with highly polar solvents tend to be less successful. One can hypothesize that the explicit solute-water hydrogen-bonding interactions may alter the relative stability of individual conformers significantly. Indeed, clear evidences of such explicit

hydrogen-bonding interactions between chiral solute and water molecules in aqueous solution were demonstrated previously using chirality transfer spectral features[13,14,34] and other characteristic changes in the VCD spectra.[4,15] For a number of small model chiral molecular systems, it has been possible to probe the chiral solute-water interacts in solution directly. Using both the implicit and explicit solvation models, the experimental VCD features observed can be accounted for in detail. For large chiral molecular systems with multiple relevant conformers, on the other hand, it may be too expensive or not feasible to utilize the explicit solvation methodology. The approach of using the IR and VCD spectral signatures simulated with the PCM model of water solvent as markers to extract information about chirality and dominant conformations is a viable alternative, as demonstrated in the current study.

It is also noted that some detailed IR spectral features could not be explained satisfactorily based on the PCM of water solvent. For example, the 15 $cm^{-1}$ blue shift of $\nu(C=O)_{ester}$ of NALCME compared to $\nu(C=O)_{ca}$ of neutral NALC was not correctly predicted. It is acknowledged that such a small vibrational shift is in general challenging to reproduce with harmonic vibrational calculations. In addition, the PCM approach does not capture the explicit hydrogen-bonding interactions between NALCME and water and between NALC and water. A plausible reason for such a blue shift is that the neutral form of NALC can engage more extensively in the hydrogen-bonding interactions between water and the –COOH group, causing $\nu(C=O)_{ca}$ to red-shifted more significantly compared to that of NALCME.

## 4.4. Conclusions

IR and VCD spectral signatures of the amide I and C=O stretching bands of NALCME and NALC were measured in water under different pHs. With the extensive conformational calculations and the detailed analyses of the resulting spectral features and structural parameters, we establish a clear relationship between the observed VCD spectral signatures and the preferred conformations. The sign inversion observed for the amide I VCD band going from neutral NALCME and NALC to depNALC is explained satisfactorily based on the changes in the corresponding conformational frame angles in these species. In addition, the geometric changes going from the gas phase to the PCM of water solvent were investigated to highlight the effects of a dielectric bulk environment. It is noted that drastically different VCD spectral signatures were predicted in the above spectral window for different conformers of neutral NALC and NALCME. This advantage allows one to confidently identify the particular conformations favored in solution, regardless of their DFT stability ordering. The present study shows that the relative free energies predicted may not reflect the actual situation in solution as demonstrated in the cases of neutral NALCME and NALC. Such deviations are rationalized in terms of the interferences from the explicit hydrogen-bonding interactions between chiral solute and water molecules. Based on the current study, it is recommended to include the PCM of water solvent in the studies of amino acids and the related chiral molecules since it is relatively inexpensive and can capture some of the main conformational changes in the presence of a dielectric solution environment.

## 4.5. Acknowledgements

This research was funded by the University of Alberta and the Natural Sciences and Engineering Research Council of Canada. We gratefully acknowledge access to the computing facilities provided by the Shared Hierarchical Academic Research Computing Network (Sharcnet). YX holds a senior Canada Research Chair in Chirality and Chirality Recognition.

## References


[1] L.A Nafie, Vibrational Optical Activity: Principles and Applications, John Wiley & Sons, Chichester, UK, 2011.

[2] P. J. Stephens, F. J. Devlin, J.-J. Pan, Chirality 20 (2006) 643-663; T. B. Freedman, X. Cao, R. K. Dukor, L. A. Nafie, Chirality 15 (2003) 743-758.

[3] P. Zhang, P. L. Polavarapu, Appl. Spectrosc. 60 (2006) 378-385; W. M. Zuk, T. B. Freedman, L. A. Nafie, J. Phys. Chem. 93 (1989) 1771-1779.

[4] M. R. Poopari, P. Zhu, Z. Dezhahang, Y. Xu, J. Chem. Phys. 137 (2012) 194308/1-7; P. Zhu, G. Yang, M. R. Poopari, Z. Bie, Y. Xu, ChemPhysChem 13 (2012) 1272-1281.

[5] T. A. Keiderling, Curr. Opin. Chem. Biol. 6 (2002) 682-688; "Vibrational circular dichroism of biopolymers. Summary of methods and applications", T. A. Keiderling, J. Kubelka, J. Hilario, in *Vibrational spectroscopy of polymers and biological systems*, Ed. M. Braiman, V. Gregoriou, Taylor&Francis, Atlanta (CRC Press, Boca Raton, FL) (2006) pp. 253-324.

[6] "Vibrational Circular Dichroism Spectroscopy of Chiral Molecules": G. Yang, Y. Xu, in Top. Curr. Chem.: Electronic and Magnetic Properties of Chiral Molecules and Supramolecular Architectures, Vol. 298 (Eds.: R. Naaman, D. N. Beratan, D. H. Waldeck), Springer, Berlin, (2011) 189-236.

[7] E. Debie, P. Bultinck, W. Herrebout, B. van der Veken, Phys. Chem. Chem. Phys. 10 (2008) 3498-3508; V. P. Nicu, E. Debie, W. Herrebout, B. Van der Veken, P. Bultinck, E. J. Baerends, Chirality 21 (2009) E287-E297.

[8] C. Gautier, T. Burgi, Chem. Commun. 43 (2005) 5393–5395.

[9] P. L. Polavarapu, N. Jeirath, S. Walia, J. Phys. Chem. A 113 (2009) 5423-5431; G. Yang, J. Li, Y. Liu, T. L. Lowary, Y. Xu, Org. Biomol. Chem. 8 (2010) 3777-3783; G. Yang, Y. Xu, J. Hou, H. Zhang, Y. Zhao, Dalton Trans. 39 (2010) 6953-6959; G. Yang, Y. Xu, J. Hou, H. Zhang, Y. Zhao, Chem. Eur. J. 16 (2010) 2518-2527; G. Yang, H. Tran, E. Fan, W. Shi, T. L. Lowary, Y. Xu, Chirality 22 (2010) 734-743.

[10] C. Merten, K. Hiller, Y. Xu, Phys. Chem. Chem. Phys. 14 (2012) 12884-12891; Z. Dezhahang, C. Merten, M. R. Poopari, Y. Xu, Dalton Trans. 41 (2012) 10817-10824.

[11] V. P. Nicu, E. J. Baerends, P.L. Polavarapu, J. Phys. Chem. A 116 (2012) 8366-8373.

[12] M. R. Poopari, Z. Dezhahang, Y. Xu, Phys. Chem. Chem. Phys. 15 (2013) 1655-1665.

[13] J. Sadlej, J. C. Dobrowolski, J. E. Rode, Chem. Soc. Rev. 39 (2010) 1478-1488.

[14] M. Losada, P. Nguyen, Y. Xu, J. Phys. Chem. A 112 (2008) 5621–5627; M. Losada, Y. Xu, Phys. Chem. Chem. Phys. 9 (2007) 3127-3135.

[15] M. R. Poopari, Z. Dezhahang, G. Yang, Y. Xu, ChemPhysChem 13 (2012) 2310-2311.

[16] J. Šebek, B. Gyurcsik, J. Šebestík, Z. Kejík, L. Bednárová, P. Bour, J. Phys. Chem. A 111 (2007) 2750-2760; V. W. Jürgensen, K. Jalkanen, Phys. Biol. 3 (2006) S63-S79.

[17] L. Borgström, B. Kågedal, O. Paulsen, Eur. J. Clinical Pharm., 31 (1986) 217-222.

[18] M. Z. Kanter, Am. J. Health-System Pharm. 63 (2006) 1821-1827.

[19] A. Krężel, W. Bal, J. Inorg. Biochem. 98 (2004) 161-166.

[20] Gaussian 09, Revision B.01, M. J. Frisch, G. W. Trucks, H. B. Schlegel, G. E. Scuseria, M. A. Robb, J. R. Cheeseman, G. Scalmani, V. Barone, B. Mennucci, G. A. Petersson, H. Nakatsuji, M. Caricato, X. Li, H. P. Hratchian, A. F. Izmaylov, J. Bloino, G. Zheng, J. L. Sonnenberg, M. Hada, M. Ehara, K. Toyota, R. Fukuda, J. Hasegawa, M. Ishida, T. Nakajima, Y. Honda, O. Kitao, H. Nakai, T. Vreven, J. A. Montgomery, Jr., J. E. Peralta, F. Ogliaro, M. Bearpark, J. J. Heyd, E. Brothers, K. N. Kudin, V. N. Staroverov, R. Kobayashi, J. Normand, K. Raghavachari, A. Rendell, J. C. Burant, S. S. Iyengar, J. Tomasi, M. Cossi, N. Rega, J. M. Millam, M. Klene, J. E. Knox, J. B. Cross, V. Bakken, C. Adamo, J. Jaramillo, R. Gomperts, R. E. Stratmann, O. Yazyev, A. J. Austin, R. Cammi, C. Pomelli, J. W. Ochterski, R. L. Martin, K. Morokuma, V. G. Zakrzewski, G. A. Voth, P. Salvador, J. J. Dannenberg, S. Dapprich, A. D. Daniels, Ö. Farkas, J. B. Foresman, J. V. Ortiz, J. Cioslowski, and D. J. Fox, Gaussian, Inc., Wallingford CT, 2009.

[21] Density Functional Methods in Chemistry, Ed. J. K. Labanowski , J. W. Andzelm, Springer-Verlag, New York, 1991.

[22] K. Kim, K. D. Jordan, J. Phys. Chem. 98 (1994) 10089-10094.

[23] P. J. Stephens, F. J. Devlin, C. F. Chabalowski, M. J. Frisch, J. Phys. Chem. 98 (1994) 11623-11627.

[24] C. T. Lee, W. T. Yang, R. G. Parr, Phys. Rev. B. *37 (*1988) 785-789.

[25] D. E. Woon, T. H. Dunning Jr., J. Chem. Phys. 98 (1993) 1358-1371.

[21] J. Tomasi, B. Mennucci, R. Cammi, Chem. Rev. 105 (2005) 2999-3093.

[27] J. He, P. L. Polavarapu, Spectrochimica Acta Part A 61 (2005) 1327-1334.

[28] B. Boeckx, R. Ramaekers, G. Maes, J. Mol. Spectrosc. 261 (2010) 73-81.

[29] N. Borho, M. A. Suhm, K. Le Barbu-Debusb, A. Zehnacker, Phys. Chem. Chem. Phys. 8 (2006) 4449-4460.

[30] N. Borho, Y. Xu, Phys. Chem. Chem. Phys. 9 (2007) 1324-1328; P. Ottaviani, B. Velino, W. Caminati, Chem. Phys. Lett. 428 (2006) 236-240.

[31] See for example, D. J. Miller and J. M. Lisy, J. Am. Chem. Soc. 130 (2008) 15393-15404.

[32] Z. Dezhahang, C. Merten, M. R. Poopari, Y. Xu, Dalton Trans. 41 (2012) 10817-10824.

[33] M. A. Muñoz, O. Muñoz, P. Joseph-Nathan, Chirality 22 (2010) 234-241.

[34] G. Yang, Y. Xu, J. Chem. Phys. 130 (2009) 164506/1-9; Y. Liu, G. Yang, M. Losada, Y. Xu, J. Chem. Phys. 132 (2010) 234513/1-11.

# 5 Chapter

## Conformational distributions of N-acetyl-*L*- cysteine in aqueous solutions: a combined implicit and explicit solvation treatment of VA and VCD spectra

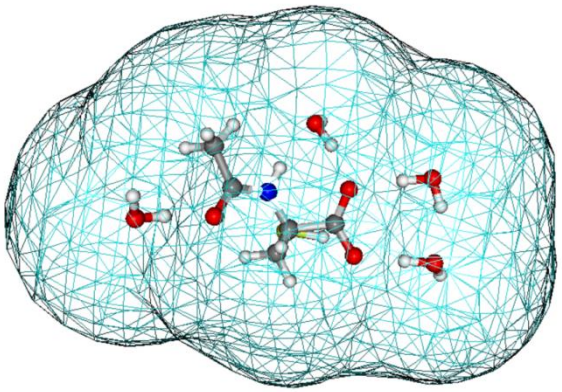

**"This chapter is directly copied from the published paper"**

M. R. Poopari, Z. Dezhahang, G. Yang, Y. Xu, "Conformational distributions of N-acetyl-L-cysteine in aqueous solutions: a combined implicit and explicit solvation treatment of VA and VCD spectra", ChemPhysChem, 13, 2012, 2310-2321

## 5.1. Introduction

N-Acetyl-L-cysteine (NALC; IUPAC: (2R)-2-acetamido-3-sulfanylpropanoic acid) is the acetylated form of L-cysteine. In recent years, there has been a significant interest in this molecule because this thio-containing amino acid is a strong antioxidant and is capable of detoxifying free radicals that are implicated in cancer and other diseases.[1,2] This pharmaceutical drug is sold as a dietary supplement for its liver protection effects and its ability to boost the glutathione (gamma-l-glutamyl-l-cysteinylglycine) level in cells.[3] It is also interesting to note that in recent years, researchers have found that an excessive amount of NALC in the body could potentially cause damage to the heart and lungs.[4] To gain a fundamental understanding of these complex biological processes, detailed knowledge of the conformations of NALC in aqueous solutions under different pH values is essential, since different conformations adopted by NALC in water may influence the NALC-induced structural changes in DNA and consequently the functionality of DNA. Indeed, much attention has been paid to the properties of NALC from both experimental and theoretical sides. This is in part due to the fact that the acetyl side chain can provide other interesting properties related to the CN amide bond, commonly encountered in peptides. As a result, NALC exhibits a conformational topology that is frequently found in biological systems.[5,6] At the same time, the system is small enough to be amenable for high-level ab initio calculations.[7,8,9,10] Gautier and Burgi studied the vibrational circular dichroism (VCD) activities of NALC molecules adsorbed on surfaces of gold nanoparticles.[11] More recently, Maes and his colleagues investigated the conformational landscape of NALC by matrix

isolation Fourier transform (FT) infrared (IR) spectroscopy in combination with ab initio calculations, in which an extensive search for the neutral NALC conformations was performed.[12] VCD spectroscopy measures the differential absorption of the left versus right circularly polarized IR radiation by a chiral molecule. It has been used extensively to probe absolute configurations and conformations of chiral organic and inorganic molecules in solution.[13,14] The magnitude and sign of a VCD feature depend on its rotational strength, that is, the imaginary part of the direct product of the electric transition dipole moment and the associated magnetic dipole moment. For this reason, VCD spectra are highly sensitive to subtle conformational differences and changes, for example, those induced by solvent–solute hydrogen-bonding interactions.[15,16,17,18] VCD spectroscopy can often discriminate more precisely among conformers than vibrational absorption (VA) spectroscopy, which is also structurally sensitive.

Herein, the detailed conformational distributions of the dominant species of NALC under different pH conditions in aqueous solutions have been investigated by using VA and VCD spectroscopy, together with ab initio and molecular dynamics (MD) simulations. In addition, UV/Vis studies have also been used to provide further evidence about the dominant species of NALC under specific conditions. Furthermore, both the implicit polarizable continuum model (PCM) and the explicit solvation model based on the solute–solvent intermolecular hydrogen-bonding interactions have been considered to account for the solvation effects. These models were applied separately and jointly to evaluate their effectiveness. Important conclusions about the conformations of

NALC and about NALC–water hydrogen-bonding interactions in aqueous solution have been obtained.

## 5.2. Results and Discussions

In this section, the VA and UV/Vis spectral evidence for the dominant species under different pH conditions is discussed, followed by the systematic DFT searches for the most stable conformers of all the important species in the gas phase and in solution with the PCM. Subsequently, the potential energy distribution (PED) analyses[19] of normal VA modes are described, followed by comparisons of the simulated PCM VA spectra with the experimental data under highly acidic and basic conditions. Finally, the combined PCM and explicit solvent model treatment of the VA and VCD spectra of deprotonated NALC is described, followed by a comparison with the VA and VCD experimental data under pH 7 conditions.

### 5.2.1. Experimental VA and UV/Vis Spectra of NALC under Different pH Conditions

The measured VA spectra of dissolved NALC in D2O at different pH values ranging from 0.65 to 13.0 are summarized in Figure 1. There are significant differences in the VA spectra as the pH value increases. This can be attributed to the presence of different NALC species. For example, dissolving NALC in $D_2O$ without adding any strong acid or base resulted in a pH value of 2.5. The pka of the carboxylic acid moiety in NALC is 3.24.[20] Based on the simple relationship, pH=pKa+log {[$A^-$]/[HA]}, one can estimate that 82% of

NALC is in the COOH form whereas 18% is in the COO form at pH 2.5. To uncover what species there are at different pH values, we examined the VA carbonyl stretching spectral features in the 1500–1800 $cm^{-1}$ region. The carboxylic (C=O) stretch in COOH and the acetyl (C=O) stretch are denoted as $\upsilon(CO)_{ca}$ and $\upsilon(CO)_{ac}$, respectively. At the two lowest pH values, the two well-resolved peaks at 1718 and 1630 $cm^{-1}$ can be unambiguously assigned to $\upsilon$(CO)ca and $\upsilon$(CO)ac, the amide I mode, respectively. As the pH increases, the intensity of the carboxylic stretching band decreases and eventually disappears completely when the pH reaches 5.6. In parallel, a new peak at 1599 $cm^{-1}$, which corresponds to the anti-symmetric stretching mode of COO, that is, $\upsilon_{as}(COO)$, becomes significant at pH 3.8. Related to this, another new band feature at 1395 $cm^{-1}$, which can be tentatively assigned to the COO symmetric stretching mode, that is, $\upsilon_s(COO)$, also becomes obvious at pH 3.8. The $\upsilon_s(COO)$ band remains essentially at the same frequency position until the pH reaches 13. Two strong peaks at 1622 and 1599 $cm^{-1}$, observed at pH 7, correspond to the $\upsilon(CO)_{ac}$ and $\upsilon_{as}(COO)$ mode, respectively. Experimentally, the position of the amide I mode was red-shifted by about 8 $cm^{-1}$ from 1630 to 1622 $cm^{-1}$ as the pH increased from 0.65 to 7.0, thus indicating that the dominant carrier of the amide I mode has changed. A further shift of about 5 $cm^{-1}$ to the red to 1617 $cm^{-1}$ was detected for this band when the pH reached 13, again indicating another change in the dominant carrier of the amide I mode.

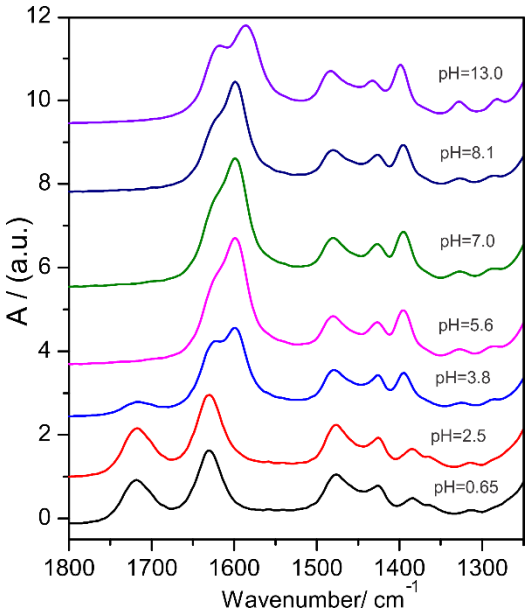


Figure 5.1. Experimental VA spectra of NALC in D2O at a series of pH values ranging from 0.65 to 13.0.

The detailed VA assignments of the peaks in the lower-wavenumber region are less obvious. These bands are related to the bending, scissoring, wagging, and rocking modes of the CH, $CH_2$, $CH_3$, NH, OH, and SH groups, as well as the skeleton modes. It is difficult to anticipate how their VA frequencies would alter due to the subtle changes in the charged state, the conformational flexibility, and the water solvent. Their assignments will be discussed in the next section in conjunction with the simulated VA spectra of the most stable conformers. From the above observation, one can conclude straightforwardly that the carboxylic group exists mostly as COOH at pH values up to ~ 2.5, whereas the $COO^-$ form becomes dominant at pH above ~ 4. These two forms coexist in the pH range of 2.5–4. In what form, that is, the protonated (Pro-), neutral (Neu-), deprotonated (Dep-) or doubly deprotonated (D-Dep-) form, the other part of NALC exists at different pH values is not obvious without the aid of the

corresponding spectral simulations. For example, does NALC exists in the protonated form at pH 0.65? The related questions are whether NALC exist in the zwitterionic form at pH ~7 and if a proton would prefer to attach to the N site rather than the O atom of the acetyl group or the S site in NALC. If one considers that the lone pair of the nitrogen atom in NALC can participate in a resonance structure with the adjacent acetyl C=O group, just as in a regular CN peptide bond, there is a partial positive charge on the N atom. This makes the N atom a highly unlikely site to accept a proton. It is interesting to point out that in recent years, there have been heated debates about the validity and the accuracy of the description provided by the amide resonance theory.[21,22,23] Addario et al. proposed that in such cases, the most likely protonated site is the oxygen atom of the acetyl group. Such a protonated structure can be stabilized by the formation of a hydrogen-bonded ring where the proton connects the two carbonyl O atoms.[24] Empirically, the pKa value of an O-protonated amide is roughly close to zero, while that of the N-protonated amide is about 7.[25] If NALC follows this trend closely, one may expect about 20% of the Pro-NALC species at a pH of 0.65, although no specific experimental pKa value is available for the Pro-NALC to our knowledge. These points will be further discussed when comparing the experimental and simulated VA spectral features of different species in the next section.

As the pH reaches 13, another new species appears, which we hypothesized to be D-Dep-NALC with $COO^-$ and $S^-$. Since the pKa for the thiol group was reported to be 9.52,[26] one can expect that the D-Dep-NALC species

becomes increasingly more important than the singly deprotonated species as the pH becomes much higher than 9.52. To obtain the direct spectral signatures related to this change, the UV/Vis spectra of NALC (Figure C1, Supporting Information, Appendix C) were measured under several different pH conditions from strongly acidic to strongly basic. At pH ~ 9.4, a new strong shoulder bump in the 220–250 nm region emerges and becomes more prominent as the pH increases. This UV/Vis band had been empirically correlated to a transition of the doubly deprotonated species containing $S^-$.[27] We calculated the UV/Vis spectra of the singly deprotonated species containing just $COO^-$ and doubly deprotonated species with both $COO^-$ and $S^-$ (Figure C1, Supporting Information). Indeed, the simulated UV/Vis spectra exhibit the expected difference between the deprotonated and the doubly deprotonated species, consistent with the hypothesis proposed before, thus confirming the dominant existence of $S^-$ pH 13.

Using the semi-empirical program SPARC, which provides pKa estimation for amino acids and peptides,[28] a general description of the various species existing at a certain pH value can be predicted. For example, at the highly acidic pH of 0.65, the only species in solution is the neutral form of NALC. As the pH increases to 2.5, this changes to 88% Neu-NALC and 12% Dep-NALC, while the percentage of Dep-NALC increases to 100% as the pH reaches 5.6. At pH values higher than 8.1, the doubly deprotonated form with both $COO^-$ and $S^-$, that is, DDep-NALC, starts to appear and becomes the dominant species with a 100% population at pH 13.0. The general trend predicted by this program is consistent with the conclusion drawn from the VA and UV/Vis spectral analyses

described above, although the detailed conformational distributions have yet to be derived based on the theoretical spectral simulations to be discussed below. For conciseness, three representative pH conditions of 0.65, 7.0 and 13.0 were selected for discussion, when only a single dominant species is expected in each solution.

### 5.2.2. Most Stable Conformers of Pro-, Neu-, Dep- and D-Dep-NALC in the Gas Phase and in D2O with the PCM

#### 5.2.2.1. Neu-NALC

The Neu-NALC monomer has seven internal rotational degrees of freedom,[12] which makes it a highly flexible molecule. This results in a large number of possible conformations and poses a significant challenge in locating true global minima, that is, the most stable conformers. Conformational searches for Neu-NALC have been reported in a number of previous studies.[29,12] We carried out a preliminary systematic search by rotating all these internal rotational degrees of freedom involving heavy atoms by either 60˚ or 180˚ sequentially. While the work was in progress, an extensive search for Neu-NALC based on a similar approach was reported.[12] The most stable conformers identified are similar to those reported in ref. [12], although a larger basis set has been used in the current study. The geometries of the five most stable ones in the gas phase are depicted in Figure C2 in the Supporting Information, Appendix C, together with their percentage Boltzmann factors at room temperature based on the relative Gibbs free energies. For a highly flexible molecule such as NALC, $D_2O$ solvent may influence the relative stability of its conformers substantially. To account for

the water solvent, geometry searches and optimizations were also carried out for Neu-NALC in the PCM of water. The geometries of the five most stable conformers in water with a total Boltzmann percentage population close to 100% are depicted in Figure 5.2.

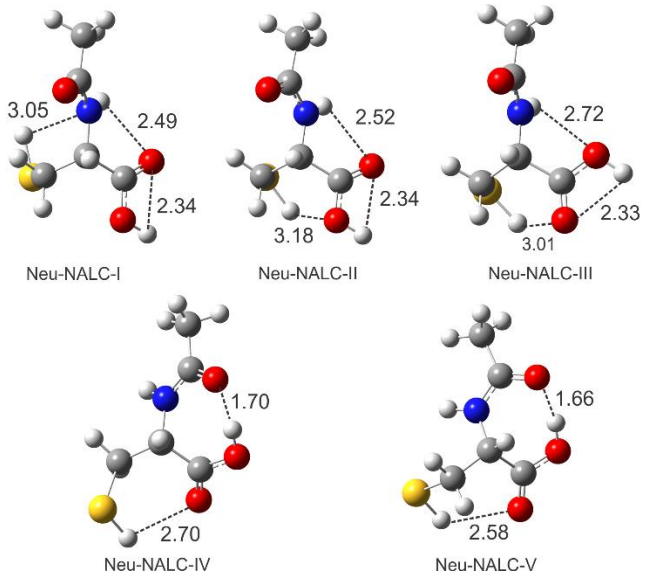


Figure 5.2. Optimized geometries of the five lowest-energy conformers of neutral NALC at the B3LYP/6-311++G(d,p) level with the PCM of $D_2O$. The intramolecular hydrogen-bond lengths and some important van der Waals bond lengths (in A˚) are indicated.

The corresponding gas-phase and PCM conformers show very similar features, although the geometries seem to be more compact in the gas phase with generally shorter intramolecular hydrogen-bond lengths than those in the PCM. The three most stable conformers obtained with the PCM all adopt the cis conformation of the COOH group, with the most important intramolecular (CO)H···O=C and NH···O=C(OH) bond lengths in the range of 2.3 to ~ 2.7 A˚ ,noticeably longer than the hydrogen bond length in the gas-phase Neu-NALC structures. The next two most stable conformers adopt the trans conformation of

the COOH group, with the O and H atoms on opposite sides of the CO bond, to facilitate the formation of an intramolecular hydrogen bond $COH\cdots(O=C)_{ac}$. These most stable conformers all adopt the trans amide bond configuration, with the carbonyl O and H atom of amide on opposite sides of the CN bond, reminiscent of the situation in the vast majority of polypeptides. The corresponding relative total energies $\Delta E^{\circ}$ and the relative Gibbs free energies $\Delta G^{\circ}$ in the PCM of water are provided in Table 5.1, together with their Boltzmann percentage population factors at room temperature.

Table 5.1. Relative total energies $\Delta E^{\circ}$ [kJ $mol^{-1}$] and relative Gibbs free energy $\Delta G^{\circ}$ [kJ $mol^{-1}$] of the most stable conformers of Neu-, Dep-, and D-DepNALC in D2O with the PCM solvation model at the B3LYP/6-311++G(d,p) level, and the Boltzmann percentage population factors at room temperature based on $\Delta E^{\circ}$ and $\Delta G^{\circ}$.

| Conformer | $\Delta E^{\circ}$ | $\Delta G^{\circ}$ | pop %, $\Delta E^{\circ}$ | pop %, $\Delta G^{\circ}$ |
|---|---|---|---|---|
| Neu-NALC | | | | |
| I | 0.00 | 0.00 | 50.45 | 43.20 |
| II | 0.61 | 0.30 | 39.37 | 38.29 |
| III | 3.97 | 2.10 | 10.14 | 18.50 |
| IV | 18.84 | 23.10 | 0.03 | 0.004 |
| V | 23.28 | 27.18 | 0.004 | 0.0007 |
| Dep-NALC | | | | |
| I | 0.00 | 0.00 | 47.33 | 43.53 |
| II | 0.82 | 1.35 | 33.90 | 25.20 |
| III | 3.37 | 2.17 | 12.10 | 18.11 |
| IV | 4.82 | 3.00 | 6.75 | 13.14 |
| D-Dep-NALC | | | | |
| I | 0.00 | 0.00 | 59.31 | 69.82 |
| II | 0.93 | 2.07 | 40.69 | 30.18 |

### 5.2.2.2. Dep-NALC

Based on the discussion in Section 5.2.1, the main species under neutral pH is Dep-NALC with the $COO^{-}$ group. There are four dihedral angles in Dep-NALC which are responsible for the orientations of the heavy atoms (see Figure

5.3 with atom labelling). To search for the possible conformers of Dep-NALC, a two-dimensional energy map of NALC along the two most important dihedral angles, $\tau_1$, that is, dihedral angle S-C1-C2-N and $\tau_2$, that is, dihedral angle C1-C2-N-H, calculated at the B3LYP/6-31G(d) level has been generated and is depicted in Figure 5.3. There are two minima on the 2D energy map where ($\tau_1$, $\tau_2$) takes on the values of (9,70) and (230,70). It should be pointed out that the third dihedral angle $\tau_3$, which corresponds to the rotation around the amide bond, is typically restricted to values of 180 or 0˚ based on the amide resonance theory, which are related to the trans or cis peptide bond orientation. In our search, we found that the trans configuration is much more stable than the cis configuration, consistent with what has been found in the majority of polypeptides. The fourth dihedral angle $\tau_4$ corresponds to the rotation of the two O atoms of the $COO^-$ group. This does not generate any new conformers by a 180˚ rotation. These two angles and the orientation of the hydrogen atom of SH were further optimized to ensure possible intramolecular hydrogen bonds among functional groups, $COO^-$, NH, SH, and C=O. The four most stable conformers of Dep-NALC were identified based on the above strategy in the gas phase and also optimized in the PCM. The gas-phase geometries are depicted in Figure C3 in the Supporting Information, Appendix C, together with their respective Boltzmann percentage factors at room temperature based on the relative Gibbs free energies. The corresponding structures obtained in the PCM are provided in Figure 5.4, with all the important intramolecular distances <3.2 A˚ indicated. As in the case of Neu-NALC, the gas-phase Dep-NALC conformers are more compact than those obtained in the PCM,

with in general shorter intramolecular hydrogen-bond lengths. The amide bond in all the conformers adopts the trans configuration.

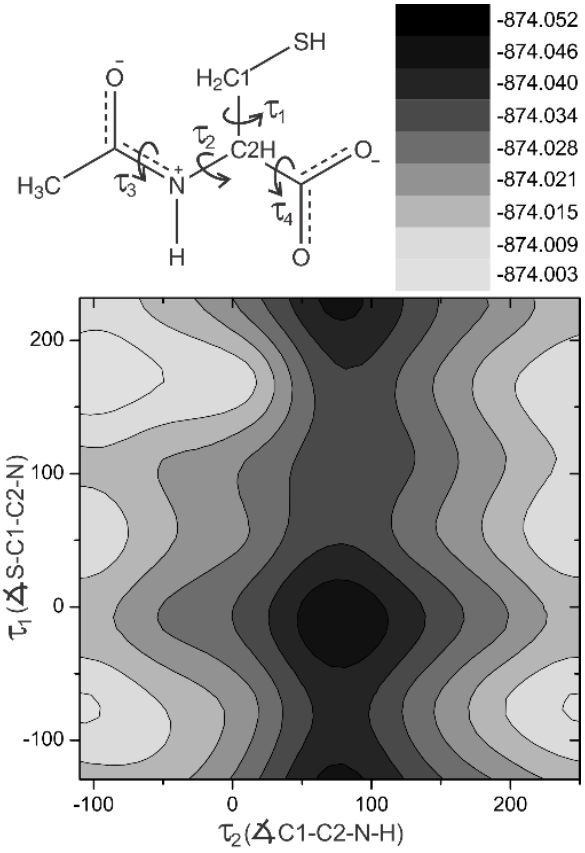


Figure 5.3. Two-dimensional energy plot of Dep-NALC at the B3LYP/6-31G(d) level, scanned along its two most important dihedral angles, $\tau_1$ and $\tau_2$. The definitions of these two dihedral angles and the related angles are also provided. The energy unit is the Hartree. See text for details.

The most important intramolecular hydrogen bond appears to be NH···OCO. While some SH···(O=C)ac and SH···OCO bond lengths in the gas phase are short enough to be classified as intramolecular hydrogen bonds, these distances are much longer in the associated conformers in the PCM, thus indicating significantly weaker interactions at these sites in the presence of water solvent. As a result, the relative Gibbs free energy ordering also alters slightly

upon going from the gas phase to solvation with the PCM. The relative total energies and relative Gibbs free energies of the four most stable Dep- NALC conformers in the PCM, together with their percentage Boltzmann factors at room temperature, are also provided in Table 5.1.

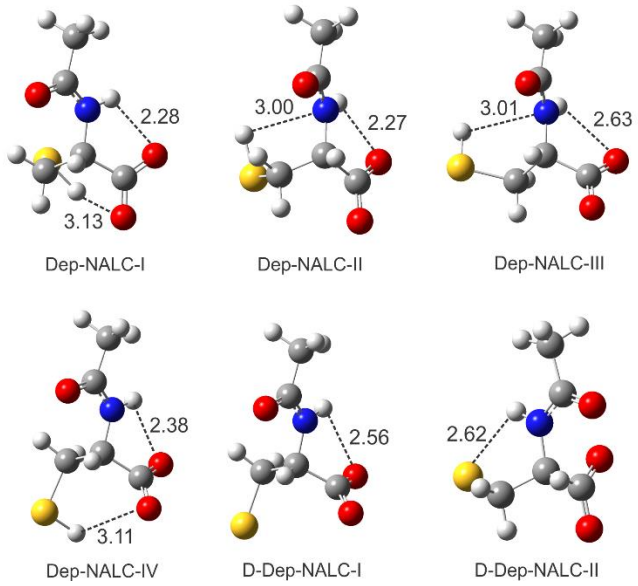


Figure 5.4. Optimized geometries of the four and two lowest-energy conformers of Dep-NALC and D-Dep-NALC, respectively, at the B3LYP/6-311++G(d,p) level with the PCM of $D_2O$. The intramolecular hydrogenbond lengths and some important intramolecular bond lengths (in A˚) are indicated.

### 5.2.2.3. D-Dep-NALC

A similar conformational search was also carried out for DDep-NALC. Here, the NH group has two choices to form intramolecular hydrogen bonds: either with the $OCO^-$ or $S^-$ moiety. Although the hydrogen-bonding interaction of the NH group with the carboxylate group tends to be stronger than with S, the energy difference between these two is generally less than 2 $kJmol^{-1}$. This gives rise to two D-Dep-NALC conformers, whose geometries and relative energies and

Gibbs free energies in the PCM are also given in Figure 5.4 and Table 5.1, respectively. The associated information for the related conformers in the gas phase is provided in Figure C3 in the Supporting Information.

### 5.2.2.4. Pro-NALC

Although Pro-NALC has been ruled out as the dominant species under the current experimental conditions, its conformational study is included here for completion. Furthermore, it is of interest to verify if one can use the VA spectral signatures in the fingerprint region to discriminate Pro-NALC from Neu-NALC directly. For the Pro-NALC conformers, as mentioned before, the oxygen atom of the acetyl group was proposed to be the most likely site for protonation.[24] Indeed, the Pro-NALC conformer with the $CO^{+}$-H unit, where the proton is attached to the O atom of the acetyl C=O group and forms an intramolecular hydrogen bond to the O atom of the carboxylic C=O group, is found to be ~13 $kcalmol^{-1}$ more stable than the conformers with the $NH_2^{+}$ unit. The structures of the most stable conformers obtained in the gas phase and with the PCM of water are depicted in Figure C4 in the Supporting Information, Appendix C, together with their percentage Boltzmann population factors at room temperature based on the relative Gibbs free energies. The above finding is consistent with the prediction from the amide resonance theory and with the empirical observations that the most typical protonated site for a peptide bond is at the O site as $CO^{+}$-H. Although the amide oxygen atom is generally considered to be the preferred

protonation site in amide, the more exotic N-protonated amides had been reported before in a few rare cases, such as medium-bridged N-protonated lactams.[30]

### 5.2.3. Simulated VA Spectra and VA Assignments of the NALC Conformers

The VA spectra of the four NALC species were simulated for all their most stable conformers obtained in the PCM. PED analyses of the fundamental normal vibrational modes of the most stable conformer of the Neu-, Dep- and D-Dep-NALC species, the relevant species under the experimental conditions of interest, were carried out. Table 5.2 shows the corresponding VA assignments in the fingerprint region of the Neu-, Dep- and DDep-NALC species based on the most stable conformer in the PCM at the B3LYP/6-311++G(d,p) level.

Before discussing the comparison of the simulated spectra with the experimental ones, one question that should be addressed is the extent of the H/D exchange since $D_2O$ was used as a solvent. In Figure 5.5c, the simulated VA spectra of Neu- NALC-I, with full to no D substitution at the COOH, NH, and SH functional groups, are provided. The VA band positions typically shift to lower frequencies upon D substitution, although by very different amounts depending on whether the proton directly contributes to the specific vibrational modes or not. The VA simulations of different deuterated isotopologues of Neu- NALC-I show that the H/D exchange at the NH site introduces the most noticeable spectral change in the region of interest, whereas deuteration at the SH and the COOH sites introduces only minor changes in the appearance of the spectrum. Most

obviously, the HNC amide II bending mode is red-shifted from 1560 $cm^{-1}$ in the non-substituted Neu-NALC-I to 1438 $cm^{-1}$ upon D substitution at the NH site. The relative intensity of this band decreases compared to those of the υ(C=O)ca and υ(C=O)ac bands. At the same time, both the υ(C=O)ca and υ(C=O)ac bands experience a small red shift upon D substitution at the NH site. From the experimental spectrum at pH 0.65 (Figure 5.5 a), one can clearly see that the strong HNC amide II bending mode at 1560 $cm^{-1}$, predicted for the species with no D substitution at the NH site, is not present in the experimental spectrum. In Neu-NALC, the NH site is a less acidic site than the SH and COOH sites. Therefore, if H/D exchange happens at the NH site, one can expect that it happens at the other two sites as well. Consequently, the dominant isotopologue of Neu-NALC-I is fully D substituted at all three functional groups discussed above. Both the gas-phase (see Figure C5, Supporting Information, Appendix C) and the PCM-simulated spectra of different isotopologues of Neu-NALC-I support this conclusion. In all the subsequent simulations, the fully deuterated species at these three functional groups have been used whenever applicable.

Table 5.2. Experimental and the corresponding calculated VA frequencies [$cm^{-1}$] and VA mode assignments of the most stable conformer of Neu-, Dep-, D-Dep-NALC at the B3LYP/6-311++G(d,p) level with the PCM.

| Exp. freq.[a] | Calc. freq.[b] | Assignment[c] | PED [%] |
|---|---|---|---|
| Neu-NALC | | | |
| 1718 | 1752 | $\nu(C{=}O)_{ca}$ | 88 |
| 1630 | 1661 | $\nu(C{=}O)_{ac}$, amide I | 80 |
| 1476 | 1488 | $\delta$(HNC) + asym $CH_3$ deformation + $\delta$(HCC) | 61 |
| 1425 | 1438 | $\delta$(HNC) + $\delta$(HCH)/a mixture of $\nu$(NC) + $\nu$(CC), amide II | 39/28 |
| 1383 | 1396 | sym $CH_3$ deformation | 82 |
| 1362 | 1372 | $\nu$(C–C) + $\nu$(N–C) | 29 |
| 1313 | 1342 | $\delta$(HCN) + $\delta$(HCC) + $\delta$(HCS) | 72 |
| Dep-NALC | | | |
| 1622 | 1643 | $\nu(C{=}O)_{ac}$, amide I | 81 |
| 1599 | 1595 | $\nu_{as}(COO^-)$ | 82 |
| 1481 | 1490 | asym $CH_3$ deformation + $\delta$(NCO) | 45 |
| 1425 | 1440 | $\delta$(HNC) + asym $CH_3$ deformation/$\nu$(NC), amide II | 46/30 |
| 1395[d] | 1395 | sym $CH_3$ deformation | 62 |
| | 1387 | $\nu_s(COO^-)$ | 53 |
| 1326 | 1352 | $\delta$(HCN) | 70 |
| D-Dep-NALC | | | |
| 1617 | 1636 | $\nu(C{=}O)_{ac}$, amide I | 77 |
| 1585 | 1575 | $\nu_{as}(COO^-)$ | 90 |
| 1484 | 1488 | asym $CH_3$ deformation + $\delta$(HCC) | 70 |
| 1432 | 1439 | $\nu$(NC)/mixture of $\delta$(HNC) + $\delta$(NCO) + $\delta$(HCH), amide II | 38/27 |
| 1398[d] | 1397 | sym $CH_3$ deformation and a mixture of $\nu_s(COO^-)$ + $\nu$(CC) | 40/33 |
| | 1390 | sym $CH_3$ deformation and a mixture of $\nu_s(COO^-)$ + $\nu$(CC) | 48/31 |
| 1328 | 1345 | $\tau$(HCCO) | 73 |
| 1283 | 1307 | $\delta$(HCC) | 65 |

[a] The experimental frequencies are taken from the VA measurements at pH 0.65, 7.0, and 13.0, where Neu-NALC, Dep-NALC or D-Dep-NALC is the only dominant species in each case, respectively. [b] In all VA simulations herein, the fully deuterated species at the COOH, NH, and SH functional groups were used wherever appropriate. See text for detailed discussions. [c] $\nu$, stretching, $\delta$, bending, and $\tau$, torsion. [d] These two bands were not resolved in the experiments. The experimentally observed shoulder at the lower-wavenumber side of this band under neutral pH conditions corresponds to a different Dep-NALC conformer. See Section 2.3 for detailed discussions.

### 5.2.3.1. Highly Acidic Conditions

For highly acidic conditions, the observed VA spectrum at pH 0.65 is compared with the population-weighted simulated VA spectra of the Neu-NALC conformers in the gas phase and in the PCM of $D_2O$ in Figure 5.5. The individual VA spectra of the three most stable conformers are also included. These three conformers account for close to 100% of the total Neu-NALC population based

on the Gibbs free energy calculation with the PCM. In general, both the population-weighted PCM and gas-phase spectra show reasonable agreement with the experimental spectrum observed at pH 0.65. The PCM spectrum gives noticeably better overall agreement. For example, the peak frequencies of the two C=O stretching bands obtained with the PCM are much closer to the experimental ones than those predicted in the gas phase. To verify if it is possible to use VA signatures alone to conclude that Pro-NALC is not the dominant species under the lowest pH conditions measured in this work, the experimental data at pH 0.65 are compared to the simulated VA spectra of Pro-NALC in the gas phase and with the PCM (see Figure C6, Supporting Information, Appendix C). The two most stable Pro-NALC conformers, with a total population close to 100 %, were included in the simulation. In the PCM, υ(C=O)ca experiences a significant redshift on going from Neu-NALCto Pro-NALC since the proton is hydrogen-bonded to the carboxylate O atom directly, whereas other vibrational modes experience much smaller shifts. As a result, the band gap between the two carbonyl groups in the 1550–1750 $cm^{-1}$ region becomes much narrower. At the same time, the next strong band in the lower-wavenumber region, corresponding mainly to a mixture of υ(CO)ac and $\upsilon(CCH_3)$ stretch, experiences a blue shift, which results in a much narrower band gap between this and the υ(C=O)ca stretch than in Neu-NALC. Clearly, the predicted Pro-NALC spectral pattern shows a very poor match with the experimental data even with the inclusion of the PCM, in contrast to the comparison with Neu-NALC. One can therefore confidently conclude that Neu-NALC is the dominant species in $D_2O$ at pH 0.65 whereas Pro-NALC is not.

### 5.2.3.2. Highly Basic Conditions

For highly basic conditions at pH 13, it was established in Section 5.2.1 that D-Dep-NALC is the most important species. The experimental VA spectrum at pH 13 is compared with the simulated VA spectra of the two most stable conformers of DDep-NALC in $D_2O$ with the polarizable continuum solvation (PCM) solvation model in Figure 5.6, and with the gas-phase simulations in Figure C7 (Supporting Information, Appendix C). In the population- weighted simulated spectrum with the PCM, the amide I band of D-Dep-NALC shifts to red by about 25 $cm^{-1}$ (unscaled) compared to that of Neu-NALC, correctly capturing the substantial red shift of 13 $cm^{-1}$ observed experimentally. A new band, corresponding to $\upsilon_{as}(COO^-)$ appears at 1585 $cm^{-1}$ experimentally, compared to a prediction of 1575 $cm^{-1}$. The next band, mainly due to the asymmetric deformation of the $CH_3$ group, was observed at 1484 $cm^{-1}$, blue-shifted by about 8 $cm^{-1}$ from that observed at 1476 $cm^{-1}$ with pH 0.65. Again, this blue shift has been correctly predicted with the simulated VA spectra with the PCM. Overall, the PCM-simulated VA spectrum shows good agreement with the experimental one. The gas-phase spectrum, on the other hand, shows a much less satisfactory agreement, thereby indicating the importance of taking the effects of water solvent into account in the VA simulation. Based on the good agreement between the PCM simulation and the experimental data, one can conclude that the two most stable conformers of D-Dep-NALC, which favour a close NH···$^-$OOC and NH···$^-$S intramolecular interaction, are the most important conformers at pH 13.0.

Overall, the population-weighted simulated VA spectra of the most stable conformers of Neu-NALC and D-Dep-NALC with the PCM demonstrate good agreements with the experimental VA spectra obtained in highly acidic and basic aqueous solutions. In these two cases, it has been shown that the inclusion of the PCM is essential for assigning the dominant species and conformational distributions with good confidence. The parallel comparison for the pH 7 condition will be discussed below. More importantly, the PCM solvation model will be further tested with both VA and VCD experimental data at pH 7 to verify if explicit solvation of water should also be considered.

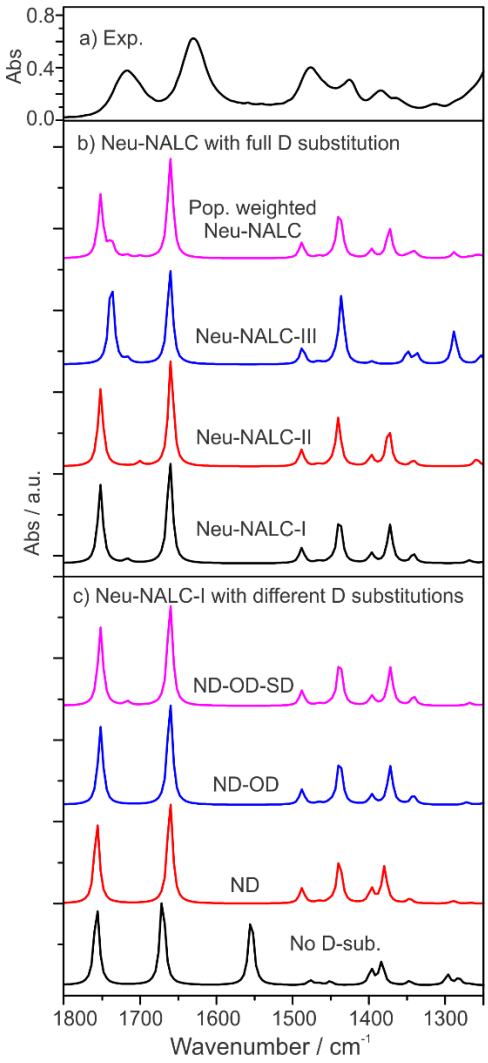


Figure 5.5. Comparisons of a) the experimental VA spectrum of NALC in D2O under highly acidic conditions at pH 0.65 with b) the simulated VA spectra of the three most stable Neu-NALC conformers with the PCM of D2O, and with their population-weighted VA spectrum based on the relative Gibbs free energies at the B3LYP/6-311++G(d,p) level at room temperature. c) Simulated VA spectra of the different deuterium isotopologues of Neu-NALC-I with the PCM of D2O at the B3LYP/6-311++G(d,p) level.

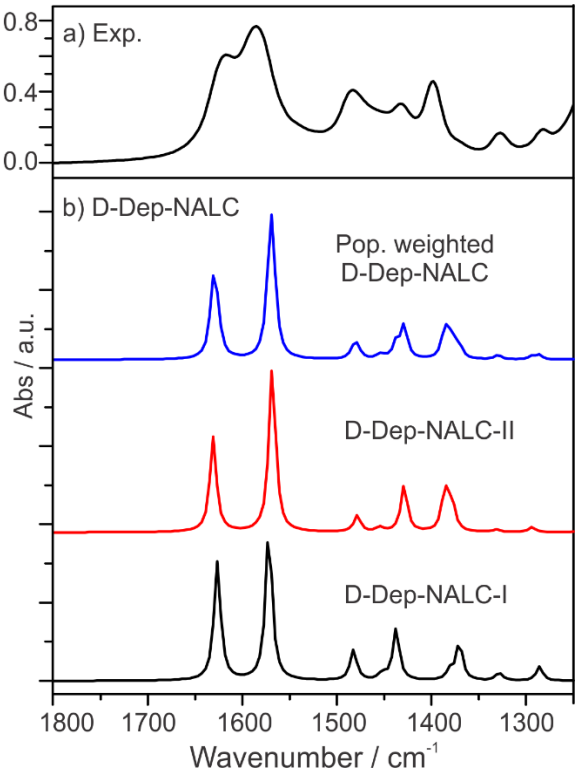


Figure 5.6. Comparisons of the experimental VA spectrum of NALC in D2O under the highly basic conditions of pH 13.0 with the simulated VA spectra of the two most stable D-Dep-NALC conformers with the PCM of D2O, and with their population-weighted VA spectrum based on the relative Gibbs free energies at the B3LYP/6-311++G(d,p) level at room temperature.

### 5.2.4. A Combined Implicit and Explicit Solvation Treatment of the VA and VCD Spectra Obtained under Neutral Conditions

NALC aqueous solutions under neutral conditions are of special biological interest. In particular, conclusive information about the conformational distributions of the most significant species would be valuable. To firmly reach the correct conclusion and to evaluate the effects of the hydrogen-bonding interactions between NALC and water on the conformational structures and stability of NALC, not only VA but also VCD measurements of NALC in $D_2O$ at pH 7.0 have been measured. The additional VCD data are highly sensitive to the

structural and conformational differences, and thus impose an even more stringent experimental test for comparison with theoretical modelling to reach a final conclusion.

From the analysis of NALC in highly acidic solution, it has been concluded that only the neutral species dominates in such a solution. It is therefore highly unlikely for NALC to exist primarily in the zwitterionic form at neutral pH. Rather, the most likely species should be Dep-NALC. In Figure 5.7, the experimental VA and VCD spectra are compared to the simulated spectra of the four most stable Dep-NALC conformers and the corresponding population-weighted spectra in the gas phase and in $D_2O$ using the PCM solvation model. The related results of the Dep-NALC conformers in the gas phase are provided in Figure C8 in the Supporting Information, for comparison. A cursory glance at the spectra predicted with the PCM and in the gas phase suggests that the inclusion of the PCM is essential to reach a good agreement with the experimental VA and VCD data. To facilitate detailed assignments, the experimentally observed VA bands are labelled with the numbers 1 to 6. The simulated VA bands are similarly labelled. Indeed, all major VA peak wavenumbers and intensities were well captured with the PCM simulation, including the experimentally observed shoulder, labelled as 5', near the main VA band 5. The corresponding VCD features are also labelled. While the main VCD features were also well predicted, some details in the 1300– 1450 cm1 region were not reproduced satisfactorily. The main discrepancy is that the medium-strength VCD band labelled as 5', observed experimentally, was not predicted. A closer examination of the

experimental spectra showed that VA band 5 corresponded to VCD band 5, both with the peak wavenumber at 1395 $cm^{-1}$. Similarly, VA band 6 corresponded to VCD band 6, both with the peak wavenumber at 1328 $cm^{-1}$. Therefore, it was speculated that VCD band 5' at 1369 $cm^{-1}$ corresponded to the shoulder band 5'. However, this band was not predicted to have a substantial VCD intensity.

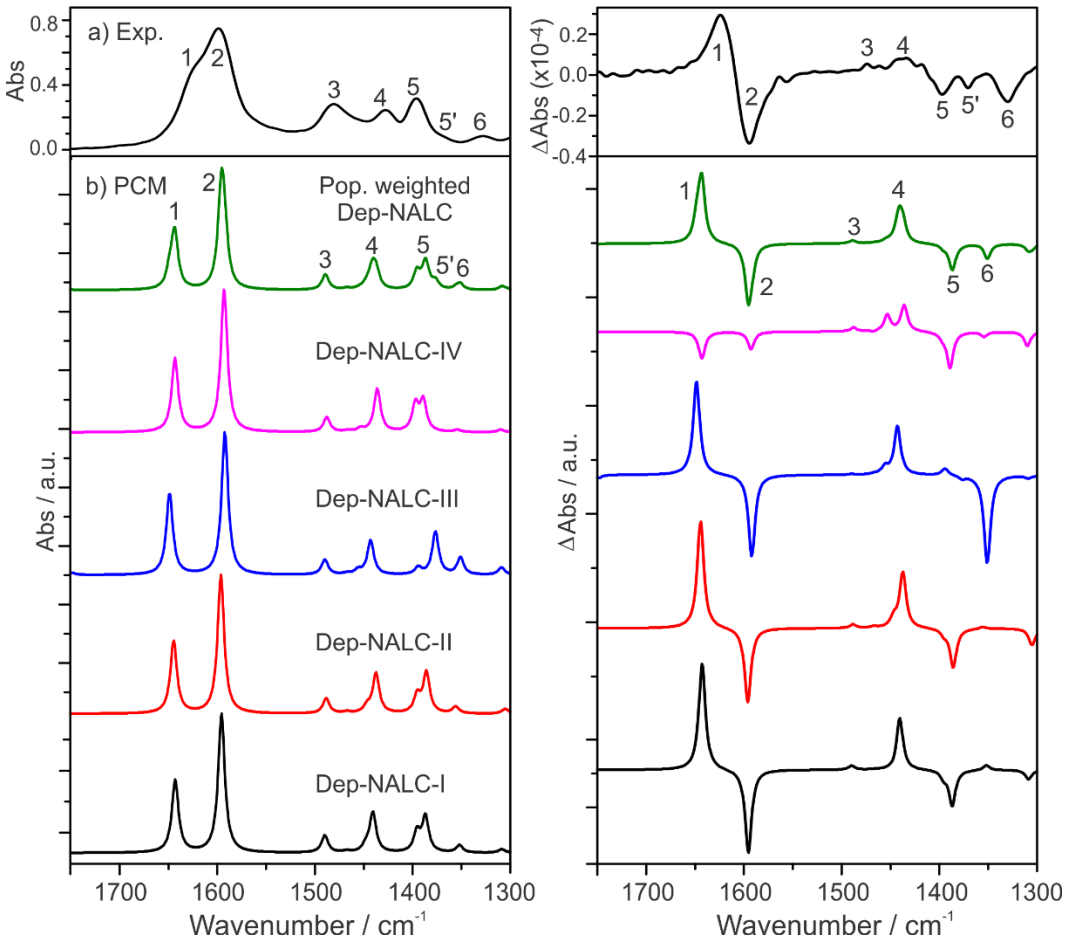


Figure 5.7. Comparisons of the experimental VA and VCD spectra of NALC in $D_2O$ at neutral pH with the simulated VA and VCD spectra of the four most stable conformers of Dep-NALC with the PCM of $D_2O$, and with the corresponding population-weighted spectra based on the relative Gibbs free energies at the B3LYP/6-311++G(d,p) level at room temperature.

At this point, the VCD modes in the fingerprint region were also checked for their robustness. The concept of robust modes was first introduced by Nicu and Baerends[31] to evaluate the sensitivity of VCD patterns to the functionals and basis sets used in the DFT simulations of VCD spectra and to assist fast, reliable, absolute configuration assignments. As mentioned before, the VCD intensity and sign are determined by the imaginary value of the dot product of the electric and magnetic transition dipole moments. For a particular VA mode whose θ, the angle between the electric and magnetic transition dipole vectors, is close to 90º, the sign of the VCD band can be altered if θ crosses 90º. As a result, the authors suggested classifying those VCD modes with q from 60 to 120º as non-robust. Gobi and Magyarfalvi[32] proposed a new alternative measure of robustness using the ratio, ξ, of dipole and rotational strengths. They further suggested using 10 ppm of this ratio as a "soft" robust mode criterion and that one should give an extra amount of scrutiny to those VCD bands with this ratio below 10 ppm. The advantages of this new alternative criterion had been discussed in detail in ref. [32]. The rotational and dipole strengths of the VCD modes in the fingerprint region of interest of the most stable conformer of Dep-NALC in the PCM and those solvated with four water molecules in the PCM are listed in Table C1 in the Supporting Information, Appendix C, together with the associated ratios. In general, all the VCD modes in this region in the PCM with high enough rotational strength to be observed experimentally can be considered robust or nearly robust.[32] It is our experience that the soft 10 ppm criterion can be further pushed to a lower limit. This and further similar examinations of other conformers,

however, do not provide a satisfactory answer to the missing VCD band. It was then hypothesized that such discrepancies could be due to the hydrogen-bonding interactions between water and NALC. Such interactions had been showed to produce chirality transfer VCD features of water solvent before.[ref 15–18] These interactions have therefore been considered below in our effort to systematically evaluate the effects of both explicit and implicit solvation with water on the respective VA and VCD spectroscopy.

#### 5.2.4.1. Estimation of the Coordination Number of the First Solvation Shell by MD Simulations

For a highly flexible molecule such as NALC in the gas phase, the intramolecular hydrogen-bonding interaction is an important factor which influences the relative stability of conformers. Upon solvation of NALC in water, on the other hand, the intermolecular hydrogen-bonding interaction between NALC and $D_2O$ can compete with the intramolecular hydrogen-bonding interaction, and therefore modify the relative stability of conformers and change their structures. To account for the NALC–water hydrogen-bonding interaction, a family of Dep-NALC–$(water)_N$ clusters with N the number of water molecules were constructed. To estimate the coordination number of the first water solvation shell, that is, the number of water molecules that are directly hydrogen-bonded to NALC, an analysis of the atom–atom radial distribution functions (RDFs) generated from the MD simulations was carried out. The details of the MD simulations are described in the Experimental and Theoretical Details section.

Five relevant RDFs, together with the atom labelling used, are depicted in Figure 5.8. An RDF, g(r), describes the density of a certain particle at a distance r from an arbitrary central atom. For example, g(r)O1HW, g(r)O2HW, and g(r)O3HW in Figure 8 show the density of the hydrogen atom of water around the two carboxylic oxygen atoms O1 and O2 and the acetyl oxygen atom O3, respectively. Each of them reaches its first maximum at 1.75 A˚ with a well-defined sharp peak, thus indicating clearly the hydrogen-bonding nature of the intermolecular interaction. Integration of this first peak out to the minimum in the aforementioned g(r)O1HW, g(r)O2HW, and g(r)O3HW gives a water coordination number of 1.5, 1.5, and 1.0, respectively. On the other hand, g(r)N1HW shows a relatively broad peak at 3.55 A˚, which indicates that there is no N1···HW hydrogen bond, although it is still possible to have an N1H···OW hydrogen bond. g(r)S1HW shows the first maximum at 2.25 A˚, which indicates a possible S1···HW hydrogen bond with a water coordination number of 0.56. Thus, the coordination number of the first water shell is about 4.

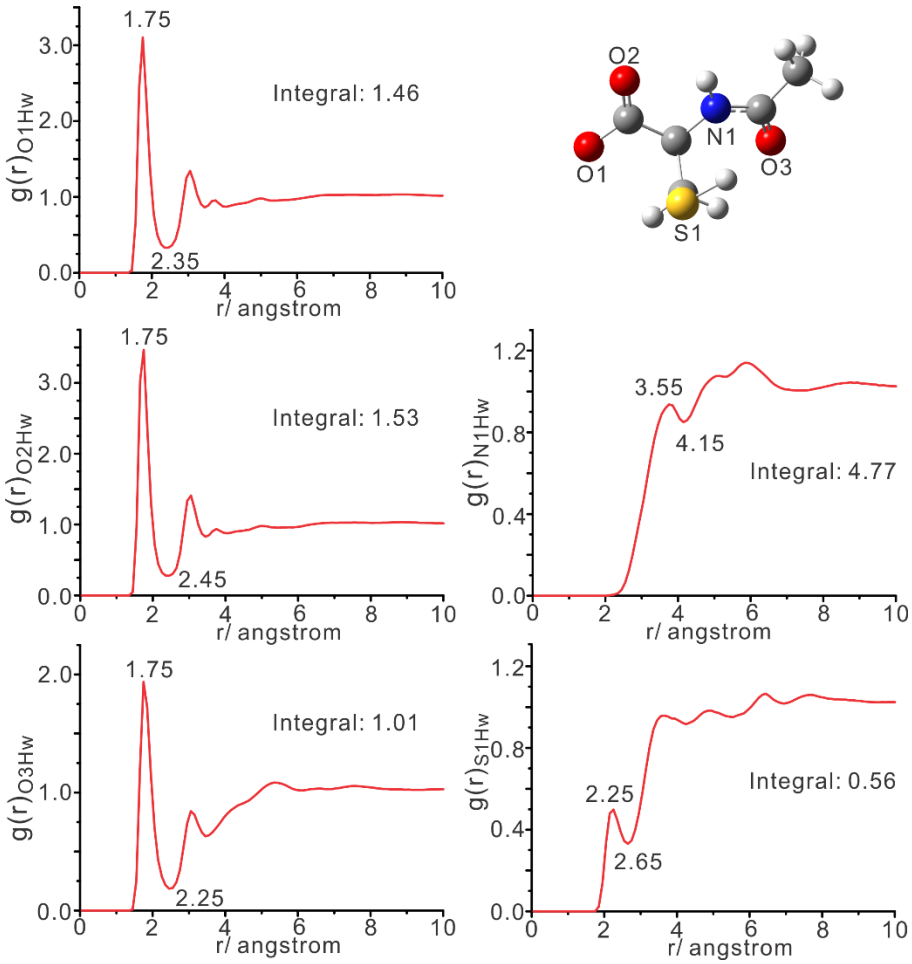


Figure 5.8. RDFs obtained from the MD simulation of NALC in water. The atom labelling for NALC is given in the upper right corner. Hw is the hydrogen atom of water.

### 5.2.4.2. Explicit and Implicit Solvation of Dep-NALC

Based on the RDF analysis and the MD snapshots, the three most stable gas-phase Dep-NALC conformers with a combined Boltzmann percentage population factor of above 90% were explicitly solvated with three and four water molecules. For the Dep-NALC–(water)3 clusters, that is, Dep-NALC-3W, two water molecules are hydrogen-bonded to the carboxylic oxygen atoms to form a five-membered heavy-atom hydrogen-bonded ring, while another water is

inserted into the existing SH···Oac ring to form the so-called insertion complex. Such insertion complexes with cooperative hydrogen-bonded rings have been investigated recently and were found experimentally to be the most favourable geometries for this type of water-solvated cluster.[33,34] For the Dep-NALC-4W clusters, the fourth water molecule is placed at the N1H site to form an N1H··OW hydrogen bond. Altogether, six low-energy conformers have been located.

To account for the existence of the bulk water environment, we further solvated the Dep-NALC-3,4W clusters with the PCM of bulk water. The optimized geometries obtained with the PCM are summarized in Figure 5.9, together with their respective percentage Boltzmann population factors at room temperature based on the relative Gibbs free energies. The important intermolecular hydrogen and van der Waals bond lengths are also indicated in Figure 5.9. The corresponding structures of Dep-NALC-3,4W clusters in the gas phase are depicted in Figure C9 in the Supporting Information, Appendix C. Interestingly, the explicit solvation of Dep-NALC with three or four water molecules has a very similar effect on the conformational stability and structures as the inclusion of the PCM bulk water. For example, the SH···N or SH···O bond lengths increase on going from the gas phase to the explicit solvation model. A similar observation was made upon going from the gas phase to the PCM solvation model. The further inclusion of the PCM for the explicitly solvated Dep-NALC-3,4W clusters introduced some additional changes, especially in their VA and VCD spectra, as discussed below.

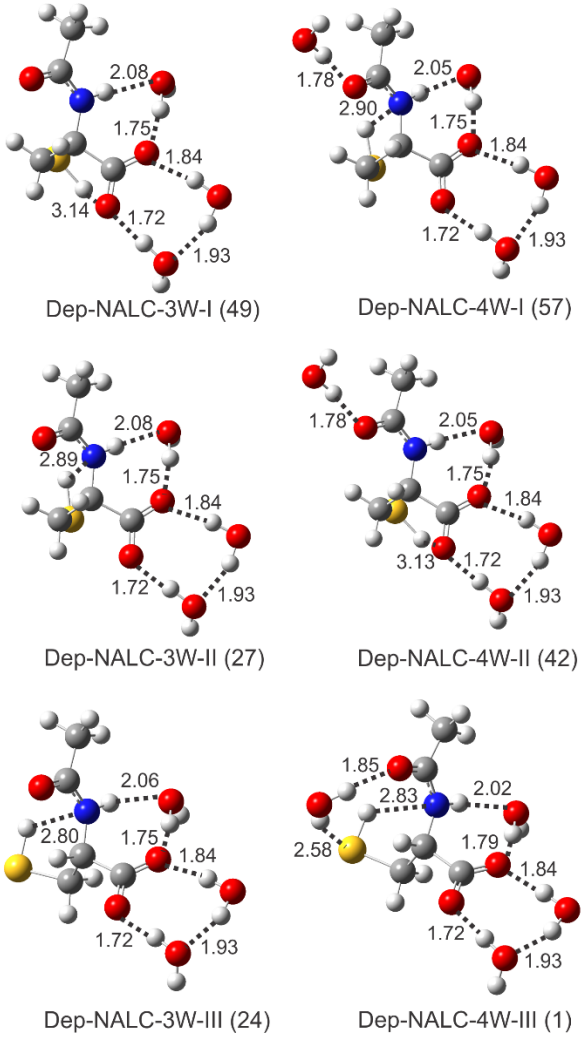


Figure 5.9. Optimized geometries of the six most stable conformers of the Dep-NALC–(water)3,4 clusters at the B3LYP/6-311++G(d,p) level with the PCM. The numbers in parentheses are the percentage Boltzmann population factors based on the relative Gibbs free energies at 298 K. The intramolecular hydrogen-bond lengths and some important van der Waals bond lengths (in A˚) are indicated.

The simulated VA and VCD spectra of the Dep-NALC-4W clusters in the gas phase and with the PCM to account for water solvent are shown in Figure 5.10, together with the experimental VA and VCD data at pH 7.0. For comparison, the related spectra of the Dep-NALC-3W clusters in the gas phase and with the PCM are provided in Figure C10 in the Supporting Information.

Explicit solvation of Dep-NALC with three or four water molecules introduced in general a moderate red shift of the $\upsilon_{as}$(COO) and $\upsilon$(C=O)ac and a small blue shift for the bands in the 1400–1500 $cm^{-1}$ region. The directions of shifts experienced were the same when either explicit or implicit solvation of Dep-NALC was incorporated into the simulations, but the extent of the red shift was much larger with the PCM. The further implicit PCM solvation of the Dep-NALC-3,4W clusters brought the predicted peak frequencies into much better agreement with the experimental ones. All seven observed bands labelled in the experimental VA spectrum correlate very well with the ones in the simulated spectrum when the implicit and explicit solvation were incorporated together (Figure 5.10a). With regard to the VCD spectral features, it is also interesting to note that the explicit solvation model has changed the major VCD features in a similar way to the implicit solvation model discussed previously for Dep-NALC. For example, the positive–negative bisignated VCD feature at the $\upsilon$(COO)as and $\upsilon$(C=O)ac bands has been predicted for the three conformers of interest with explicit solvation as with the PCM solvation model. The further PCM solvation of the Dep-NALC-3,4W clusters brought some additional changes to the VCD features, most noticeably in the 1300–1500 $cm^{-1}$ region. For all three solvated conformers, the VCD band 3 has now been predicted to be positive, albeit with a small intensity, compared to the negative sign predicted with explicit solvation only. Although we do acknowledge that the experimentally observed intensity for the VCD band 3 is quite weak, only slightly above noise level, it is nevertheless encouraging that both the sign and magnitude of this VCD band have been correctly reproduced

with this combined solvation model. More importantly, the previously missing VCD band 5' is now visible, although the relative intensity of VCD bands 5' and 6 is still out of accord with experiment if one applies the population factors based on the DFT relative free energies for these solvated water clusters. A more detailed examination of the simulated VA and VCD spectra of the conformers revealed that although the VA spectra for all conformers are very similar in this region, the VCD features are somewhat different. For example, Dep-NALC-4W-III conformer shows much more intense negative VCD bands at the positions of bands 5' and 6, in accord with the experimental observation. It is plausible that this conformer actually contributes more than the Boltzmann factor predicted by the DFT relative Gibbs free energies. New VA and VCD spectra generated with an empirical population ratio of 25:25:50% for these conformers are also provided in Figure 5.10. This empirical factor was chosen to best reproduce the experimental spectral features. One rationale behind this is that the DFT spectral features have been generally regarded as quite reliable, whereas the DFT relative Gibbs free energies for hydrogen-bonded clusters are typically only reliable to a few kcal $mol^{-1}$. It is satisfying that the empirically weighted VA and VCD spectra have captured all the VA and the more subtle VCD details discussed above. This demonstrates that both explicit and implicit solvation with water play important roles in interpreting VA and, in particular, VCD measurements in aqueous solution. The inclusion of both solvation models can significantly improve the agreement with the experimental data and provide a more accurate and detailed description of the conformational distributions in aqueous solution.

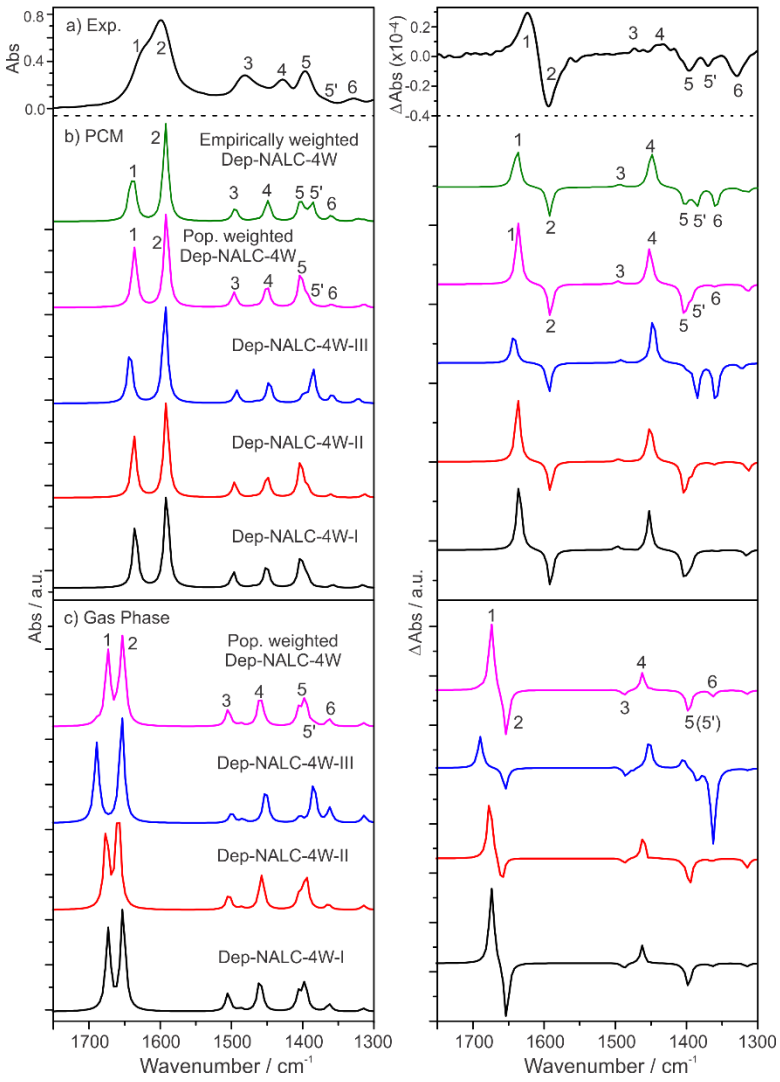


Figure 5.10. Comparisons of a) the experimental VA and VCD spectra of NALC in D2O under neutral pH conditions with b) the corresponding spectra of the most stable Dep-NALC-4W conformers with the PCM of D2O and c) in the gas phase at the B3LYP/6-311++G(d,p) level. The DFT and empirically population-weighted spectra are also provided.

## 5.3. Conclusions

The conformations of NALC, the acetylated form of cysteine, under different pH conditions have been investigated using VA and VCD spectroscopy, complemented with ab initio calculations and MD simulations. It has been shown that the inclusion of the polarizable continuum bulk water solvation model is

essential to obtain correct VA assignments and conformational distributions of Neu-, Dep- and D-Dep-NALC in aqueous solutions. It has been further established that hydrogen-bonding interactions between NALC and water molecules play an important role in the appearance of the VA and VCD spectra. The results presented indicate that the inclusion of both explicit water solvation and implicit solvation with the PCM is crucial to capture all the VCD features in addition to the VA features observed, and thus provide accurate information about conformational distributions of NALC in water.

## 5.4. Experimental and Theoretical Details

FTIR VA and VCD Measurements: NALC was purchased from Aldrich and used without further purification. All solutions were prepared in deuterium oxide ($D_2O$; 99.99% D, Aldrich) to avoid strong absorption due to the H2O bending band at ~1640 $cm^{-1}$, which interferes with the amide I band of NALC. VA and VCD spectra were measured by using an FTIR spectrometer Vertex 70 with a PMA50 module (Bruker). To obtain a good VCD spectrum, the concentration and path length were optimized to ensure that the VA absorption coefficients for the bands of interest were between 0.2 and 0.8. A low-pass filter with a cutting wavelength at ~1800 $cm^{-1}$ was used. All reported data were obtained using a $BaF_2$ sample cell (International Crystal Laboratories) with an optimized path length of 0.015 mm and concentration of 1.4m. A 0.015 mm PTFE spacer (International Crystal Laboratories) was used for this purpose without calibration. NALC solutions with pH values ranging from 0.65 to 13.0 were

prepared by adding a small amount of 6m DCl or 6m NaOD dropwise. For the pH 7 solution, the raw VCD spectrum was measured with a total collection time of 6 h (32 h) and a resolution of 4 $cm^{-1}$. The final VCD spectrum was obtained by subtracting the solvent spectrum obtained under identical conditions since the opposite enantiomer of NALC is not available commercially.[13]

*UV/Vis Measurements*: UV/Vis spectra of 0.0014m NALC in aqueous solution at several different pH values ranging from 3.0 to 12.3 were collected on a Hewlett Packard 8453 UV/Vis spectrophotometer using a PTFE cell with a 1 cm path length.

*DFT Calculations*: Conformational investigations, geometry optimizations, and calculations of harmonic vibrational frequencies and VA and VCD intensities of the species of interest were carried out using the Gaussian 03[35] and Gaussian 09[36] programs. The combination B3LYP/6-31G was used initially to locate the possible lowest-energy conformers of the Pro-, Neu-, Dep-, and D-Dep-NALC monomers. The hybrid functional B3LYP[37,38] was chosen because it has been extensively used in describing strong hydrogen bonded complexes[39,40,41] and because of its well-documented reliability in predicting VCD intensities.[42,43,44,45] To account for solvation, both the integral equation formalism (IEF) implicit PCM solvation model and the explicit solvation model based on the hydrogen bonded clusters of Dep-NALC–$(water)_N$ were employed. The dielectric constant of $D_2O$, e=78.3553, was used in the PCM. The significant aspects of the PCM solvation model had been reviewed in detail previously.[46] The number of water molecules hydrogen bonded to Dep-NALC was estimated from the analysis of the

RDFs obtained from the MD simulations described below. In addition, the solvated Dep-NALC–$(D_2O)$N was placed inside a PCM solvation model to account simultaneously for the explicit hydrogen-bonding interactions between Dep-NALC and water molecules and the effects of bulk water. For the final calculations, B3LYP/6-311++G(d,p) was used for geometry optimizations and subsequent calculations of harmonic vibrational frequencies and VA and VCD intensities of all four species without and with the PCM, as well as for the much larger Dep-NALC–$(H_2O)_N$ clusters without and with the PCM. For the simulation of VA and VCD spectra, a Lorentzian line shape with a half width at half maximum of 4 $cm^{-1}$ was used.

*Molecular Dynamics Simulations*: All MD simulations were performed using the Sander module in the AMBER 9[47] suite of programs. The xLeap graphical interface module was used to build the starting configuration of NALC. The AMBER ff99 force field based on molecular mechanics was used. The NALC molecule was solvated in a rectangular periodic box with the pre-equilibrium TIP3P[48] water molecules with a cut-off of 10.0 A˚. The initial configuration was relaxed in two sequential runs: first, 500 steps of steepest descent algorithm were applied to remove any bad contacts, followed by another 500 steps of conjugate gradient algorithm. The final configuration obtained was then used as the starting point for a 600 ps heating and equilibrating MD simulation under NVT conditions. The system was first heated from 0 to 300 K in 200 ps and was then equilibrated at 300 K in 400 ps to ensure equilibrium was reached completely. A

6 ns production MD simulation was then performed under NPT conditions (T=300 K, P= 1 atm) with a time step of 2 fs.

## 5.5. Acknowledgements

This research was funded by the University of Alberta, the Natural Sciences and Engineering Research Council of Canada, Petro-Canada, and the Canada Research Chairs Program. We gratefully acknowledge access to the computing facilities provided by the Academic Information and Communication Technology group at the University of Alberta.

## References


[1] S. De Flora, R. Balansky, C. Bennicelli, A. Camoirano, F. D'Agostini, A. Izzotti, C. F. Cesarone in Drugs, Diet and Disease: Mechanistic Approaches to Cancer, Vol. 1 (Eds.: C. Ioannides, D. F. V. Lewis), Harwood, New York, 1995, pp. 151 –203.

[2] D. C. Malins, K. E. Hellstrçm, K. M. Anderson, P. M. Johnson, M. A. Vinson, Proc. Natl. Acad. Sci. USA 2002, 99, 5937 –5941.

[3] M. Berk, D. L. Copolov, O. Dean, K. Lu, S. Jeavons, I. Schapkaitz, M. Anderson- Hunt, A. L. Bush, Biol. Psychiatry 2008, 64, 468– 475.

[4] L. A. Palmer, A. Doctor, P. Chhabra, M. L. Sheram, V. E. Laubach, M. Z. Karlinsey, M. S. Forbes, T. Macdonald, B. Gaston, J. Clin. Invest. 2007, 117, 2592 –2601.

[5] G. Albrecht, R. B. Corey, J. Am. Chem. Soc. 1939, 61, 1087 –1103.

[6] F. R. Tortonda, J. L. Pascual-Ahuir, E. Silla, I. Tunonon, F. J. Ramirez, J. Chem. Phys. 1998, 109, 592 –602.

[7] S. Gronert, R. A. J. O'Hair, J. Am. Chem. Soc. 1995, 117, 2071 –2081.

[8] E. Tajkhorshid, K. J. Jalkanen, S. Suhai, J. Phys. Chem. B 1998, 102, 5899 – 5913.

[9] C. F. Correia, P. O. Balaj, D. Scuderi, P. Maitre, G. Ohanessian, J. Am. Chem. Soc. 2008, 130, 3359– 3370.

[10] Z. Ji, R. Santamaria, I. L. Garzon, J. Phys. Chem. A 2010, 114, 3591 –3601.

[11] C. Gautier, T. Burgi, Chem. Commun. 2005, 5393– 5395.

[12] B. Boeckx, R. Ramaekers, G. Maes, J. Mol. Spectrosc. 2010, 261, 73– 81.

[13] "Vibrational Circular Dichroism Spectroscopy of Chiral Molecules": G. Yang, Y. Xu, in Top. Curr. Chem.: Electronic and Magnetic Properties of Chiral Molecules and Supramolecular Architectures, Vol. 298 (Eds.: R. Naaman, D. N. Beratan, D. H. Waldeck), Springer, Berlin, 2011, pp. 189 – 236.

[14] a) T. B. Freedman, X. Cao, D. A. Young, L. A. Nafie, J. Phys. Chem. A 2002, 106, 3560 – 3565; b) T. B. Freedman, X. Cao, L. A. Nafie, A. Solladi_-Cavallo, L. Jierry, L. Bouerat, Chirality 2004, 16, 467– 474.

[15] M. Losada, H. Tran, Y. Xu, J. Chem. Phys. 2008, 128, 014508.

[16] M. Losada, P. Nguyen, Y. Xu, J. Phys. Chem. A 2008, 112, 5621 –5627.

[17] G. Yang, Y. Xu, J. Chem. Phys. 2009, 130, 164506.

[18] M. Losada, Y. Xu, Phys. Chem. Chem. Phys. 2007, 9, 3127 – 3135.

[19] M. H. Jamroz, Vibrational Energy Distribution Analysis VEDA 4, Warsaw, 2004–2010.

[20] Remington's Pharmaceutical Sciences, 16th ed. (Ed.: A. Osol), Mack Publishing Co., Easton, 1980, p. 805.

[21] K. B. Wiberg, C. M. Breneman, J. Am. Chem. Soc. 1992, 114, 831– 840.

[22] J. I. Mujika, J. M. Matxain, L. A. Eriksson, X. Lopez, Chem. Eur. J. 2006, 12, 7215 –7224.

[23] C. R. Kemnitz, M. J. Loewen, J. Am. Chem. Soc. 2007, 129, 2521– 2528.

[24] V. Addario, Y. Guo, I. K. Chu, Y. Ling, G. Ruggerio, C. F. Rodriquez, A. C. Hopkinson, K. W. M. Siu, Int. J. Mass Spectrom. 2002, 219, 101 –114.

[25] A. J. Williams, J. Am. Chem. Soc. 1976, 98, 5645 –5651.

[26] M. Friedman, J. F. Cavins, J. S. Wall, J. Am. Chem. Soc. 1965, 87, 3672 – 3682.

[27] G. E. Clement, T. P. Hartz, J. Chem. Educ. 1971, 48, 395–397.

[28] "Estimation of Chemical Reactivity Parameters and Physical Properties of Organic Molecules Using SPARC": L. A. Carreira, S. Hilal, S. W. Karickhoff, Theoretical and Computational Chemistry, Quantitative Treatment of Solute/Solvent Interactions (Eds.: P. Politzer, J. S. Murray), Elsevier, Amsterdam, 1994.

[29] a) M. A. Zamora, H. A. Baldoni, J. A. Bombasaro, M. L. Mak, A. Perczel, O. Farkas, R. D. Enriz, J. Mol. Struct. THEOCHEM 2001, 540, 271– 283; b) J. A. Bombasaro, M. A. Zamora, H. A. Baldoni, R. D. Enriz, J. Phys. Chem. A 2005, 109, 874 –884.

[30] M. Szostak, L. Yao, V. W. Day, D. R. Powell, J. Aub_, J. Am. Chem. Soc. 2010, 132, 8836 – 8837.

[31] V. P. Nicu, E. J. Baerends, Phys. Chem. Chem. Phys. 2009, 11, 6107 – 6118.

[32] S. Gobi, G. Magyarfalvi, Phys. Chem. Chem. Phys. 2011, 13, 16130 – 16133.

[33] Z. Su, Y. Xu, Angew. Chem. 2007, 119, 6275 – 6278; Angew. Chem. Int. Ed. 2007, 46, 6163 –6166.

[34] Z. Kisiel, E. Białkowska-Jaworska, D. P. Zaleski, J. L. Neill, A. L. Steber, B. H. Pate, International Symposium on Molecular Spectroscopy, 66th Meeting, June 20–24, 2011, http://molspect.chemistry.ohio-state.edu/symposium/, abstract #WH10.

[35] Gaussian 03 (Revision E.01), M. J. Frisch, G. W. Trucks, H. B. Schlegel, G. E. Scuseria, M. A. Robb, J. R. Cheeseman, J. A. Montgomery, Jr., T. Vreven, K. N. Kudin, J. C. Burant, J. M. Millam, S. S. Iyengar, J. Tomasi, V. Barone, B. Mennucci, M. Cossi, G. Scalmani, N. Rega, G. A. Petersson, H. Nakatsuji, M. Hada, M. Ehara, K. Toyota, R. Fukuda, J. Hasegawa, M. Ishida, T. Nakajima, Y. Honda, O. Kitao, H. Nakai, M. Klene, X. Li, J. E. Knox, H. P. Hratchian, J. B. Cross, V. Bakken, C. Adamo, J. Jaramillo, R. Gomperts, R. E. Stratmann, O. Yazyev, A. J. Austin, R. Cammi, C. Pomelli, J. W. Ochterski, P. Y. Ayala, K. Morokuma, G. A. Voth, P. Salvador, J. J. Dannenberg, V. G. Zakrzewski, S. Dapprich, A. D. Daniels, M. C. Strain, O. Farkas, D. K. Malick, A. D. Rabuck, K. Raghavachari, J. B. Foresman, J. V. Ortiz, Q. Cui, A. G. Baboul, S. Clifford, J. Cioslowski, B. B. Stefanov, G. Liu, A. Liashenko, P. Piskorz, I. Komaromi, R. L. Martin, D. J. Fox, T. Keith, M. A. Al-Laham, C. Y. Peng, A. Nanayakkara, M. Challacombe, P. M. W. Gill, B. Johnson, W. Chen, M. W. Wong, C. Gonzalez, J. A. Pople, Gaussian, Inc., Wallingford, CT, 2004.

[36] Gaussian 09 (Revision B.01), M. J. Frisch, G. W. Trucks, H. B. Schlegel, G. E. Scuseria, M. A. Robb, J. R. Cheeseman, G. Scalmani, V. Barone, B. Mennucci, G. A. Petersson, H. Nakatsuji, M. Caricato, X. Li, H. P. Hratchian, A. F. Izmaylov, J. Bloino, G. Zheng, J. L. Sonnenberg, M. Hada, M. Ehara, K. Toyota, R. Fukuda, J. Hasegawa, M. Ishida, T. Nakajima, Y. Honda, O. Kitao, H. Nakai, T. Vreven, J. A. Montgomery, Jr., J. E. Peralta, F. Ogliaro, M. Bearpark, J. J. Heyd, E. Brothers, K. N. Kudin, V. N. Staroverov, R. Kobayashi, J. Normand, K. Raghavachari, A. Rendell, J. C. Burant, S. S. Iyengar, J. Tomasi, M. Cossi, N. Rega, J. M. Millam, M. Klene, J. E. Knox, J. B. Cross, V. Bakken, C. Adamo, J. Jaramillo, R. Gomperts, R. E. Stratmann, O. Yazyev, A. J. Austin, R. Cammi, C. Pomelli, J. W. Ochterski, R. L. Martin, K. Morokuma, V. G. Zakrzewski, G. A. Voth, P. Salvador, J. J. Dannenberg, S. Dapprich, A. D. Daniels, _. Farkas, J. B. Foresman, J. V. Ortiz, J. Cioslowski, D. J. Fox, Gaussian, Inc., Wallingford CT, 2009.

[37] A. D. Becke, J. Chem. Phys. 1993, 98, 5648 – 5652.

[38] C. T. Lee, W. T. Yang, R. G. Parr, Phys. Rev. B 1988, 37, 785 –789.

[39] A. K. Chandra, S. Parveen, T. Zeegers-Huyskens, J. Phys. Chem. A 2007, 111, 8884 – 8891.

[40] J. N. Woodford, J. Phys. Chem. A 2007, 111, 8519 – 8530.

[41] P. I. Dem'yanov, R. M. Gschwind, Organometallics 2006, 25, 5709 –5723.

[42] P. J. Stephens, F. J. Devlin, C. F. Chabalowski, M. J. Frisch, J. Phys. Chem. 1994, 98, 11623–11627.

[43] T. Kuppens, W. Herrebout, B. van der Veken, P. Bultinck, J. Phys. Chem. A 2006, 110, 10191 –10200.

[44] L. Ducasse, F. Castet, A. Fritsch, I. Huc, T. Buffeteau, J. Phys. Chem. A 2007, 111, 5092 – 5098.

[45] T. Brotin, D. Cavagnat, J.-P. Dutasta, T. Buffeteau, J. Am. Chem. Soc. 2006, 128, 5533–5540.

[46] J. Tomasi, B. Mennucci, R. Cammi, Chem. Rev. 2005, 105, 2999 –3093.

[47] D. A. Case, T. A. Darden, T. E. Cheatham, C. L. Simmerling, J. Wang, R. E. Duke, R. Luo, K. M. Merz, D. A. Pearlman, M. Crowley, R. C. Walker, W. Zhang, B. Wang, S. Hayik, A. Roitberg, G. Seabra, K. F. Wong, F. Paesani, X. Wu, S. Brozell, V. Tsui, H. Gohlke, L. Yang, C. Tan, J. Mongan, V. Hornak, G. Cui, P. Beroza, D. H. Mathews, C. Schafmeister, W. S. Ross, P. A. Kollman, AMBER 9, University of California, San Francisco, CA, 2006.

[48] W. L. Jorgensen, C. Jenson, J. Comput. Chem. 1998, 19, 1179.

# 6 Chapter

# Vibrational absorption and vibrational circular dichroism spectra of leucine in water under different pH conditions: hydrogen-bonding interactions with water

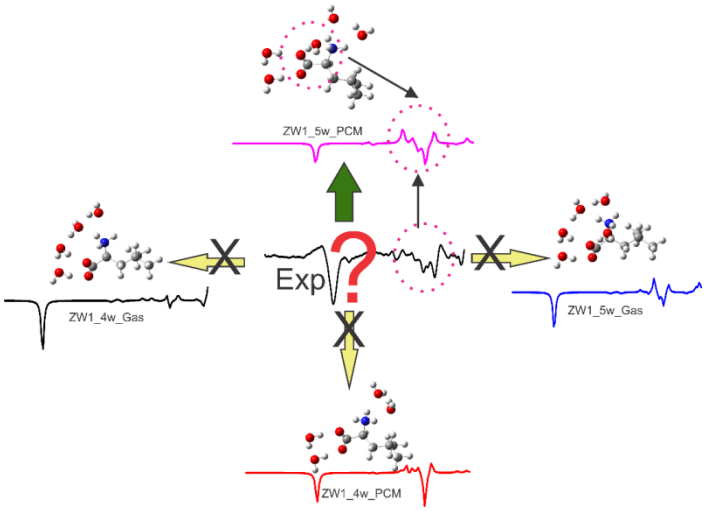


**"This chapter is directly copied from the published paper"**

M. R. Poopari, P. Zhu, Z. Dezhahang, Y. Xu, "Vibrational absorption and vibrational circular dichroism spectra of leucine in water under different pH conditions: hydrogen-bonding interactions with water", J. Chem. Phys., 137, 2012, 194308

## 6.1. Introduction

Leucine is one of the essential amino acids which cannot be synthesized by animals or humans. On the other hand, it can be produced in plants or microorganisms from pyruvic acid.[1] Human body obtains the necessary amount of leucine by digesting it as part of proteins in human diet. Leucine is the only amino acid capable of stimulation of muscle protein synthesis[2] and is found to play an important role in slowing down the rate of degradation of muscle tissues by increasing the synthesis of muscle proteins.[3] Because of its biological importance and its relative small number of electrons which makes it amenable to high-level quantum chemistry calculations, leucine has attracted considerable interest from both experimentalists and theorists. Conformations of neutral leucine in the gas phase were investigated by jet-cooled rotational spectroscopy.[4] An extensive exploration of the conformational space was performed to characterize all possible gas phase structures of canonical leucine using the density functional theory (DFT) method[5,6] where the proton affinity and the gas phase basicity were also determined. It has been established that amino acids tend to stay in the neutral form in the gas phase,[7,8,9] whereas under physiological conditions with nearly neutral pH in aqueous solution, they prefer the Zwitterionic form. Indeed, theoretical calculations indicated that zwitterions of leucine are not stable in the gas phase.[10] In a recent report, Rai et. al used DFT together with the polarizable continuum model (PCM) to study the conformations of the Zwitterionic and the canonical forms of leucine in solution.[10] Vibrational and dielectric properties of leucine, as well as a group of other amino acids, were studied using the DFT

method implemented within the plane wave pseudopotential framework.[11] Ji and Shen reported a sum frequency vibrational spectroscopic study of leucine molecules at the air–water interface from solutions with different concentrations and pH values.[12]

In the current study, experimental vibrational absorption (VA) and vibrational circular dichroism (VCD) measurements have been utilized, in combination with molecular dynamics (MD) and DFT calculations, to investigate the dominant species and conformational distributions of leucine in aqueous solution under three representative pHs, i.e. strongly acidic (pH=1), near neutral (pH=6), and strongly basic (pH=13). Experimental and theoretical VCD spectroscopic studies of some amino acids were reported before.[13] VCD spectroscopy, which measures the differential absorption of the left verses right circularly polarized light by a chiral molecule, is highly sensitive to subtle conformational changes and to intermolecular interactions of chiral solutes with water.[14-18] The most stable conformers of the Zwitterionic, protonated and deprotonated leucine in water have been identified. Both implicit and explicit solvation models have been considered to account for the solvent effects. While the VA spectra of leucine under three pH conditions can be adequately interpreted using the implicit polarizable continuum model (PCM), the complex and delicate VCD features require detailed analyses of the hydrogen bonding interactions between leucine and water molecules. The radial distribution function (RDF) analysis has been performed to aid the constructions of the explicit solvation model, i.e. the leucine-$(water)_N$ clusters. Some very interesting different

behaviours have been observed between the leucine-$(water)_N$ clusters in the gas phase and with the PCM of water. These observations have been discussed in terms of the role that the bulk water environment plays in stabilizing or destabilizing the hydrogen bonding interactions between water molecules and leucine. Further discussions about the importance of the choice of the leucine-$(water)_N$ clusters used and their initial conformations have also been presented. It has been found that inclusion of implicit solvation model, i.e. PCM, together with the explicit solvation model is crucial to capture the experimentally observed spectral features.

## 6.2. Experimental and Computational Details

### 6.2.1. VA and VCD measurements

L-, D- and racemic-leucine (98%, 99%, and 99% purity, respectively) were purchased from Sigma Aldrich and used without further purification. All samples were prepared by dissolving leucine in $D_2O$ solvent (purity 99.9%) in order to access the finger print region from 1800 to 1250 $cm^{-1}$. To record the VA and VCD spectra, a Fourier Transform Infrared (FTIR) spectrometer (Vertex 70, Bruker) with a VCD optical bench (PMA 50) is used. A sample cell which consists of a pair of $BaF_2$ windows and a Teflon spacer between them was used. Leucine is considered a hydrophobic amino acid because of its branched aliphatic side-chain, i.e. isobutyl group, $(CH_3)_2CH$. As a result, its solubility in water is strongly reduced. This low solubility makes it challenging to perform VCD

measurements of leucine in water. To minimize solvent interference and to optimize the experimental condition for VCD measurements, a concentration of 0.15 M with a path length of 50 μm were used. The VA spectra were measured at three representative pHs, i.e. pH=1, pH=6, and pH=13 corresponding to the strongly acidic, near neutral, and strongly basic condition, respectively. The acidic and basic conditions were obtained by adding concentrated DCl and NaOD drop wise to reach the desired pHs. The VCD intensities under the strongly acidic and basic conditions were found to be very weak. Consequently, reliable VCD measurements could not be obtained for these conditions. Therefore, only VCD spectrum obtained under neutral condition is reported. The raw VCD spectrum was measured with a total collection time of 4 h (4x1h) and a resolution of 4 $cm^{-1}$. Although the racemic leucine is also available commercially, its solubility in water is much lower than the enantiopure samples and was therefore not used for the VCD measurements. The final VCD spectra were obtained by subtracting the solvent measurements under identical conditions. The D- and L-leucine VCD spectra show good mirror image quality. For simplicity, we use L-leucine throughout the paper.

### 6.2.2. DFT calculations

Gaussian09 suite of programs has been used to perform all geometry optimizations, potential energy surface scan, harmonic frequency calculations, and the VA and VCD intensities predictions.[19] The Becke, three-parameter, Lee-

Yang-Parr (B3LYP), combined with a triple zeta basis set with the addition of two polarization and diffuse functions, i.e. 6-311++G (d, p), have been used for all the geometry searches and optimizations of the most stable conformers of the protonated, deprotonated, and Zwitterionic forms of leucine and the Zwitterionic leucine-$(water)_N$ clusters. For leucine in $D_2O$, there is D/H exchange and all the hydrogen atoms in the OH and NH groups of leucine were replaced by D in the calculations. The integral equation formalism version of PCM[20] using the universal force field (UFF) radii was applied in order to account for the effects of solvent water molecules implicitly. For this purpose, the dielectric constant of water, 78.3553, was used. A Lorentzian line shape with a half-width at half-height (HWHH) of 4 $cm^{-1}$ was used for the simulations of VA and VCD spectra. No scaling factor was applied to the harmonic frequencies.

### 6.2.3. MD Simulations

MD simulations were performed for leucine in water using PMEMD module built in the AMBER 11 suite packages.[21] The goal was to locate the most likely hydrogen bonding sites between leucine and water and to estimate the number of water molecules directly hydrogen bonded to leucine. To build up the initial configuration for MD simulations, the xLeap graphical interface was utilized. The AMBER *ff*99 force field based on molecular mechanics was used. A leucine molecule was solvated with 620 pre-equilibrated TIP3P water molecules in a rectangular periodic box with a cut-off of 10 Å. Initial minimization was

performed in two sequential steps. First, to remove any bad contacts, 1000 steps of the steepest descent algorithm were used and then 1000 steps of the conjugate gradient algorithm were applied. Second, a 600 ps heating and equilibrating MD simulation was performed under NVT conditions for the configuration obtained from the minimization process. In this step, the system was first heated from 0 to 300 K in 200 ps and then was equilibrated at 300 K for 400 ps to ensure that the equilibrium was reached. Finally, a 5 ns MD production was carried out under NPT condition at 300K and with a time step of 2 fs. To estimate the number of water molecules directly hydrogen bonded to leucine, the related RDFs have been calculated based on the MD results and analyzed.

## 6.3. Results and Discussions

### 6.3.1. Experimental and simulated VA spectra under three pH conditions

It was recognized in our initial conformational searches in the gas phase and with the PCM of water that the amine group tends to make intramolecular hydrogen bonding interactions with its adjacent $COO^-$ or COOH group, making this part molecule almost rigid. Two dihedral angles, namely $\tau_1$ ($N_6$-$C_5$-$C_4$-$C_2$) and $\tau_2$ ($C_5$-$C_4$-$C_2$-$C_1$) (see figure 6.1 for atom labelling), corresponding to the rotations around the two C-C bonds, are the most effective dihedral angles in generating new conformations. It was also recognized that the inclusion of the implicit water solvent can have substantial effects on the resulting conformations of flexible chiral molecules. Therefore, it is desirable to include the PCM of water in the

initial geometry searches. A potential energy surface (PES) scan along these two dihedral angles was carried out at the B3LYP/6-311++G(d,p) level with the PCM of water for the Zwitterionic form of leucine. In the previous theoretical studies of leucine, conformational searches had been carried out for the neutral species in the gas phase[4,5,6] and for the Zwitterionic species at a lower level with B3LYP/6-311G(d).[10] The resulting PES is shown in Figure 6.1. Several minima were found and those which are potentially important at room temperature are indicated in the figure.

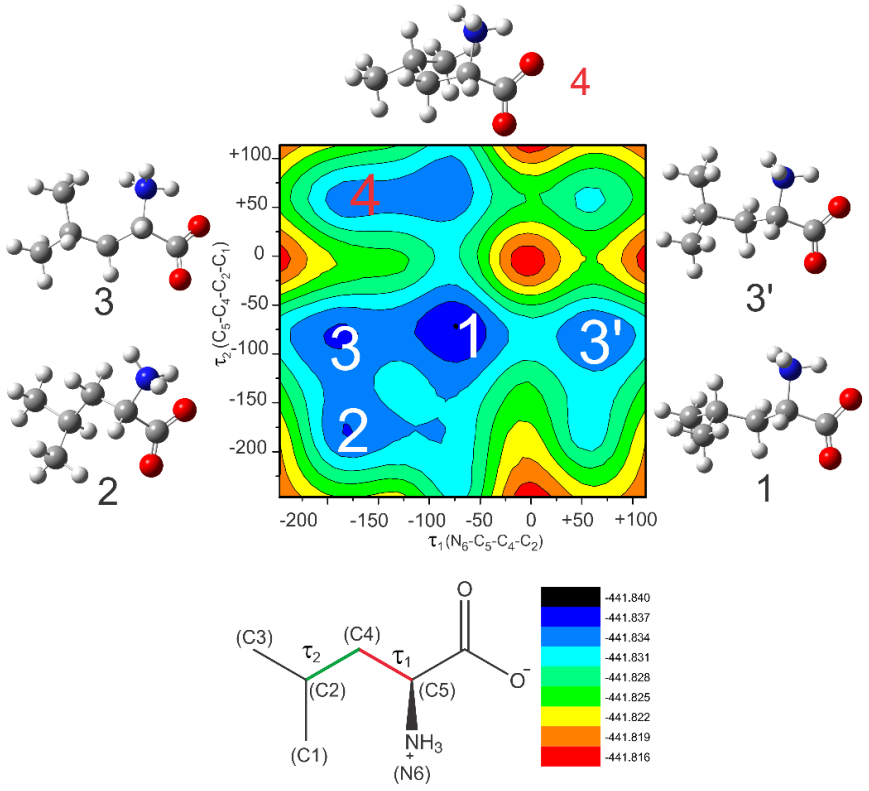


Figure 6.1. Two-dimensional PES plot of the Zwitterionic form of leucine at the B3LYP/6-311++G(d,p) level, scanned along its two dihedral angles, $\tau_1$ and $\tau_2$ (in degree). The atom labelling of leucine and the two C-C bonds associated with these two dihedral angles are shown at the bottom. The energy unit is in Hartree. Several low energy minima are indicated, together with the corresponding conformations.

Final geometry optimizations at the B3LYP/6-311++G (d,p) level with the PCM of water were carried out for the minima identified in the PES scan. The harmonic frequency calculations at the same level of theory were then performed to verify whether the optimized geometries are true minima or not. No imaginary frequency was detected for all the stable structures identified. As it turned out, the conformer at 3' changed into the same one at 3 (see Figure 6.1) during the optimization process. The conformer at 4 has negligible contribution at room temperature and is not considered in the later calculations. Similar searches were performed for the protonated and deprotonated species. Figure 6.2 summarizes the three most stable structures of the Zwitterionic, protonated and deprotonated forms of leucine obtained. Table 6.1 lists the relative zero-point corrected energies and Gibbs free energies of the three most stable conformers of the three species obtained at the B3LYP/6-311++G (d,p) level with the PCM of water. The Boltzmann percentage population factors at 298 K of the three most stable conformers in each category are also listed.

**TABLE 6.1.** The relative zero-point energy corrected total energies and Gibbs free energies of the three most stable conformers of the Zwitterionic, deprotonated, and protonated forms of leucine at the B3LYP/6-311++G (d, p) level with the PCM of water, together with their percentage Boltzmann population factors at 298 K.

| Conformers | ΔE (kJ/mol) | Pop%-ΔE | ΔG(kJ/mol) | Pop%-ΔG |
|---|---|---|---|---|
| ZW1 | 0 | 80.4 | 0 | 88.5 |
| ZW2 | 5.82 | 7.7 | 6.45 | 6.5 |
| ZW3 | 5.67 | 8.1 | 8.08 | 3.4 |
| DEP1 | 0 | 74.1 | 0 | 90.7 |
| DEP2 | 2.82 | 23.8 | 6.14 | 7.6 |
| DEP3 | 8.82 | 2.1 | 9.93 | 1.7 |
| PRO1 | 0 | 76.1 | 0 | 83.9 |
| PRO2 | 3.42 | 19.1 | 4.50 | 13.8 |
| PRO3 | 6.82 | 4.9 | 8.98 | 2.2 |

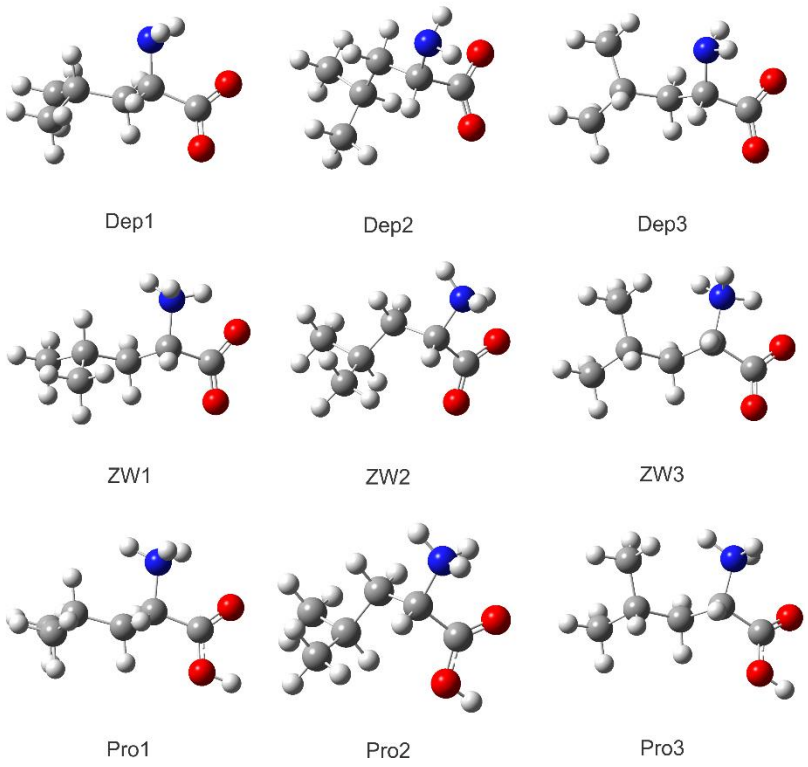


Figure 6.2. Three most stable structures of the deprotonated (top), Zwitterionic (middle), and protonated (bottom) forms of leucine obtained at the B3LYP/6-311++G(d,p) level with the PCM of water.

In Figure 6.3, the experimental VA spectra in $D_2O$ obtained at the three aforementioned pHs are compared with the population weighted VA spectra of the deprotonated, Zwitterionic and protonated forms of leucine. The VA spectra at these three pHs are noticeably different, characteristic of the existence of different dominant species under each pH. One main difference is the band positions of the carbonyl stretches of the carboxylic groups. Such difference is nicely captured by the calculated VA spectra of the three leucine species. Under the strongly acidic condition where the protonated form of leucine is expected to be the main species, the C=O stretch appears at the highest wavenumber, 1723 $cm^{-1}$. This observation is consistent with the fact that this C=O stretch is from the COOH group. In the near neutral solution, a 112 $cm^{-1}$ red-shift from the acidic solution is observed for the C=O stretch. This is because the Zwitterionic form of leucine becomes dominant and the corresponding asymmetric carboxylate stretch emerges at 1611 $cm^{-1}$. Lastly, another 43 $cm^{-1}$ red-shift is seen when the pH value reaches ~13, i.e., under strongly basic condition. This additional red shift is due to the changes in the intramolecular hydrogen bonding interactions, going from $COO^{-}\cdots H_3N^{+}$ in the Zwitterionic form of leucine to $COO^{-}\cdots H_2N$ in the deprotonated form. We also further checked if one could discriminate the neutral and Zwitterionic species of Leucine by using the VA data alone. The simulated VA spectra of the two most stable Zwitterionic and neutral leucine conformers, i.e. ZW1, ZW2, Neu1, and Neu2, respectively, are provided in Figure 6.4, together with the experimental VA spectrum under near neutral condition. At this pH, the most intense experimental peak appears at 1611$cm^{-1}$, corresponding well to the simulated peaks of ZW1 at

1648 $cm^{-1}$ and ZW2 at about 1650 $cm^{-1}$, whereas the associated peaks of Neu1 and Neu2 emerge at a much higher wavenumber of 1763 $cm^{-1}$. Clearly, the dominant species of leucine under near neutral pH condition is in the Zwitterionic form. Overall, the VA pattern is highly structurally sensitive and can be used to tell apart different dominant species in this case by focusing on the carbonyl stretch region. Detailed assignments for the lower frequency region are less obvious because of severe peak-overlapping, although the general patterns predicted for ZW1 and ZW2 are roughly consistent with the experimental data. It appears that the VA data can be well interpreted without the detailed consideration of the explicit hydrogen bonding interactions between Leucine and water molecules. The situation is, however, different with the VCD measurements (see next section).

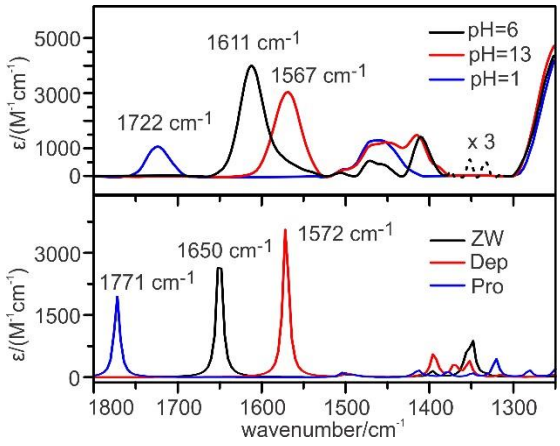


Figure 6.3. Comparison of the experimental VA spectra of leucine under three representative pH conditions with the simulated VA spectra of the most stable conformer of the deprotonated, Zwitterionic and protonated forms of leucine at 298 K.

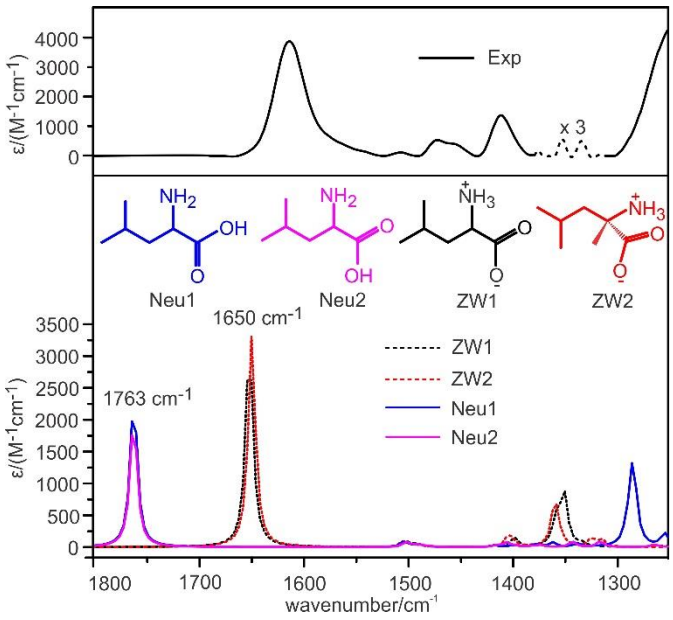


Figure 6.4. Comparison of the VA spectra of the two most stable conformers of the Zwitterionic and neutral forms of leucine and the experimental VA spectrum under near neutral condition.

### 6.3.2. Explicit and implicit solvent effects in the VCD spectrum under neutral condition

Although the VA spectra can be satisfactorily interpreted by modeling leucine with the PCM of water, the VCD spectrum obtained under neutral condition, on the other hand, could not be well interpreted without considering the explicit hydrogen bonding interactions of leucine with water molecules. This can be seen by comparing the experimental data with the simulated VA and VCD spectra of ZW1 and ZW2 in the gas phase and with the PCM of water (Figure D1, supporting information[22], Appendix D). To systematically investigate such effects, we started with the construction of leucine-$(water)_N$ clusters based on the MD calculations performed. RDF measures the probability of finding an atom at certain distance from a center atom of interest over the whole simulation time.

The analysis of such RDFs can help to identify the number of water molecules directly hydrogen bonded to leucine. Figure 6.5 shows the RDF calculations carried out for the Zwitterionic form of leucine. Each RDF reaches its first maximum at ~1.75 Å with a well-defined sharp peak, indicating the hydrogen bonding nature of the interactions. Integration of this first peak out to the minimum provides the water coordination numbers which are also included in the figure. For example, the integrals for the RDFs centered at the two oxygen atoms of the carboxylate group are roughly 1 in each case, suggesting that the $COO^-$ are explicitly solvated by about two water molecules on average. The corresponding integration values for the three H atoms of $NH_3^+$ are between 0.6 and 1, indicating the existence of about one water molecule per binding site. Altogether, about four to five water molecules are directly hydrogen bonded to leucine on average. Based on the MD snap shots and chemical intuition, two different hydrogen bonding configurations were proposed. Both with two water molecules hydrogen bonded to $COO^-$. At the amine site, one configuration involves two water molecules hydrogen bonded to the two amine hydrogen atoms while the third amine hydrogen atom is intramolecular hydrogen bonded to $COO^-$. The other one has the third amine hydrogen atom also involved in intermolecular hydrogen bonding with water. The above considerations lead to the leucine-$(water)_4$ and leucine-$(water)_5$ clusters. Since the first two most stable Zwitterionic leucine monomeric conformers carry more than 95% of the total population, we used only these two dominant Zwitterionic leucine conformers to build the leucine-$(water)_N$ clusters. The explicit hydrogen bonded solvated water clusters based on these two

leucine conformers with 4 or 5 water molecules are ZW1_4w, ZW2_4w, ZW1_5w and ZW2_5w (see Figure 6.6). These structures are also optimized at the B3LYP/6-311++G(d,p) level with the PCM of water. The optimized geometries are summarized in Figure 6.6. The Cartesian coordinates of the relevant species at the PCM/B3LYP/6-311++G(d,p) level are provided in Table D1-3, supporting information, Appendix D.

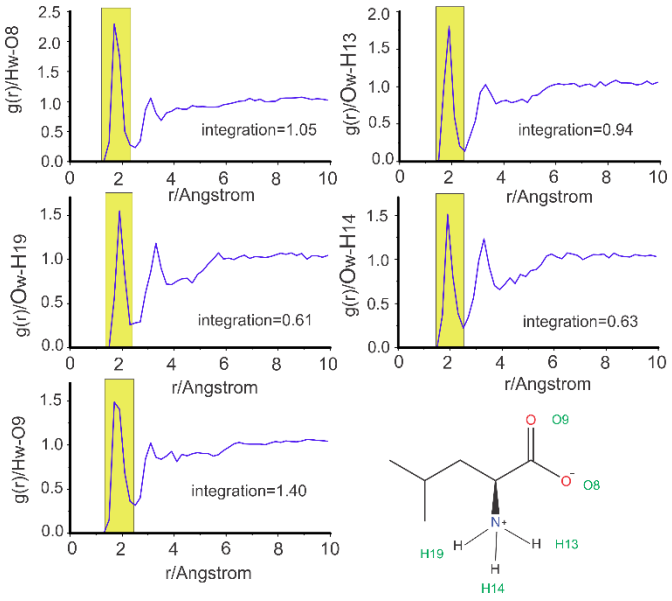


Figure 6.5. RDFs obtained from the MD simulations of the Zwitterionic form of leucine in water. The atom labelling of leucine used in the graphs is presented at the bottom. $H_W$ and $O_W$ refer to the hydrogen and oxygen atom of water molecules, respectively.

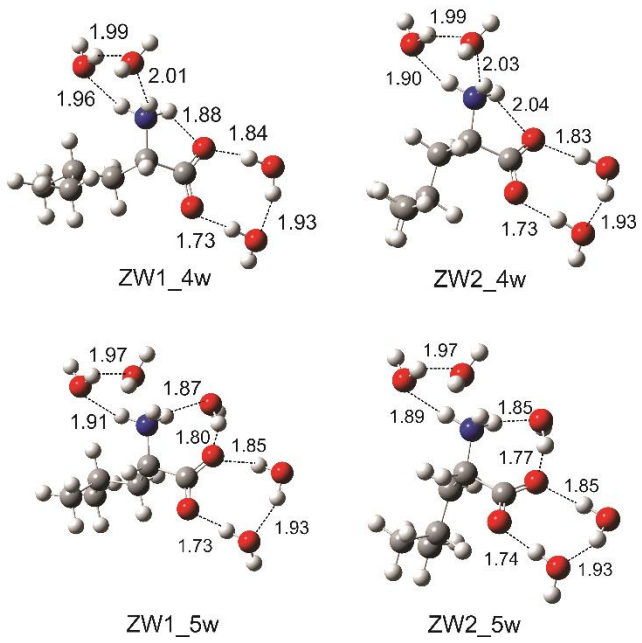


Figure 6.6. Optimized geometries of the most stable conformers of the Zwitterionic leucine-$(water)_{4,5}$ clusters at the B3LYP/6-311++G(d,p) level with the PCM of water. The important hydrogen bonding lengths (in Å) are also indicated.

It is worthwhile to point out some interesting observations about these water solvated clusters during their geometry optimizations in the gas phase and with the PCM of water. We observed, for example, that in the optimization of ZW1_4w, the structure converged more quickly with the inclusion of the PCM of water than in the gas phase, using the same initial geometry. The number of steps required for optimization with PCM model is 33 while that in the gas phase is 77. This observation is illustrated in Figure 6.7. In the gas phase, the system experienced a good number of large oscillations before finally converged. This is because the water molecules can move freely and attempt to maximize the possible hydrogen bonding interactions primarily among themselves and also with Leucine. The inclusion of the PCM of water provides a dielectric medium which also restricts the movement of the water molecules involved and directs them to

best solvate the solute molecule. It therefore prevents severe alternations in the hydrogen bonding arrangements, resulting in smoother and faster geometry optimizations of such solvated clusters in solution. It is also worth mentioning that the total job cpu time for the PCM calculation was almost one third of that for the gas phase calculation. It was noted by ourselves and in some previous publications[23] that the inclusion of the PCM of water may sometimes tear apart the intermolecular hydrogen bonding interactions between chiral solute and water molecules proposed in the initial solvated water clusters. In retrospect, those initial geometries proposed were most likely based largely on maximizing the possible hydrogen bonds among water molecules and with solute, i.e. to stabilize the small solvated clusters without the bulk solvent environment. It is therefore not too surprising that such proposed clusters may not be favored in solution. The present initial structures, on the other hand, were proposed based on the MD snapshots when bulk solvent had been included. These discussions highlight the importance of choosing the suitable initial geometries of the solvated water clusters. The main point is that the faster optimization we observed with PCM is due to the fact that the initial geometry proposed based on the MD snapshots is more closer to the true explicit solvated cluster in water than that based on the lowest energy gas phase solvated clusters. Overall, the explicit solvation arrangement between solute and water molecules in solution is more faithfully captured when the bulk solvent environment is taken into account than in the gas phase.

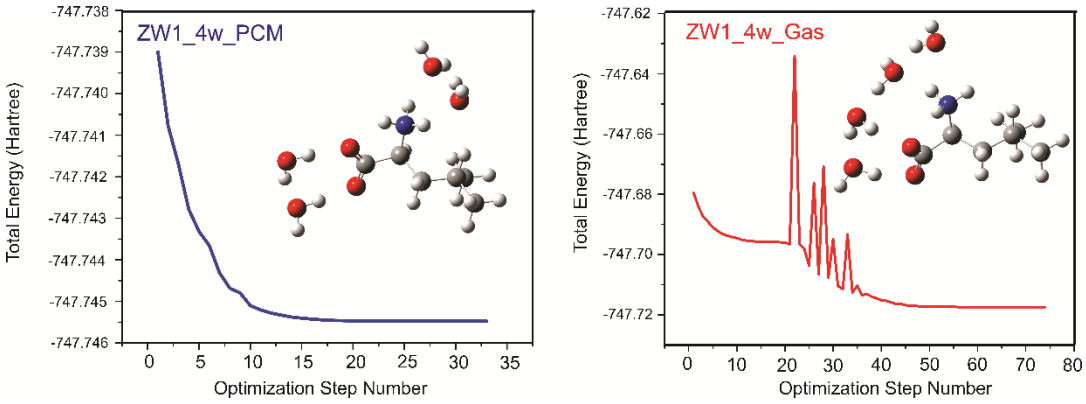


Figure 6.7. Comparison of the optimization step numbers of ZW1_4w at the B3LYP/6-311++G(d,p) level with the PCM of water (left) and in the gas phase (right).

The calculated VA and VCD spectra of the ZW1_4w and ZW1_5w clusters in the gas phase and with the PCM of water are compared with the related experimental data in Figure 6.8. The calculated VA and VCD spectra of ZW1 with the PCM of water are also included in Figure 6.8, while ZW1 by itself is unstable in the gas phase. It is clear that ZW1 with the PCM of water provides poor agreement with the experimental spectra, especially the VCD spectral features. Since the ZW2_4w and ZW2_5w clusters carry only about 6% of the total population, to simplify the following discussions, we focus only on the ZW1-$(water)_{4,5}$ clusters. The corresponding VA and VCD spectra of ZW2-$(water)_{4,5}$ clusters in the gas phase and with the PCM of water are given in Figure D2, supporting information, Appendix D.[22] The robust mode calculations for ZW1-$(water)_5$ are summarized in Table D4, supporting information, Appendix D. As can be seen from Table D1, most of the strong to medium VCD features in the observed MI-VCD spectrum are robust, except the $COO^-$ band at 1611$cm^{-1}$. From the VA spectral comparison in figure 6.8(a), the carboxylic vibrational mode

positions predicted with PCM, highlighted in the figure, are in better agreement with the experiment than the gas phase ones. In fact, the gas phase predictions for both 4w and 5w water solvated clusters are blue-shifted by more than 50 $cm^{-1}$. It also appears that the relative intensities of the most prominent observed VA bands in the 1500-1350 $cm^{-1}$ region are better presented with the inclusions of both the explicit and implicit water solvation models than with the implicit model alone. For the VCD spectral comparison, the delicate and complex signatures observed in the 1500-1300 $cm^{-1}$ region in the highlighted part of figure 6.8(b) is best captured by the +/+/-/-/+ VCD bands of ZW1_5w with PCM. It was recognized through closer examination that the insertion of a water molecule between the $COO^-$ and the $NH_3^+$ groups, which is locked into the position by the inclusion of the PCM of water, is important to reproduce such complex VCD features. Without such an insertion, such as in ZW1_4w, the complex VCD signatures could not be reproduced. The usage of the PCM of water, as discussed before, is an essential and economic means to adequately account for the bulk water environment. To achieve similar results with explicit water molecules, it would require additional layers of water molecules in order to provide a faithful representation of the continuous solvent environment. Such modelling is computationally much more expensive.

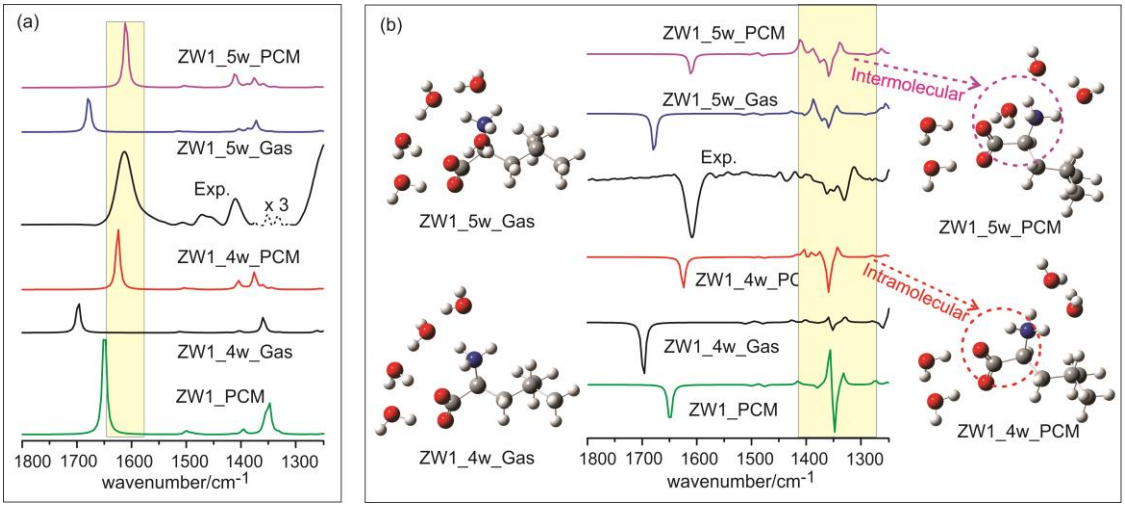


Figure 6.8. Comparison of the VA (a) and VCD (b) spectra of ZW1_4w and ZW1_5w in the gas phase and with the PCM of water with the corresponding experimental data under near neutral condition.

## 6.4. Conclusions

VA and VCD spectra of leucine in water under three representative pHs have been evaluated. The measured VA spectra clearly show the existence of different species under strongly acidic, nearly neutral, and strongly basic. Such differences have been well interpreted with the calculated VA spectra of the protonated, Zwitterionic, and deprotonated leucine conformers with the PCM of water. The complex and delicate VCD spectral signatures obtained for leucine in water under near neutral condition, on the other hand, require the consideration of both explicit and implicit solvation models. It was found that the insertion of a water molecule between the $COO^-$ and $NH_3^+$ functional groups is critical to reproduce the complex VCD signatures observed in the 1500 – 1300 $cm^{-1}$.

Furthermore the inclusion of the PCM of water is essential to lock water molecules which are directly hydrogen bonded to leucine into the positions expected in solution. Some interesting behaviors of the explicit solvated water clusters were observed during their geometry optimizations with and without PCM. Such behaviors have been discussed in terms of the effects of bulk water environment and the initial geometries proposed. To faithfully account for the solvent effects of leucine in water, the inclusion of the implicit solvent model combined with the explicit water solvated clusters has been found to be critical.

## 6.5. Acknowledgments

This research was funded by the University of Alberta, the Natural Sciences and Engineering Research Council of Canada. We thank Dr. G. Yang for discussions at the early stage of this project. We also gratefully acknowledge access to the computing facilities provided by the Academic Information and Communication Technology group at the University of Alberta and by the Western Canada Research Grid (Westgrid). YX holds a Tier I Canada Research Chair in Chirality and Chirality Recognition.

## References


[1] D. L. Nelson and M. M. Cox, "Lehninger Principles of Biochemistry" 3rd Ed. Worth Publishing: New York, ISBN 1-57259-153-6, (2000).

[2] M. R. Etzel, Manufacture and use of dairy protein fractions, J. Nutrition, **134** (4), 996S (2004).

[3] L. Combaret, D. Dardevet , I. Rieu , M. Pouch, D. Béchet, D. Taillandier, J. Grizard and D. Attaix, J. Physiology, **569**, 489 (2005).

[4] E. J. Cocinero, A. Lesarri, J. Grabow, J. C. Lopez , and J. L. Alonso, ChemPhysChem. **8**, 599 (2007).

[5] A. K. Rai, C. Song, and Z. Lin, Spectrochimica Acta Part A: Mol. Bio. Spectrosc. **73**(5), 865 (2009).

[6] S. Dokmaisrijan, V. S. Lee, and P. Nimmanpipug, J. Mol. Struc.:Theo., **953**, 28 (2010).

[7] M. J. Locke and R. T. McIver Jr, J. Am. Chem. Soc. **105**, 4226 (1983).

[8] P. D. Godfrey and R. D. Brown, J. Am. Chem. Soc. **117,** 2019 (1995).

[9] M. Chen, Z. Huang, and Z. Lin, J. Mol. Struct. **719**, 153 (2005).

[10] A. K. Rai, X. Xu, Z. Lin, and D. K. Rai, Vib. Spectrosc. **56**, 74 (2011).

[11] P.R. Tulip and S.J. Clark, J. Chem. Phys. **121**, 5201 (2004).

[12] N. Ji and Y.-R. Shen, J. Chem. Phys. **120**, 7107 (2004).

[13] Z. Ji, R. Santamaria, and I. L. Garzon, J. Phys. Chem. A , **114**, 3591 (2010); P. Zhang and P. L. Polavarapu , Applied Spectroscopy, **60**, 378 (2006); E. Tajkhorshid, K. J. Jalkanen, and S. Suhai, J. Phys. Chem. B , **102**, 5899 (1998).

[14] M. Losada and Y. Xu, Phys. Chem. Chem. Phys. **9**, 3127 (2007).

[15] M. Losada, H. Tran, and Y. Xu, J. Chem. Phys. **128**, 014508/1-11(2008); M. Losada, P. Nguyen, and Y. Xu, J. Phys. Chem. A. **112**, 5621 (2008).

[16] G. Yang and Y. Xu, Vibrational Circular Dichroism Spectroscopy of Chiral Molecules, in *Top. Curr. Chem*., Volume: Electronic and Magnetic Properties of Chiral Molecules and Supramolecular Architectures, Eds R. Naaman, D.N.Beratan, D.H.Waldeck, Springer-Verlag Berlin Heidelberg, 298, 189-236 (2011); G. Yang and Y. Xu, J. Chem. Phys. **130**, 164506 (2009).

[17] J. Sadlej, J. C. Dobrowolski, and J. E. Rode, Chem. Soc. Rev. **39**, 1478 (2010).

[18] P. Zhu, G. Yang, M. R. Poopari, Z. Bie, and Y. Xu, ChemPhysChem. **13**, 1272 (2012); M. R. Poopari, Z. Dezhahang, G. Yang, and Y. Xu, ChemPhysChem. **13**, 2310 (2012).

[19] M. J. Frisch, G. W. Trucks, H. B. Schlegel, G. E. Scuseria, M. A. Robb, J. R. Cheeseman, G. Scalmani, V. Barone, B. Mennucci, G. A. Petersson, H. Nakatsuji, M. Caricato, X. Li, H. P.

Hratchian, A. F. Izmaylov, J. Bloino, G. Zheng, J. L. Sonnenberg, M. Hada, M. Ehara, K. Toyota, R. Fukuda, J. Hasegawa, M. Ishida, T. Nakajima, Y. Honda, O. Kitao, H. Nakai, T. Vreven, J. A. Montgomery, Jr., J. E. Peralta, F. Ogliaro, M. Bearpark, J. J. Heyd, E. Brothers, K. N. Kudin, V. N. Staroverov, R. Kobayashi, J. Normand, K. Raghavachari, A. Rendell, J. C. Burant, S. S. Iyengar, J. Tomasi, M. Cossi, N. Rega, J. M. Millam, M. Klene, J. E. Knox, J. B. Cross, V. Bakken, C. Adamo, J. Jaramillo, R. Gomperts, R. E. Stratmann, O. Yazyev, A. J. Austin, R. Cammi, C. Pomelli, J. W. Ochterski, R. L. Martin, K. Morokuma, V. G. Zakrzewski, G. A. Voth, P. Salvador, J. J. Dannenberg, S. Dapprich, A. D. Daniels, Ö. Farkas, J. B. Foresman, J. V. Ortiz, J. Cioslowski, and D. J. Fox, Gaussian 09, Revision B.01, Gaussian, Inc., Wallingford CT (2009).

[20] J. Tomasi, B. Mennucci, and R. Cammi, Chem. Rev. **105**, 2999 (2005).

[21] D. A. Case, T. A. Darden, T. E. Cheatham, III, C. L. Simmerling, J. Wang, R. E. Duke, R. Luo, R. C. Walker, W. Zhang, K. M. Merz, B. Roberts, B. Wang, S. Hayik, A. Roitberg, G. Seabra, I. Kolossváry, K. F. Wong, F. Paesani, J. Vanicek, J. Liu, X. Wu, S. R. Brozell, T. Steinbrecher, H. Gohlke, Q. Cai, X. Ye, J. Wang, M.-J. Hsieh, G. Cui, D. R. Roe, D. H. Mathews, M. G. Seetin, C. Sagui, V. Babin, T. Luchko, S. Gusarov, A. Kovalenko, and P. A. Kollman AMBER 11, University of California, San Francisco (2010).

[22] See supporting information, Appendix D, for VA and VCD spectra of some leucine and leucine-$(water)_N$ conformers in the gas phase and with the PCM of water. For information on supporting information, see http://www.aip.org/pubservs/epaps.htm

[23] V. W. Jürgensen and K. Jalkanen, Phys. Biol. **3,** S63 (2006).

# 7 Chapter

# Conclusions & Future Work

## 7.1. Conclusions

My PhD thesis work presented here focuses on developing a suitable approach to properly account for solvent effects in solution spectroscopic measurements and on providing significant insights into the intermolecular interactions between the solvent, in particular water, and the solute. Specifically, I utilize VCD spectroscopy to identify subtle conformational changes and to monitor how the solvent influences the conformational distributions and conformational geometries in solution.

As indicated in Chapter 3, one aim of this thesis is to evaluate the performance of the implicit solvent model, i.e. integral equation formalism polarizable continuum model (IEF-PCM), for accounting for solvent effects in VCD spectra, etc. I would like to emphasize that VCD spectroscopy is a particularly well-suited spectroscopic method for capturing even subtle solvent effects, for example, those caused by nonpolar or weakly polar solvents, such as $CCl_4$ and $CDCl_3$. For example, this exquisite sensitivity of VCD measurements to the solvent environment is illustrated in Figure 7.1 for solvated N-Acetyl-L-Cysteine systems. The VA and VCD spectra of three representative solvated clusters in the gas phase and with PCM have been compared. In addition, the population weighted spectra of all these systems are reported. Overall, the gas-IR and PCM-based IR spectra of these clusters are very similar and agree well with the experimental spectra. However, superior agreement is achieved when the NALC-$(Water)_4$ clusters are implicitly solvated. For example, the peak labelled as 3 in the simulated VCD spectra is negative for all three clusters in the gas phase

whereas the corresponding peak converts to a positive peak with the PCM model, corresponding to what is obtained experimentally. The other advantage of the combined approach is that the peaks' positions are more accurate. While the peak 5' is hidden under peak 5 in the gas phase simulation, the corresponding peak is shifted to a lower frequency with the implicit solvent model.

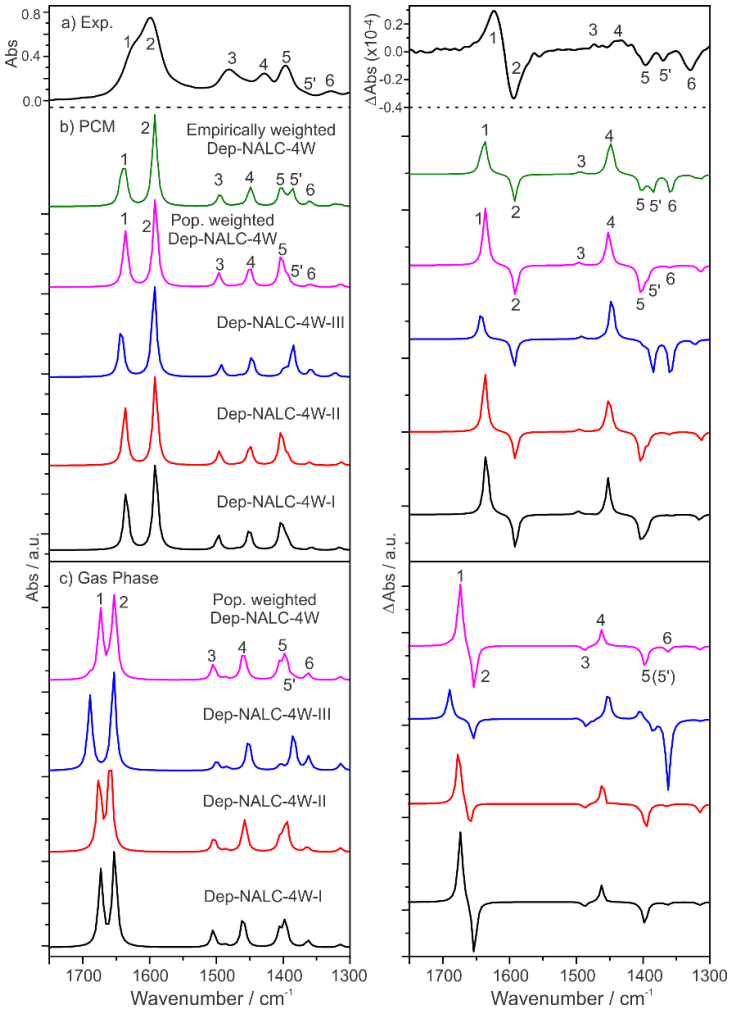


Figure 7.1. Comparisons of a) the experimental VA and VCD spectra of NALC in $D_2O$ under neutral pH conditions with b) the corresponding spectra of the most stable Dep-NALC-4W conformers with the PCM of $D_2O$ and c) in the gas phase at the B3LYP/6-311++G(d,p) level. The DFT and empirically population-weighted spectra are also provided. (Taken from Ref: *ChemPhysChem*, 2012, 13, 2310 – 2321)

The high sensitivity of VCD spectroscopy to subtle structural changes and therefore to solvent environment is utilized in all my investigations of solvent effects. It has been further demonstrated in chapters 3 to 6 of my thesis that the VCD technique is also highly sensitive to hydrogen-bonding interactions between solute and solvent molecules. In addition, the conformational distortions in the order of picoseconds time scale can be detected using VCD spectroscopy. The contributions of all available conformers can be obtained through Boltzmann population factor analyses. VCD spectroscopy therefore offers considerable advantages over NMR spectroscopy, another commonly used spectroscopic technique for solution conformational studies. The typical time scale of NMR spectroscopy is ca. $10^{-6}$ ~ $10^{-1}$ second, much slower than many inter- and intramolecular motions and rearrangements in solution.

In chapter 3, I examined the VCD signatures of methyl mandelate in a number of organic solvents, i.e. chloroform, dimethyl sulfoxide, and methanol. This study was mainly focused on how solvent polarity and solvent hydrogen-bonding formation capability influence the VCD spectral signatures. The overall conclusion is that the inclusion of both explicit and implicit solvent effects has a significant impact on the appearance of the VA and VCD spectra when solvents are capable of strong hydrogen-bonding interactions with solutes. For solvents which have no strong hydrogen-bonding tendency, such as chloroform, the gas phase monomer model is adequate for spectral interpretation, although the inclusion of implicit solvation is highly recommended to improve the frequency

agreement with experiment, and also to account for more subtle geometry changes in solution.

Because of the significant importance of aqueous solution, the rest of the research, i.e. chapters 4 to 6, deals with water solvent. It has been shown that the combined explicit-implicit approach improves the accuracy of the simulated spectral features to considerable extents. In this approach, we combine both the explicit solvation model, i.e. chiral solute-water hydrogen-bonded clusters, and the implicit solvent model to account for the bulk water environment. There are, however, a number of major challenges which one needs to address in order to utilize this approach successfully. For example, how do these important hydration clusters look like? Is there a systematic way to build these clusters? What are the effects of the bulk water environment on these hydration clusters? My thesis work provides some valuable insights into intermolecular interactions between chiral solute and water molecules and how to construct these hydration clusters. Through a number of example case studies, I present ways to overcome some of the challenges mentioned above.

The molecular systems I chose are several amino acids and their derivatives. They are building blocks of larger entities such as peptides and proteins which make use of the same or similar functional groups in their hydrogen-bonding interactions with water. Equally important, these systems are small enough to be amenable to high level ab initio calculations. One can therefore make rigorous comparisons between experimental and theoretical spectral features to appreciate the nature of chiral solute-water interactions.

In chapter 4, I explored the reliability of the PCM-based VCD spectral simulations in finding the right conformations in water where strong hydrogen-bonding interactions are expected. For this purpose, I focused on two specific vibrational modes, namely carboxylic and amide I vibrations. A clear structural-spectral relationship between the VCD spectral signatures and the preferred conformations was established by introducing a specific "conformational frame angle". Furthermore, the inclusion of the PCM for bulk water was shown to be important in identifying dominant conformers in water. Such conformational searches with PCM provide better suited starting conformations for further studies using explicit solvent models at a compromised computational cost.

In Chapter 5, the acetylated form of cysteine was studied in aqueous solution. The study shows that the experimental VCD spectral features cannot be reproduced satisfactorily without the combined approach, i.e. the first shell of hydration between *N*-Acetyl-*L*-cysteine and water is treated explicitly while the rest of the water molecules are treated as a bulk solvent environment using PCM. It was demonstrated in this study that the inclusion of both explicit and implicit solvation models at the same time provides a decisively better agreement between theory and experiment. One can therefore obtain conclusive information about the conformational distributions of NALC in water and about hydrogen-bonding interactions between *N*-Acetyl-*L*-cysteine and water molecules.

In Chapter 6, I applied the same methodology implemented in the previous chapter to leucine in aqueous solution to test the validity of the approach. Indeed, the same results have been achieved which authenticate the usage of such an

approach for solute-solvent interactions investigations. Figure 7.2 shows the most representative MD snap shots of the hydration clusters of leucine. Then, these clusters were optimized with the inclusion of water solvation using the PCM model. It was found that the implicitly solvated clusters with PCM, i.e. PCM-Leu-$(Water)_N$, converged much faster to a final geometry which is similar to the initial MD snap shot.[1] The geometry optimization process with the same starting point but without the bulk water took significantly longer time to reach convergence and to a final geometry which is very different from the initial MD snap shot.

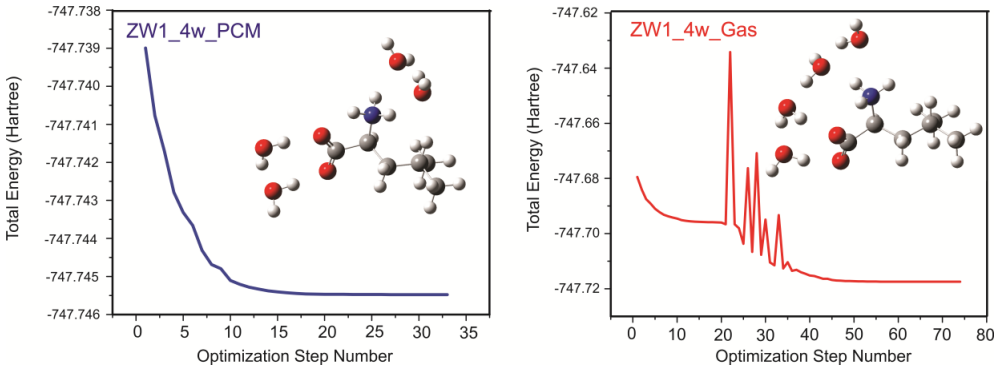


Figure 7.2. Comparison of the optimization step numbers of the ZW1_4w cluster (shown in the insert) at the B3LYP/6-311++G(d,p) level with the PCM of water (left) and in the gas phase (right). The initial geometry was taken from a representative MD snapshot in a box of water molecules. [Taken from Ref: *J. Chem. Phys*., 2012, 137 (19), 194308.]

In summary, my thesis research work demonstrates that VCD spectroscopy is a very powerful spectroscopic tool for studying intermolecular interactions between chiral solute and solvent molecules in solution. This work also shows that one can interpret the IR and VCD spectra obtained in water adequately using the combined explicit and implicit solvent approach.

## 7.2. Future work

My thesis is centered on studies of solute-solvent interactions in solution, especially in water using VCD spectroscopy complemented with DFT calculations. Molecular dynamics simulation is used to find the initial hydration clusters which can be used later for high-level quantum chemistry calculations. In bulk solution, the first solvation shell, is believed to play the most important role in the solvation process, is considered explicitly, while the rest of the water molecules are replaced by the dielectric constant of the solvent. I will be applying the mixed QM/MM methodology on the larger hydration clusters considering several shells of solvents to monitor the solute and solvent molecules interactions more precisely and simulate the spectral signatures at higher level of confidence. Since the spectral window for VCD technique is limited to 900 $cm^{-1}$-1800 $cm^{-1}$, it would also be beneficial to examine chiroptical features in wider spectral regions using other analogous technique such as Raman optical activity (ROA). I will be able to cover the region from 200 $cm^{-1}$ to 2000 $cm^{-1}$ in the experimental measurements. With this technique, I will be able to access the low wavenumber regions associated with water vibrational modes like libration and also intermolecular vibrational modes. Recently, Cheeseman et al.[2] reported a ROA spectroscopic study of methyl-β-D-glucose in water. It was found that ROA spectral features in the region between 500- 900 $cm^{-1}$ are particularly sensitive to

water solvation effects. Therefore, such studies will provide further valuable data to evaluate water solvent behaviors and the approach developed here.

It has been shown in the previous study[3] that solvent influences the VA and VCD spectral appearances and it has been found that three main perturbations making the spectral signatures look different via Boltzmann populations, electronic structures, and normal modes. Furthermore, as can be seen in Figure 7.3, the VA and VCD spectral simulations of a typical chiral molecule are highly sensitive to the choice of functional. Noticeably, a negative/positive derivative band shape at above 1700 $cm^{-1}$ is red shifted considerably when B3LYP functional is employed with respect to the others. I will test the sensitivity of different functionals and basis sets on the solute-solvent interactions to monitor the subtle changes in spectral appearance and structural deformations caused by different methods. Another point that might be worth testing is why the same vibrational mode gives rise to a different VCD signature with respect to the choice of functional and solvent model considerations.

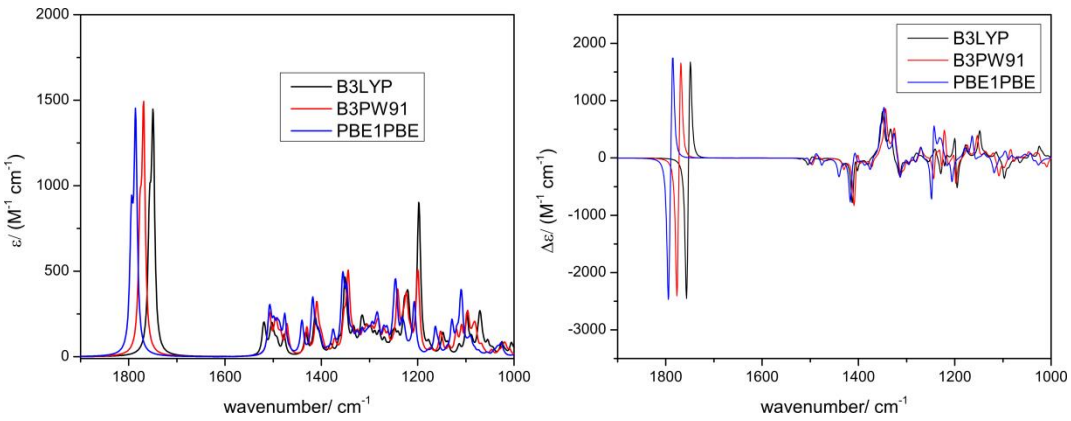


Figure7.3. The VA and VCD spectral comparison of a typical chiral molecule using three different functional namely B3LYP, B3PW91, and PBE1PBE1. (Unpublished data)

## References

[1] M. R. Poopari, P. Zhu, Z. Dezhahang, Y. Xu, *J. Chem. Phys*., 2012, 137 (19), 194308.

[2] J. R. Cheeseman, M. S. Shaik, P. L. A. Popelier, E. W. Blanch, *J. Am. Chem. Soc.*, 2011, 133, 4991–4997.

[3] V. P. Nicu, E. J. Baerends, P. L. Polavarapu, *J. Phys. Chem. A*, 2012, 116, 8366−8373.

# Appendix A

**Supporting Information of chapter 3**

A comparative VCD study of methyl mandelate in methanol, dimethyl sulfoxide, and chloroform: explicit and implicit solvation models

Mohammad Reza Poopari, Zahra Dezhahang, Yunjie Xu*

Department of Chemistry, University of Alberta, Edmonton, Alberta, Canada
*Tel:1-780-492-1244, Fax:1-780-492-8231, Email: yunjie.xu@ualberta.ca

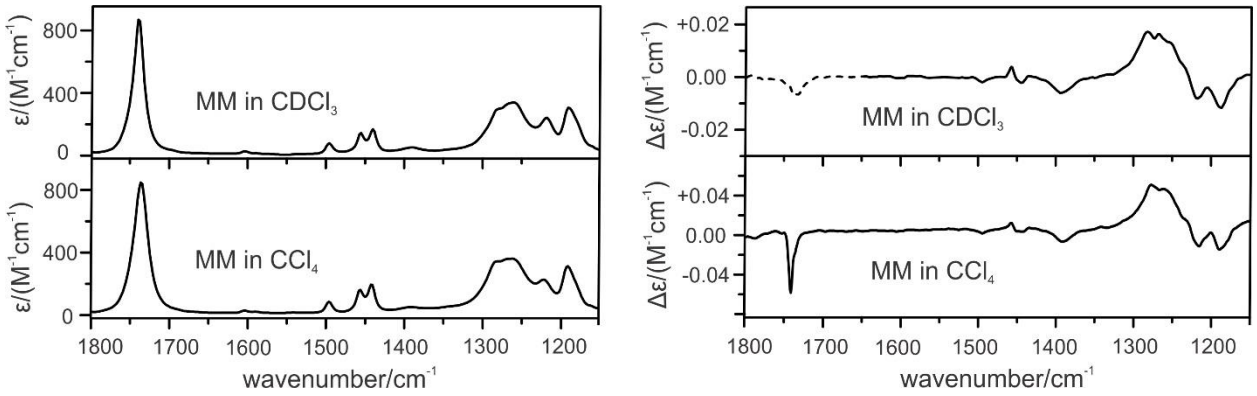


**Figure A1.** Comparison of the experimental VA (left) and VCD (right) spectra of MM in $CDCl_3$ and $CCl_4$.

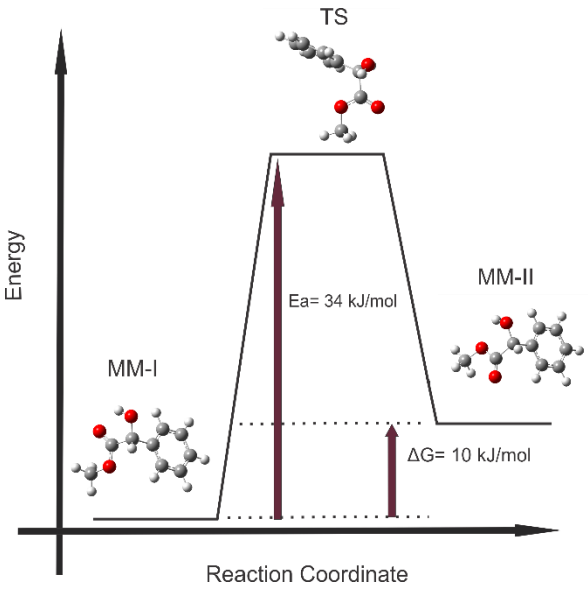


**Figure A2.** The conversion barriers between the two most stable conformers of MM at the B3LYP/cc-pVTZ level. The QST2 option implemented in Gaussian 09 with the Synchronous Transit-Guided Quasi-Newton (STQN) method has been used to locate the transition state between these two lowest energy conformers.

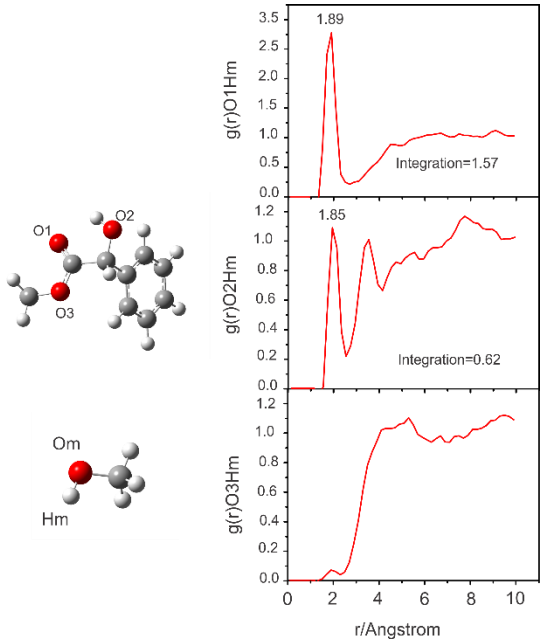


**Figure A3.** RDFs obtained from the MD simulation of MM in methanol. The atom labelling for MM is given at the left. Om and Hm are the oxygen and hydrogen atoms of methanol, respectively.

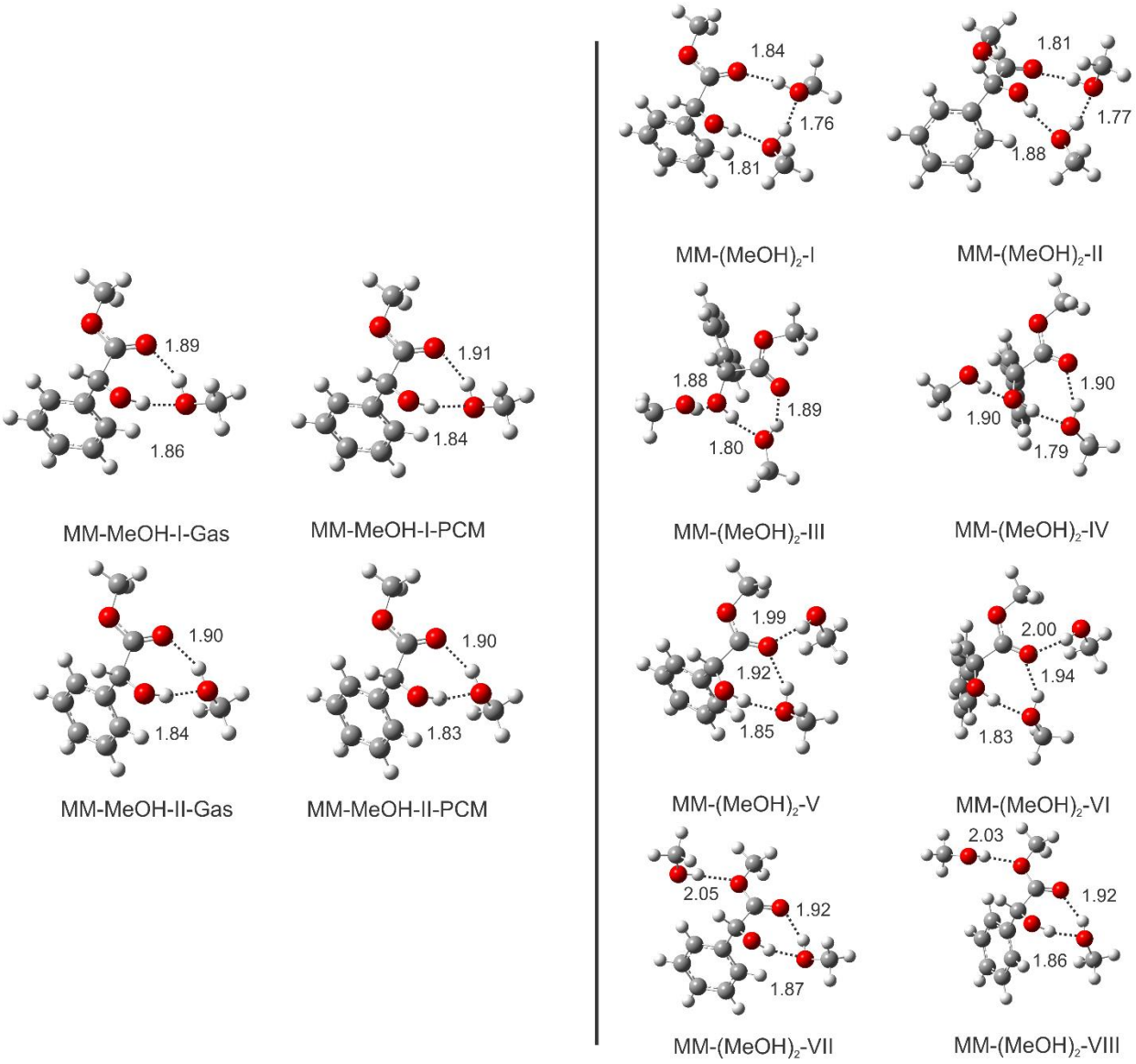


**Figure A4.** Optimized geometries of the two lowest energy conformers of MM-MeOH in the gas phase and with PCM of methanol and eight lowest energy conformers of MM-$(MeOH)_2$ at the B3LYP/cc-pVTZ level in the gas phase. The intermolecular hydrogen-bond lengths (in Å) are indicated.

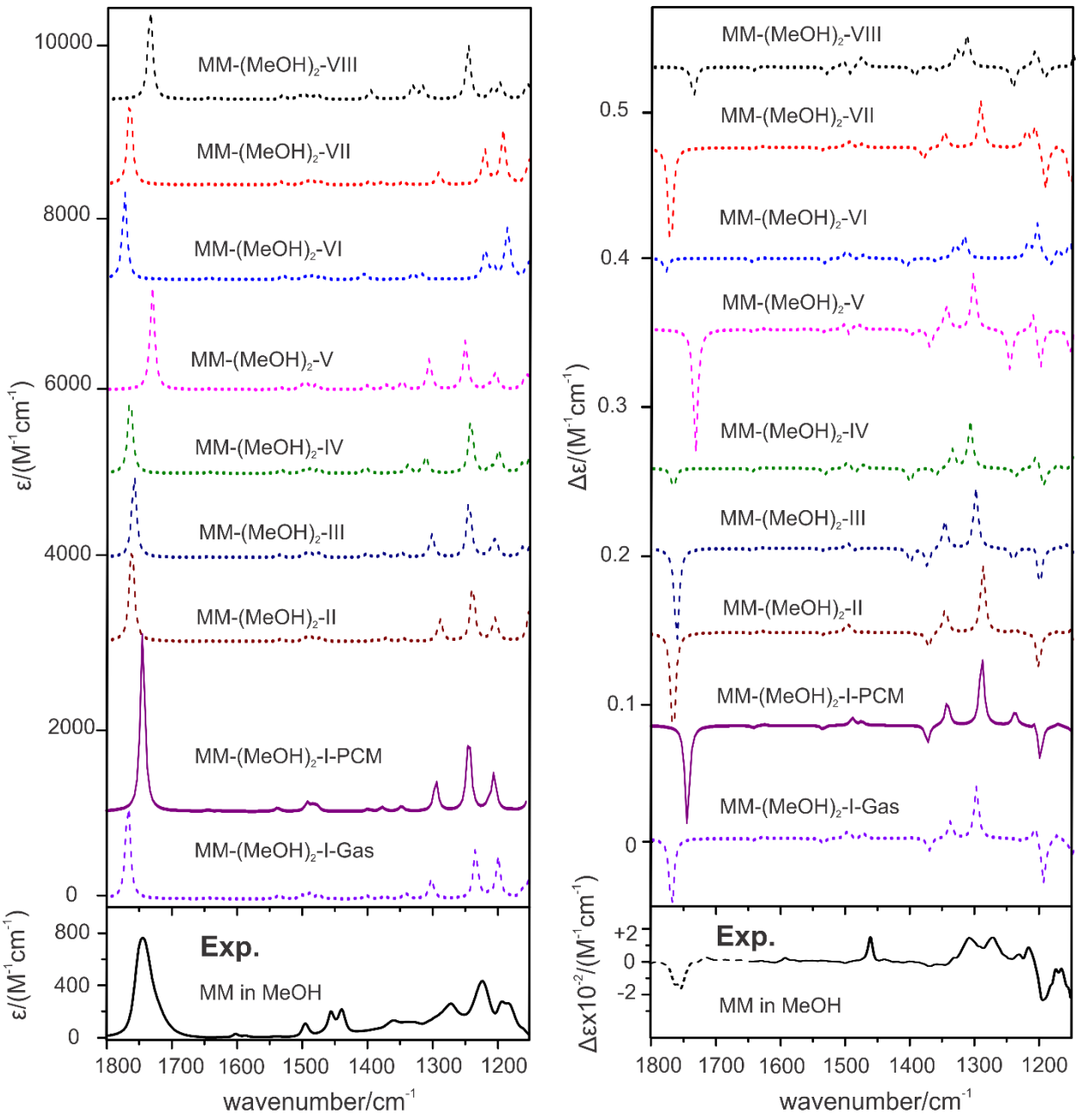


**Figure A5.** The experimental VA and VCD spectra of MM in MeOH and the corresponding simulated spectra of the conformers of the MM-$(MeOH)_2$ complex in the gas phase calculated at the B3LYP/cc-pVTZ level. The VA and VCD spectra of MM-$(MeOH)_2$-I with the PCM of methanol are also included.

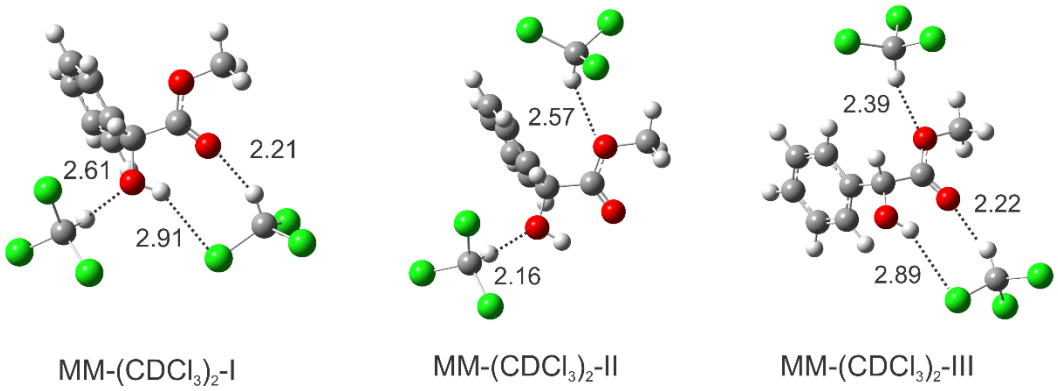


**Figure A6.** Optimized geometries of the three low energy conformers of the 1:2 MM-$(CDCl_3)_2$ complex at the B3LYP/cc-pVTZ level in the gas phase. The intermolecular hydrogen-bond lengths are indicated.

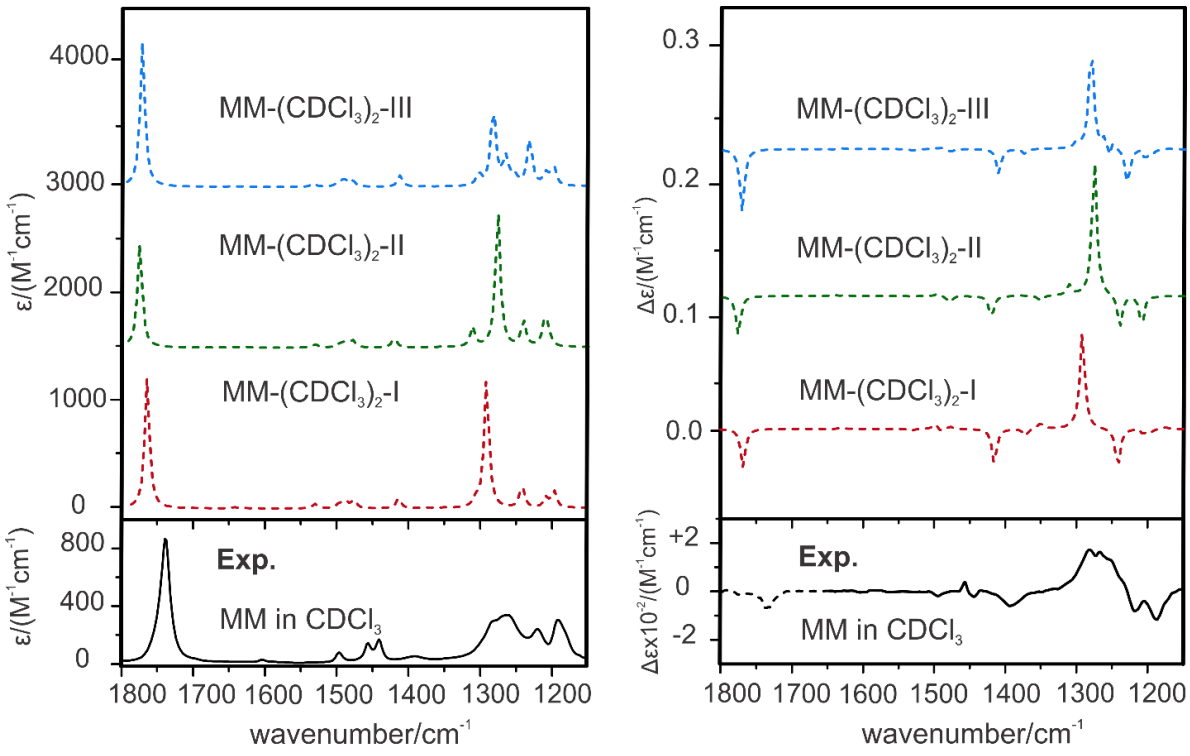


**Figure A7.** Comparisons of the experimental VA/VCD spectra of MM in $CDCl_3$ (bottom) with three most stable conformers of MM-$(CDCl_3)_2$ in the gas phase (top) calculated at the B3LYP/cc-pVTZ level at room temperature.

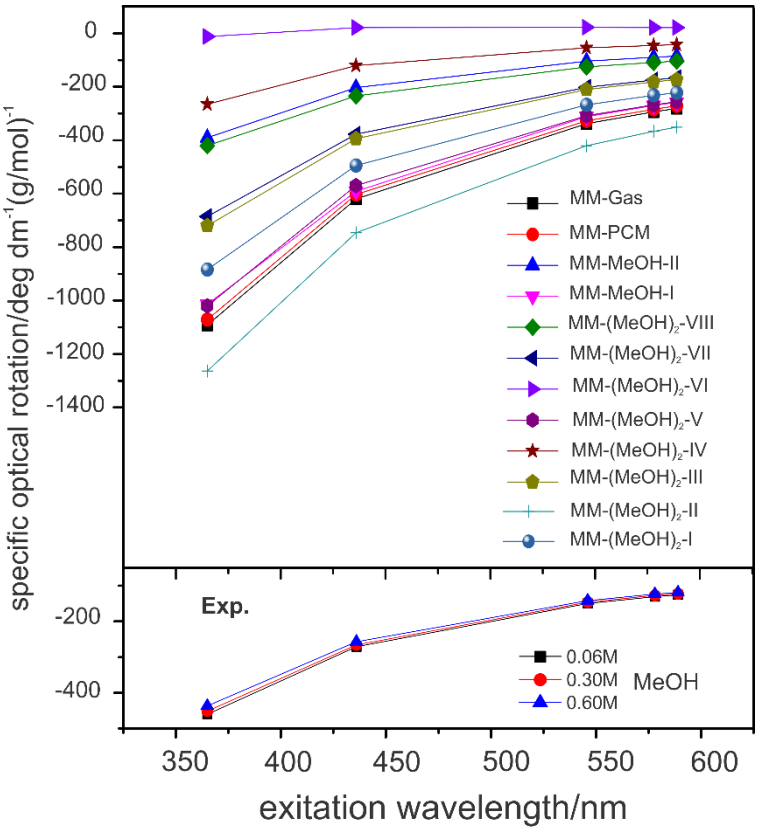


**Figure A8.** Comparison of the experimental specific ORD values of MM in methanol and the calculated specific ORD values of the MM monomer and its complexes with methanol in the gas phase and with PCM. The theoretical specific ORD values calculated using Gaussian 09 are the specific ORD values for the particular species specified in the calculations. The experimental specific ORD values were obtained using the concentration of the solute, i.e. MM, alone in g/mol. To compare the calculated specific rotation values directly obtained from Gaussian 09 and plotted in the figure, it is necessary to multiply the values by the particular $\frac{(M)_{complex}}{(M)_{solute}}$ factor in each case.

# Appendix B

**Supporting Information of chapter 4**

Identifying dominant conformations of N-acetyl-L-cysteine methyl ester and N-acetyl-L-cysteine in water: VCD signatures of the amide I and the C=O stretching bands

Mohammad Reza Poopari, Zahra Dezhahang, and Yunjie Xu*

Department of Chemistry, University of Alberta, Edmonton, Alberta, Canada
*Tel:1-780-492-1244, Fax:1-780-492-8231, Email: yunjie.xu@ualberta.ca

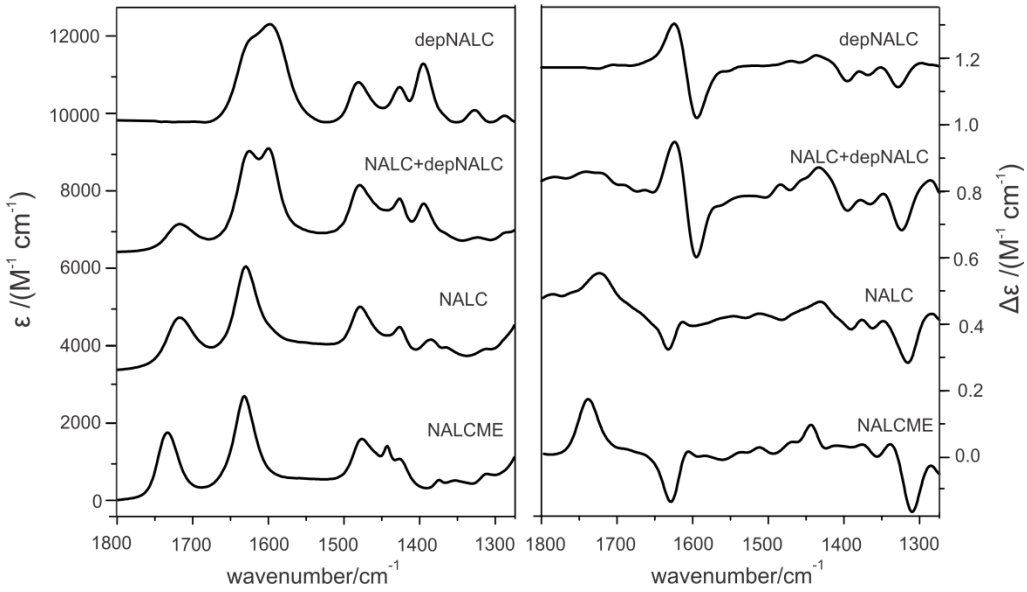


**Figure B1.** VA and VCD spectra from 1800 to1300 $cm^{-1}$ of depNALC, neutral NALC, and neutral NALCME in water. The corresponding pH values are 7, 3.1, 2.5, and 6.6 from top to bottom.

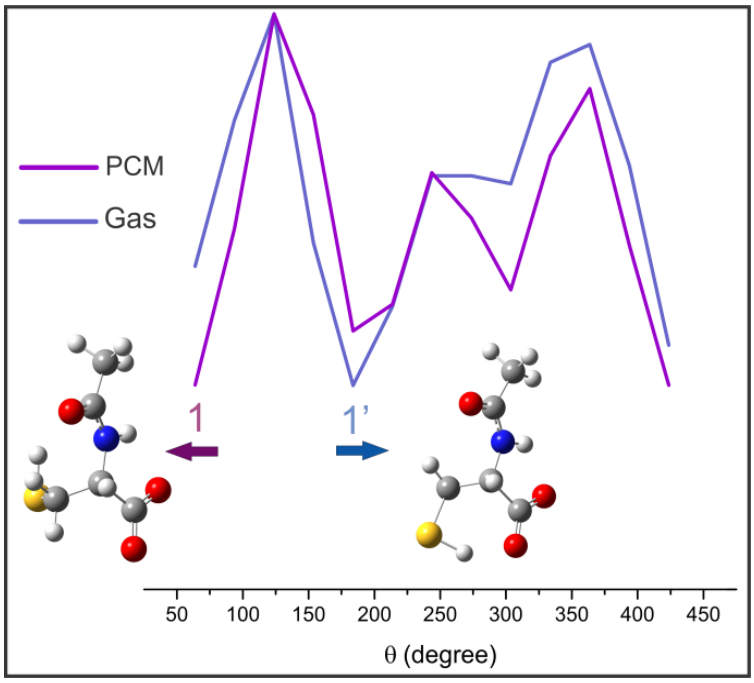


**Figure B2.** The potential energy surface scan of depNALC along the conformational angle θ = τ($N_1$-$C_3$-$C_5$-$H_6$) in the gas phase and with the PCM of water solvent at the B3LYP/aug-ccpVTZ level.

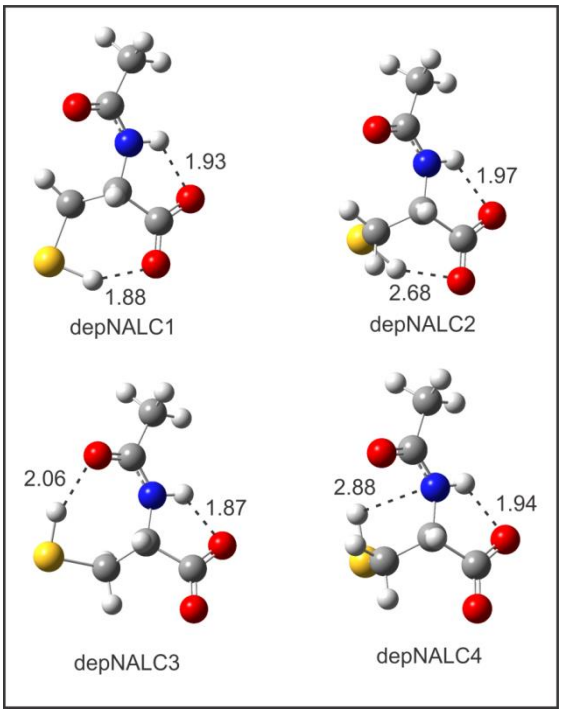


**Figure B3.** Geometries of the four most stable conformers of depNALC in the gas phase optimized at the B3LYP/aug-cc-pVTZ level. All relevant intramolecular bonds with a bond length less than 3 Å are indicated. Please note that the Arabic numbers indicate the stability ordering of the conformers based on the ΔG values obtained in the gas phase, with "1" being the most stable conformer.

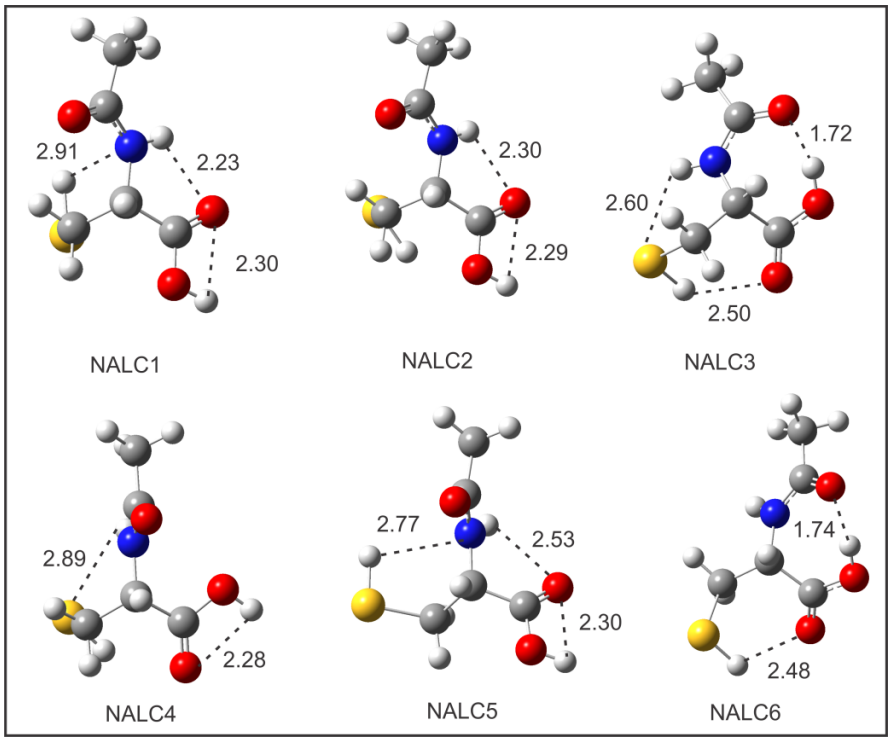


**Figure B4.** Geometries of the six most stable conformers of neutral NALC in the gas phase optimized at the B3LYP/aug-cc-pVTZ level. All relevant intramolecular bonds with a bond length less than 3 Å are indicated. Please note that the Arabic numbers indicate the stability ordering of the conformers based on the ΔG values obtained in the gas phase, with "1" being the most stable conformer.

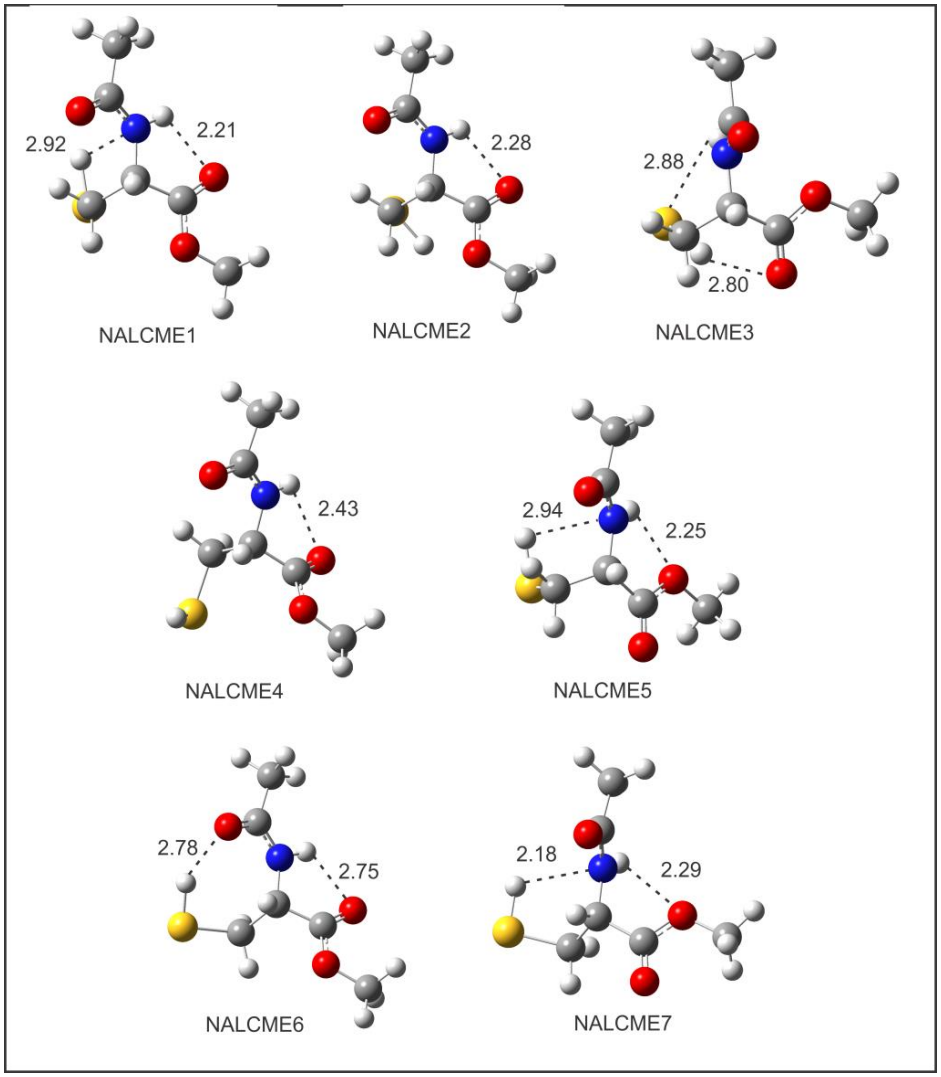


**Figure B5.** Geometries of the seven most stable conformers of NALCME in the gas phase optimized at the B3LYP/aug-cc-pVTZ level. All relevant intramolecular bonds with a bond length less than 3 Å are indicated. Please note that the Arabic numbers indicate the stability ordering of the conformers based on the ΔG values obtained in the gas phase, with "1" being the most stable conformer.

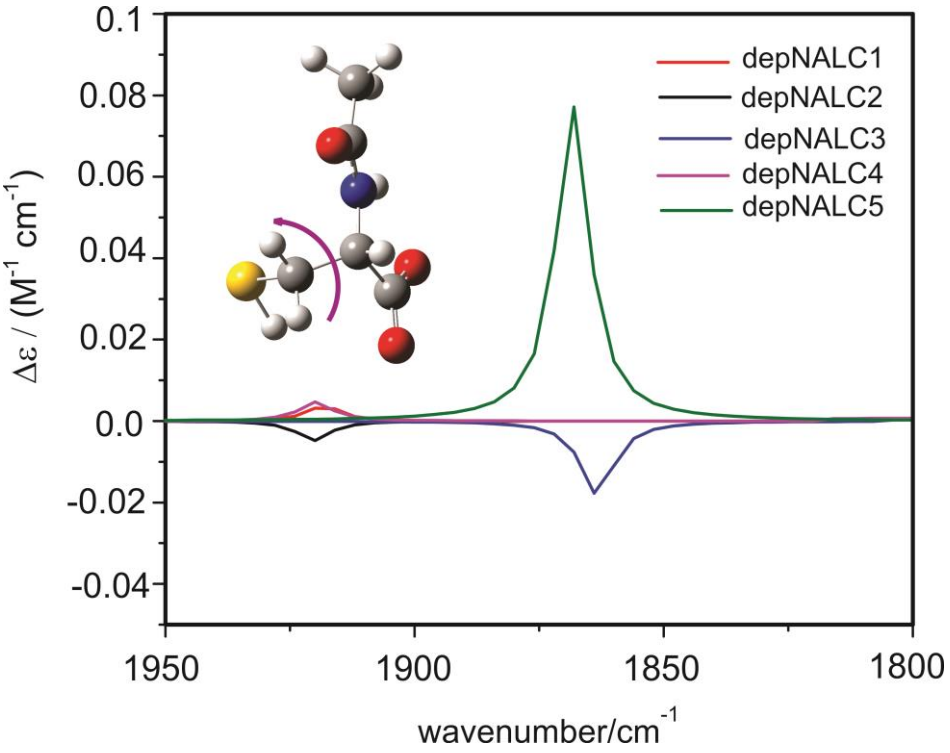


**Figure B6.** Simulated VCD spectral features of the –SD stretching mode of the five depNALC conformers at the PCM/B3LYP/aug-cc-pVTZ level. The –SD group was used since the experimental was performed in $D_2O$.

# Appendix C

**Supporting Information of chapter 5**

Conformational distributions of N-acetyl-L-cysteine in aqueous solutions: a combined implicit and explicit solvation treatment of VA and VCD spectra

Mohammad Reza Poopari, Zahra Dezhahang, Guochun Yang, Yunjie Xu*

Department of Chemistry, University of Alberta, Edmonton, Alberta, Canada
*Tel:1-780-492-1244, Fax:1-780-492-8231, Email: yunjie.xu@ualberta.ca

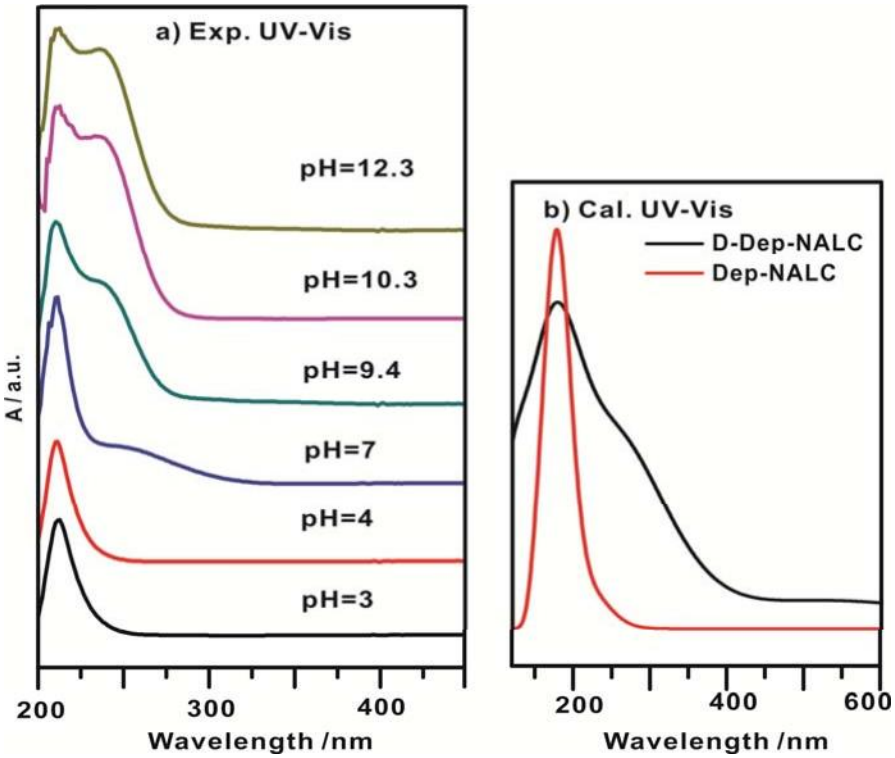


**Figure C1.** (a) The experimental UV-Vis spectra of NALC in water under a series of different pH values ranging from 3 to 12.3. (b) Simulated UV-Vis spectra of the singly and the doubly deprotonated NALC species. The most stable conformers found for each species in Table 1 were used for the calculations.

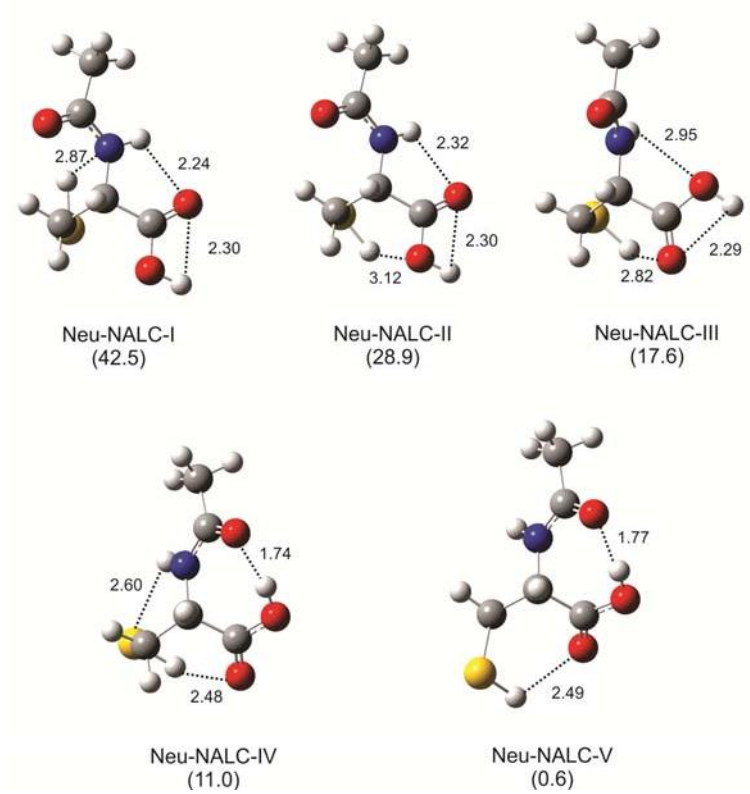


**Figure C2.** Optimized geometries of the five lowest energy conformers of Neu-NALC in the gas phase at the B3LYP/6-311++G(d,p) level. The numbers in the parenthesis are the percentage Boltzmann population factors based on the relative Gibbs free energies at 298 K. The intramolecular hydrogen bond lengths and some importance van der Waals bond lengths (in Å) are indicated.

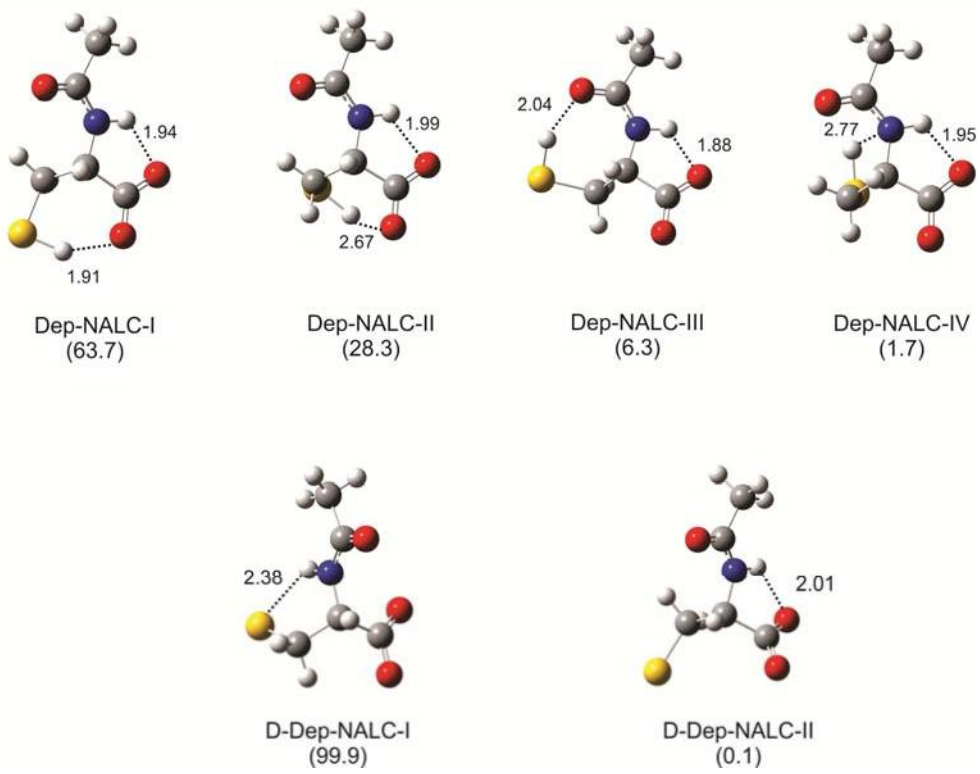


**Figure C3.** Optimized geometries of the four and two lowest energy conformers of Dep- and D-Dep-NALC in the gas phase, respectively, at the B3LYP/6-311++G(d,p) level. The numbers in the parenthesis are the percentage Boltzmann population factors based on the relative Gibbs free energies at room temperature. The intramolecular hydrogen bond lengths and some importance van der Waals bond lengths (in Å) are indicated.

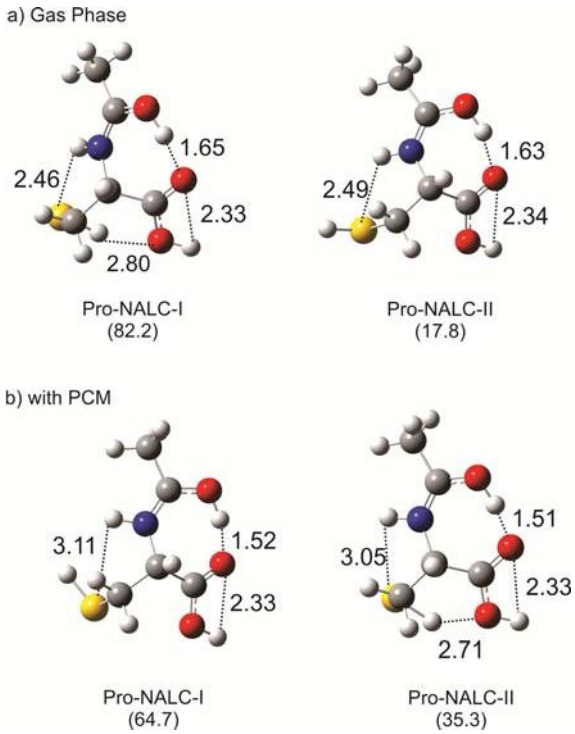


**Figure C4.** Optimized geometries of the two lowest energy conformers of protonated NALC in the gas phase and with the PCM of water at the B3LYP/6-311++G(d,p) level. The numbers in the parenthesis are the percentage Boltzmann population factors based on the relative Gibbs free energies at room temperature. The intramolecular hydrogen bond lengths and some importance van der Waals bond lengths (in Å) are indicated.

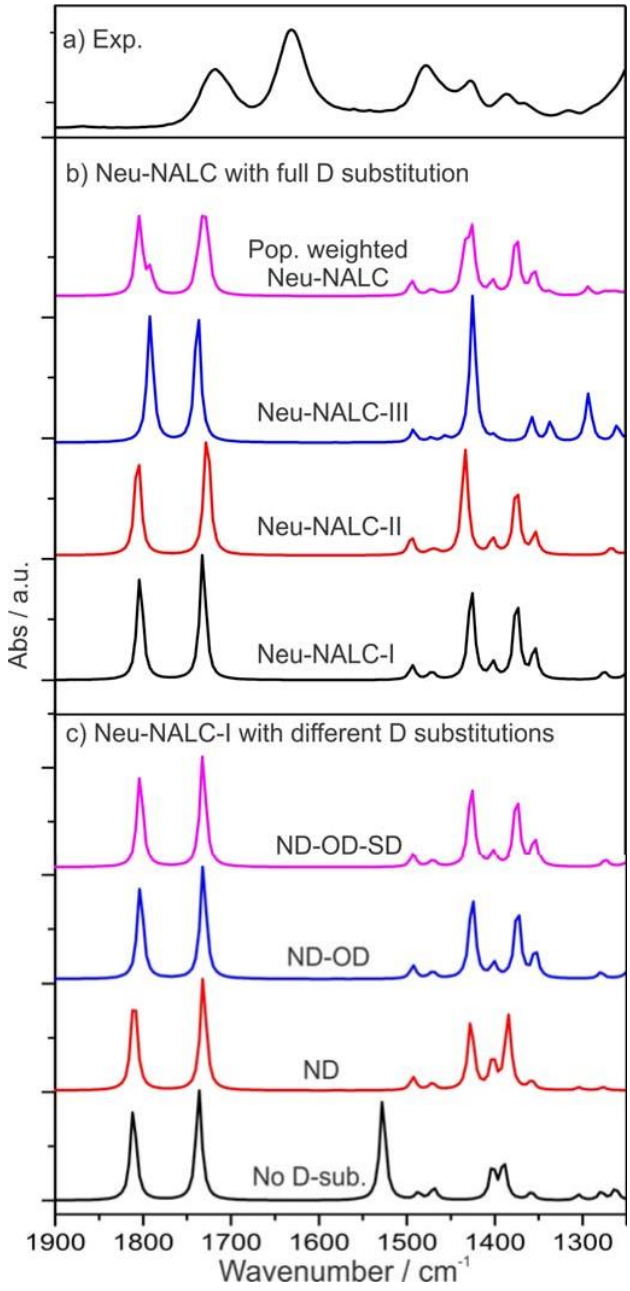


**Figure C5.** Comparisons of (a) the experimental VA spectrum of NALC in $D_2O$ under the highly acidic condition (pH=0.65) with (b) the simulated VA spectra of the three most stable Neu-NALC conformers in the gas phase and their population weighted VA spectrum based on the relative Gibbs free energies at room temperature. (c) Simulated VA spectra of the different deuterium isotopologues of Neu-NALC-I in the gas phase. All simulations are at the B3LYP/6-311++G(d,p) level.

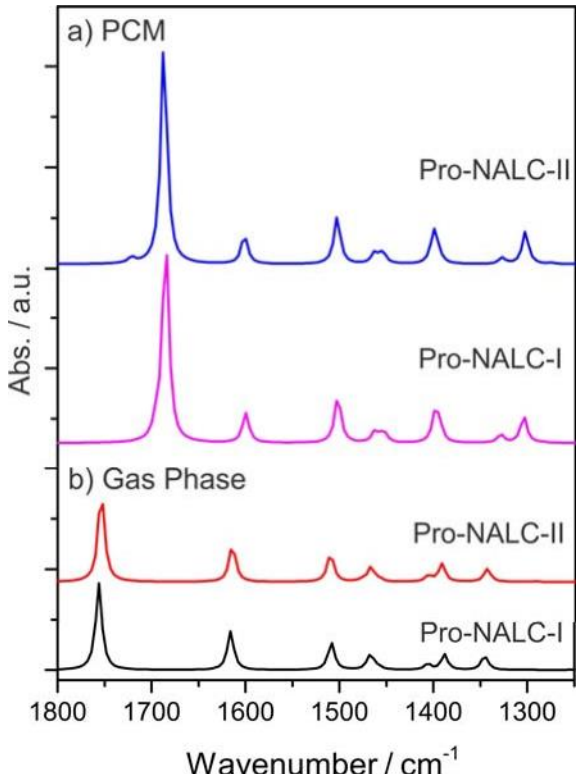


**Figure C6.** Simulated VA spectra of the two most stable Pro-NALC conformers in the gas phase and with PCM of $D_2O$ at the B3LYP/6-311++G(d,p) level.

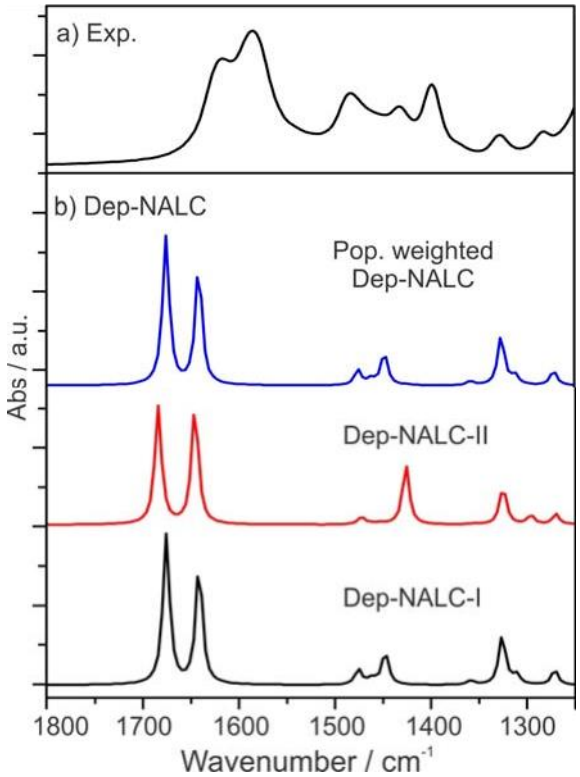


**Figure C7.** Comparisons of the experimental VA spectrum of NALC in $D_2O$ under the highly basic condition (pH=13) with the simulated VA spectra of the two most stable D-Dep-NALC conformers in the gas phase and with the corresponding population weighted VA spectrum based on the relative Gibbs free energies at room temperature at the B3LYP/6-311++G(d,p) level .

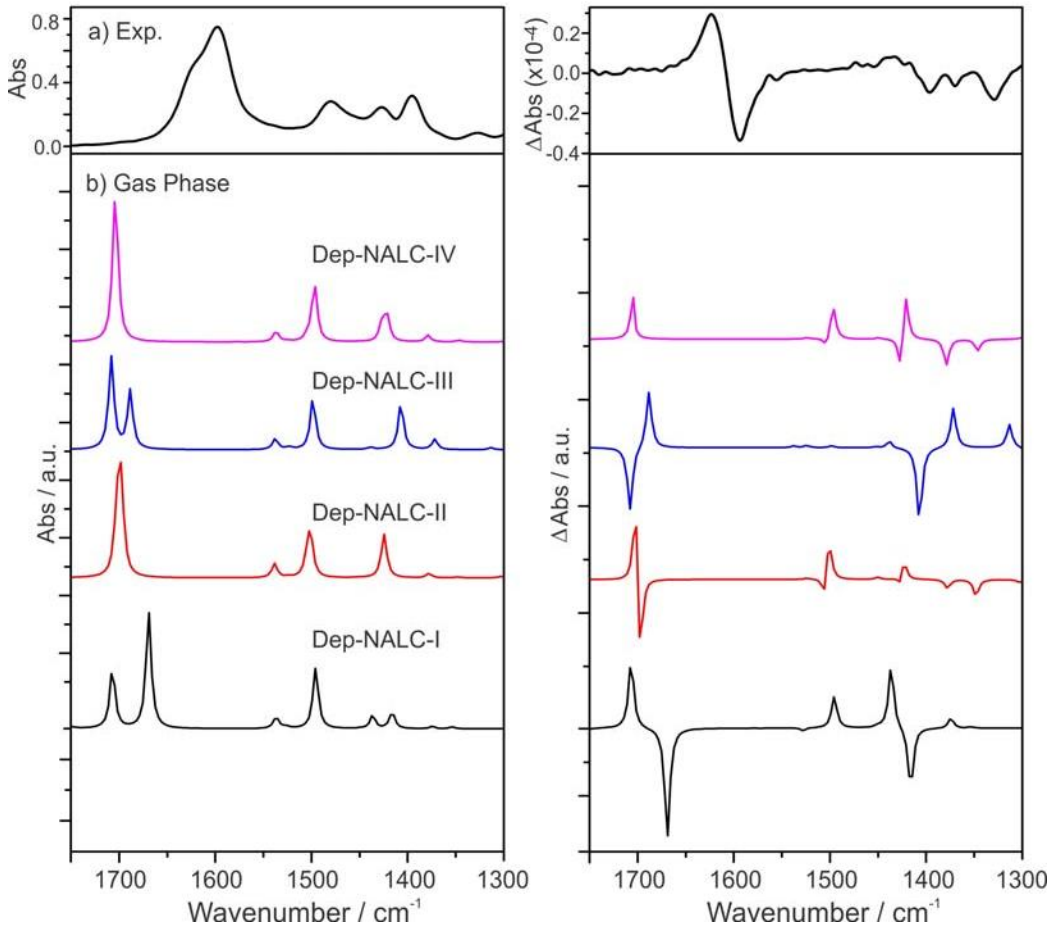


**Figure C8.** Comparisons of the experimental VA and VCD spectra of NALC in $D_2O$ at the neutral pH with the simulated VA and VCD spectra of the four most stable conformers of Dep-NALC in the gas phase at the B3LYP/6-311++G(d,p) level.

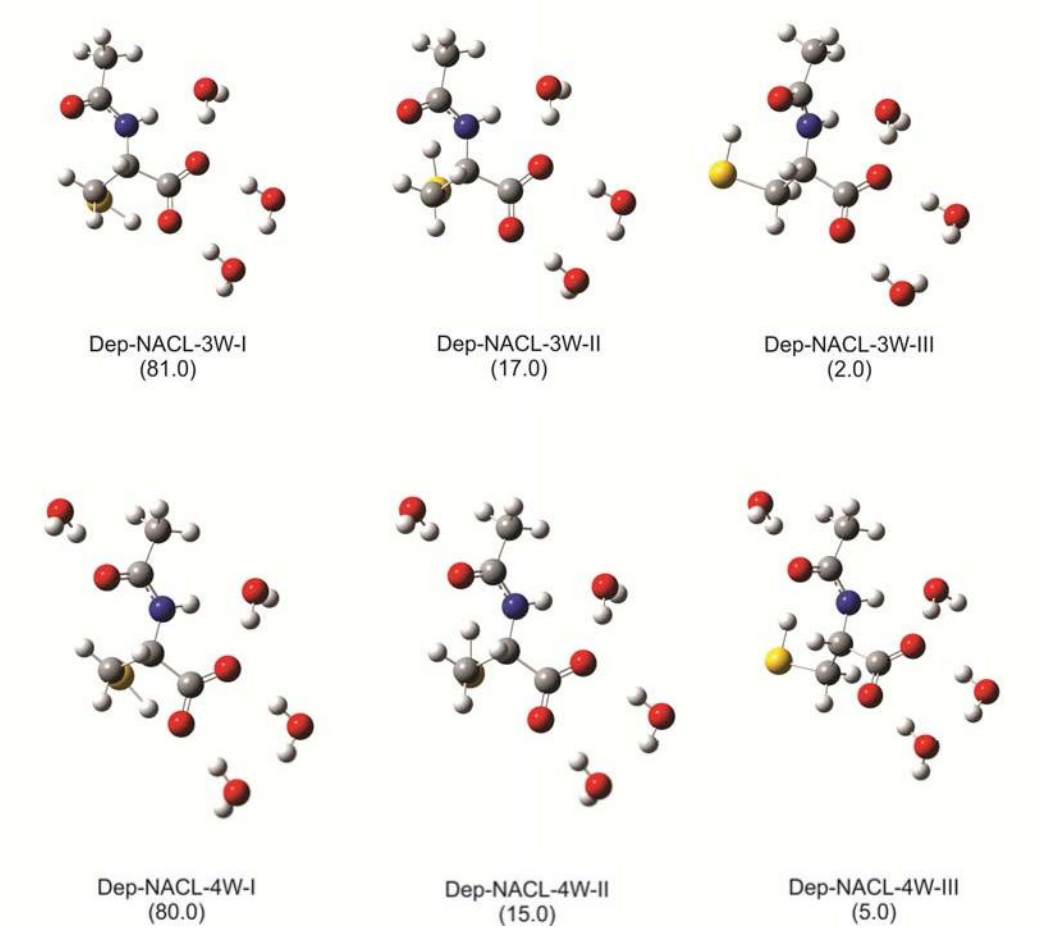


**Figure C9.** Optimized geometries of the six lowest energy conformers of the Dep-NALC-3W and Dep-NALC-4W clusters in the gas phase at the B3LYP/6-311++G(d,p) level. The numbers in the parenthesis are the percentage Boltzmann population factors based on the relative Gibbs free energies at room temperature.

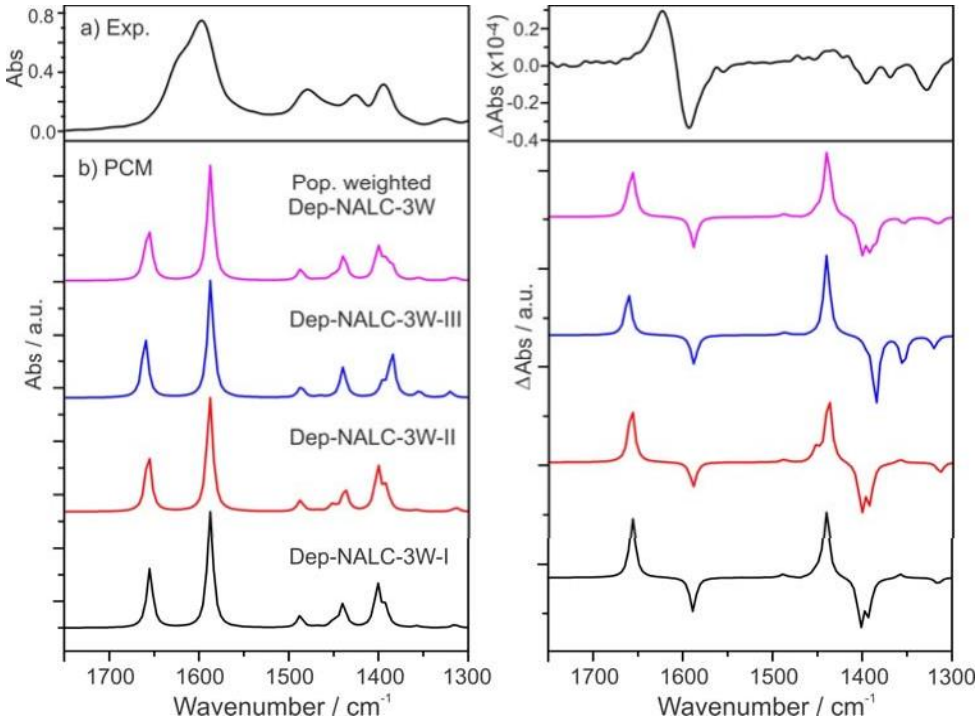


**Figure C10.** Simulated VA (left) and VCD (right) spectra of the three most stable conformers of Dep-NALC-3W and the corresponding population weighted spectra in the gas phase based on the relative Gibbs free energies at room temperature at the B3LYP/6-311++G(d,p) level.

**Table C1.** Calculated normal mode frequencies and the related rotational strengths (R), electric strengths (D), the angles (θ) between the magnetic and electric dipole vectors, and the ratios (ʒ) for Dep-NALC-I in PCM and Dep-NALC-4W-I in PCM at the B3LYP/6-311++G(d,p) level.

| Mode | Freq ($cm^{-1}$) | R ($x10^{-44}$ $esu^2$ $cm^2$) | D ($1x0^{-40}$ $esu^2$ $cm^2$) | ʒ=R/D (ppm) |
|---|---|---|---|---|
| Dep-NALC-I PCM | | | | |
| 32 | 1352 | 11.56 | 188.04 | 6.147628164 |
| 33 | 1387 | -83.12 | 894.67 | -9.290576414 |
| 34 | 1395 | -14.5 | 477.19 | -3.038621933 |
| 35 | 1440 | 115.67 | 951.92 | 12.1512312 |
| 38 | 1490 | 8.8 | 392.46 | 2.242266728 |
| 39 | 1595 | -167.73 | 3011.47 | -5.569705161 |
| 40 | 1643 | 204.98 | 1529.09 | 13.40535874 |
| Dep-NALC-4W-I PCM | | | | |
| 60 | 1360 | -10.5636 | 116.9824 | -9.030076319 |
| 61 | 1393 | -45.2202 | 303.2956 | -14.90961293 |
| 62 | 1402 | -142.7112 | 1394.5924 | -10.23318355 |
| 63 | 1449 | 76.2629 | 607.115 | 12.56152459 |
| 64 | 1453 | 90.8285 | 221.3349 | 41.03668242 |
| 66 | 1495 | 10.6485 | 526.6639 | 2.02187771 |
| 67 | 1591 | -110.5789 | 3152.7801 | -3.507345787 |
| 68 | 1637 | 226.5698 | 1960.0519 | 11.55937759 |

# Appendix D

**Supporting Information of chapter 6**

Vibrational absorption and vibrational circular dichroism spectra of leucine in water under different pH conditions: hydrogen-bonding interactions with water

Mohammad Reza Poopari, Peiyan Zhu, Zahra Dezhahang and Yunjie Xu*

Department of Chemistry, University of Alberta, Edmonton, Alberta, Canada
*Tel:1-780-492-1244, Fax:1-780-492-8231, Email: yunjie.xu@ualberta.ca

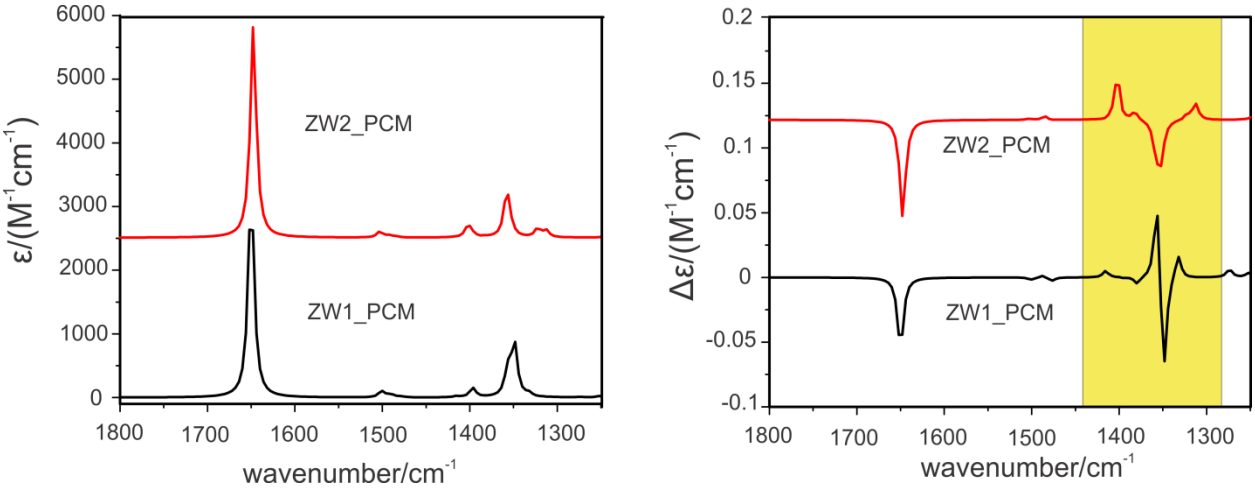


Figure D1. Comparison of the simulated VA and VCD spectra of ZW1 and ZW2 of leucine at the B3LYP/6-311++G(d,p) level with the PCM of water.

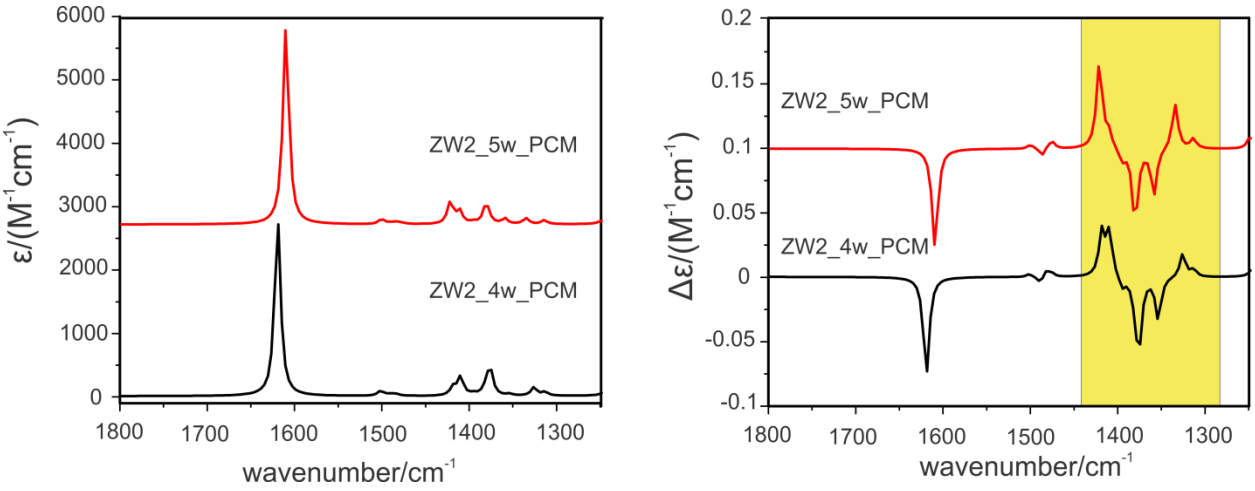


Figure D2. Comparison of the simulated VA and VCD spectra of ZW2_4w and ZW2_5w of leucine at the B3LYP/6-311++G(d,p) level with the PCM of water.

Table D1. Cartesian coordinates of ZW1 obtained at PCM/B3LYP/6-311++G(d,p)

| | | | |
|---|---|---|---|
| C | -2.31154100 | -0.24907400 | 1.35085400 |
| C | -1.91141300 | 0.22382900 | -0.05361400 |
| C | -2.95313900 | -0.21572500 | -1.09249800 |
| C | -0.51748500 | -0.28998100 | -0.46910300 |
| C | 0.66384800 | 0.22746000 | 0.35109000 |
| N | 0.90121600 | 1.70646700 | 0.11874000 |
| C | 2.01867300 | -0.47484300 | -0.00374200 |
| O | 2.93623400 | 0.30351100 | -0.38922700 |
| O | 2.05402500 | -1.70821000 | 0.14049800 |
| H | -1.89815600 | 1.32227600 | -0.04945700 |
| H | -0.49666000 | -1.38034000 | -0.39312700 |
| H | -0.33812800 | -0.05119000 | -1.52489100 |
| H | 1.90874300 | 1.71368400 | -0.18242200 |
| H | 0.77644100 | 2.27813800 | 0.95282900 |
| H | -3.30749800 | 0.12011500 | 1.61001800 |
| H | -2.33665300 | -1.34304700 | 1.39778300 |
| H | -1.62307500 | 0.10410900 | 2.12311300 |
| H | 0.49084500 | 0.09548900 | 1.41885200 |
| H | 0.32035400 | 2.09539900 | -0.62413100 |
| H | -3.94637300 | 0.16034000 | -0.83260400 |
| H | -2.70218400 | 0.15556500 | -2.09024700 |
| H | -3.01189800 | -1.30821500 | -1.14498200 |

Table D2. Cartesian coordinates of ZW1-(water)$_4$ obtained at PCM/B3LYP/6-311++G(d,p)

| | | | |
|---|---|---|---|
| C | -2.40065200 | -2.05237300 | 1.31542600 |
| C | -2.14384200 | -1.63850700 | -0.14043100 |
| C | -2.58722200 | -2.74784100 | -1.10559100 |
| C | -0.66272600 | -1.29459200 | -0.40000000 |
| C | -0.10510200 | -0.08434700 | 0.35794500 |
| N | -0.70825000 | 1.20777100 | -0.13313000 |
| C | 1.43529100 | 0.03991100 | 0.18358800 |
| O | 1.84020200 | 1.04296600 | -0.46228200 |
| O | 2.11646200 | -0.87495100 | 0.69698100 |
| H | -2.75621900 | -0.75456100 | -0.35694200 |
| H | -0.04235900 | -2.15122800 | -0.12209900 |
| H | -0.50660400 | -1.13161100 | -1.47328100 |
| H | 0.07596200 | 1.69569900 | -0.60349000 |
| H | -1.06437200 | 1.80762000 | 0.62222200 |
| H | -3.45504600 | -2.30246700 | 1.46200100 |
| H | -1.80764000 | -2.93489200 | 1.57895900 |
| H | -2.15441000 | -1.25873300 | 2.02605600 |
| H | -0.31682100 | -0.16306700 | 1.42339300 |
| H | -1.50182200 | 1.10633300 | -0.78404600 |
| H | -3.64329600 | -2.99147000 | -0.96059700 |
| H | -2.45098600 | -2.44652600 | -2.14825200 |
| H | -2.00726100 | -3.66259500 | -0.94146500 |
| O | 4.83372700 | -0.99364200 | 0.57873700 |
| H | 5.07480600 | -1.83704200 | 0.18144300 |
| H | 3.84524800 | -0.98789500 | 0.61844200 |
| O | 4.59183800 | 1.42126000 | -0.93601400 |
| H | 4.91270500 | 0.62145800 | -0.48331600 |
| H | 3.62332100 | 1.35556400 | -0.81121800 |
| O | -3.30534600 | 1.75843000 | -1.20471800 |
| H | -3.55111900 | 2.26208600 | -1.98854100 |
| H | -3.33779900 | 2.38354600 | -0.46037200 |
| O | -2.55372000 | 3.00635100 | 1.26114600 |
| H | -2.35305600 | 3.94683200 | 1.34633300 |
| H | -3.02527500 | 2.77172900 | 2.07025100 |

Table D3. Cartesian coordinates of ZW1-(water)$_5$ obtained at PCM/B3LYP/6-311++G(d,p)

| | | | |
|---|---|---|---|
| C | 2.84809500 | -1.92875100 | -1.24887900 |
| C | 2.45171800 | -1.64340700 | 0.20635300 |
| C | 2.91796800 | -2.77966500 | 1.12848600 |
| C | 0.93113400 | -1.44108200 | 0.37215800 |
| C | 0.32153400 | -0.22214100 | -0.33572300 |
| N | 0.83949100 | 1.05596600 | 0.26522000 |
| C | -1.22581200 | -0.25997400 | -0.27465600 |
| O | -1.80450200 | 0.51219000 | 0.54060700 |
| O | -1.76344900 | -1.08151100 | -1.04872500 |
| H | 2.97119600 | -0.73194200 | 0.52870100 |
| H | 0.41324300 | -2.32231400 | -0.01739600 |
| H | 0.68633000 | -1.38119400 | 1.43877500 |
| H | 0.57567500 | 1.14272700 | 1.26414000 |
| H | 0.46273200 | 1.87825600 | -0.22429200 |
| H | 3.92756700 | -2.08347600 | -1.32834600 |
| H | 2.35190700 | -2.83455700 | -1.61367600 |
| H | 2.58752400 | -1.10878000 | -1.92306600 |
| H | 0.60687100 | -0.20489500 | -1.38743100 |
| H | 1.86440100 | 1.15246800 | 0.17048900 |
| H | 3.99865700 | -2.92604800 | 1.05038400 |
| H | 2.68084800 | -2.56656400 | 2.17476400 |
| H | 2.43161300 | -3.72318000 | 0.85849300 |
| O | -4.44637800 | -1.51275800 | -1.25856200 |
| H | -4.63067500 | -2.42034300 | -0.99468200 |
| H | -3.46764400 | -1.40144500 | -1.17530900 |
| O | -4.62800700 | 0.67949700 | 0.56749800 |
| H | -4.81529900 | -0.06833900 | -0.02678900 |
| H | -3.65024300 | 0.67720400 | 0.60110200 |
| O | 3.33184000 | 2.15912300 | -0.54359600 |
| H | 4.03564200 | 2.56739100 | -0.02744700 |
| H | 2.77414800 | 2.88794200 | -0.86696700 |
| O | 0.96104000 | 3.56566400 | -1.27751500 |
| H | 0.70363200 | 4.41231900 | -0.89178600 |
| H | 0.70483500 | 3.62129000 | -2.20659400 |
| O | -0.50920700 | 1.40605500 | 2.76924600 |
| H | -0.50841600 | 0.80418400 | 3.52164800 |
| H | -1.17950100 | 1.06157300 | 2.14067600 |

Table D4. Calculated normal mode frequencies and the related rotational strengths (R), electric strengths (D), and the ratios ($\varsigma$)[a] between the magnetic and electric dipole vectors of ZW1-(water)$_5$ in the PCM of water at the B3LYP/6-311++G(d,p) level.

| Mode | Freq ($cm^{-1}$) | R ($x10^{-44}$ $esu^2$ $cm^2$) | D ($1x0^{-40}$ $esu^2$ $cm^2$) | $\varsigma$=R/D (ppm) |
|---|---|---|---|---|
| ZW1-(water)$_5$ PCM | | | | |
| 70 | 1338.54 | 56.3147 | 39.134 | 143.90 |
| 71 | 1358.63 | -96.9797 | 164.4457 | -58.97 |
| 72 | 1375.08 | -32.6602 | 438.0435 | -7.46 |
| 73 | 1388.79 | 24.3747 | 117.4032 | 20.76 |
| 75 | 1410.39 | 60.5349 | 671.3769 | 9.02 |
| 82 | 1610.46 | -74.0573 | 2837.5508 | -2.61 |

[a] Góbi and Magyarfalvi (S. Góbi, G. Magyarfalvi, Phys. Chem. Chem. Phys., 2011, 13, 16130-16133) suggested to $\varsigma$= 10 ppm as a soft limit for robust mode.

# Appendix E

## Contributed Journal Papers

CHEMPHYSCHEM

DOI: 10.1002/cphc.201101003

# Conformations of Serine in Aqueous Solutions as Revealed by Vibrational Circular Dichroism

Peiyang Zhu,[a] Guochun Yang,[a, b] Mohammad Reza Poopari,[a] Zhi Bie,[a] and Yunjie Xu*[a]

Vibrational circular dichroism (VCD) spectroscopy is utilized to reveal the detailed conformational distributions of the dominant serine species in aqueous solutions under three representative pH conditions of 1.0, 5.7, and 13.0, together with vibrational absorption (VA) spectroscopy, density functional theory (DFT), and molecular dynamics simulation. The experimental VA and VCD spectra of serine in $H_2O$ and $D_2O$ in the fingerprint region under three pH values are obtained. DFT calculations at the B3LYP/6-311++G(d,p) level are carried out for the protonated, zwitterionic, and deprotonated serine species. The lowest-energy conformers of all three species are identified and their corresponding VA and VCD spectra simulated. A comparison between the gas-phase simulations and the experimental VA and VCD spectra suggests that one or two of the most stable conformers of each species contribute predominantly to the observed data, although some discrepancies are noted. To account for the solvent effects, both the polarizable continuum model and the explicit solvation model are considered. Hydrogen-bonded protonated, zwitterionic, and deprotonated serine–$(water)_6$ clusters are constructed based on radial distribution function analyses and molecular dynamics snapshots. Geometry optimization and VA and VCD simulations are performed for these clusters at the B3LYP/6-311++G(d,p) level. Inclusion of the explicit water molecules is found to improve the agreement between theory and experiment noticeably in all three cases, thus enabling conclusive conformational distribution analyses of serine in aqueous solutions directly.

## 1. Introduction

Amino acids are bifunctional compounds which contain an amine and a carboxylic acid group and have a side chain that varies among different amino acids.[1,2] They are essential in life since they serve as building blocks of proteins and also often as intermediates in metabolism. Amino acids have attracted considerable attention from computational chemists because they contain a variety of intramolecular interactions and exhibit conformational topologies that are commonly found in biological systems, and because they are amenable to high-level ab initio calculations.[3–6]

Serine is one of the 20 naturally occurring amino acids and contributes significantly to the structures of proteins since it readily forms several hydrogen bonds with other protein side groups.[7,8] Recently, new attention has been paid to serine from both the experimental and theoretical sides. Gronert and O'Hair had reported probably the most complete theoretical investigation of the potential energy surface of a neutral serine monomer. These authors surveyed a starting set of 324 conformers based on all possible combinations of the so-called single-bond rotamers.[3] In a subsequent Fourier transform (FT) infrared (IR) Ar-matrix study of the neutral serine monomer, Lambie et al.[9] interpreted their experimental data by using the simulated IR spectra of several lowest-energy neutral conformers identified in ref. [3]. More recently, a number of theoretical studies[10–12] predicted the gas-phase basicities and acidities of serine. An IR multiphoton dissociation spectrum of protonated serine in the gas phase was also reported.[13] Serine has also been intensively investigated by using mass spectrometry in the search for the origin of homochirality of life, because the protonated serine octamers demonstrate a strong preference for homochirality.[14] Vibrational circular dichroism (VCD) spectra of serine in the C–H stretching region were reported and interpreted within the framework of the ring-current mechanism.[15] More recently, an FTIR study of serine in water under neutral pH conditions showed that the experimental vibrational absorption (VA) spectrum was consistent with that of a zwitterionic form of serine.[10] So far, no detailed conformational distribution analyses of serine in aqueous solution under different pH conditions have been published.

From a biological point of view, it would be of substantial interest to gain accurate insights into the conformational properties of serine in water and its intermolecular hydrogen-bonding interactions with water since water is ubiquitous in life.[16–18] VCD spectroscopy has experienced significant advances in both the experimental and theoretical modeling aspects in recent years.[19,20] Its high sensitivity to conformational changes of a chiral molecule, and to explicit hydrogen-bond-

[a] P. Zhu, Prof. Dr. G. Yang, M. R. Poopari, Z. Bie, Prof. Dr. Y. Xu
Department of Chemistry
University of Alberta
Edmonton, Alberta, T6G 2G2 (Canada)
E-mail: yunjie.xu@ualberta.ca

[b] Prof. Dr. G. Yang
Department of Chemistry
Northeast Normal University
Changchun 130024, Jilin (China)

Supporting information for this article is available on the WWW under http://dx.doi.org/10.1002/cphc.201101003.

ing interactions with solvent molecules such as water, makes it a powerful new spectroscopic tool to investigate the important structural properties of chiral molecules directly in aqueous solution.[21–26] Furthermore, the concept of "robust modes" had been developed to better understand the sensitivity of simulated VCD modes, in particular those related to chirality transfer by a relatively weak intermolecular interaction, with respect to different combinations of functionals and basis sets.[27] In the present study, we utilized VCD and VA spectroscopy in the fingerprint region together with DFT to investigate the conformations of the dominant serine species under three representative pH values in both water and deuterated water. To account for the solvent effects, the polarizable continuum model (PCM)[28,29] and the explicit serine–water intermolecular hydrogen-bonding interactions were examined. Comparisons between the simulated and experimental VA, and in particular VCD spectra recorded in $H_2O$ and $D_2O$, provide the decisive discrimination for reaching conclusions about the conformational distributions and the importance of the hydrogen bonding with water.

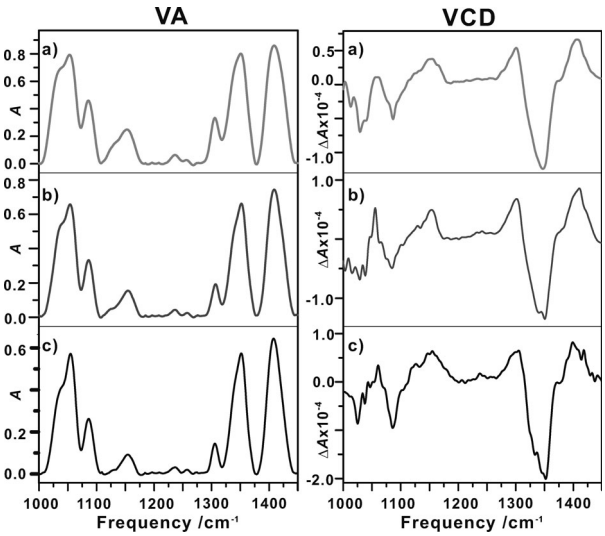


**Figure 1.** Experimental VA and VCD spectra of L-serine in water at three different concentrations: a) 3.0, b) 2.0, and c) 1.0 M.

## 2. Results and Discussion

### Experimental VA and VCD Spectra

To estimate the degree of self-aggregation of L-serine in water in the concentration range relevant to the current study, the concentration dependence of the VA spectra in water was measured first. The VA spectra in the frequency region from 1000 to 1450 $cm^{-1}$ with eight different concentrations ranging from 0.1 M to the saturated solution are shown in Figure S1 in the Supporting Information. Because of the strong $H_2O$ absorption at $\approx$1600 $cm^{-1}$, the useful region is 1000–1450 $cm^{-1}$ with $H_2O$ as solvent. No noticeable band shifts or new bands have been observed, and the intensities of peaks increase linearly with increasing concentration. This suggests that no severe self-aggregation occurs in the concentration range used and additionally that the dominant conformations have not changed. To further verify this conclusion, the VCD spectra at the three representative concentrations of 1.0, 2.0, and 3.0 M were measured and are provided in Figure 1. Again, the VCD spectral features at the three concentrations appear to be very similar, further supporting the VA conclusion.

While a naturally occurring amino acid exists mostly in its neutral form ($H_2N$-CHR-COOH) in the gas phase and in a nonpolar solvent, it exists primarily as ionic species in water and undergoes dissociation equilibria based on the acid dissociation constants of the amino and carboxylic acid functional groups. Such equilibria can be shifted by varying the pH of the solution. In strongly acidic or basic aqueous solutions, the protonated or deprotonated forms can be expected to dominate, respectively, whereas zwitterions ($^+H_3N$-CHR-$COO^-$) are typically the most abundant species in water at a neutral pH and in crystals. The experimental dissociation constants, p$K_a$, of serine, are 2.21 and 9.15,[30] which correspond to the dissociation of the COOH group and $NH_3^+$ group, respectively. One would therefore expect the protonated and the deprotonated species to become dominant at the pH of 1.0 and 13.0, respectively, whereas zwitterions are the dominant species at a pH value close to 7.

The VA and VCD measurements in $H_2O$ at the pH values of 1.0 and 13.0 are provided in Figure 2, together with the corresponding measurements at neutral pH. There are a number of noticeable differences in the VA and VCD spectra at different pH values. In the 1300–1450 $cm^{-1}$ region, the dominant VA bands are quite similar for all three pH values. In the 1200–1300 $cm^{-1}$ region, one of the most obvious differences in the VA spectra is the appearance of a new strong VA feature at $\approx$1258 $cm^{-1}$ with a shoulder at 1244 $cm^{-1}$ at pH 1, which is not there at either pH 13 or neutral pH. In the 1100–1200 $cm^{-1}$ region, the band at $\approx$1154 $cm^{-1}$ at both pH 1 and neutral pH

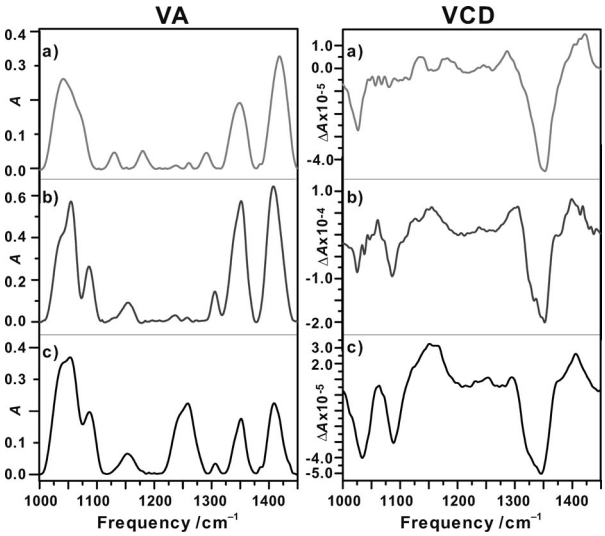


**Figure 2.** Comparisons of the experimental VA and VCD spectra of L-serine in $H_2O$ at three different pH values: a) 13.0, b) 5.68 (denoted as "neutral" in the text; see the Experimental Section for details), and c) 1.0.

  

is replaced by two bands at ≈1130 and 1178 $cm^{-1}$ in pH 13 solution. Also at pH 13, the shape of the dominant feature in the 1000–1100 $cm^{-1}$ region differs noticeably from that at pH 1 or at the neutral pH. In the corresponding VCD spectra, one of the most noticeable differences is the disappearance of the negative VCD feature at ≈1187 $cm^{-1}$ at pH 13. Interestingly, except for the aforementioned differences at pH 1 and neutral pH, the main VA and VCD spectral features in the 1000–1100 and 1300–1450 $cm^{-1}$ regions actually look similar in terms of their relative intensities and their peak frequencies, which correspond within 1 $cm^{-1}$. This suggests that the same zwitterionic species that exist at the neutral pH are at least partly responsible for these peaks at pH 1.

The related VA and VCD measurements in $D_2O$ at these three different pD values are summarized in Figure 3. In the

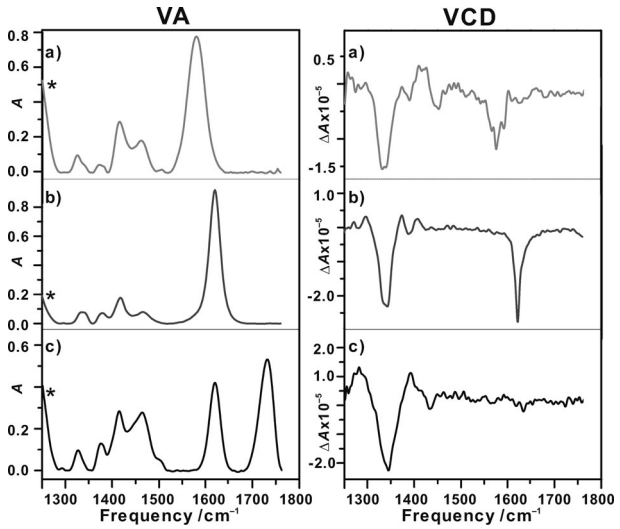


**Figure 3.** Comparisons of the experimental VA and VCD spectra of L-serine in $D_2O$ at three different pD values: a) 13.0, b) 5.68, and c) 1.0. * is due to the strong $D_2O$ bending band.

1550–1800 $cm^{-1}$ region, the peak at 1620 $cm^{-1}$ in the neutral $D_2O$ measurement is assigned to the asymmetric stretch of $CO_2^-$, that is, $\nu_{as}(CO_2^-)$, of the serine zwitterions, whereas the peak at 1579 $cm^{-1}$ at pH 13 corresponds to $\nu_{as}(CO_2^-)$ of the deprotonated serine ionic species. There are two VA bands in this region for the pH 1 solution. One at 1731 $cm^{-1}$ is clearly the carbonyl stretch of COOD, while the other at exactly the same frequency as in the neutral pH solution could be confidently assigned to $\nu_{as}(CO_2^-)$. The above VA assignment indicates that the deprotonated and zwitterionic species are the only dominant species at pH 13 and at neutral pH, respectively, whereas both protonated and zwitterionic species coexist at pH 1. This corroborates the conclusion reached with the $H_2O$ measurements discussed above. Using the semiempirical program SPARC[31] or a simple p$K_a$ calculation, a mixture of about 11% zwitterionic and 89% protonated serine species was predicted at pH 1, further supporting the above experimental conclusion.

The detailed assignments of the VA bands in the frequency region from 1000–1500 $cm^{-1}$ in $H_2O$ and 1200–1500 $cm^{-1}$ in $D_2O$ are less obvious. This is the region where the bending, scissoring, wagging, and rocking modes of the CH, $CH_2$, $NH_2$, and $NH_3^+$ groups are expected, as well as those related to the skeleton modes. Although some empirical assignments can be achieved tentatively by comparison to molecules with the same functional groups, there is substantial room for alternative assignments because it is very difficult to foresee the effects due to the conformational flexibility and the water solvent.

It is essential to apply theoretical modeling to unravel the conformational complexity and the effects of water on the observed VA and VCD spectra in order to conclusively identify the conformations of the dominant species of serine in water. In particular, the VCD features are highly sensitive to conformational changes and hydrogen bonding with water.[21,24–26] The assignments of the VA and VCD bands, and the dominant conformations, will thus be discussed below in the context of the VA and VCD simulations.

### Simulations of the VA and VCD Spectra of the Monomeric Conformers of Neutral, Zwitterionic, Protonated, and Deprotonated Serine

In the present work, the geometry optimization of the L-serine neutral monomer was carried out at the B3LYP/6-311++G(d,p) level with the starting geometries taken from ref. [3] with a smaller basis set. The 12 lowest-energy conformers of the serine monomer were obtained and are shown in Figure S2 in the Supporting Information, together with the Boltzmann populations based on their relative Gibbs free energies at 298 K. The corresponding calculated VA and VCD spectra of the four most stable conformers are provided in Figure 4. Although it is difficult to discount the contributions of the neutral serine conformers based on the comparison of the experimental and theoretical VA spectra, the calculated VCD features of these most stable conformers, with an overall population of ≈80%, on the other hand, differ significantly from the experimental ones under the three different pH conditions. In contrast, the experimental VA spectrum of serine in cold Ar matrix was reported to be well reproduced with several lowest-

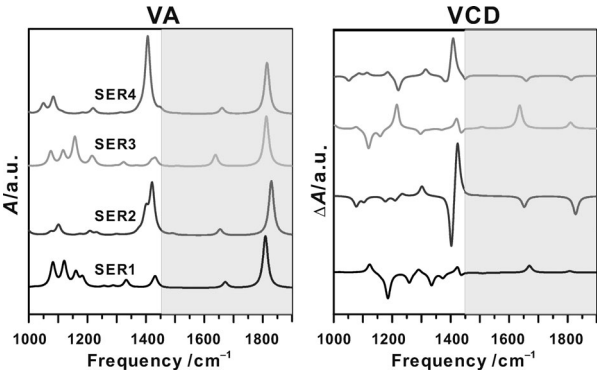


**Figure 4.** Simulated VA and VCD spectra of the four most stable neutral serine conformers at the B3LYP/6-311++G(d,p) level. The wavenumber regions relevant to the experimental data are left unshaded.

  

energy neutral serine conformers at the B3LYP/6-31++G(d,p) level.[9]

In the following, we will discuss the theoretical VA and VCD spectra of the lowest-energy serine conformers of the three ionic species mentioned above, together with the corresponding species with deuterium substitution at the COOH, OH, and $NH_2$ or $NH_3^+$ group. The calculated results were compared with the corresponding experimental data in $H_2O$ and $D_2O$ to extract information about the most important serine conformers under each pH condition. The results will be presented in the following order: from the neutral, to the basic, and finally to the acidic condition.

The optimized geometries of the four lowest-energy conformers of the zwitterionic, deprotonated, and protonated forms of the serine monomer are shown in Figure 5, together with their Boltzmann population factors calculated based on their relative Gibbs free energies. The preferred site for deprotonation in the standard amino acids is typically the carboxyl group, although a recent theoretical calculation proposed that the most acidic site of cysteine is at the thio group.[32] In the four most stable protonated conformers, the amino group is protonated, as expected for a standard amino acid.[33] The important intermolecular bond distances are also indicated in Figure 5.

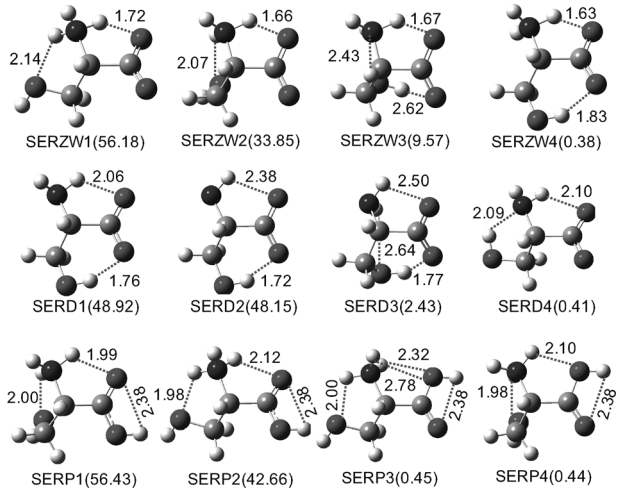


**Figure 5.** Optimized geometries of the four lowest-energy conformers of the zwitterionic, deprotonated, and protonated monomeric serine conformers at the B3LYP/6-311++G(d,p) level. The numbers in parentheses are the percentage populations at room temperature for each species separately based on the relative Gibbs free energies. The intermolecular hydrogen-bond and secondary hydrogen-bond lengths are indicated. In the latter cases, the H···O bond lengths are larger than ≈2 Å and shorter than 3 Å.

The predicted VA and VCD spectra of the four most stable conformers of the zwitterionic form of serine are depicted in Figure 6a. The initial inspection based on the VA spectra suggested that SERZW1 provides the best agreement with the experimental data, although SERZW2 and 3 also show some resemblance to the experimental data. Based on the simulated VA spectrum of SERZW1, the experimental spectrum from the 1000–1450 $cm^{-1}$ region could be assigned as follows. The

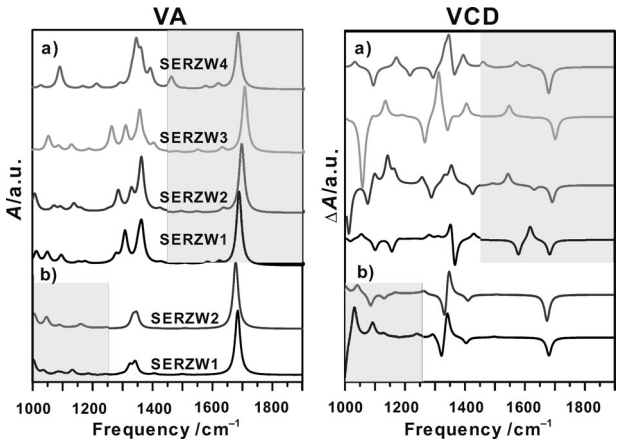


**Figure 6.** Simulated VA and VCD spectra of a) the four most stable zwitterionic serine conformers and b) the two most stable deuterated zwitterionic serine conformers at the B3LYP/6-311++G(d,p) level. See text for discussions on the deuterated species. The wavenumber regions relevant to the experimental data are left unshaded.

three overlapped experimental peaks at 1038, 1054, and 1086 $cm^{-1}$ correspond to the C–N stretching with some contribution from the O–H bending, the C–O stretching, and a mixture of N–H and C–H rocking modes, respectively, based on the GaussView visualization. The experimental band at 1154 $cm^{-1}$ was tentatively assigned to a mixture of C–H, O–H, and N–H rocking modes. Finally, the three peaks at 1306, 1352, and 1408 $cm^{-1}$ in the higher-wavenumber end of the spectrum are related to the modes dominated by the C–H bending, N–H bending, and a mixture of C–H and N–H bending, respectively. Although at first glance the theoretical VCD spectrum of SERZW1 shows dominant VCD features in reasonable agreement with the experimental data, some discrepancies in the peak frequencies of the VA and VCD spectra were noted. This point will be further discussed in the implicit and explicit solvation section below.

The simulated VA and VCD spectra of the deuterated zwitterionic serine conformers are provided in Figure 6b. The strong experimental band at 1620 $cm^{-1}$ could be unambiguously assigned to the asymmetric stretching of $CO_2^-$. The experimental VA and VCD features for this band were well reproduced theoretically. On the other hand, neither the multiple VA peaks observed experimentally in the 1250–1550 $cm^{-1}$ region nor the corresponding strong VCD features were as well reproduced theoretically. The possible cause for such discrepancies is most likely the strong hydrogen-bonding interactions between serine and water molecules.

To understand the VA and VCD spectra at pH 13, the VA and VCD spectra of the four most stable deprotonated serine conformers were simulated and are depicted in Figure 7a. Based on the VA spectrum of SERD1, the severely overlapped bands at 1041 and 1072 $cm^{-1}$ in the experimental VA spectrum could be assigned to a mixture of the C–H and N–H rocking modes, and the C–O stretching mode, respectively. The band at 1131 $cm^{-1}$ was tentatively assigned to the C–N stretching mode, and the band at 1178 $cm^{-1}$ to a mixture of C–H bending and $NH_2$ twisting together with a little bit of O–H bending.

  

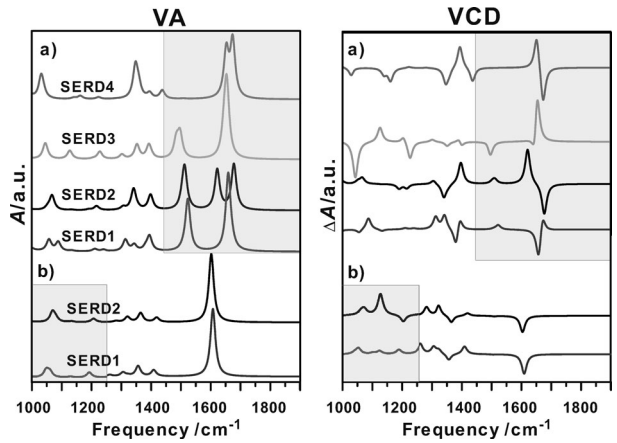


**Figure 7.** Simulated VA and VCD spectra of a) the four most stable deprotonated serine conformers and b) the two most stable deuterated deprotonated serine conformers at the B3LYP/6-311++G(d,p) level. See text for discussions on the deuterated species. The wavenumber regions relevant to the experimental data are left unshaded.

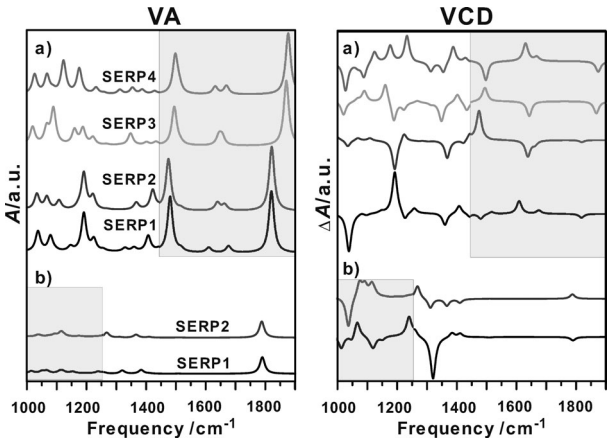


**Figure 8.** Simulated VA and VCD spectra of a) the four most stable protonated serine conformers and b) the two most stable deuterated protonated serine conformers at the B3LYP/6-311++G(d,p) level. See text for discussions on the deuterated species. The wavenumber regions relevant to the experimental data are left unshaded.

Only two bands were predicted for SERD1 in the 1000–1100 $cm^{-1}$ region versus three for SERZW1, consistent with the fact that the third VA peak at 1086 $cm^{-1}$ at neutral pH was not observed experimentally at pH 13. The assignment of the three peaks in the 1300–1400 $cm^{-1}$ region is similar to that of SERZW1. The corresponding complex VCD features in the same wavenumber region were well reproduced theoretically, whereas the VCD features in the 1000–1100 $cm^{-1}$ region were not well captured.

The deuterated forms of both SERD1 and SERD2 show similar VA and VCD spectral features (Figure 7b) that resemble the experimental ones in $D_2O$ closely. The simulation confirmed the assignment of the strong VA band at 1578 $cm^{-1}$ to the asymmetric stretching band of $CO_2^-$. The theoretical predictions also captured the experimentally observed red shift of $\approx$42 $cm^{-1}$ upon going from the neutral solution to pH 13 nicely, with a theoretical red shift of $\approx$73 $cm^{-1}$ (unscaled). Furthermore, the negative VCD feature at this wavenumber was well reproduced by the theoretical prediction. Finally, the strongly negative VCD band at 1343 $cm^{-1}$ observed experimentally was also captured theoretically.

In Figure 8a, the simulated VA and VCD spectra of the four most stable protonated serine conformers are depicted. The extra experimental VA features at pH 1, with a peak frequency at 1258 $cm^{-1}$ and a shoulder at 1244 $cm^{-1}$, were captured with both SERP1 and SERP2 conformers, whereas such features were not predicted with either SERZW1 or SERZW2. These bands are associated with the O–H bending modes in COOH and COH. For the deuterated species, the simulated VA and VCD spectra are given in Figure 8b. The VA measurement in $D_2O$ shows a well-isolated peak at 1731 $cm^{-1}$, which corresponds to the carbonyl stretching modes of COOD in SERP1 and/or SERP2 which were predicted to be at essentially the same wavenumber. The experimental VA peak at 1620 $cm^{-1}$ is due to antisymmetric $CO_2^-$ stretching, that is, $\nu_{as}(CO_2^-)$, of the zwitterionic species, keeping in mind that the zwitterionic species coexists at this pH. The experimentally observed red shift of 111 $cm^{-1}$ from $\nu_{as}$(COOD) to $\nu_{as}(CO_2^-)$ was correctly predicted theoretically with a value of 110 $cm^{-1}$ using SERP1 and SERZW1. At the same time, weak- to medium-intensity VCD signals with opposite signs were predicted for these SERP1 and SERP2 conformers. If both conformers are similarly populated as predicted, one would expect no VCD signal at this wavenumber. This is exactly what was observed experimentally. Furthermore, the experimentally observed trisignate (+−+) VCD feature at 1343 $cm^{-1}$ could be reproduced by SERP1.

The above discussions show that one can extract information about the most important conformers of the zwitterionic, deprotonated, and protonated species of serine under the three different pH conditions, based on the gas-phase calculations of these species. That being said, it is noted that in some cases, the agreements between experimental and theoretical data are only marginal. It is well known that solvent can have severe effects on the experimental VA and VCD spectra. In particular, the solute-induced chirality effects on solvent have been demonstrated in a number of molecular systems.[20,21,24–26] It is therefore desirable to include water in the spectral simulation.

One way to accomplish this is to use the continuum solvent models, such as PCM. On the other hand, the explicit hydrogen bonding with water molecules has been shown to be important in reproducing the experimental VA and VCD data, and consequently in extracting important information about the conformations of the dominant species in solution. Therefore, in the following we will compare the results using both approaches with the experimental data obtained in $H_2O$ and $D_2O$ solutions.

### Explicit and Continuum Solvation Models of Zwitterionic, Deprotonated, and Protonated Serine with Water

The radial distribution functions (RDFs) obtained from molecular dynamics (MD) simulations (details at the end of the article) are plotted in Figure S3 in the Supporting Information, togeth-

  

er with the atom labeling, to provide some general information about the number of water molecules directly hydrogen-bonded to serine. For example, the RDF $g_{N1Ow}(r)$ provides information about the distribution of the oxygen atom of water from the selected origin, that is, the N atom of serine, as a function of the distance, $r$, between them. The first maximum of $g_{N1Ow}(r)$ appears at 2.85 Å, and the integration to the next minimum gives a value of 3.16, which corresponds to three water molecules in the first shell surrounding the N atom of serine. Similarly, there are about 2.59 and 2.75 water molecules surrounding O2 and O3 (see Figure S3 in the Supporting Information) of serine, the other two hydrogen-bonding sites of serine. A closer look at the MD snapshots revealed that some water molecules surrounding N1, O2, and O3 are counted twice. Therefore, based both on the RDF analysis and MD snapshots, we decided to solvate each serine species with six water molecules.

The two most stable monomeric serine conformers of each species have a combined population of 90 to 97% in all three cases of interest. We therefore added six water molecules to these two most stable conformers in each category to build serine–$(water)_6$ clusters. The possible starting geometries were generated by using the MD snapshots, by maximizing the formation of cyclic hydrogen-bonding rings, and by considering the hydrogen-bonding capability of each functional group in serine. The theoretical results reveal that the geometry of the serine core does change slightly upon solvation with water. The relative energies and Gibbs free energies of the six most stable zwitterionic, deprotonated, and protonated serine–$(water)_6$ clusters are summarized in Table 1, together with their percentage Boltzmann populations at room temperature. The geometries of the five most stable clusters of the solvated zwitterionic, deprotonated, and protonated serine are depicted in Figure 9. In the following discussions, we used the comparison of the unique experimental and theoretical spectral features to guide our assignments of the most important species in solution. The theoretical relative Gibbs free energies were utilized only as a rough guide since the DFT free energy values are typically only reliable to a few kcal mol$^{-1}$.

For the neutral pH experiment, the simulated VA and VCD spectra of the five zwitterionic serine–$(water)_6$ conformers are provided in Figure 10a, together with the experimental data in $H_2O$ and the corresponding PCM simulations of SERZW1 and SERZW2 in $H_2O$ for comparison. Considering the VA and in particular the VCD features, 6ZW5 provides the best agreement with the experimental data. The more detailed assignments of the dominant bands are indicated by arrows in Figure 10a. It is worth noting that the bands which have the same peak frequencies in the experimental VA and the corresponding VCD spectra could now be well correlated with those which also have the same peak frequencies in the simulated VA and VCD spectra. This was not exactly the case when the gas-phase

**Table 1.** Relative total energies $\Delta E$ [kcal mol$^{-1}$] and relative Gibbs free energies $\Delta G$ [kcal mol$^{-1}$] of zwitterionic, deprotonated, and protonated serine–$(water)_6$ clusters at the B3LYP/6-311++G(d,p) level of theory and their percentage Boltzmann distributions ($B_f$) at room temperature.

| System | $\Delta E$ | $B_f(\Delta E)$ | $\Delta G^\circ$ | $B_f(\Delta G^\circ)$ |
|---|---|---|---|---|
| *jbn* | | | | |
| 6ZW1 | 0.12 | 44.04 | 0 | 50.03 |
| 6ZW2 | 2.16 | 1.38 | 0.35 | 27.55 |
| 6ZW3 | 0 | 54.26 | 0.60 | 18.05 |
| 6ZW4 | 3.06 | 0.31 | 1.52 | 3.81 |
| 6ZW5 | 5.04 | 0.01 | 2.80 | 0.44 |
| 6ZW6 | 6.47 | ≈0 | 4.41 | 0.03 |
| 6DEP1 | 0.98 | 11.83 | 0 | 39.84 |
| 6DEP2 | 1.64 | 3.87 | 0.31 | 23.60 |
| 6DEP3 | 0.62 | 21.81 | 0.38 | 21.00 |
| 6DEP4 | 0 | 61.66 | 0.68 | 12.56 |
| 6DEP5 | 3.62 | 0.14 | 1.59 | 2.73 |
| 6DEP6 | 3.21 | 0.27 | 3.21 | 0.18 |
| 6PRO1 | 0.91 | 5.96 | 0 | 57.74 |
| 6PRO2 | 0.75 | 7.77 | 0.49 | 24.87 |
| 6PRO3 | 0 | 54.83 | 1.05 | 9.85 |
| 6PRO4 | 0.41 | 27.48 | 1.54 | 4.26 |
| 6PRO5 | 1.20 | 3.63 | 1.72 | 3.15 |
| 6PRO6 | 3.17 | 0.13 | 4.05 | 0.06 |

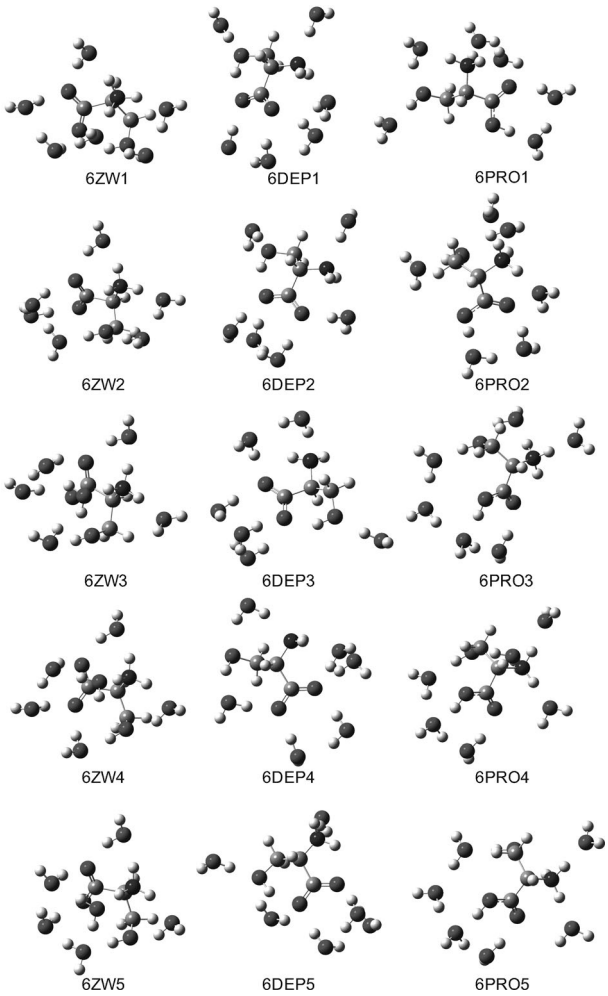


**Figure 9.** Optimized geometries of the five most stable zwitterionic, deprotonated, and protonated serine–$(water)_6$ clusters at the B3LYP/6-311++G(d,p) level.

  

SERZW1 VA and VCD features were used to explain the observed spectra. So the inclusion of explicit serine–water interactions provides better agreement between theory and experiment. The agreement between the experimental data and the PCM simulations of the two SERZW conformers, on the other hand, is poor.

The VA and VCD simulations for the five corresponding deuterated zwitterionic serine–$(D_2O)_6$ conformers are provided in Figure 10b, together with the experimental data in $D_2O$ and the corresponding PCM simulations of the deuterated SERZW1 and SERZW2 in $D_2O$ for comparison. Again, the 6ZW5 conformer provides the best agreement with the experimental data. Specifically, it captured the main VA and VCD features, although the experimental VCD feature centered at about 1337 $cm^{-1}$ was not so well reproduced. Overall, it is satisfying to see that the explicit solvation of the 6ZW5 conformer provides good agreements with both the VA and VCD experimental data in $H_2O$ and $D_2O$.

For the experiment at pH 13, the simulated VA and VCD spectra of the four most stable deprotonated serine–$(water)_6$ conformers are provided in Figure 11a, together with the experimental data in $H_2O$ and the related PCM simulations of SERD1 and SERD2 for comparison. The related simulated VA and VCD spectra of the four most stable deprotonated deuterated serine–$(D_2O)_2$ conformers are provided in Figure 11b, together with the experimental data in $D_2O$ and the related PCM

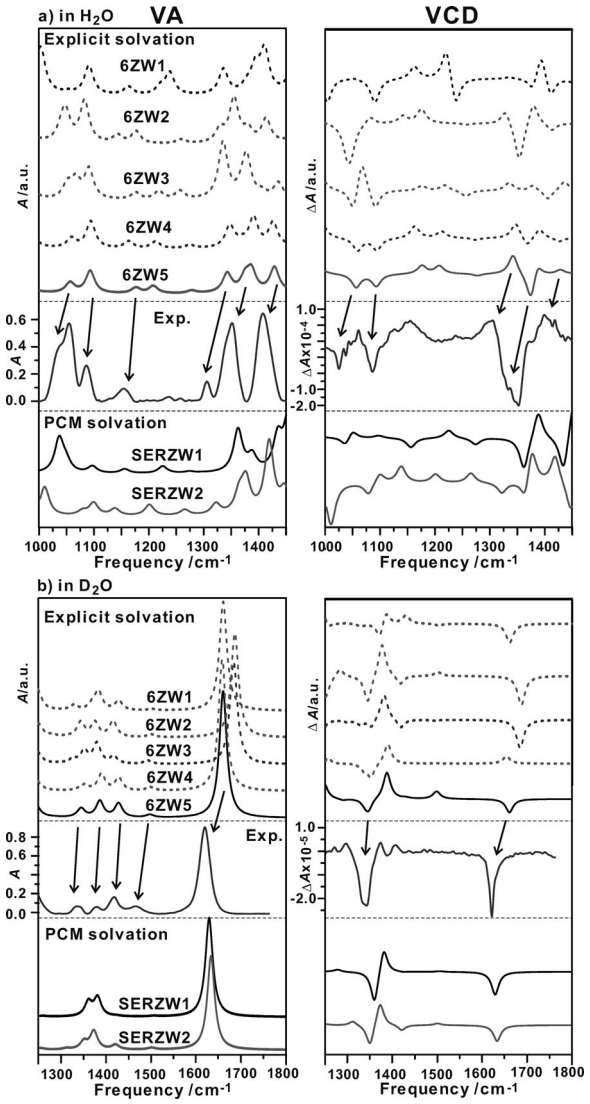


**Figure 10.** a) Comparisons of the simulated VA and VCD spectra of the five most stable zwitterionic serine–$(water)_6$ conformers with the related experimental data in water at neutral pH. The corresponding simulated VA and VCD spectra of SERZW1 and SERZW2 in the PCM of water are depicted at the bottom. b) Comparisons of the simulated VA and VCD spectra of the five most stable deuterated zwitterionic serine–$(D_2O)_6$ conformers with the related experimental data in $D_2O$ at neutral pH. The corresponding simulated VA and VCD spectra of the deuterated SERZW1 and SERZW2 in the PCM of $D_2O$ are depicted at the bottom.

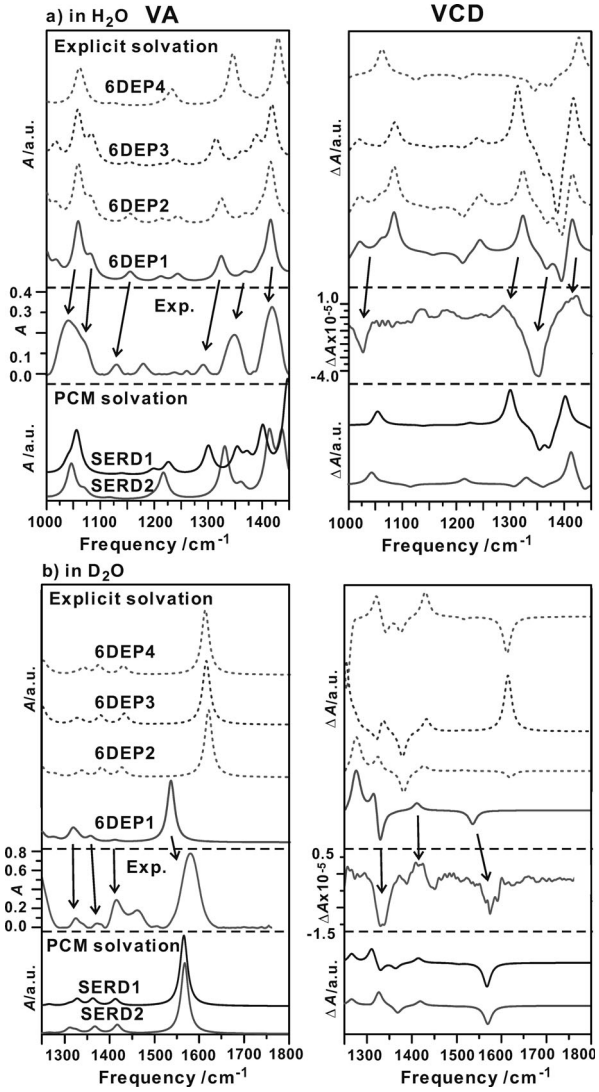


**Figure 11.** a) Comparisons of the simulated VA and VCD spectra of the four most stable deprotonated serine–$(water)_6$ conformers with the related experimental data in water at pH 13. The corresponding simulated VA and VCD of SERD1 and SERD2 in the PCM of water are depicted at the bottom. b) Comparisons of the simulated VA and VCD spectra of the four most stable deuterated deprotonated serine–$(D_2O)_6$ conformers with the related experimental data in $D_2O$ at pH 13. The corresponding simulated VA and VCD spectra of the deuterated SERD1 and SERD2 in the PCM of $D_2O$ are depicted at the bottom.

  

simulations for comparison. Taking into account both the normal and the deuterated species in the theory–experiment comparison, the explicit-solvated 6DEP1 conformer provides the best overall agreement with all the available experimental data. The assignments for the dominant spectral features are indicated by arrows in Figure 11.

For the experiment at pH 1, the simulated VA and VCD spectra of the four protonated serine–$(water)_6$ conformers are provided in Figure 12a, together with the experimental data in $H_2O$ and the related PCM simulations of SERP1 and SERP2 for comparison. Since the theoretical VA and VCD features do not differ dramatically from one conformer to the next, we also present the population-weighted VA and VCD spectra, labeled as 6PRO Av. As discussed above, it is necessary to consider the zwitterionic species to explain the observed spectra. An empirical weighting ratio of 50:50% for 6ZW5 and 6PRO Av was used to simulate the ZW+PRO VA and VCD spectra in Figure 12a. With this approach, most of the experimental VA and VCD features could be explained and the corresponding assignments are indicated by arrows. We would like to caution against taking this empirical 1:1 weighting ratio too literally since the spectra presented herein are complicated with some severely overlapped lines. Even small frequency shifts in the simulated VA peaks can result in a noticeable change in the intensities of the overlapped peaks and therefore this estimated ratio. The PCM VA spectra of SERP1 and SERP2 fail to reproduce the strong extra VA feature observed experimentally at 1258 $cm^{-1}$ when changing from the neutral pH to pH 1. At the same time, the simulated VCD spectra with PCM show poor correlation to the observed data.

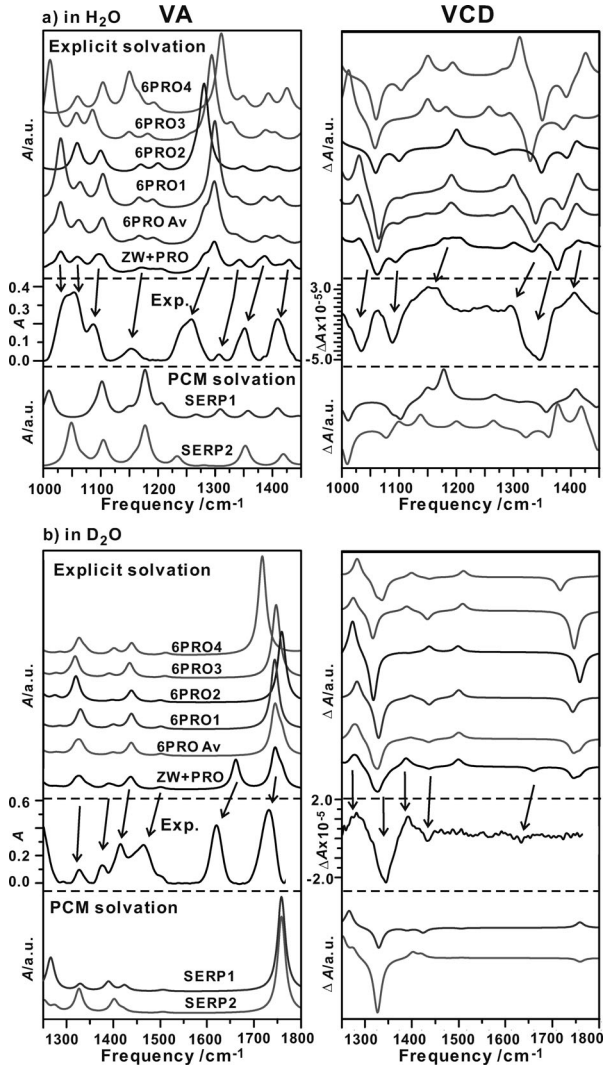


**Figure 12.** a) Comparisons of the simulated VA and VCD spectra of the four most stable protonated serine–$(water)_6$ conformers with the related experimental data in water at pH 1. The population-weighted VA and VCD spectra of the protonated species and the simulated VA and VCD spectra with a combination of zwitterionic and protonated species are also provided. See text for detailed discussions. The corresponding simulated VA and VCD spectra of SERP1 and SERP2 in the PCM of water are depicted at the bottom. b) Comparisons of the simulated VA and VCD spectra of the four most stable deuterated protonated serine–$(D_2O)_6$ conformers with the related experimental data in $D_2O$ at pH 1. The population-weighted VA and VCD spectra of the protonated species and the simulated VA and VCD spectra with a combination of zwitterionic and protonated species are also provided. The corresponding simulated VA and VCD spectra of the deuterated SERZP1 and SERP2 in the PCM of $D_2O$ are depicted at the bottom.

The related simulated VA and VCD spectra of the four most stable protonated deuterated serine–$(D_2O)_6$ conformers are provided in Figure 12b, together with the experimental data in $D_2O$ and the related PCM simulations for comparison. As with the normal species, the 6PRO Av and ZW+PRO VA and VCD spectra are also provided. Here an empirical ratio of 80:20% for 6PRO Av versus 6ZW5 was used to reproduce the experimentally observed ratio between the VA bands at 1620 and 1731 $cm^{-1}$. Again, the ZW+PRO VA and VCD spectra captured all the essential features observed experimentally. The related assignments are indicated by the arrows in Figure 12b. Considering both the normal and deuterated data, the explicitly solvated protonated and zwitterionic serine species with water have again provided an overall satisfactory explanation of the observed spectra. The implicit solvation with PCM in this particular case, on the other hand, was inadequate for a detailed VA and VCD spectral assignment.

## 3. Conclusions

The detailed conformational distributions of the dominant serine species under three representative pH values, that is, strongly acidic, near neutral, and strongly basic conditions, have been investigated using VA and VCD spectroscopy, together with ab initio calculations and MD simulations. Based on the gas-phase simulations of the most stable conformers of the protonated, deprotonated, and zwitterionic serine species, the experimental VA and VCD spectra could be reasonably interpreted, although some discrepancies have been noted. Inclusions of the water solvent by PCM and by the explicit serine–water hydrogen-bonding interactions have been performed. It was found that the inclusion of the serine–water hydrogen-bonding interactions improved the agreements between the experimental and simulated VA and VCD spectra noticeably in all the cases examined. The availability of the experimental VA and VCD spectra in both $H_2O$ and $D_2O$ was crucial for identifying the dominant conformers confidently. For a flex-

  

ible chiral molecule with multiple hydrogen-bonding sites, such as serine, inclusion of explicit solvent–solute hydrogen-bonding interactions is important for the precise interpretation of the solution VA and VCD spectra. This report demonstrates that VCD spectroscopy in combination with quantum chemistry and MD calculations is an attractive new spectroscopic tool to explore directly the mechanism of solvation of highly flexible chiral molecules and their conformational distributions in an aqueous environment.

## Experimental and Theoretical Details

Experimental Methods: An FTIR spectrometer, Vertex 70, connected to a VCD optical bench, PMA 50, was used to record the VA and VCD spectra. The details of the instrument were described before.[26] For the measurements described herein, a pair of $BaF_2$ windows (International Crystal Laboratories) with variable path lengths was used. For the VCD measurements, a collection time of 180 to 240 min and a 4 $cm^{-1}$ resolution were applied. L- (99%) and D-serine (98%) were purchased from Sigma–Aldrich and used without further purification. Doubly distilled water and $D_2O$ (99.99%) from Sigma–Aldrich were used as solvents. For the concentration dependence study, a series of VA spectra of L-serine in water was measured at concentrations ranging from 0.1 M to saturation and with a path length of 15 μm. To obtain reliable VCD measurements, it was highly desirable to maintain the VA absorption coefficients in the range of 0.2 to 0.8. To achieve this, the VCD spectra of L-serine at three representative concentrations of 1.0, 2.0, and 3.0 M were measured with a path length of 50, 25, and 15 μm, respectively. The VCD measurements of L-serine were corrected with the corresponding measurements of D-serine under identical experimental conditions to minimize any VCD artifacts.[34] No experiments were carried out with racemic solutions, given the fact that racemic serine has a much lower solubility in water.[35] The pH values of 1.0 and 13.0 were achieved by adding a highly concentrated 6 M HCl solution and NaOH solution, respectively, whereas a pH of 5.68 was obtained experimentally when no strong acid or base was added. For simplicity, this condition where no strong acid or base was added is referred to as "neutral" in the main text. Because the C=O stretching region is obscured by the strong absorption of water, further measurements in $D_2O$ under the three pH values mentioned above were also carried out. In this case, 0.5 M L-serine in $D_2O$ with a path length of 25 μm was used. For the pH 1.0 and 13.0 solutions, 6 M DCl and 6 M NaOD solutions were used to adjust the solution to the desired pD value, respectively, while a pD value of 5.68 was measured experimentally when no strong acid or base was added. The same VA and VCD correction procedures used for the $H_2O$ solutions were also applied to the $D_2O$ measurements.

MD Simulation: To survey the geometries of a large number of possible small serine–$(water)_N$ clusters and to aid the estimation of the number of water molecules explicitly hydrogen-bonded to a serine molecule in water, a MD simulation was carried out by using the Sander module in the AMBER9 suite of programs.[36] The AMBER *ff*99 force field[36] based on molecular mechanics and the TIP3P[37] water model were used in the simulation. An octagonal box with 21 serine molecules and 1001 water molecules, corresponding to the 1 M experimental concentration, was used in the simulation. The initial configuration was relaxed by applying 500 steps of steepest descent algorithm, followed by 500 steps of conjugate gradient algorithm to remove any bad contacts. To obtain the final configuration, the system was first heated from 0 to 298 K in 100 ps and was then equilibrated for 300 ps to ensure that the equilibrium was reached completely under NVT conditions. Finally, a 7 ns production MD simulation was performed under NPT conditions ($T=298$ K, $P=1$ atm) with a time step of 2 fs. The long-range electrostatic interactions were treated with the particle mesh Ewald summation method[38] and the SHAKE algorithm[39] was used to constrain all covalent bonds involving hydrogen atoms. For the noncovalent interactions, a 7 Å cutoff was introduced.

DFT Calculations: All final geometry optimizations, harmonic frequency calculations, and VA and VCD intensity predictions were performed at the B3LYP/6-311++G(d,p) level of theory, by using the Gaussian 03 program package.[40] The B3LYP[41,42] hybrid functional has been widely used in describing strong hydrogen-bonded complexes.[43–45] Its reliability in predicting VCD intensities has also been well documented.[46–49] The 6-311++G(d,p) basis set was chosen for its ability to successfully characterize hydrogen-bonded systems and to provide structures, and VA and VCD signatures, in good agreement with the experimental data for these types of molecules and complexes.[50–53] The tightest convergence criteria were used in the geometry optimizations to capture the small differences in bond length. To confirm that the optimized geometries were true minima, their harmonic frequency calculations were checked to be without any imaginary frequencies. The predicted harmonic frequencies were not scaled. To simulate the VA and VCD spectra, a Lorentzian line shape with a half width at half maximum of 10 $cm^{-1}$ was used. To account for the water solvent, the VA and VCD spectra were also simulated with the IEF version of PCM[28,29] as implemented in Gaussian 03. Within this model, the water solvent was treated as a continuum dielectric environment and a permittivity value of $\varepsilon_0=78.390$ was used. The solution VA and VCD spectra were also further simulated with the explicit hydrogen-bonding solvation considerations described in the main text.

## Acknowledgements

*This research was funded by the University of Alberta, the Natural Sciences and Engineering Research Council of Canada, Petro-Canada, and the Canada Research Chairs Program. We gratefully acknowledge access to the computing facilities provided by the Academic Information and Communication Technology group at the University of Alberta.*

**Keywords:** ab initio calculations · amino acids · circular dichroism · conformation analysis · vibrational spectroscopy

[1] G. Albrecht, R. B. Corey, *J. Am. Chem. Soc.* **1939**, *61*, 1087–1103.
[2] F. R. Tortonda, J. L. Pascual-Ahuir, E. Silla, I. Tunonon, F. J. Ramirez, *J. Chem. Phys.* **1998**, *109*, 592–602.
[3] S. Gronert, R. A. J. O'Hair, *J. Am. Chem. Soc.* **1995**, *117*, 2071–2081.
[4] E. Tajkhorshid, K. J. Jalkanen, S. Suhai, *J. Phys. Chem. B* **1998**, *102*, 5899–5913.
[5] C. F. Correia, P. O. Balaj, D. Scuderi, P. Maitre, G. Ohanessian, *J. Am. Chem. Soc.* **2008**, *130*, 3359–3370.
[6] Z. Ji, R. Santamaria, I. L. Garzón, *J. Phys. Chem. A* **2010**, *114*, 3591–3601.
[7] C. H. Görbitz, *Acta Chem. Scand.* **1990**, *44*, 584–590.
[8] T. M. Korter, R. Balu, M. B. Campbell, M. C. Beard, S. K. Gregurick, E. J. Heilweil, *Chem. Phys. Lett.* **2006**, *418*, 65–70.
[9] B. Lambie, R. Ramaekers, G. Maes, *J. Phys. Chem. A* **2004**, *108*, 10426–10433.
[10] F. J. Ramírez, I. Tuñón, E. Silla, *Chem. Phys.* **2004**, *303*, 85–96.

  

[11] I.-S. Jeon, D.-S. Ahn, S.-W. Park, S. Lee, B. Kim, *Int. J. Quantum Chem.* **2005**, *101*, 55 – 66.
[12] R. Miao, C. Jin, G. Yang, J. Hong, C. Zhao, L. Zhu, *J. Phys. Chem. A* **2005**, *109*, 2340 – 2349.
[13] R. Wu, T. B. McMahon, *ChemPhysChem* **2008**, *9*, 2826 – 2835.
[14] S. C. Nanita, R. G. Cooks, *Angew. Chem.* **2006**, *118*, 568 – 583; *Angew. Chem. Int. Ed.* **2006**, *45*, 554 – 569.
[15] W. M. Zuk, T. B. Freedman, L. A. Nafie, *J. Phys. Chem.* **1989**, *93*, 1771 – 1779.
[16] G. A. Jeffrey, W. Saenger, *Hydrogen Bonding in Biological Structure*, Springer, Berlin, **1991**.
[17] P. Ball, *$H_2O$: A Biography of Water*, Weidenfeld & Nicolson, London, **1999**.
[18] M. Yves, *The Hydrogen Bond and the Water Molecule*, Elsevier, New York, **2007**.
[19] L. A. Nafie, R. K. Dukor, T. B. Freedman, *Handbook of Vibrational Spectroscopy, Vol. 1* (Eds.: J. M. Chalmers, P. R. Griffiths), Wiley, Chichester, **2002**, pp. 731 – 744.
[20] "*Vibrational Circular Dichroism Spectroscopy of Chiral Molecules", G. Yang, Y. Xu in Top. Curr. Chem. Volume 298: Electronic and Magnetic Properties of Chiral Molecules and Supramolecular Architectures*, (Eds.: R. Naaman, D. N. Beratan, D. H. Waldeck), Springer, Berlin, **2011**, pp. 189 – 236.
[21] J. Sadlej, J. Cz. Dobrowolski, J. E. Rode, *Chem. Soc. Rev.* **2010**, *39*, 1478 – 1488.
[22] C. Gautier, T. Bürgi, *Chem. Commun.* **2005**, 5393 – 5395.
[23] M. Losada, H. Tran, Y. Xu, *J. Chem. Phys.* **2008**, *128*, 014508.
[24] M. Losada, P. Nguyen, Y. Xu, *J. Phys. Chem. A* **2008**, *112*, 5621 – 5627.
[25] G. Yang, Y. Xu, *J. Chem. Phys.* **2009**, *130*, 164506.
[26] M. Losada, Y. Xu, *Phys. Chem. Chem. Phys.* **2007**, *9*, 3127 – 3135.
[27] V. P. Nicu, E. Debie, W. Herrebout, B. Van der Veken, P. Bultinck, E. J. Baerends, *Chirality* **2010**, *21*, E287 – E297.
[28] S. Miertuš, E. Scrocco, J. Tomasi, *Chem. Phys.* **1981**, *55*, 117 – 129.
[29] J. Tomasi, M. Persico, *Chem. Rev.* **1994**, *94*, 2027 – 2094.
[30] C. P. Woodbury, *Biochemistry for the Pharmaceutical Sciences*, Jones & Bartlett Learning, Sudbury, MA, **2011**.
[31] S. H. Hilal, S. W. Karickhoff, L. A. Carreira, *Quant. Struct. Act. Relat.* **1995**, *14*, 348 – 355.
[32] Z. Tian, A. Pawlow, J. C. Poutsma, S. R. Kass, *J. Am. Chem. Soc.* **2007**, *129*, 5403 – 5407.
[33] M. Noguera, L. Rodrı'guez-Santiago, M. Sodupe, J. Bertran, *J. Mol. Struct.* **2001**, *537*, 307 – 318.
[34] X. L. Cao, R. K. Dukor, L. A. Nafie, *Theor. Chem. Acc.* **2008**, *119*, 69 – 79.
[35] D. G. Blackmond, M. Klussmann, *Chem. Commun.* **2007**, 3990 – 3996.
[36] D. A. Case, T. A. Darden, T. E. Cheatham, C. L. Simmerling, J. Wang, R. E. Duke, R. Luo, K. M. Merz, D. A. Pearlman, M. Crowley, R. C. Walker, W. Zhang, B. Wang, S. Hayik, A. Roitberg, G. Seabra, K. F. Wong, F. Paesani, X. Wu, S. Brozell, V. Tsui, H. Gohlke, L. Yang, C. Tan, J. Mongan, V. Hornak, G. Cui, P. Beroza, D. H. Mathews, C. Schafmeister, W. S. Ross, P. A. Kollman, AMBER 9, University of California, San Francisco, **2006**.
[37] W. L. Jorgensen, C. Jenson, *J. Comput. Chem.* **1998**, *19*, 1179 – 1186.
[38] U. Essmann, L. Perera, M. L. Berkowitz, T. Darden, H. Lee, L. G. Pedersen, *J. Chem. Phys.* **1995**, *103*, 8577 – 8593.
[39] J. P. Ryckaert, G. Ciccotti, H. J. C. Berendsen, *J. Comput. Phys.* **1977**, *23*, 327 – 341.
[40] Gaussian 03 (Revision E.01), M. J. Frisch, G. W. Trucks, H. B. Schlegel, G. E. Scuseria, M. A. Robb, J. R. Cheeseman, J. A. Montgomery, Jr., T. Vreven, K. N. Kudin, J. C. Burant, J. M. Millam, S. S. Iyengar, J. Tomasi, V. Barone, B. Mennucci, M. Cossi, G. Scalmani, N. Rega, G. A. Petersson, H. Nakatsuji, M. Hada, M. Ehara, K. Toyota, R. Fukuda, J. Hasegawa, M. Ishida, T. Nakajima, Y. Honda, O. Kitao, H. Nakai, M. Klene, X. Li, J. E. Knox, H. P. Hratchian, J. B. Cross, V. Bakken, C. Adamo, J. Jaramillo, R. Gomperts, R. E. Stratmann, O. Yazyev, A. J. Austin, R. Cammi, C. Pomelli, J. W. Ochterski, P. Y. Ayala, K. Morokuma, G. A. Voth, P. Salvador, J. J. Dannenberg, V. G. Zakrzewski, S. Dapprich, A. D. Daniels, M. C. Strain, O. Farkas, D. K. Malick, A. D. Rabuck, K. Raghavachari, J. B. Foresman, J. V. Ortiz, Q. Cui, A. G. Baboul, S. Clifford, J. Cioslowski, B. B. Stefanov, G. Liu, A. Liashenko, P. Piskorz, I. Komaromi, R. L. Martin, D. J. Fox, T. Keith, M. A. Al-Laham, C. Y. Peng, A. Nanayakkara, M. Challacombe, P. M. W. Gill, B. Johnson, W. Chen, M. W. Wong, C. Gonzalez, J. A. Pople, Gaussian, Inc., Wallingford, CT, **2004**.
[41] A. D. Becke, *J. Chem. Phys.* **1993**, *98*, 5648 – 5652.
[42] C. T. Lee, W. T. Yang, R. G. Parr, *Phys. Rev. B* **1988**, *37*, 785 – 789.
[43] A. K. Chandra, S. Parveen, T. Zeegers-Huyskens, *J. Phys. Chem. A* **2007**, *111*, 8884 – 8891.
[44] J. N. Woodford, *J. Phys. Chem. A* **2007**, *111*, 8519 – 8530.
[45] P. I. Dem'yanov, R. M. Gschwind, *Organometallics* **2006**, *25*, 5709 – 5723.
[46] P. J. Stephens, F. J. Devlin, C. F. Chabalowski, M. J. Frisch, *J. Phys. Chem.* **1994**, *98*, 11623 – 11627.
[47] T. Kuppens, W. Herrebout, B. van der Veken, P. Bultinck, *J. Phys. Chem. A* **2006**, *110*, 10191 – 10200.
[48] L. Ducasse, F. Castet, A. Fritsch, I. Huc, T. Buffeteau, *J. Phys. Chem. A* **2007**, *111*, 5092 – 5098.
[49] T. Brotin, D. Cavagnat, J.-P. Dutasta, T. Buffeteau, *J. Am. Chem. Soc.* **2006**, *128*, 5533 – 5540.
[50] S. Scheiner, *Hydrogen Bonding: A Theoretical Perspective*, Oxford University Press, New York, **1997**.
[51] "*Case Studies in Cooperativity in Hydrogen-Bonded Clusters and Polymers", A. Karpfen in Molecular Interactions: From van der Waals to Strongly Bound Complexes* (Ed.: S. Scheiner), Wiley, Chichester, **1997**, pp. 265 – 296.
[52] N. Borho, Y. Xu, *Angew. Chem.* **2007**, *119*, 2326 – 2329; *Angew. Chem. Int. Ed.* **2007**, *46*, 2276 – 2279.
[53] A. Borba, M. Albrecht, A. Gómez-Zavaglia, L. Lapinski, M. J. Nowak, M. A. Suhm, R. Fausto, *Phys. Chem. Chem. Phys.* **2008**, *10*, 7010 – 7021.

Received: December 14, 2011
Published online on February 14, 2012

  

Journal of Molecular Structure 1024 (2012) 123–131

Contents lists available at SciVerse ScienceDirect

Journal of Molecular Structure

journal homepage: www.elsevier.com/locate/molstruc

# Conformations of [(R,R)-1,5-diaza-cis-decalin] copper (II) complex and its hydrogen bonding interaction with the crystal water: A combined experimental VA, UV–Vis and ECD spectroscopic and DFT study

Zahra Dezhahang, Mohammad Reza Poopari, Yunjie Xu *

*Department of Chemistry, University of Alberta, Edmonton, Alberta, Canada T6G 2G2*

## HIGHLIGHTS

- Conformation study of 1,5-diaza-cis-decalin ligand is presented.
- Conformation study of 1,5-diaza-cis-decalin copper (II) complex is presented.
- Experimental VA and ECD disagreed with the simulated spectra of the complex itself.
- Inclusion of crystal water in the complex brings good agreement with experiment.
- Crystal water has a significant impact on the appearance of the VA and ECD spectra.

## ARTICLE INFO

*Article history:*
Received 26 February 2012
Received in revised form 25 April 2012
Accepted 26 April 2012
Available online 4 May 2012

*Keywords:*
1,5-Diaza-cis-decalin
Copper complex
Chiroptical spectroscopy
Density functional theory
Hydrogen bonding interaction
Crystal water

## ABSTRACT

Chiral 1,5-diaza-cis-decalin ligand and its copper-complexes have found considerable applications in catalyzing enantioselective organic reactions. In the present article, (R,R)-1,5-diaza-cis-decalin ligand and its copper (II) hydroxide iodine hydrate complex have been investigated by using vibrational absorption (VA), ultraviolet–visible (UV–Vis), and electronic circular dichroism (ECD) experimental spectroscopic measurements, as well as density functional theory modeling. An extensive theoretical conformational analysis of the ligand has revealed that the ligand can adopt a good number of orientations in terms of its frame conformations, i.e. Chair–Chair, Chair–Boat, and Boat–Boat, the proximal (also denoted as in) and distal (out) positions for its two N atoms, and the equatorial (e) and axial (a) positions of its two amine H atoms. The most dominant conformation at room temperature was predicted to take on the Chair–Chair N-in H-ea configuration, based on the relative Gibbs free energy ordering at the B3LYP/6-31++G(d,p) level. The VA, vibrational CD, UV–Vis, and ECD spectra of the ligand conformers have been simulated. Conformational searches have also been carried out for the titled copper complex at the B3LYP/LanL2DZ level and the dominant conformer was predicted to have the Chair–Chair N-in H-ee configuration for its ligands, with a close to 100% Boltzmann population factor at room temperature. Furthermore, geometry optimizations and spectral simulations have been performed for the hydrogen bonded cluster of the complex with the crystal water. The effects of hydrogen bonding interaction with the crystal water on the VA, VCD, UV–Vis, and ECD spectra have been discussed. The interaction with the water molecule has been found to have significant impacts on the appearance of VA, VCD and ECD spectra and its inclusion is essential to obtain satisfactory interpretations of the experimental VA and ECD spectra.



## 1. Introduction

1,5-Diaza-cis-decalin and its derivatives are important chiral diamine ligands which have found much application in metal-meditated and metal-catalyzed asymmetric organic reactions. For example, it was shown to provide high selectivity with an enantiomeric excess of 90–93% in enantioselective oxidative biaryl coupling reactions [1]. Considerable research efforts have been paid to their syntheses and to the conformational flexibility of the ligand which can have significant impacts on their catalytic ability [2–7]. Kozlowski and co-workers investigated the effects of different substitutions at the two amines groups of 1,5-diaza-cis-decalin and at the decalin ring on the conformational equilibrium position [2,4]. The authors found that these ligands exist in two conformations: N-in and N-out (Scheme 1) and that the position of the conformational equilibrium depends mainly on the substitution at the amine groups [2]. Furthermore, the catalytic properties of 1,5-dia-

* Corresponding author. Tel.: +1 780 492 1244; fax: +1 780 492 8231.
*E-mail address:* yunjie.xu@ualberta.ca (Y. Xu).

0022-2860/$ - see front matter © 2012 Elsevier B.V. All rights reserved.
http://dx.doi.org/10.1016/j.molstruc.2012.04.079

za-cis-decalin, a highly stable bidentate ligand, can vary noticeably with different metal center atoms. For example, the catalytic abilities of several complexes formed using 1,5-diaza-cis-decalin ligand and a few different metals were evaluated for the oxidative asymmetric biaryl coupling of 3-substitued 2-naphthols [7]. In all these studies, it is recognized that the conformations of the chiral metal complexes are an important deciding factor in their catalytic abilities. It is therefore of considerable interest to carry out conformational analysis of the [(R,R)-1,5-diaza-cis-decalin] and its copper (II) hydroxide iodine hydrate complex.

Several spectroscopic methods, namely vibrational absorption (VA), ultraviolet–visible (UV–Vis) and electronic circular dichroism (ECD) spectroscopy have been utilized in this study, in combination with density functional theory (DFT) calculations. Such experimental and theoretical spectroscopic combinations have been used extensively in the last few years to obtain information about conformations and absolute configurations of many important chiral biological, organic, and inorganic molecules [1,8,9], thanks to the significant theoretical advances. Furthermore, in recent years, the effects of hydrogen bonding interactions have been hypothesized as a possible cause of the discrepancies between calculated and experimental ECD spectra [10], although little has been reported on the subject [11,12]. The copper (II) compound available commercially contains one crystal water molecule. It would therefore be of substantial interest to investigate whether the hydrogen bonding interaction between the copper(II) complex and water has any important effects on the appearance of the ECD spectrum.

In the present investigation, the VA measurement, and the UV–Vis and ECD measurements of the titled copper complex have been performed using a KBr pellet and in acetonitrile solutions, respectively. Extensive conformational analyses have been carried out for 1,5-diaza-cis-decalin ligand, the corresponding [(R,R)-1,5-diaza-cis-decalin] copper (II) hydroxide iodine complex, and the associated hydrogen bonded cluster consisting of the copper (II) complex and one additional water molecule using DFT. The experimental VA, UV–Vis and ECD spectra have been compared to the simulated data using DFT and time dependent (TD)-DFT. Important conclusions about the conformations of the complex and the effects of hydrogen bonding interaction on the appearance of these spectra have been obtained.

## 2. Experimental and theoretical details

### 2.1. Spectroscopic measurements

[(R,R)-1,5-diaza-cis-decalin] cupper (II) hydroxide iodine hydrate was purchased from Sigma Aldrich (Canada) and used without any further purification. The UV and ECD measurements were carried out using a *HP 8453* UV–Vis instrument and *Olis DSM 17* CD spectrophotometer, respectively. A path-length of 0.5 cm was used for the UV–Vis and ECD measurements. Solutions of the copper (II) complex in acetonitrile with a concentration of $3.4 \times 10^{-5}$ M and $1.1 \times 10^{-3}$ M were used for the UV and ECD measurements in the 190–300 nm and 300–500 nm regions, respectively, because of the much low absorption intensity in the longer wavelength region. The VA measurements in the finger print region from 700 to 1800 $cm^{-1}$ were performed using a KBr pellet with a 0.6% concentration using VERTEX 70 FTIR spectrometer (Bruker) module [13]. It is in principle possible to obtain a vibrational CD (VCD) measurement of the KBr pellet. However, we found that the artefacts were too severe and no solid state VCD measurements were further pursued in the present study. The targeted copper complex has very low solubility in all common solvents such as methanol, water, chloroform, and acetonitrile, with the highest solubility in acetonitrile. Even in acetonitrile (both normal and $CD_3CN$), we were not able to obtain reliable VA spectral features because the solvent absorption features in the same spectral range completely overwhelm those of the complex. Consequently, we were not able to obtain solution VCD spectra either.

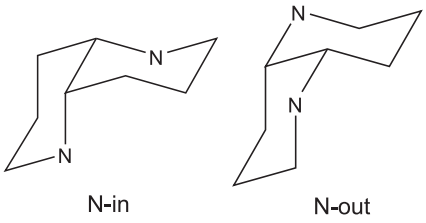


**Scheme 1.** Two main conformations of 1,5-diaza-cis-decalin ligand identified in Refs. [2,6]. Both N atoms are in the proximal position in N-in, and both N atoms are in the distal position in N-out.

### 2.2. Theoretical calculations

The geometry optimizations, vibrational frequencies, and VA and VCD intensities, as well as frequencies and intensities of UV and ECD spectra have been performed using the Gaussian03 program package [14]. B3LYP exchange correlation functional has been widely used for structural studies of transition metal complexes with reliable results [15–18]. It is also known to provide structural and VA and VCD spectral predictions in good agreement with the experimental data for hydrogen-bonded systems [19–23]. Therefore, geometry optimizations of the ligand and the copper complex without and with the hydrogen bonded water molecule were carried out at this level of theory with 6-31++G(d,p) for the ligand and with LanL2DZ basis set for the copper complex. The corresponding Boltzmann population analyses based on the relative energies and Gibbs free energies were performed. To confirm that the optimized geometries were true minima, their harmonic frequency calculations were checked to be without any imaginary frequencies. The predicted harmonic VA frequencies are not scaled in the current study. The calculations of the corresponding UV–Vis and ECD spectra were completed using TD-DFT. To simulate the VA and VCD spectra, a Lorentzian line shape with a half width at half maximum of 4 $cm^{-1}$ was used, whereas a half width at half maximum of 0.3 eV was used for the UV–Vis and ECD simulations [24]. To account for the solvent effects in the UV–Vis and ECD solution measurements, the integral equation formalism (IEF) version of implicit polarization continuum model (PCM) [25,26] as implemented in Gaussian 03 was applied. Within this model, the $CH_3CN$ solvent was treated as a continuum dielectric environment and a permittivity value of $\varepsilon_0 = 36.64$ was used. No scaling factor was applied to the predicted electronic transition wavelengths in this paper.

## 3. Results and discussions

### 3.1. Conformational analysis and spectral simulation of the [(R,R)-1,5-diaza-cis-decalin] ligand

Two major conformations, associated with the proximal and distal position of the N atoms, of 1,5-diaza-cis-decalin, had been discussed before in literature [2,6]. Since chiroptical measurements can be quite sensitive to even the more subtle conformations resulted from different orientations of the amine hydrogen atoms in the ligand [27], a further conformational search was carried out. For the N-in and N-out conformations, the H atoms of the two amine groups can be either in the equatorial (e) position or axial (a) position, giving rise to three conformations, labeled as H-ee, H-ea and H-aa, in each case. This resulted in a total of six conform-

ers as shown in Fig. 1. It should be pointed out here that in all these six conformations, the decalin rings have been kept in the Chair–Chair conformation which has a close to 100% Boltzmann population factor based on the relative Gibbs free energies, as discussed in the next paragraph. Please note that H-ea and H-ae are the same here since the two decalin rings are identical. The calculated relative energies and Gibbs free energies are listed in Table 1, together with the corresponding percentage Boltzmann population factors at room temperature based on the relative energies and Gibbs free energies. From Table 1, one can conclude that the N-in conformers are much more stable than the N-out conformers and that the N-in H-ea conformer is the most stable ligand conformer with a dominating Boltzmann factor of 88% at room temperature. Clearly, the nitrogen atoms favorite the proximal position, i.e. N-in, consistent with the finding reported previously [2]. The two amine hydrogen atoms, on the other hand, prefer to occupy two different positions, i.e. one axial and one equatorial. This might be due to an energetically favorable interaction between the axial hydrogen atom with the other nitrogen atom in the H-ea conformation while none of the other five conformers can enable such an interaction. Indeed, the distance of N(axial) and H(equatorial), $r_{N(axial)\cdots H(equatorial)}$, is about 2.72 Å, considerably shorter than a regular van der Waals distance [28].

Besides the conformations associated with the amine N and H atoms, the decalin rings can also take on different conformations, such as Chair–Chair, Chair–Boat, Boat–Chair, and Boat–Boat, although only the Chair–Chair conformation had been explicitly considered in the previous literature [2,3,6]. For completion, we used two most stable conformers, i.e. N-in H-ea and N-in H-ee, as starting points for considering the decalin ring conformations. This resulted in four ring conformers of N-in H-ea and three of N-in H-ee, which are depicted in Fig. 2. The corresponding relative energies and Gibbs free energies are provided in Table 2. Clearly, the Chair–Chair conformers are by far the most stable structures in the gas phase with a close to 100% Boltzmann population factor at room temperature in both cases. We therefore considered only the Chair–Chair conformation in the spectral simulation of the ligand.

**Table 1**
Calculated relative energies, Gibbs free energies, and the corresponding percentage Boltzmann population factors at room temperature of the six most stable conformers of the Chair–Chair 1,5-diaza-cis-decalin ligand at the B3LYP/6-31++G(d,p) level.

| Conformers of ligand | $\Delta E^o$ (kcal/mol) | $\Delta G^o$ (kcal/mol) | Pop% ($\Delta E^o$) | Pop% ($\Delta G^o$) |
|---|---|---|---|---|
| N-in H-ee | 0.50 | 1.14 | 21.12 | 12.19 |
| N-in H-ea | 0.00 | 0.00 | 48.84 | 82.98 |
| N-in H-aa | 0.80 | 1.86 | 12.65 | 3.60 |
| N-out H-ee | 1.19 | 3.19 | 6.58 | 0.38 |
| N-out H-ea | 1.23 | 2.84 | 6.14 | 0.68 |
| N-out H-aa | 1.39 | 3.66 | 4.67 | 0.17 |

The VA and VCD spectra of the six most stable Chair–Chair ring conformers are shown in Fig. 3. While the three N-out conformers have fairly similar VA spectra, the VA spectra of the three N-in conformers are noticeably different among themselves and from those of the N-out conformers, especially in the 600–800 $cm^{-1}$ region. The bands in the 600–800 $cm^{-1}$ region correspond mainly to those associated with the N–H bending motion. Clearly, different placements of the nitrogen atoms in the decalin rings are responsible for this. The equatorial and axial orientations of the amine hydrogen atoms introduce only minor differences in the VA spectra of the N-out conformers. In contrast, such orientations have very noticeable effects on the appearance of VA spectra of the N-in conformers, most likely due to the forming and breaking of the intramolecular hydrogen bond (or at least strong interaction) between

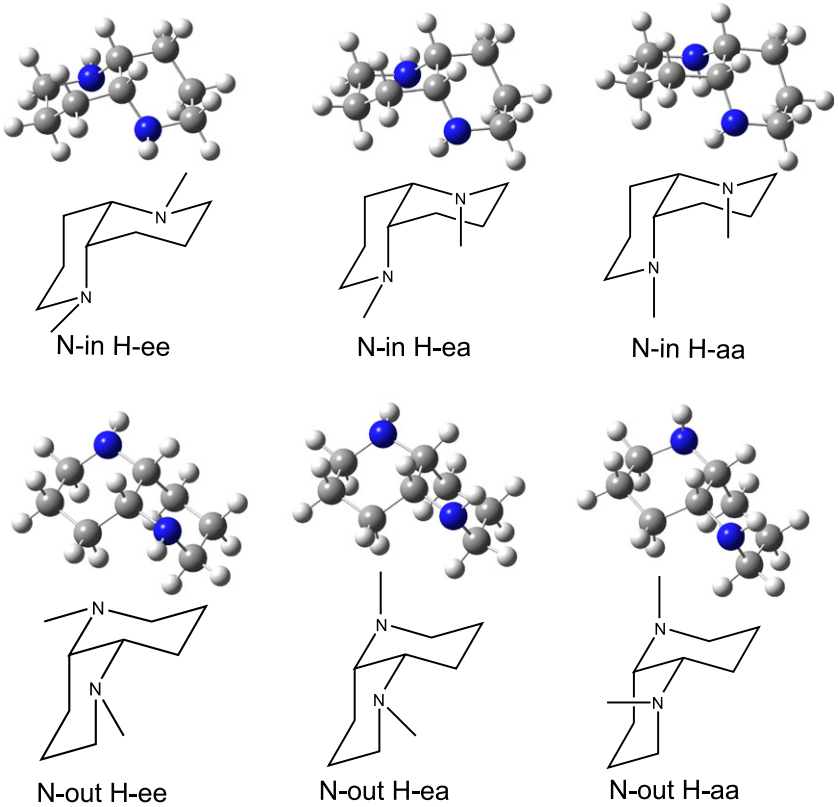


**Fig. 1.** Six most stable conformers of the Chair–Chair 1,5-diaza-cis-decalin ligand at the B3LY/6-31++G(d,p) level of theory.

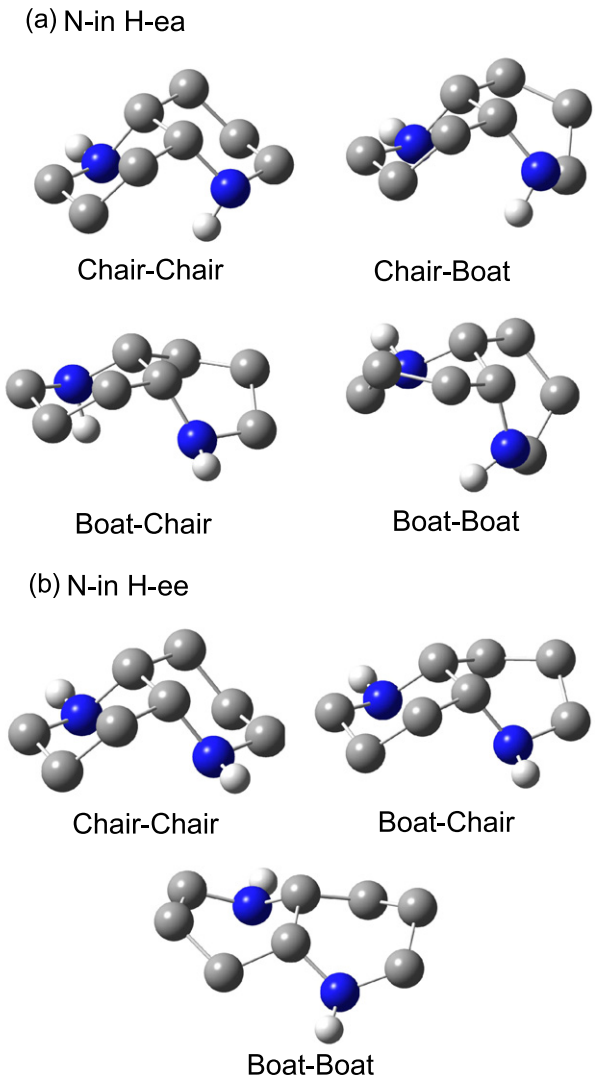


**Fig. 2.** Geometries of the decalin ring conformers of (a) N-in H-ea and (b) N-in H-ee 1,5-diaza-cis-decalin ligand at the B3LY/6-31++G(d,p) level. Hydrogen atoms attached to the carbon atoms are not displayed for simplicity.

the N and H atoms. The VCD spectra of the six conformers are as expected very different from each other because of the high sensitivity of VCD spectra to variations in dihedral angles. Unfortunately, 1,5-diaza-cis-decalin ligand is not available commercially and no experimental VA and VCD data of the ligand have been obtained.

The UV–Vis and ECD spectra of the two most stable Chair–Chair ring conformers, i.e. N-in H-ea and N-in H-ee, have also been

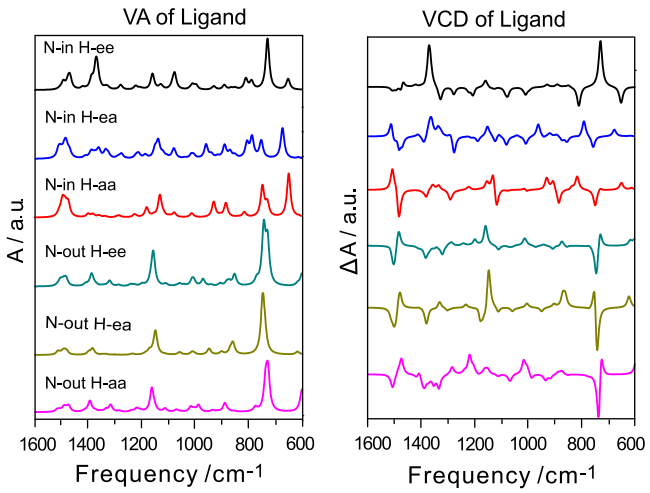


**Fig. 3.** Simulated VA and VCD spectra of the six most stable conformers of the Chair–Chair 1,5-diaza-cis-decalin ligand listed in Table 1 at the B3LYP/6-31++G(d,p) level.

simulated with TDDFT in order to compare to the experimental ECD spectrum reported in Ref. [3]. To account for the effects of $CH_3CN$ solvent, the geometries of these two conformers have been re-optimized with PCM of $CH_3CN$ and the related spectra simulated. These simulated UV–Vis and ECD spectra are summarized in Fig. 4. The effects of a polar solvent on the appearances of the UV–Vis and ECD spectra of a range of chiral molecules [29] have been investigated theoretically using the conductor-like screening model (COSMO) [30,31] and PCM, both of the continuum solvent model type. For a conformationally rigid system, such as methyloxirane [29] and $[Co(en)_3]^{3+}$ [32], the inclusion of the continuum solvent model seems to only shift some band frequencies and relative band intensities slightly in UV–Vis spectra and introduce minor changes in the shapes of ECD spectra [32]. For a more flexible system, such as 3,3′,4,4′,7-flavanpentol [33], the ECD features of some conformers experience more dramatic intensity alternations, while others remain more or less the same. From Fig. 4, one can see that the inclusion of PCM produced only minor changes in the appearance of the UV–Vis and ECD spectra. It is interesting to note that the ECD spectra for these two conformers appear quite different. The simulated ECD spectrum of N-in H-ea shows a positive broad first Cotton band in the longer wavelength region, in good agreement with the observed spectrum for (R,R)-1,5-diaza-cis-decalin reported in Ref. [3]. The simulated ECD spectrum of N-in H-ee, on the other hand, shows essentially no ECD activity in the same region. The comparison of the simulated and experimental ECD data therefore supports the conclusion that N-in H-ea is the dominant ligand conformer at room temperature.

**Table 2**
Calculated relative energies, relative Gibbs free energies and the corresponding percentage Boltzmann population factors at room temperature of the decalin ring conformers of the N-in H-ea and N-in H-ee 1,5-diaza-cis-decalin ligands at the B3LYP/6-31++G(d,p) level.

| Conformers of ligand | $\Delta E^o$ (kcal/mol) | $\Delta G^o$ (kcal/mol) | Pop% ($\Delta E^o$) | Pop% ($\Delta G^o$) |
|---|---|---|---|---|
| *Four decalin ring conformers of N-in H-ea* | | | | |
| Chair–Chair | 0.00 | 0.00 | 100.00 | 99.99 |
| Chair–Boat | 6.61 | 5.99 | 0.00 | 0.00 |
| Boat–Chair | 6.23 | 5.80 | 0.00 | 0.01 |
| Boat–Boat | 13.59 | 12.97 | 0.00 | 0.00 |
| *Three decalin ring conformers of N-in H-ee* | | | | |
| Chair–Chair | 0.00 | 0.00 | 100.00 | 99.98 |
| Chair–Boat | 11.37 | 8.87 | 0.00 | 0.01 |
| Boat–Boat | 13.59 | 10.48 | 0.00 | 0.00 |

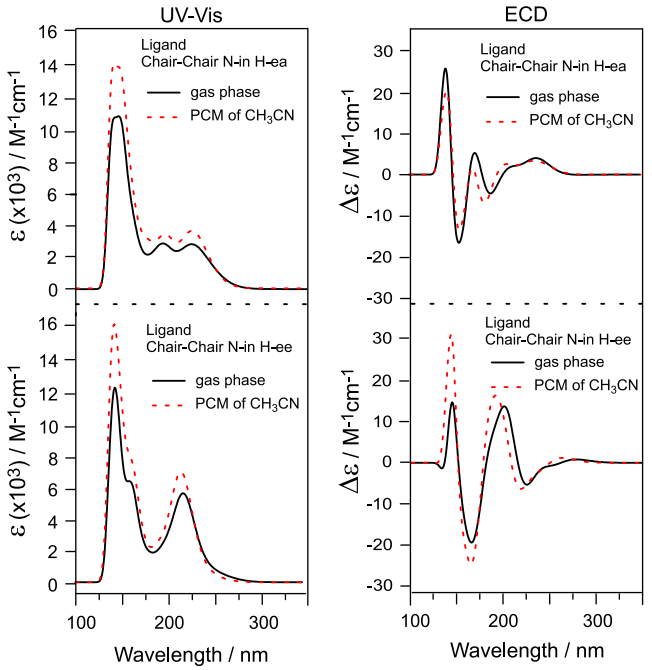


**Fig. 4.** Simulated UV–Vis and ECD spectra of the two most stable conformers of Chair–Chair [(R,R)-1,5-diaza-cis-decalin] ligand in the gas phase and with PCM of $CH_3CN$ solvent at the B3LYP/6-31++G(d,p) level.

### *3.2. Conformational analysis and spectral simulations of the [(R,R)-1,5-diaza-cis-decalin] copper (II) hydroxide iodine complex*

As discussed in the previous section, the 1,5-diaza-cis-decalin ligand strongly prefers the Chair–Chair conformation for the decalin rings, the N-in conformation for the nitrogen atoms, and the ea conformation for the amine hydrogen atoms. On the other ha nd, based on the geometric consideration and the results from previous studies [2,3], only the N-in H-ee ligand conformers are capable of forming coordination bonds to the copper atom. Consequentially, the coordination to the copper atom must have moved the equilibrium towards the N-in H-ee ligand conformer from the dominating N-in H-ea ligand conformer. It would also be interesting to investigate if binding to copper can also alter the preferred conformation of the decalin rings. Therefore, four N-in H-ee conformers of the copper complex were constructed where each decalin ring can have either chair or boat conformations. These are Chair–Chair, Chair–Boat where the iodine ligand is adjacent to the Chair ring, Boat–Chair where the iodine ligand is adjacent to the Boat ring, and Boat–Boat. The optimized geometries of these four conformers are presented in Fig. 5 and the calculated relative energies and relative Gibbs free energies are summarized in Table 3, together with the corresponding percentage Boltzmann population factors at room temperature. As one can see, the Chair–Chair conformer is still favoured with a commanding Boltzmann population factor of 99%, while the rest of conformers have only negligible contributions at room temperature. This indicates that while the preferred orientation of the amine H atoms changes from ea to ee to accommodate the coordination binding, the coordination to copper imposes little effect on the preferred geometries taken by either the decalin rings or the N-atoms.

The simulated VA and VCD spectra of the above four conformers of the copper complex are depicted in Fig. 6. The experimental VA spectrum of [(R,R)-1,5-diaza-cis-decalin] copper (II) hydroxide iodine hydrate measured with a translucent KBr pellet is also shown in Fig. 6a for comparison. The VA spectra of all four conformers show similar main features although some minor differences exist. The main VCD features, on the other hand, are more different among these conformers. This is consistent with the general observation that VCD spectra are more sensitive to conformational changes than the related VA spectra. The observed VA spectrum, however, shows little resemblance to that of the most stable conformer, i.e. C-I Chair–Chair N-in H-ee conformer, of [(R,R)-1,5-diaza-cis-decalin] copper (II) hydroxide iodine complex, or to those of any other minor conformers. Since a complete conformational search has been carried out for the complex, the disagreement between the experimental and the simulated spectra suggests that one may need to consider the crystal water molecule in the simulation. This point will be addressed in Section 3.3.

The simulated UV–Vis and ECD spectra of the above four conformers of the copper complex are depicted in Fig. 7, together with the experimental UV–Vis and ECD spectra of the [(R,R)-1,5-diaza-cis-decalin] copper (II) hydroxide iodine hydrate measured in $CH_3CN$ solution. All the conformers show similar simulated UV–Vis spectra, whereas some minor differences can be seen in the related ECD spectra. The experimental UV–Vis spectrum can be correlated to the simulated UV–Vis features reasonably well. The experimental ECD spectrum, however, shows little resemblance to that of any conformer, including the dominant conformer, C-I Chair–Chair N-in H-ee of the complex. We therefore hypothesized that the hydrogen bonding interaction between the complex and the crystal water molecule may be responsible for the disagreement between theory and experiment, just as in the case of the VA comparison discussed above. This issue will be addressed in Section 3.3.

### *3.3. Hydrogen bonding effects on the VA, VCD, UV–Vis and ECD spectra of the [(R,R)-1,5-diaza-cis-decalin] copper (II) hydroxide iodine complex*

There is one water molecule for each coordination complex in the sample purchased from Sigma Aldrich. It had been demonstrated both theoretically and experimentally that hydrogen bonding interactions with water molecules can have dramatic effects on

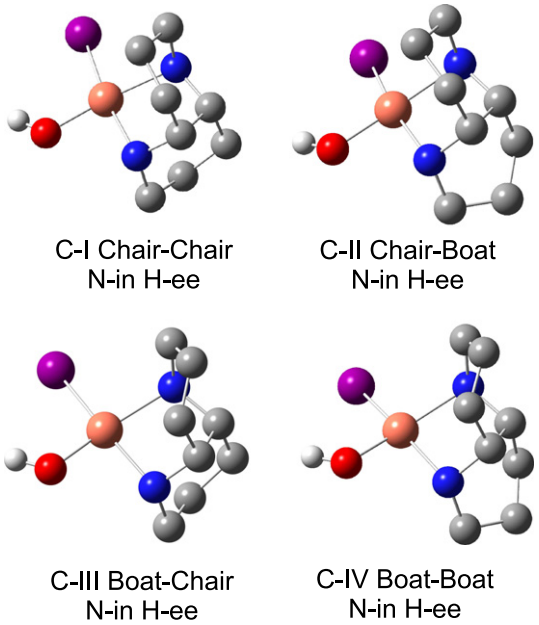


**Fig. 5.** Optimized geometries of the four decalin ring conformers of N-in H-ee [(R,R)-1,5-diaza-cis-decalin] copper (II) hydroxide iodine complex at the B3LYP/LanL2DZ level. Hydrogen atoms attached to the carbon atoms are not displayed for simplicity.

**Table 3**
Calculated relative energies, relative Gibbs free energies and the corresponding percentage Boltzmann population factors at room temperature of the four conformers of [(R,R)-1,5-diaza-cis-decalin] copper (II) hydroxide iodine complex at the B3LYP/LanL2DZ level.

| Conformers of complex | $\Delta E^o$ (kcal/mol) | $\Delta G^o$ (kcal/mol) | Pop% ($\Delta E^o$) | Pop% ($\Delta G^o$) |
|---|---|---|---|---|
| C-I Chair–Chair N-in H-ee | 0.00 | 0.00 | 99.96 | 99.94 |
| C-II Chair–Boat N-in H-ee | 5.17 | 4.75 | 0.02 | 0.03 |
| C-III Boat–Chair N-in H-ee | 5.17 | 4.90 | 0.02 | 0.03 |
| C-IV Boat–Boat N-in H-ee | 9.78 | 9.33 | 0.00 | 0.00 |

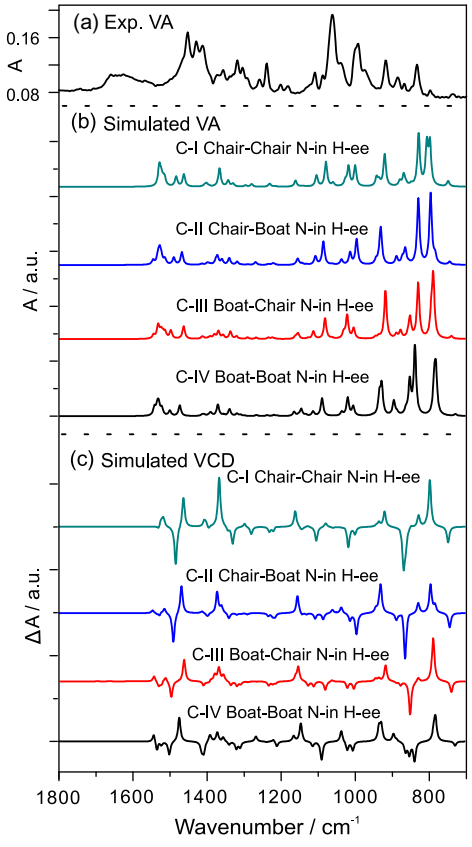


**Fig. 6.** Simulated VA and VCD spectra of the four conformers of [(R,R)-1,5-diaza-cis-decalin] copper (II) hydroxide iodine complex listed in Table 3 at the B3LYP/LanL2DZ level. The experimental VA spectrum obtained with a KBr pellet is also included for comparison.

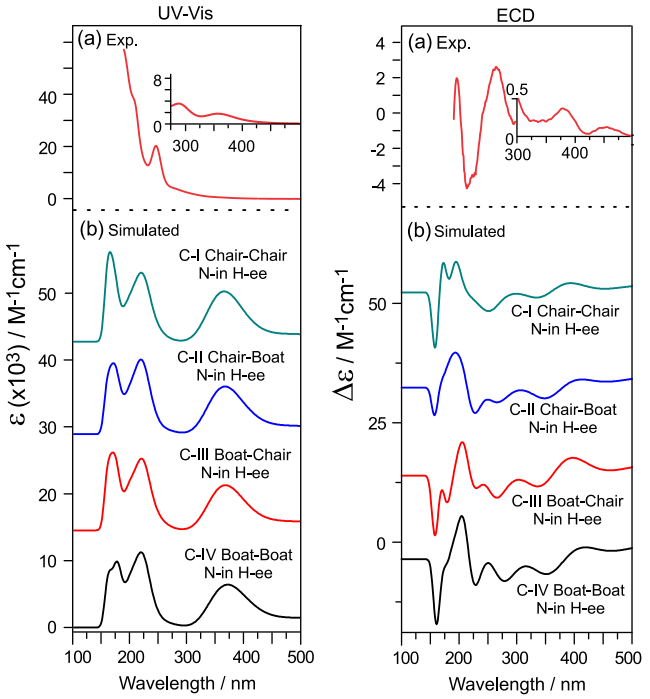


**Fig. 7.** Simulated UV–Vis and ECD spectra of the four conformers of [(R,R)-1,5-diaza-cis-decalin] copper (II) hydroxide iodine complex listed in Table 3 at the B3LYP/LanL2DZ level. The experimental UV–Vis and ECD spectra obtained in $CH_3CN$ solution are also included for comparison. The inserts were measured with a higher concentration (see Section 2.1 for details).

the VCD spectral signatures [8,22,34,35]. This encouraged us to investigate the effects of the hydrogen bonding interaction of the copper complex with water on the spectra observed. A water molecule can bind to the copper complex with two hydrogen bonds simultaneously. This resulted in three possible geometries using the dominant C-I Chair–Chair N-in H-ee conformer as the starting point. The main conformer, W-I ($NH_d$–$O_a$), refers to the conformer of the hydrogen bonded cluster where the amine H and O atoms of the copper complex serve as the proton donor and acceptor to simultaneously form the NH···OwHw and OwHw···O hydrogen bonds, respectively. Here Ow and Hw are the oxygen and hydrogen atoms of water, respectively. We use "W" to signify the inclusion of the crystal water molecule. This conformer has a 100% Boltzmann population factor at room temperature. The next most stable conformer, W-II ($NH_d$–$I_a$), designates the hydrogen bonding conformer with the NH···OwHw and OwHw···I hydrogen bonds. The third most stable conformer, W-III ($OH_d$–$I_a$), refers the conformer containing the OH···OwHw and OwHw···I hydrogen bonds. The most stable one has two strong hydrogen bonds involving the highly electronegative N and O atoms. The other two, on the other hand, contain one OwHw···I hydrogen bond in addition to the NH···OwHw or OH···OwHw bond. Since the iodine ligand is bigger and less electronegative than the oxygen and nitrogen atoms involved in a hydrogen bond, it is not surprising that $NH_d$–$O_a$ is the most stable conformer among them. The corresponding theoretical relative energies and relative Gibbs free energies are listed in Table 4, while the optimized geometries are given in Fig. 8 where the intermolecular hydrogen bond lengths are indicated.

The simulated VA and VCD spectra of these water hydrogen bonded conformers are depicted in Fig. 9, together with the experimental VA spectrum of the complex. First of all, the hydrogen bonding interaction with water at different binding sites introduces significant differences to both VA and VCD spectra among the three conformers. Second, the hydrogen bonding interaction with water also leads to drastic changes in the VA and VCD spectra, compared to those of the starting conformer, C-I Chair–Chair N-in H-ee (Fig. 6), where water was not included. There are two strong bands at 1056 $cm^{-1}$ and 1684 $cm^{-1}$ in the W-I VA spectrum which correspond mainly to the bending of OH group in the complex and that of water, respectively, and which do not show up as prominently or at all in the VA spectrum of C-I Chair–Chair N-in H-ee. The VA pattern predicted for W-I correlated very well with the observed VA spectrum measured with a KBr pellet, whereas the other two conformers alone show much poorer agreement. This indicates that W-I is the dominant conformational structure favoured at room temperature. It is plausible that W-II and W-III also make some minor contributions to the observed VA spectrum since the

water bending band observed is quite broad, suggesting that the local environment to water is not uniform. The comparison discussed above clearly demonstrates the importance of including crystal water in such simulations.

The corresponding simulated UV–Vis and ECD spectra of the hydrogen bonded clusters of the copper complex with water are given in Fig. 10, together with the experimental UV–Vis and ECD spectra. The two strong absorption bands observed at the shorter wavelength region were well captured by the simulated UV–Vis spectra of all three conformers since there are no significant differences among them. In general, the TDDFT method seems to underestimate the wavelengths of these strong electronic transitions. In the longer wavelength region, two experimental bands (insert of Fig. 10) are visible with much lower relative intensities than the two in the shorter wavelength region. This can be compared to the simulated band with a very broad profile, although it was predicted with much higher relative intensity than that observed experimentally. Since the UV–Vis spectra for all three water containing conformers are similar, it is difficult to conclude which one of them dominates in solution. In the 190–300 nm range, the experimental ECD spectrum shows a series of prominent ECD features with sequentially positive–negative–positive (+/−/+) signs. This correlated well with the predicted ECD spectrum of W-I in the short wavelength region. The predicted ECD spectra of W-II and W-III are noticeably different from the experimental one. For example, W-III exhibits a series of ECD features with sequentially negative–positive–negative (−/+/−) signs in the shorter wavelength region, almost exactly the opposite of what was detected

**Table 4**
Calculated relative energies, relative Gibbs free energies and the corresponding percentage Boltzmann population factors at room temperature of the three most stable hydrogen bonded conformers of C-I Chair–Chair N-in H-ee [(R,R)-1,5-diaza-cis-decalin] copper (II) hydroxide iodine complex with the crystal water at the B3LYP/LanL2DZ level.

| Conformers of complex | $\Delta E^o$ (kcal/mol) | $\Delta G^o$ (kcal/mol) | Pop% ($\Delta E^o$) | Pop% ($\Delta G^o$) |
|---|---|---|---|---|
| W-I ($NH_d$–$O_a$) | 0.00 | 0.00 | 100.00 | 100.00 |
| W-II ($NH_d$–$I_a$) | 9.98 | 8.97 | 0.00 | 0.00 |
| W-III ($OH_d$–$I_a$) | 15.48 | 15.48 | 0.00 | 0.00 |

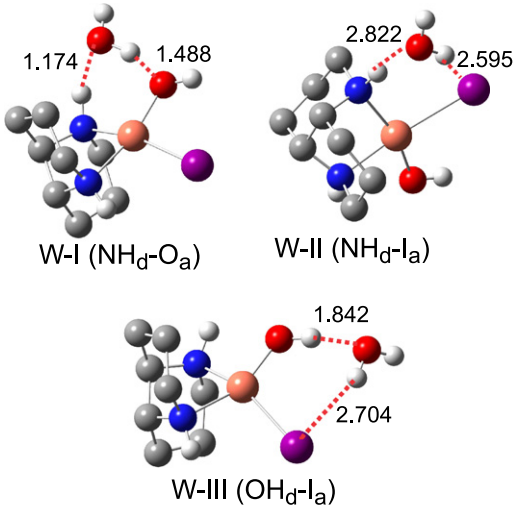


**Fig. 8.** Geometries of the three most stable conformers of the hydrogen bonded cluster of C-I Chair–Chair N-in H-ee [(R,R)-1,5-diaza-cis-decalin] copper (II) hydroxide iodine complex with a crystal water molecule obtained at the B3LYP/LanL2DZ level. Hydrogen atoms attached to the carbon atoms are not displayed for simplicity. The important hydrogen bond lengths (in Å) are also indicated.

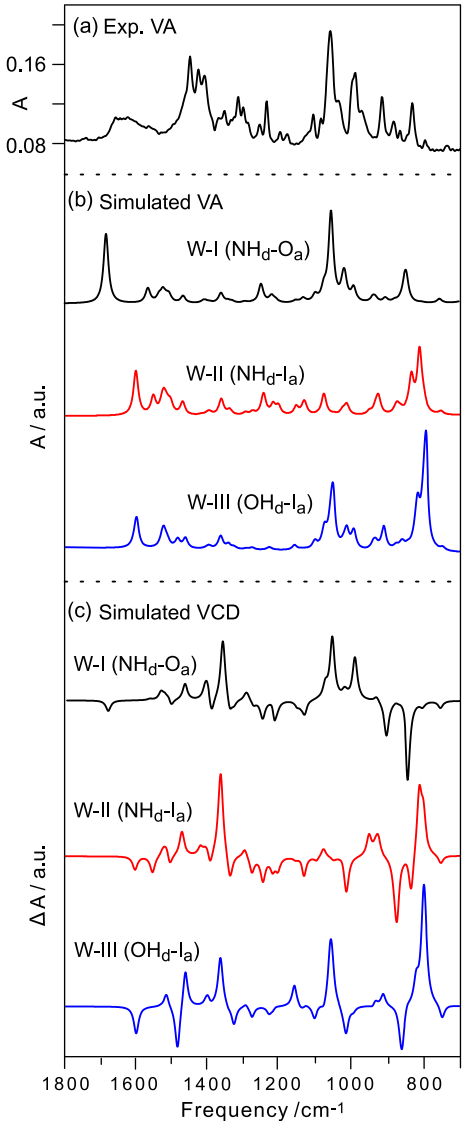


**Fig. 9.** Comparison of the experimental VA spectrum of the copper complex obtained with a KBr pellet with the simulated VA and VCD spectra of the three most stable hydrogen bonded conformers of C-I Chair–Chair N-in H-ee [(R,R)-1,5-diaza-cis-decalin] copper (II) hydroxide iodine complex with water, listed in Table 4, at the B3LYP/LanL2DZ level.

experimentally. In the longer wavelength region, the ECD spectrum measured with a higher concentration was again qualitatively captured by the W-I conformer. Overall, the comparison of the experimental and simulated ECD spectra discussed above led to the conclusion that W-I is the dominant species in solution at room temperature. It is gratifying to see that the detailed VA analysis pointed to the same conclusion that W-I is the main species at room temperature. Clearly, the inclusion of the crystal water in modeling is essential for achieving such consistent conclusions.

From Fig. 10, one can see that the main features in the simulated UV–Vis spectra of the three conformers are quite similar, although there are some minor differences in the appearances of the unresolved shoulders. Furthermore, the UV–Vis spectrum of W-I is comparable to that of C-I Chair–Chair N-in H-ee, (Fig. 7). Since $H_2O$ is not directly bonded to the copper atom, one may anticipate that its inclusion has only minor effects on the main electronic transition dipole moments of the metal complex. The predicted ECD spectra, on the other hand, are dramatically different among these three water containing conformers and from that

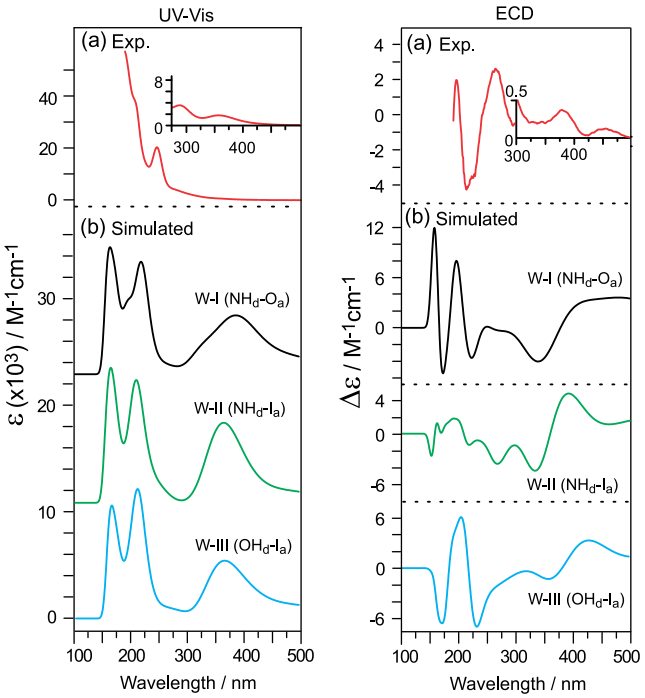


**Fig. 10.** Comparison of the experimental UV–Vis and ECD spectra of the copper complex with the corresponding simulated spectra of the three most stable hydrogen bonded conformers of C-I Chair–Chair N-in H-ee [(R,R)-1,5-diaza-cis-decalin] copper (II) hydroxide iodine complex with water, listed in Table 4, at the B3LYP/LanL2DZ level.

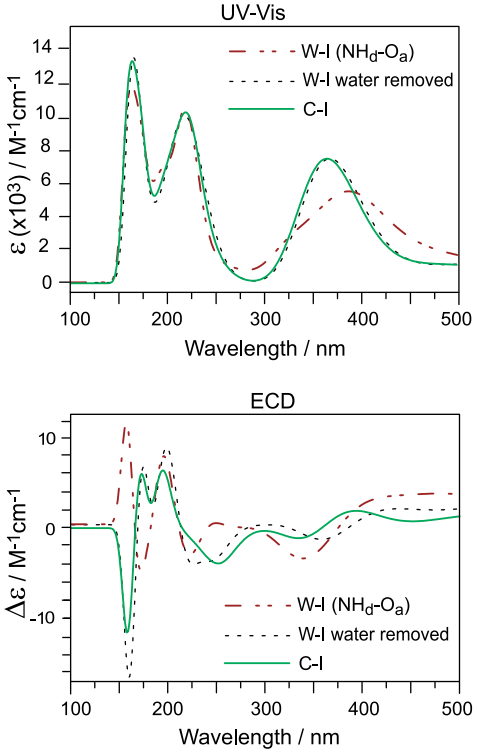


**Fig. 11.** Comparison of the simulated UV–Vis and ECD spectra at the B3LYP/LanL2DZ level of C-I Chair–Chair N-in H-ee [(R,R)-1,5-diaza-cis-decalin] copper (II) hydroxide iodine complex, of its most stable hydrogen bonded cluster W-I, and of the hypothetical molecular system where the structure of W-I was frozen and the crystal water was removed for spectral simulation.

of C-I Chair–Chair N-in H-ee (Fig. 7). This was somewhat surprising at first glance, especially since the UV–Vis spectra for all conformers remain similar upon inclusion of $H_2O$. On the other hand, ECD spectra can sense different hydrogen bonding environments much more sensitively than UV–Vis spectra, in a similar fashion as VCD verses VA in the mid-infrared region [36]. Drastic effects of hydrogen bonding interactions on the ECD spectra had been discussed only in a limited number studies [11], although the degree of effects seems to depend on the specific cases [12].

Why does the inclusion of crystal water have such a strong impact on the appearance of the ECD spectrum here? Since ECD spectra are in general highly sensitive to variations in dihedral angles of conformers, it would be of interest to examine if the changes in ECD are mainly due to the structural modifications of the complex itself upon hydrogen bonding with water. To test this, the geometry of W-I was frozen at its optimized geometry and then water was removed for the subsequent UV–Vis and ECD simulation. The resulting UV–Vis and ECD spectra are summarized in Fig. 11, together with those of W-I and C-I Chair–Chair N-in H-ee for comparison. Clearly, the UV–Vis spectra remain more or less the same throughout. It is interesting to note that the ECD spectrum of the frozen W-I with the crystal water removed looks very similar to that of C-I. This suggests that the small conformational changes induced by the hydrogen bonding interaction to water are not the main reason for the drastically different ECD appearances of C-I and W-I. Rather the associated magnetic transition dipoles and their orientations relative to the related electric transition dipoles have been modified to generate the noticeable changes in the ECD spectrum.

## 4. Conclusion

In the present report, extensive structural searches of the [(R,R)-1,5-diaza-cis-decalin] ligand and its associated copper(II) hydroxide iodine hydrate show that the ligand favors the Chair–Chair N-in H-ea conformation, whereas the same ligand in the copper complex favors the Chair–Chair N-in H-ee conformation. The comparison of the experimental VA and ECD spectra of the copper complex with the corresponding simulated spectra of [(R,R)-1,5-diaza-cis-decalin] copper (II) hydroxide iodine hydrate showed poor agreement. The inclusion of the hydrogen bonding interaction of crystal water with the complex resulted in one dominant hydrogen bonded cluster whose VA and ECD exhibit close resemblance to the experimental data. The current study demonstrates the importance of inclusion of the hydrogen bonding interaction with the crystal water in interpreting the experimental VA and ECD spectra. The results show that VA and ECD spectroscopy complemented with DFT calculations is a powerful method for probing not only conformations but also specific hydrogen bonding interactions in transition metal complexes.

## Acknowledgments

This research was funded by the University of Alberta, the Natural Sciences and Engineering Research Council of Canada, and the Canada Research Chairs Program. We thank Dr. J. Cooke and W. Moffat for their assistance in preparing KBr pellets and in the electronic circular dichroism measurements and Dr. C. Merten for discussions. We also gratefully acknowledge access to the computing facilities provided by the Academic Information and Communication Technology group at the University of Alberta.

## References

[1] X. Li, J. Yang, M.C. Kozlowski, Org. Lett. 3 (2001) 1137.
[2] M.C. Kozlowski, Z. Xu, A. Gil Santos, Tetrahedron 57 (2001) 4537.

[3] J. Fleischhauer, G. Raabe, A.G. Santo, J. Schiffer, A. Wollmer, Z. Naturforsch 53a (1998) 896.
[4] B. Ganguly, D.A. Freed, M.C. Kozlowski, J. Org. Chem. 66 (2001) 1103.
[5] Z. Xu, M.C. Kozlowski, J. Org. Chem. 67 (2002) 3072.
[6] A. Santos, W. Klute, J. Torode, V.P.W. Böhm, E. Cabrita, J. Runsink, R.W. Hoffmann, New J. Chem. (1998) 993.
[7] X. Li, L.B. Schenkel, M.C. Kozlowski, Org. Lett. 2 (2000) 875.
[8] G. Yang, Y. Xu, in: R. Naaman, D.N. Beratan, D.H. Waldeck (Eds.), Top. Curr. Chem., Volume: Electronic and Magnetic Properties of Chiral Molecules and Supramolecular Architectures, Springer-Verlag, Berlin Heidelberg, vol. 298, 2011, pp. 189.
[9] T. Mori, Y. Inoue, in: R. Naaman, D.N. Beratan, D.H. Waldeck (Eds.), Top. Curr. Chem., Volume: Electronic and Magnetic Properties of Chiral Molecules and Supramolecular Architectures, Springer-Verlag, Berlin Heidelberg, vol. 298, 2011, pp. 99.
[10] N. Berova, L. Di Bari, G. Pescitelli, Chem. Soc. Rev. 36 (2007) 914.
[11] J. Sÿebek, B. Gyurcsik, J. Sÿebestík, Z. Kejík, L. Bednárová, P. Bouř, J. Phys. Chem. A 111 (2007) 2750.
[12] H. Hussain, I. Ahmed, B. Schulz, S. Draeger, U. Flörke, G. Pescitelli, K. Krohn, Chirality 23 (2011) 617.
[13] M. Losada, Y. Xu, Phys. Chem. Chem. Phys. 9 (2007) 3127.
[14] M.J. Frisch, G.W. Trucks, H.B. Schlegel, G.E. Scuseria, M.A. Robb, J.R. Cheeseman, J.A. Montgomery Jr., T. Vreven, K.N. Kudin, J.C. Burant, J.M. Millam, S.S. Iyengar, J. Tomasi, V. Barone, B. Mennucci, M. Cossi, G. Scalmani, N. Rega, G.A. Petersson, H. Nakatsuji, M. Hada, M. Ehara, K. Toyota, R. Fukuda, J. Hasegawa, M. Ishida, T. Nakajima, Y. Honda, O. Kitao, H. Nakai, M. Klene, X. Li, J.E. Knox, H.P. Hratchian, J.B. Cross, C. Adamo, J. Jaramillo, R. Gomperts, R.E. Stratmann, O. Yazyev, A.J. Austin, R. Cammi, C. Pomelli, J.W. Ochterski, P.Y. Ayala, K. Morokuma, G.A. Voth, P. Salvador, J.J. Dannenberg, V.G. Zakrzewski, S. Dapprich, A.D. Daniels, M.C. Strain, O. Farkas, D.K. Malick, A.D. Rabuck, K. Raghavachari, J.B. Foresman, J.V. Ortiz, Q. Cui, A.G. Baboul, S. Clifford, J. Cioslowski, B.B. Stefanov, G. Liu, A. Liashenko, P. Piskorz, I. Komaromi, R.L. Martin, D.J. Fox, T. Keith, M.A. Al-Laham, C.Y. Peng, A. Nanayakkara, M. Challacombe, P.M.W. Gill, B. Johnson, W. Chen, M.W. Wong, C. Gonzalez, J.A. Pople, Gaussian 03, Revision B.01, Gaussian 03, Revision E.01., Gaussian, Inc., Pittsburgh, PA, 2003.
[15] P.J. Stephens, F.J. Devlin, C. Villani, F. Gasparrini, S. Levi Mortera, Inorg. Chem. Acta 361 (2008) 987.
[16] H. Sato, T. Taniguchi, K. Monde, S.-I. Nishimura, A. Yamagashi, Chem. Lett. 35 (2006) 364.
[17] H. Sato, T. Taniguchi, A. Nakahashi, K. Monde, A. Yamagashi, Inorg. Chem. 46 (2007) 6755.
[18] C. Merten, M. Amkreutz, A. Hartwig, J. Mol. Struct. 970 (2010) 101.
[19] W.L. Qian, S. Krimm, J. Phys. Chem. A 106 (2002) 6628.
[20] A. Kovacs, A. Szabo, D. Nemcsok, I. Hargittai, J. Phys. Chem. A 106 (2002) 5671.
[21] B. Kirchner, M. Reiher, J. Am. Chem. Soc. 124 (2002) 6206.
[22] M. Losada, H. Tran, Y. Xu, J. Chem. Phys. 128 (2008) 014508.
[23] G. Yang, Y. Xu, Phys. Chem. Chem. Phys. 10 (2008) 6787.
[24] A. Vlček Jr., S. Záliš, Coord. Chem. Rev. 251 (2007) 258.
[25] S. Miertus, E. Scrocco, J. Tomasi, Chem. Phys. 55 (1981) 117.
[26] J. Tomasi, M. Persico, Chem. Rev. 94 (1994) 2027.
[27] G. Yang, Y. Xu, J. Hou, H. Zhang, Y. Zhao, Chem. Eur. J. 16 (2010) 2518.
[28] Z. Su, Q. Wen, Y. Xu, J. Am. Chem. Soc. 128 (2006) 6755.
[29] M. Pecul1, D. Marchesan, K. Ruud, S. Coriani, J. Chem. Phys. 122 (2005) 024106.
[30] A. Klamt, G. Schüürmann, J. Chem. Soc. Perkin. Trans. 2 (1993) 799.
[31] C.C. Pye, T. Ziegler, Theo. Chem. Acc. 101 (1999) 396.
[32] L. Jensen, M. Swart, P.Th. Van Duijnen, J. Autschbach, Int. J. Quan. Chem. 106 (2006) 2479.
[33] C. Cappelli, S. Bronco, S. Monti, Chirality 17 (2005) 577.
[34] J. Sadlej, J. Cz Dobrowolski, J.E. Rode, M.H. Jamróz, Phys. Chem. Chem. Phys. 8 (2006) 101.
[35] G. Yang, Y. Xu, J. Chem. Phys. 130 (2009) 164506.
[36] See for example G. Yang, Y. Xu, J. Hou, H. Zhang, Y. Zhao, Dalton Trans. 39 (2010) 6953.

Dalton Transactions

Cite this: *Dalton Trans.*, 2012, **41**, 10817

www.rsc.org/dalton

PAPER

# Vibrational circular dichroism spectroscopy of two chiral binaphthyl diphosphine ligands and their palladium complexes in solution†

**Zahra Dezhahang, Christian Merten, Mohammad Reza Poopari and Yunjie Xu***

***Received 1st June 2012, Accepted 10th July 2012***
**DOI: 10.1039/c2dt31184d**



BINAP (2,2′-diphenylphosphino-1,1′-binaphthyl) is a unique binaphthyl diphosphine ligand with axial chirality. The palladium complexes of BINAP and of its derivative TOLBINAP have found extensive applications in the field of asymmetric syntheses. The conformational changes in the BINAP and TOLBINAP ligands before and after coordination with palladium have been investigated using density functional theory, vibrational absorbance (VA) and vibrational circular dichroism (VCD) spectroscopy. VA and VCD spectra of these two chiral ligands and their corresponding palladium complexes have been recorded in $CDCl_3$ solution. Extensive conformational searches have been carried out for both the ligands and the associated palladium complexes. Coordination with palladium has been found to introduce structural rigidity to the ligands. The calculated VA and VCD spectra of the ligands and complexes in the gas phase show substantial differences to the experimental data. Incorporation of the implicit polarisable continuum solvation model has provided much better agreement between theory and experiment, especially for the complexes, allowing clear identification of the species and conformations. This and the high specificity of VCD spectral signatures to chirality and to conformations suggest the potential applications of VCD spectroscopy for following these important catalytic species in solution reactions directly.

## Introduction

1,1′-Binaphthyl compounds are a special class of biaryl molecules. Considerable amounts of experimental effort have been concentrated on introducing structural modifications to the biaryl groups in order to improve the enantio-selectivity of the catalysts. It was reported that a smaller dihedral angle between the naphthyl rings may lead to better stereo-discrimination in some reactions.[1] BINAP (2,2′-diphenylphosphino-1,1′-binaphthyl, Fig. 1), a unique binaphthyl diphosphine chiral ligand devised by Noyori (winner of the Nobel Prize in Chemistry in 2001),[2] signifies an important milestone in the development of binaphthyl chemistry. BINAP exhibits axial chirality since the rotation about the bond linking the two naphthyl rings is strongly hindered. As a result of their highly stable chiral configuration, BINAP and its derivative TOLBINAP (also shown in Fig. 1) have found extensive applications in the field of asymmetric syntheses, such as hydrogenation of olefins[3] and ketones,[4] and isomerisation of allylamines,[5] and have demonstrated outstanding chirality discrimination abilities. Their complexes with transition metals, such as palladium, rhodium, and ruthenium, are widely used as catalysts in stereoselective organic syntheses, for example, in the commercial production of the enantiopure anti-inflammatory drug naproxen.[6] In particular, BINAP– and TOLBINAP–Pd complexes, the two titled complexes investigated here, have been utilized widely as catalysts for the amination of aryl halides, a practical synthetic route for C–N bond formation,[7,8] and for the Mannich-type C–C bond formation reactions.[9,10] For their extensive applications as catalysts in stereoselective syntheses, there has been intensive interest in their catalytic mechanism.[11,12] It is, however, highly challenging to establish a mechanism equivocally. While NMR spectroscopy and kinetic studies have been used widely to verify the existence of certain intermediate species and establish reaction orders, it is desirable to have other complementary techniques which can be applied directly in solution and which are also exquisitely

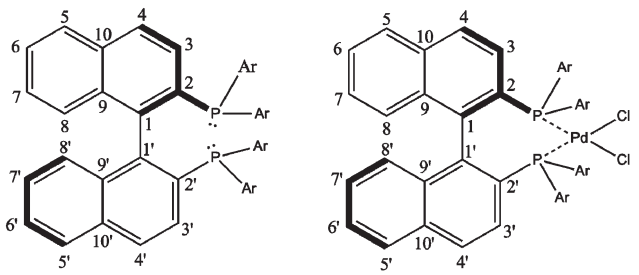


**Fig. 1** Structures of the BINAP (**1**, Ar═$C_6H_5$) and TOLBINAP (**2**, Ar═4-$CH_3$–$C_6H_4$) ligands (left) and their corresponding palladium complexes (right) investigated in this report.

*Department of Chemistry, University of Alberta, Edmonton, Alberta, Canada, T6G 2G2. E-mail: yunjie.xu@ualberta.ca; Fax: +1-780-492-8231; Tel: +1-780-492-1244*

†Electronic supplementary information (ESI) available. See DOI: 10.1039/c2dt31184d

sensitive to chirality of the species involved, such as reactants, intermediates, and products.

Vibrational circular dichroism (VCD) spectroscopy[13] has emerged in recent years as a powerful chiroptical spectroscopic tool to examine variation of dihedral angles in these BINAP metallic complexes and to potentially follow their catalytic processes. VCD spectroscopy measures the preferential absorption of the left *versus* right circularly polarized light accompanying a vibrational transition. VCD spectroscopy in combination with density functional theory (DFT) modeling[14] has been applied successfully to determine the absolute configurations of chiral molecules in solution, thanks to the significant advances in both the experimental technique and the theoretical modelling. In organometallic chemistry, VCD spectroscopy has been applied to probe structures and other properties of metal complexes of different chiral topologies.[15] For example, it has been used to study a star-burst type tetranuclear Ru(III) complex[16] and to evaluate the effects of counter ions in $Co(en)_3^{2+}$ complexes[17] and of low-lying electronic transitions in a spin-triplet bis-(biuretato) cobaltate(III) coordination complex.[18] Since neither the ligands nor their metal complexes had been studied using the VCD approach before, we measured the VCD spectra of the BINAP and TOLBINAP ligands, together with their respective palladium complexes, *i.e.* Pd(BINAP)$Cl_2$ and Pd(TOLBINAP)-$Cl_2$. One main objective is to examine the conformational changes, in particular the chiral dihedral angles, in the BINAP and TOLBINAP ligands before and after coordination to palladium. The second main objective is to assert how well the observed VCD features in solution can be produced by the theoretical modelling. To be able to evaluate the effects of solvation adequately is important since solvents may even alter a reaction mechanism and influence the enantiomeric excess of an asymmetric synthesis. These studies can be regarded as the first step towards establishing the VCD method as a new spectroscopic tool for monitoring reaction species in asymmetric syntheses involving BINAP and its derivative metallic catalysts.

## Results and discussions

### Experimental spectra

The experimental VA and VCD spectra of *R*-BINAP (**1**) and *R*-TOLBINAP (**2**) in $CDCl_3$ solution, obtained in the fingerprint region from the 1000–1700 $cm^{-1}$ region, are given in Fig. 2. The experimental VA and VCD spectra of the corresponding palladium complexes, *i.e.* *R*-Pd(**1**)$Cl_2$ and *R*-Pd(**2**)$Cl_2$ in $CDCl_3$, are also summarized in Fig. 2. The experimental VCD spectra of both *R*- and *S*-enantiomers of BINAP, TOLBINAP and Pd(TOL-BINAP)$Cl_2$ in $CDCl_3$ solution and their related noise levels are provided in Fig. S1, available as ESI.† As one can see, the VCD spectra of the enantiomeric pairs show good mirror images (see also "Experimental and computational details"). First of all, the VA spectra of the **1** and **2** ligands show easily recognizable resemblance to their respective metal complexes. This is not surprising since the VA bands in this region correspond largely to the ligand vibrational modes, whereas the metal related VA modes, such as the Pd–Cl stretching bands, are at ~290–310 $cm^{-1}$,[19] outside the range of the instrument. Despite their similarity, there are noticeable changes in the relative band intensities, especially for **2** and its complex. Secondly, although the most intense VCD features at ~1400 $cm^{-1}$ remain similar for **1** and its Pd complex, there are obvious changes in the 1100–1300 $cm^{-1}$ region going from the ligand to its Pd complex. For **2** and its Pd complex, the associated VCD spectra are drastically different from each other. These observations demonstrate the sensitivity of VCD features to the binding with Pd. Thirdly, the VA and VCD spectra of the **1** and **2** ligands are visibly different, although there are only four extra methyl groups at the *para* positions of the phenyl rings for **2** compared

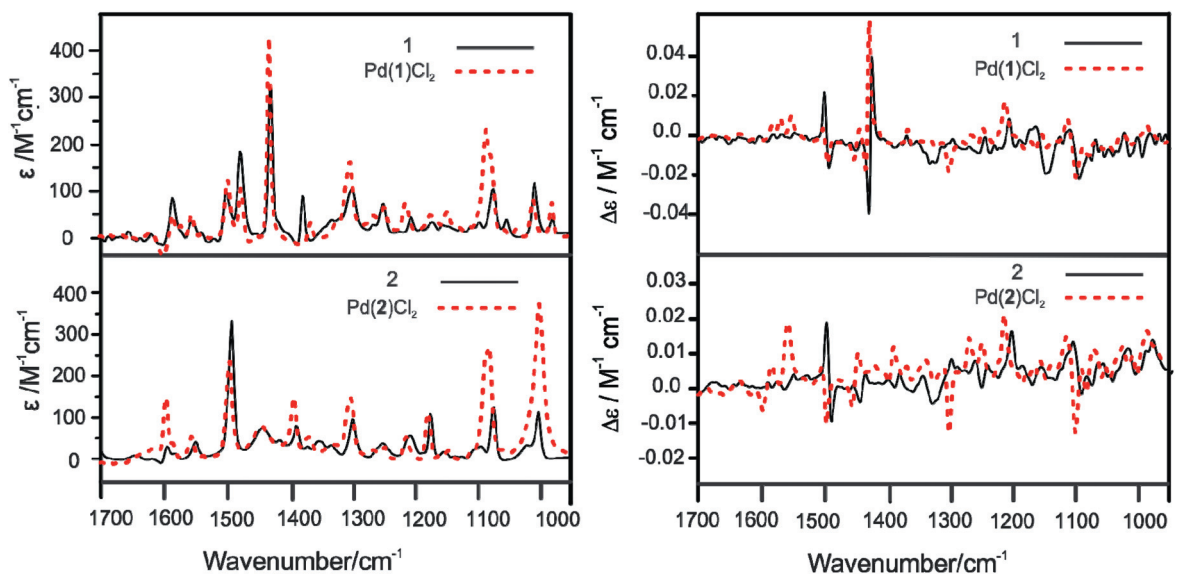


**Fig. 2** The experimental VA (left) and VCD (right) spectra of *R*-**1**, *R*-Pd(**1**)$Cl_2$, *R*-**2**, and *R*-Pd(**2**)$Cl_2$ in $CDCl_3$.

 

to **1**. For example, the strongest VA and VCD features in **1** are noticeably weak or non-existing in **2**.

### Conformations of the 1 and 2 ligands and of the Pd(1)$Cl_2$ and Pd(2)$Cl_2$ complexes

1,1′-Binaphthyl has a rotation barrier of 23.5 kcal $mol^{-1}$ [20] around the 1–1′ C–C bond, thus allowing the isolation of the related enantiomers at room temperature. It was discovered in 1971 that the racemic solution of 1,1′-binaphthyl underwent spontaneous resolution to form either *R* or *S* enantiomeric crystals.[21] The substitution at the 2 and 2′ positions, on the other hand, is likely to introduce strong steric repulsion, thus preventing rotation about the bridge C–C bond and generating very stable enantiomers and transoid or cisoid conformers where the dihedral angle between the two naphthalene rings is larger or smaller than 90 degrees, respectively. This dihedral angle was reported to be as high as 108 degrees with the large $OSO_2CF_3$ substituents and as low as 52 degrees with a bridge substituent $PO_4H$ at the 2 and 2′ positions of 1,1′-binaphthyl, respectively, in a previous VCD study.[22] Because of the bulky substituents at the 2 and 2′ positions in the case of **1** and **2**, one may expect that the two naphthalene rings adopt a roughly perpendicular position with each other due to the steric hindrance and spatial repulsion. At the same time, the phenyl groups may adopt different spatial orientation with respect to each other, and this conformational freedom may be coupled to the dihedral angle mentioned before. Our searches for possible conformers by using the DFT method ended up with three conformers whose geometries are depicted in Fig. 3. The dihedral angle values predicted for these conformers are listed in Table 1. Several interesting points warrant attention with regard to the conformational geometries obtained. First, the dihedral angles between two naphthalene rings are very close to 90 degrees, *i.e.* the two rings are perpendicular to each other. The 2–1–1′–2′ dihedral angle (see Fig. 1 for atom numbering), *i.e.*, the dihedral angle between two naphthalene rings, varies slightly from ~87 degrees to ~95 degrees for the three conformers of the **1** and **2** ligands. This implies that there is not much flexibility coming from the naphthalene part of such molecules. Next we consider the possible conformers resulting from relative orientations of the phenyl rings. The two phenyl rings, which are connected to two different P atoms and are closest to each other, were arranged in three possible starting orientations, *i.e.* face to face, displaced face to face, and edge to face, analogous to the benzene dimer.[23] It was found that the other two phenyl rings adjusted themselves in the geometry optimization processes accordingly, even if one put them in different starting orientations. Overall, this resulted in the three possible conformers.

In Table 2, the relative energies, the relative Gibbs free energies, and the corresponding Boltzmann population factors of the three stable conformers of **1** and **2** in the gas phase are given. The relative stability of the **1** conformers in the gas phase can be understood in terms of the π–π stacking interactions of the phenyl groups. Three possible conformations previously proposed for the benzene dimers by Burley and Petsko[23] are based on the electrostatic interactions:[24] face to face (or parallel), displaced face to face, and edge to face. According to this model, the face to face interaction destabilizes the dimer because of the repulsive nature of the interaction, whereas the face to edge orientation is a true ground state due to π–σ attraction. The stabilities of the first and second conformers of each ligand (**1** and **2**) have their adjacent phenyl groups forming the edge to face and the displaced face to face orientations which are more favourable. The third conformer which has the face to face spatial arrangement is the least populated one in the gas phase.

Coordination to palladium introduces further constraints to the spatial orientation of the **1** and **2** ligands (Fig. 1) in Pd(**1**)$Cl_2$ and Pd(**2**)$Cl_2$. Despite extensive searches, only one conformer was located for the Pd(**1**)$Cl_2$ and Pd(**2**)$Cl_2$ complexes where the di-phenyl rings take on the edge–face arrangement. Clearly, coordination increases the rigidity of the di-phenyl ligand parts. As a result, the rigidity of the entire structure is significantly enhanced. The values of the associated dihedral angle between the two naphthalene rings are given in Table 1 for comparison

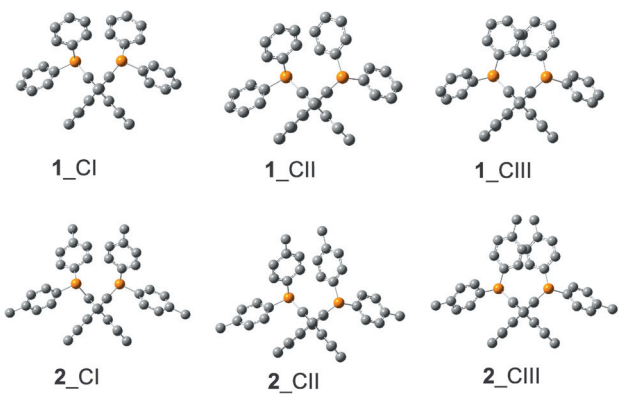


**Fig. 3** Three most stable conformers of *R*-**1** and *R*-**2** at the B3LYP/6-31G(d,p) level viewed along the C1–C1′ bond.

**Table 1** Calculated dihedral angle values (in degrees) between the two naphthalene rings for **1** and **2** and their corresponding Pd complexes

| Ligands | **1**_CI | **1**_CII | **1**_CIII | **2**_CI | **2**_CII | **2**_CIII |
|---|---|---|---|---|---|---|
| Angle[a] 2–1–1′–2′ | 86.64 (88.31) | 94.17 (90.05) | 94.82 (95.04) | 86.35 (88.34) | 94.47 (94.10) | 95.05 (95.06) |
| Complexes | | Pd(**1**)$Cl_2$ | | | Pd(**2**)$Cl_2$ | |
| Angle[a] 2–1–1′–2′ | | 75.24 (74.58) | | | 75.08 (74.45) | |

[a] The values were calculated at the B3LYP/6-31G(d,p) level for the **1** and **2** ligands and all atoms of the complexes except Pd where the LanL2DZ basis set was used for the Pd atom in both complexes. The gas phase values are listed first and the values with the polarizable continuum model (PCM) of the chloroform solvent are in brackets. Please see the "Inclusion of solvent effects with PCM" section for a description of PCM.

with those of ligand conformers. As one can see, the dihedral angles are essentially the same for both Pd complexes and are considerably smaller than those of the related ligand conformers.

### Interpretation of the experimental VA and VCD spectra of the 1 and 2 ligands and their palladium complexes

**The gas phase simulation.** The calculated population weighted VA and VCD spectra of the three conformers of **1** are compared with the related experimental data in Fig. 4, left panel. The corresponding comparison of **2** is given in Fig. 4, right panel. The simulated VA and VCD spectra for each conformer of **1** and **2** are provided in Fig. S2, ESI.† While the VA spectra of the three conformers of **1** are essentially the same, noticeable differences are present in the VCD spectra. A similar observation can be made for the conformers of **2**. In particular, the differences in the VCD features among the conformers of **2** are quite prominent. To get a rough understanding of the large number of VA bands encountered here, related calculations have been performed for 1,1′-binaphthyl which shares the same core structure as **1** and **2**. It is tedious and not so informative to provide detailed VA band assignments. Rather, the comparison with the simpler 1,1′-binaphthyl system is provided in Fig. S3, ESI.† Most of the prominent bands present are from the C–C stretching and C–H bending vibrational modes of the binaphthyl rings which are the common parts among **1**, **2** and 1,1′-binaphthyl. More detailed discussions are given in Fig. S2.† In Fig. 4, the experimental VA and VCD spectra are also compared with the corresponding calculated spectra in the gas phase. Overall, for the **1** and **2** ligands, the calculated and experimental VA spectra are in reasonable agreement. The same cannot be said for the VCD comparison, especially for that of **2**. For example, the strong VCD signature predicted at the ~1550 $cm^{-1}$ region was not observed experimentally for **2**.

**Table 2** Predicted relative energies and Gibbs free energies (in kcal $mol^{-1}$) of the three most stable conformers of the **1** and **2** ligands and their Boltzmann factors at room temperature

| Conf. | $\Delta E^a$ | $\Delta G^a$ | pop% ($\Delta E$) | pop% ($\Delta G$) |
|---|---|---|---|---|
| **1**_CI | 0.00 (0.17) | 1.52 (1.12) | 49.98 (35.92) | 45.70 (8.64) |
| **1**_CII | 0.13 (0.00) | 0.00 (0.31) | 40.13 (47.82) | 50.81 (34.01) |
| **1**_CIII | 0.96 (0.64) | 1.59 (0.00) | 9.90 (16.24) | 3.49 (57.35) |
| **2**_CI | 0.00 (3.67) | 0.31 (4.36) | 50.33 (0.15) | 36.48 (0.06) |
| **2**_CII | 0.11 (0.00) | 0.00 (0.00) | 41.72 (73.13) | 61.91 (97.88) |
| **2**_CIII | 1.09 (0.60) | 2.16 (2.29) | 7.96 (26.52) | 1.61 (2.06) |

[a] $\Delta E$ and $\Delta G$ values were calculated at the B3LYP/6-31G(d,p) level. The gas phase values are listed first and the values with PCM of chloroform solvent are in brackets.

The experimental and calculated VA and VCD spectra of Pd(**1**)$Cl_2$ and Pd(**2**)$Cl_2$ are compared in Fig. 5. Again, the VA spectra show reasonable agreement between experiment and theory for both complexes, while the same cannot be said about the VCD spectral comparison. Since these two complexes are more rigid than their corresponding ligands and have only one dominant conformer, one would expect better agreement between the simulated and experimental spectra because any deviations due to conformational degrees of freedom are no longer a concern. The above observation indicates that other factors must be responsible for this. Larger basis sets with more sophisticated polarization and diffuse functions were considered

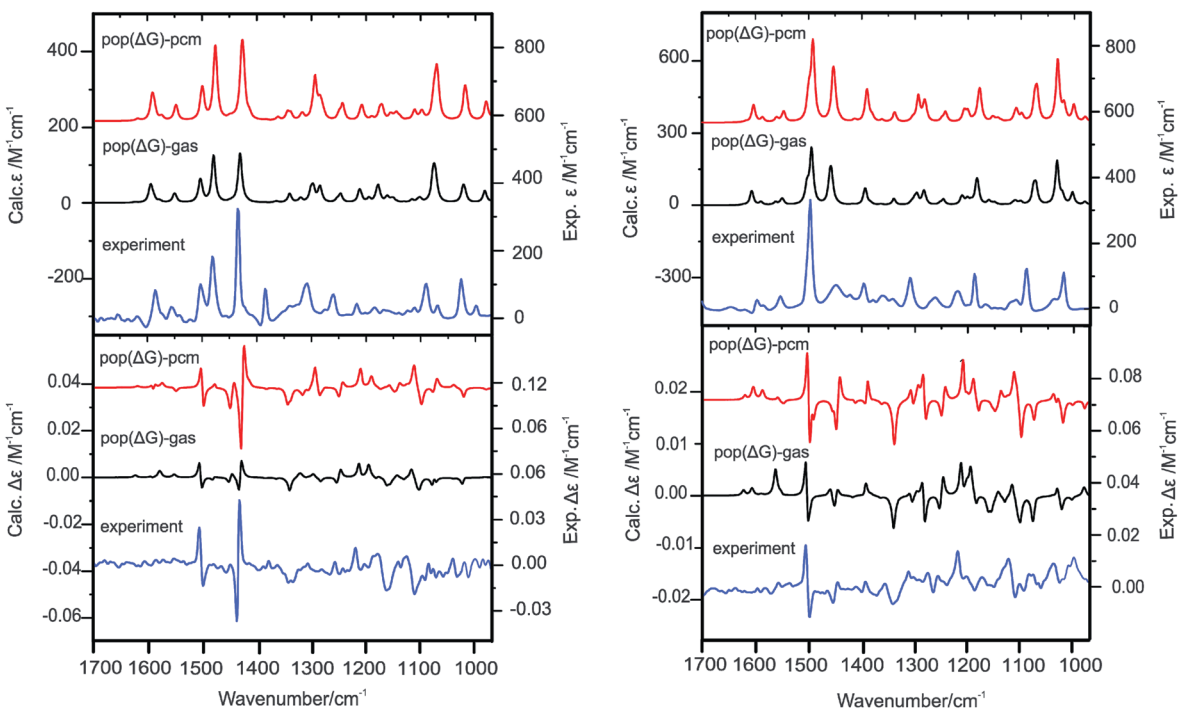


**Fig. 4** Comparison of the simulated VA and VCD spectra in the gas phase and with the PCM for chloroform with the corresponding experimental spectra of **1** (left) and **2** (right).

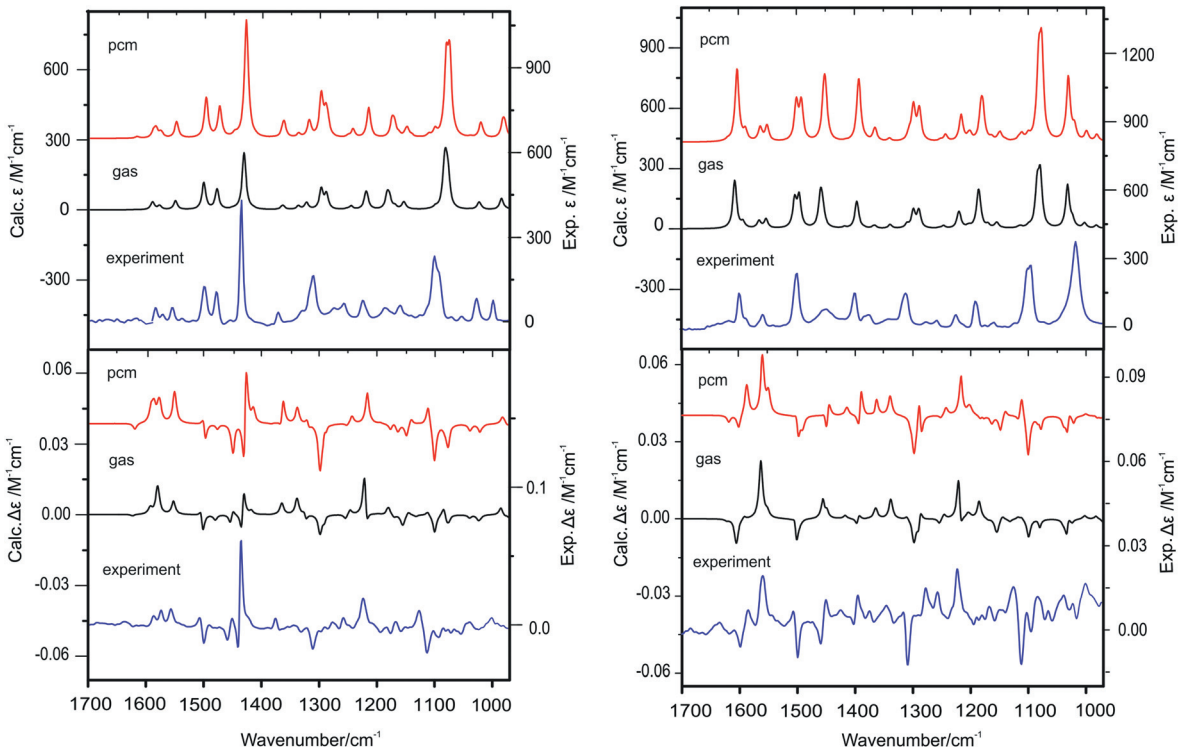


**Fig. 5** Comparison of the simulated VA and VCD spectra in the gas phase and with the PCM for chloroform with the corresponding experimental spectra of Pd(**1**)$Cl_2$ (left) and Pd(**2**)$Cl_2$ (right).

in order to better describe the interaction with a transition metal center. Another possible source of discrepancy is the effect of solvent. Although the effects of DMSO were found to be negligible in the previous VCD study of the small 1,1′-binaphthyl derivatives,[22] their effects on the transition metal complexes may be much more severe. These considerations are described in the next two sections.

**Basis set consideration.** The previously used basis set 6-31G-(d,p) is comparatively small and may in general influence the results of spectral calculations since weak intramolecular interactions, such as those between the phenyl rings, might not be accurately described. To test if the basis set selection is the reason for the discrepancies observed between the simulated and experimental data, several basis sets with various polarizations and diffuse functions, *i.e.* 6-31+G(d), 6-31+G(d,p), 6-31G-(2d,2p), 6-31++G(d,p), were also used for the C, H, Cl, and P atoms with the LanL2DZ basis set for the Pd atom. The geometry of the Pd(**2**)$Cl_2$ complex was re-optimized and the VA and VCD spectra of the complex re-simulated with the B3LYP functional and the new basis sets chosen. The results are summarized in Fig. 6. We chose to do such testing on one representative complex because the targeted system is quite large with 93 atoms and 438 electrons and its geometry optimization and frequency calculation took a significant amount of time. As clearly demonstrated in Fig. 6, the simulated spectra obtained with all these basis sets are comparable to each other and no significant improvement was achieved by increasing the size of the basis set. It thus appears that for a rigid metal complex with one main conformer, adding polarization and diffuse functions does not alter the appearance of the VA or VCD features noticeably.

**Inclusion of solvent effects with PCM.** A solvent may have a significant effect on stability of solute conformers since it can establish strong explicit solute–solvent hydrogen-bonding interactions[25] and/or provide an implicit dielectric environment. Since $CDCl_3$ is unlikely to form any strong hydrogen bonding interaction with the bulky ligands and their complexes investigated here, we treated the solvent by applying an integral equation formalism (IEF) version of the PCM solvation model.[26] In this model, the solvent is treated as a continuum dielectric environment and no explicit intermolecular interactions are taken into account. In this continuum dielectric environment, the solute is hosted inside a molecularly shaped cavity defined through interlocking van der Waals spheres centered at the atomic positions. The electrostatic, dispersion, repulsion, and cavity contributions are included for the energy calculations. Geometries of the predicted conformers were re-optimized and harmonic frequency calculations and intensities of VA and VCD bands were re-calculated. The calculated dihedral angles, the relative energies and the Gibbs free energies of all conformers of the **1** and **2** ligands and their palladium complexes obtained with the PCM of chloroform are listed in Tables 1 and 2, respectively. Indeed, the solvent has noticeable effects on the relative stability of conformers for the chiral ligands. Although the geometries of individual conformers appear more or less the same with the PCM of chloroform solvent as in the gas phase, such a solvent environment may affect the relative stability of the conformers and optical responses to the chiral polarized light. Indeed, the

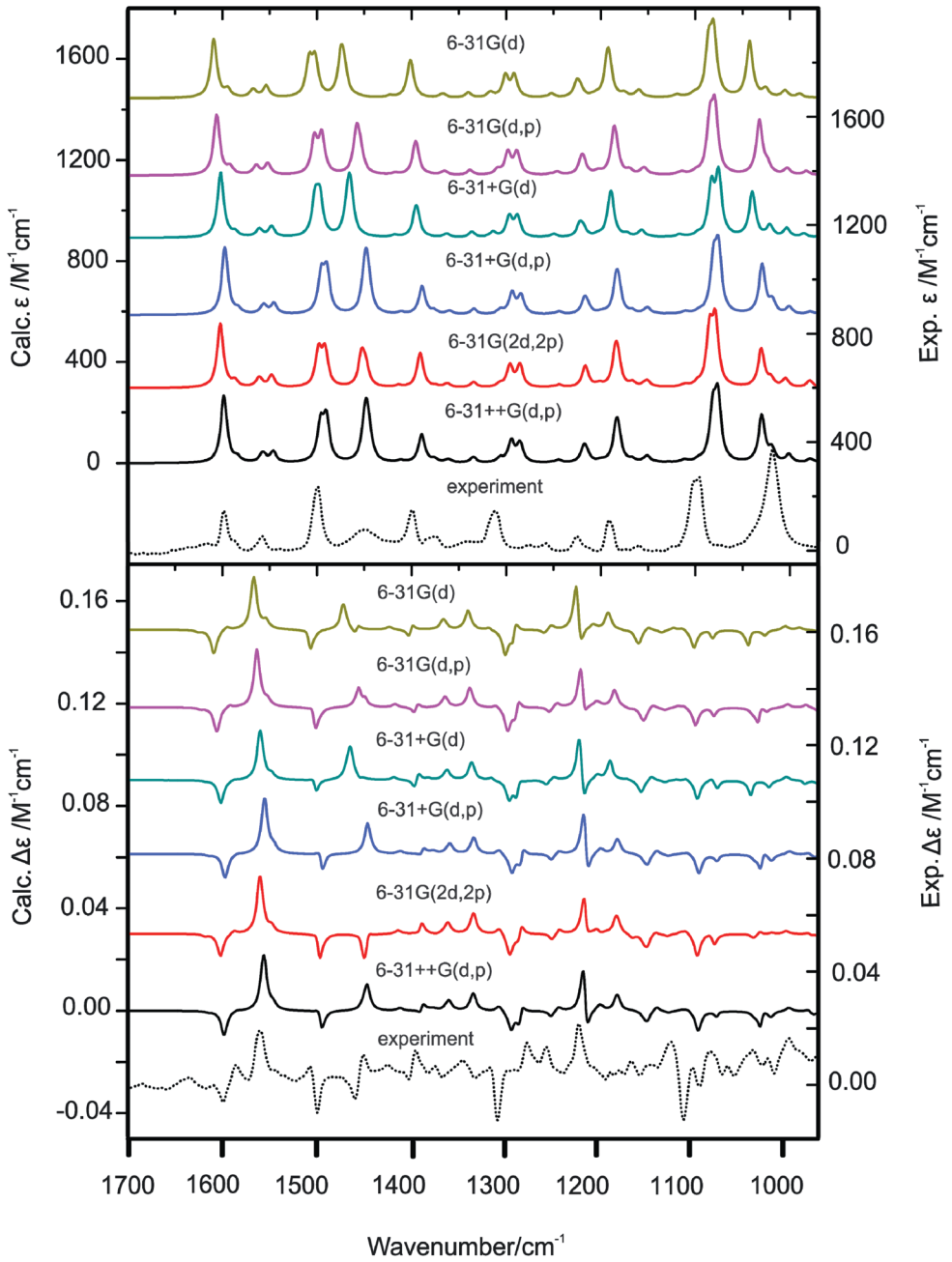


**Fig. 6** Comparison of the experimental VA and VCD spectra of Pd(**2**)$Cl_2$ with the corresponding calculated spectra using several different basis sets.

relative stability of the three conformers of **1** and **2** changes. Their relative energies, the relative Gibbs free energies, and the corresponding Boltzmann population factors with PCM are given in Table 2, while the corresponding values for the dihedral angle between the two naphthalene rings are summarized in Table 1. The calculated VA and VCD spectra of **1** and **2** with PCM are also included in Fig. 4 for comparison with the experimental data. The corresponding simulated spectra of the individual conformers of the **1** and **2** ligands are provided in Fig. S4, ESI.†

The simulated VA and VCD spectra of the two palladium complexes with **1** and **2** with PCM are provided in Fig. 5 for comparison with the gas phase calculation and the associated experimental data. The values for the dihedral angle between the two naphthalene rings for these two complexes with PCM are also summarized in Table 1. There are a number of bands which are not visible in the gas phase simulation but become much more prominent in the PCM spectra. For instance, for both Pd complexes, the positive–negative bands at 1100 $cm^{-1}$, which correspond to a mixture of the C=C vibrational modes and the C–H bending of naphthalene rings, appear only in the PCM spectra. For Pd(**2**)$Cl_2$, the VCD signatures predicted with PCM in the 1600–1400 $cm^{-1}$ region show very good agreement with the experimental data. The corresponding gas phase features, on the other hand, are very different from the experimental ones, making it not possible to draw any definite conclusion. Overall,

 

the calculated VA and VCD spectra with PCM are in much better agreement with the experimental data than the gas phase ones, allowing one to identify the species and possible conformers in solution confidently.

## Experimental and computational details

*R*-**1**, *R*-**2**, *R*-Pd(**1**)$Cl_2$ (purity 97%) and *R*-Pd(**2**)$Cl_2$ (purity 97%) samples were purchased from Sigma Aldrich and used without further purification. Sample solutions were prepared using deuterated chloroform, $CDCl_3$ (Sigma Aldrich, purity 99.9%). The VA absorbance coefficients were optimized to be in the range of 0.2 to 0.8 for the main vibrational bands in the 1000–1800 $cm^{-1}$ region for the subsequent VCD measurements by varying sample concentrations and path lengths. The optimum concentration and path length used are 0.1 M and 100 μm, respectively. The VA and VCD spectra were collected using a Fourier transform IR spectrometer (Vertex 70, Bruker) which is equipped with a PMA 50 VCD module (Bruker).[27] Each VCD spectrum was averaged over 25 000 recorded in four blocks of 1 h accumulation time and the related solvent spectrum under identical condition was subtracted off for base line correction. Because $CDCl_3$ exhibits a strong absorption band at ~920 $cm^{-1}$, the usable region of the measured spectra is from ~970 to 1700 $cm^{-1}$. For BINAP, TOLBINAP and Pd(TOLBINAP)$Cl_2$ whose *S*-enantiomers were available to us commercially, comparisons of the VCD spectra of the *R*- and *S*-enantiomers of these molecular systems in $CDCl_3$ solution are provided in Fig. S1,† together with their related noise levels. The noise levels were obtained as described on page 240 of ref. 13*a*. Each enantiomeric pair shows good mirror image spectral features, except a few broad features at the very low wavenumber region. This is likely due to the strong absorption by the solvent starting at about 970 $cm^{-1}$. The VCD spectrum of Pd(BINAP)$Cl_2$ is expected to have similar good quality as the other three systems studied.

Geometry optimization, harmonic vibrational frequencies, and intensities of vibrational and vibrational circular bands of all conformers of the **1** and **2** ligands and their related palladium complexes were performed using the Gaussian 03 program packages.[28] Density functional theory with the B3LYP functional and the 6-31G(d,p) basis set was used for all the results reported. Several basis sets, *i.e.* 6-31+G(d), 6-31+G(d,p), 6-31G-(2d,2p), 6-31++G(d,p), were also used for the C, H, P, Cl atoms and LanL2DZ for the Pd atom for the calculations of Pd(**2**)$Cl_2$. Lorentzian band shape with a half width at half height of 4 $cm^{-1}$ is used to simulate all the VA and VCD spectra. To properly account for the solvent effects of $CDCl_3$, an integral equation formalism (IEF) version of the PCM solvation model[26] was utilized where the solvent is treated as a continuum dielectric environment with a dielectric constant of 4.71.

## Conclusions

In this report, conformational analyses for the **1** and **2** ligands show that the naphthalene rings are nearly rigid, while the flexibility of the ligands originates from the orientations of the phenyl rings with respect to each other. The flexibility of both ligands decreases upon coordination to the palladium metal ion. The VA and VCD measurements of both ligands and the complexes show noticeable differences from the calculated ones in the gas phase. In particular, the differences between experiment and theory are so large for the two palladium complexes studied here that it would be extremely difficult to identify them based on the VA and VCD data. Inclusion of the solvent effects with PCM in the calculations results in much better agreement for both VA and VCD spectra of all the ligands and complexes studied, allowing the species and their conformations to be identified. With proper care for locating the possible conformers and accounting for solvent effects, one can potentially use VA and especially VCD spectroscopy, because of its high sensitivity to chirality and conformation, to follow these important species in reactions.

## Acknowledgements

This research was funded by the University of Alberta, the Natural Sciences and Engineering Research Council of Canada, and the Canada Research Chairs Program. CM thanks the Alexander von Humboldt foundation for a Feodor-Lynen postdoctoral fellowship. We gratefully acknowledge access to the computing facilities provided by the Academic Information and Communication Technology group at the University of Alberta.

## References

1 I. G. Rios, A. Rosas-Hernandez and E. Martin, *Molecules*, 2011, **16**, 970–1010, DOI: 10.3390/molecules16010970.
2 R. Noyori and T. Ohkuma, *Angew. Chem., Int. Ed.*, 2001, **40**(1), 40–73.
3 T. Ohkuma, M. Kitamura and R. Noyori, *Catalytic Asymetric Synthesis*, John Wiley & Sons, 2nd edn, 2000, pp. 1–110.
4 R. Noyori, T. Ohkuma, M. Kitamura, H. Takaya, N. Sayo, H. Kumobayashi and S. Akutagawa, *J. Am. Chem. Soc.*, 1987, **109**, 5856–5858.
5 S. Akutagawa and K. Tani, *Catalytic Asymmetric Synthesis*, John Wiley & Sons, 2nd edn, 2000, pp. 145–161.
6 R. Noyori, *Asymmetric Catalysis in Organic Synthesis*, John Wiley & Sons, 1994.
7 J. F. Hartwig, in *Handbook of Organopalladium Chemistry for Organic Synthesis*, ed. E. I. Negishi, Wiley-Interscience, New York, 2002, vol. 1, p. 1051.
8 A. R. Muci and S. L. Buchwald, *Top. Curr. Chem.*, 2002, **219**, 131–209.
9 E. F. Kleinman, in *Comprehensive Organic Synthesis*, ed. B. M. Trost and I. Fleming, Pergamon, Oxford, 1991, ch. 4.1, vol. 2.
10 Y. Hamashima, N. Sasamoto, D. Hotta, H. Somei, N. Umebayashi and M. Sodeoka, *Angew. Chem., Int. Ed.*, 2005, **44**, 1525–1529.
11 J. Hao, M. Hatano and K. Mikami, *Org. Lett.*, 2000, **2**, 4059–4062.
12 S. Shekhar, P. Ryberg, J. F. Hartwig, J. S. Mathew, D. G. Blackmond, E. R. Strieter and S. L. Buchwald, *J. Am. Chem. Soc.*, 2006, **128**(11), 3584–3591.
13 (*a*) L. A. Nafie, *Vibrational Optical Activity: Principles and Applications*, John Wiley & Sons, Ltd, Chichester, 2011; (*b*) Y. He, B. Wang, R. K. Dukor and L. A. Nafie, *Appl. Spectrosc.*, 2011, **65**(7), 699–723; (*c*) G. Yang and Y. Xu, Vibrational circular dichroism spectroscopy of chiral molecules, in *Top. Curr. Chem., Volume: Electronic and Magnetic Properties of Chiral Molecules and Supramolecular Architectures*, ed. R. Naaman, D. N. Beratan and D. H. Waldeck, Springer-Verlag, Berlin, Heidelberg, 2011, vol. 298, pp. 189–236.
14 (*a*) P. J. Stephens, F. J. Devlin and J. J. Pan, *Chirality*, 2008, **20**(5), 643–663; (*b*) M. Gábor, T. György and V. Elemér, Vibrational circular dichroism, *WIREs Comput. Mol. Sci.*, 2011, **1**, 403–425, DOI: 10.1002/wcms.39.
15 (*a*) F. D. Montigny, L. Guy, G. Pilet, N. Vanthuyne, C. Roussel, R. Lombardi, T. B. Freedman, L. A. Nafie and J. Crassous, *Chem. Commun.*, 2009, 4841–4843; (*b*) V. A. Soloshonok, T. Ono, H. Ueki,

N. Vanthuyne, T. S. Balaban, J. Brück, H. Fliegl, W. Klopper, J.-V. Naubron, T. T. T. Bui, A. F. Drake and C. Roussel, *J. Am. Chem. Soc.*, 2010, **132**(30), 10477–10483; (*c*) C. Merten, M. Amkreutz and A. Hartwig, *J. Mol. Struct.*, 2010, **970**, 101–105.
16 (*a*) H. Sato, F. Sato, M. Taniguchi and A. Yamagishi, *Dalton Trans.*, 2012, **41**, 1709–1712; (*b*) H. Sato, T. Taniguchi, A. Nakahashi, K. Monde and A. Yamagishi, *Inorg. Chem.*, 2007, **46**, 6755–6766.
17 V. P. Nicu, M. Heshmat and E. J. Baerends, *Phys. Chem. Chem. Phys.*, 2011, **13**, 8811–8825.
18 C. Johannessen and P. W. Thulstrup, *Dalton Trans.*, 2007, 1028–1033.
19 (*a*) B. J. V. Verkuijl, B. Schuur, A. J. Minnaard, J. G. de Vries and B. L. Feringa, *Org. Biomol. Chem.*, 2010, **8**, 3045–3054; (*b*) C. H. Perry, D. P. Athans, E. F. Young, J. R. Durig and B. R. Mitchell, *Spectrochim. Acta*, 1967, **23A**, 1137–1147.
20 A. S. Cooke and M. M. Harris, *J. Chem. Soc.*, 1963, 2365–2373.
21 R. E. Pincock, R. R. Perkins, A. S. Ma and K. R. Wilson, *Science*, 1971, **174**, 1018–1020.
22 V. Setnička, M. Urbanová, P. Bouř, V. Král and K. Volka, *J. Phys. Chem. A*, 2001, **105**(39), 8931–8938.
23 S. K. Burley and G. A. Petsko, *Science*, 1985, **229**, 23–28.
24 C. A. Hunter and J. K. M. Sanders, *J. Am. Chem. Soc.*, 1990, **112**(14), 5525–5534.
25 (*a*) M. R. Poopari, Z. Dezhahang, G. Yang and Y. Xu, *ChemPhysChem*, 2012, **13**, 2310–2321; (*b*) P. Zhu, G. Yang, M. R. Poopari, Z. Bie and Y. Xu, *ChemPhysChem*, 2012, **13**, 1272–1281.
26 J. Tomasi, B. Mennucci and R. Cammi, *Chem. Rev.*, 2005, **105**, 2999–3093.
27 M. Losada and Y. Xu, *Phys. Chem. Chem. Phys.*, 2007, **9**, 3127–3135.
28 Gaussian 03, Revision B.01, M. J. Frisch, G. W. Trucks, H. B. Schlegel, G. E. Scuseria, M. A. Robb, J. R. Cheeseman, J. A. Montgomery Jr., T. Vreven, K. N. Kudin, J. C. Burant, J. M. Millam, S. S. Iyengar, J. Tomasi, V. Barone, B. Mennucci, M. Cossi, G. Scalmani, N. Rega, G. A. Petersson, H. Nakatsuji, M. Hada, M. Ehara, K. Toyota, R. Fukuda, J. Hasegawa, M. Ishida, T. Nakajima, Y. Honda, O. Kitao, H. Nakai, M. Klene, X. Li, J. E. Knox, H. P. Hratchian, J. B. Cross, C. Adamo, J. Jaramillo, R. Gomperts, R. E. Stratmann, O. Yazyev, A. J. Austin, R. Cammi, C. Pomelli, J. W. Ochterski, P. Y. Ayala, K. Morokuma, G. A. Voth, P. Salvador, J. J. Dannenberg, V. G. Zakrzewski, S. Dapprich, A. D. Daniels, M. C. Strain, O. Farkas, D. K. Malick, A. D. Rabuck, K. Raghavachari, J. B. Foresman, J. V. Ortiz, Q. Cui, A. G. Baboul, S. Clifford, J. Cioslowski, B. B. Stefanov, G. Liu, A. Liashenko, P. Piskorz, I. Komaromi, R. L. Martin, D. J. Fox, T. Keith, M. A. Al-Laham, C. Y. Peng, A. Nanayakkara, M. Challacombe, P. M. W. Gill, B. Johnson, W. Chen, M. W. Wong, C. Gonzalez and J. A. Pople, *GAUSSIAN 03 (Revision C.02)*, Gaussian, Inc., Pittsburgh, PA, 2003.



 

CHEMISTRY
AN ASIAN JOURNAL
ACES
FULL PAPER

DOI: 10.1002/asia.201300070

# Vibrational Circular Dichroism Spectroscopy of Three Multidentate Nitrogen Donor Ligands: Conformational Flexibility and Solvent Effects

**Zahra Dezhahang, Mohammad Reza Poopari, and Yunjie Xu*[a]**

**Abstract:** A series of multidentate nitrogen donor ligands have been synthesized and characterized and their conformational distributions in solution have been investigated. Vibrational absorption (VA) and vibrational circular dichroism (VCD) spectroscopy, complemented with DFT calculations, have been used to probe the conformations of these important ligands in solution directly. These three ligands demonstrate very different conformational flexibility; the pyridine subunits and amine groups may adopt a number of different conformations. Experimental VA and VCD data measured in $CDCl_3$ have been compared to the theoretical spectra of all possible most stable conformers. Solvent effects have been taken into account by using the implicit polarizable continuum model and explicit solvation model. The explicit hydrogen-bonding solvation model is important for explaining the VCD sign-reverse phenomenon in the amide I region. Good agreement has been achieved between experimental and predicted spectra for all three ligands; thus allowing detailed examination of the related conformational structures and distributions in solution.

**Keywords:** conformational analysis · hydrogen-bonding interactions · N ligands · solvent effects · vibrational circular dichroism spectroscopy

## Introduction

Picolylamine-type ligands, such as *N*,*N*′-bis(pyridine-2-ylmethylene)-(*S*,*S*)-1,2-cyclohexanediamine (*SS*-**1**), *N*,*N*′-bis(-pyridine-2-ylmethyl)-(*S*,*S*)-1,2-cyclohexanediamine (*SS*-**2**), and {(*S*,*S*)-2-[(2-pyridinylcarbonyl)amino]cyclohexyl}-2-pyridinecarboxamide (*SS*-**3**), are multidentate nitrogen-donor ligands with amine and/or pyridine-type nitrogen atoms. These nitrogen lone pairs can form transition-metal complexes with, for example, copper and silver.[1,2] They are called $N_3$ or $N_4$ donor ligands, depending on the number of nitrogen atoms that are involved in coordination to the metal atoms. Many of these transition-metal complexes show catalytic activities in asymmetric reactions, such as the Ullmann reaction, Henry (nitroaldol) reaction, and allylation reaction.[1–3] In addition, cobalt and zinc complexes with the $N_3$ and $N_4$ ligands have also been used to mimic biological systems, such as coenzyme vitamin B-12,[4] and some of their crystal structures have been reported.[5]

Although some $N_3$ and $N_4$ ligands, such as diiminopyridine, dipicolylamine, tripicolylamine, and pyridinophane, are achiral compounds, we focused on the three chiral multidentate nitrogen-donor ligands shown in Figure 1. Chirality is an essential aspect in asymmetric catalysis and in molecular-recognition events in biological systems. Conformational flexibility in these chiral $N_3$ and $N_4$ ligands often plays a crucial role in their catalytic capabilities in asymmetric reactions. It has also been documented that the solvent may influence the catalytic activity of a certain copper complex of *SS*-**1**.[2] While X-ray crystallography can provide detailed structural information of a single crystal, it is desirable to have a spectroscopic tool that can probe the chirality and conformations of these important species in solution directly. Vibrational circular dichroism (VCD) spectroscopy measures the preferential absorption of left versus right circularly polarized light that accompanies a vibrational transition. It therefore has unique specificity to chirality and is also

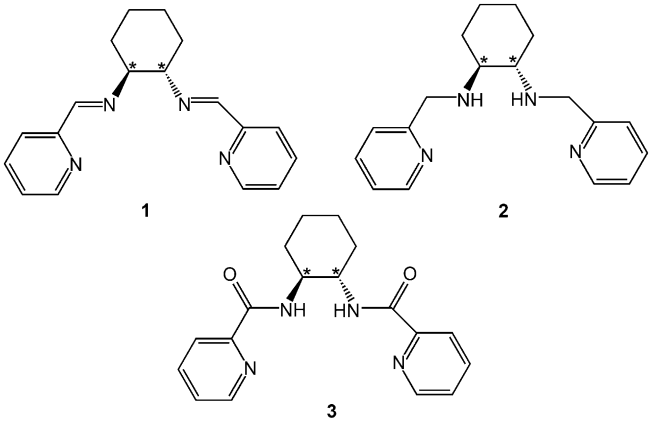


Figure 1. 2D stereochemical structures of compounds *SS*-**1**, *SS*-**2**, and *SS*-**3** reported herein. * indicates the stereogenic center of the compounds.

[a] Z. Dezhahang, M. R. Poopari, Prof. Dr. Y. Xu
Department of Chemistry, University of Alberta
Edmonton, Alberta, T6G 2G2 (Canada)
Fax: (+1) 780-492-8231
E-mail: yunjie.xu@ualberta.ca

Supporting information for this article is available on the WWW under http://dx.doi.org/10.1002/asia.201300070.

highly sensitive to conformations.[6] In recent years, VCD spectroscopy has emerged as a powerful tool to determine chirality and conformations of chiral inorganic compounds in solution when combined with DFT calculations.[7–16] For example, Sato et al. recently applied VCD spectroscopy to probe interesting chiroptical properties of coordinated bis-β-diketonato ligands[15] and a starburst-type tetranuclear ruthenium(III) complex.[13] Herein, we report extensive conformational searches for the three chiral $N_4$ inorganic ligands presented in Figure 1. Vibrational absorption (VA) and VCD spectra of all three ligands have been measured and compared with simulated spectra. One main objective is to obtain structural information and conformational distributions of these chiral ligands in solution. The second objective is to compare the similarity and dissimilarity of the VA and VCD spectral features of these three related ligands to further the ultimate goal of following these ligands in reactions in solution. Finally, we wish to evaluate the effects of solvent on the observed VCD features through theoretical modeling.

## Results and Discussion

Figure 2 shows the experimental VA and VCD spectra of **1**, **2**, and **3** in $CDCl_3$. Experimental VCD spectra of both enantiomers, which show good mirror images for the three compounds studied, are provided in Figure S1 in the Supporting Information. The *S*,*S* enantiomers of **1**, **2**, and **3** were used throughout, unless otherwise indicated. To highlight the similarities and differences in the VA and VCD spectra, we examined the experimental spectra in five regions marked A to E in Figure 2. In region A, there is a strong VA band corresponding to the C=N and C=O stretching vibrational modes of **1** and **3**, respectively, whereas **2** shows no band in this region. This amide I band of **3** is somewhat broadened, possibly as a result of hydrogen-bonding interactions with the solvent. In region B, two bands associated with vibrational modes of the pyridine rings are visible for all three compounds. In region C, only **3** exhibits a strong and somewhat broadened band that corresponds to the amide II vibrational mode. No such bands are detected for **1** and **2** because these two compounds do not contain a peptide bond, which is present in **3**. In region D, three closely spaced bands are visible for all three compounds; these are associated with vibrational motions of the cyclohexane and pyridine rings. Lastly, region E contains a number of low-intensity vibrational bands related to the vibrational motions of mainly C–C and C–H of the cyclohexane rings. Although one can correlate the VA features in regions A–D straightforwardly among these three compounds, the differences are drastic for the associated VCD features. For example, whereas the VA spectra of compounds **1** and **2** are similar in regions B and D, their corresponding VCD spectra differ greatly. This may be surprising at first glance because **1** and **2** differ only in that the two C=N functional groups of **1** are hydrogenated in **2**. On the other hand, this observation highlights the sensitivity of VCD spectroscopy to even small structural and conformational differences.

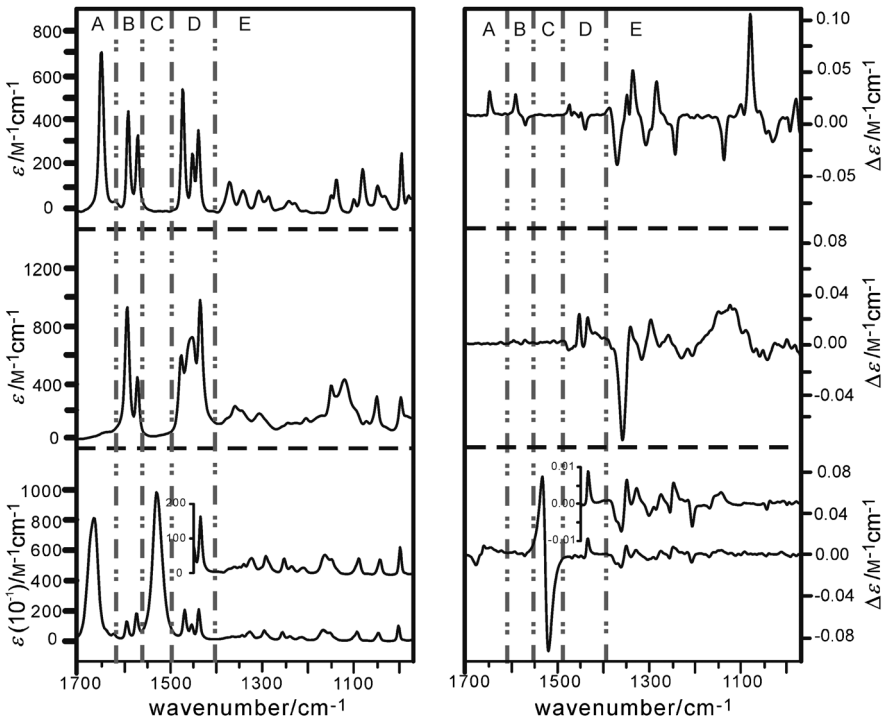


Figure 2. Experimental VA (left) and VCD (right) spectra of **1**, **2**, and **3** in $CDCl_3$ from top to bottom, respectively. The VA and VCD spectra of **1** and **2**, as well as the inserted spectrum of **3**, were recorded with a path length of 0.1 mm. The VA and VCD spectra of **3** were recorded with a shorter path length of 0.025 mm.

### Compound 1

Compound **1** has a number of rotatable bonds that make it a fairly flexible molecule. In this system, the cyclohexane ring is in its chair configuration because the boat configuration is much less stable at room temperature.[17] The two nitrogen atoms may adopt either equatorial or axial positions at the cyclohexane ring. We use the subscripts "equ" and "ax" to describe the equatorial and axial orientations, respectively, of the nitrogen atoms at the cyclohexane rings. In addition, the nitrogen atoms of the pyridine rings may take on either *cis* or *trans* orientations with respect to the nitrogen atoms of the C=N groups (see Figure 3 for a definition of the *cis* and *trans* arrangements).

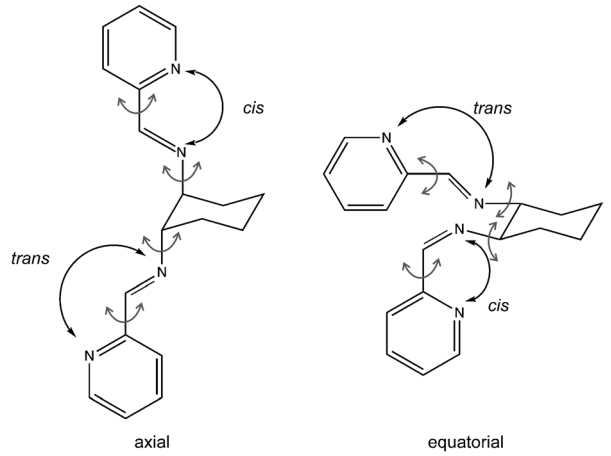


Figure 3. The *cis* and *trans* configurations of compound **1** with axial and equatorial substitutions. The rotatable C–$C_{pyridine}$ and N–$C_{hexane}$ bonds are indicated by small arrows.

The dihedral angle NCCN does not need to be 0 or 180° in the case of the *cis* or *trans* configurations, respectively. Rather these dihedral angles vary as the pyridine subunits rotate about the C–C bond to achieve stable conformations. Similarly, the whole substituted units can rotate around the N–$C_{hexane}$ bond. These motions are indicated with arrows in Figure 3. Altogether, such a flexible molecule may accommodate a substantial number of conformers, labeled [*trans–cis*]$_{equ}$, [*trans–cis*]$_{ax}$, and so forth in Figure 4.

To account for the implicit solvent effect, a polarization continuum model (PCM) with $CDCl_3$ as the solvent was applied. The lowest energy conformers obtained at the PCM/B3PW91/cc-pVTZ level are summarized in Figure 4, along with the relative Gibbs free energies and the corresponding percentage Boltzmann factors at room temperature. Based on the calculations, the equatorial orientation is significantly favored over the axial orientation in all three possible pyridine orientations, that is, *trans–cis*, *trans–trans*, and *cis–cis*. The preference for the axial position can be attributed to the opportunity to form secondary hydrogen-bonding interactions between a hydrogen atom of the cyclohexane ring and a nitrogen atom of the pyridine rings or between a hydrogen atom of one pyridine ring with the nitrogen atom of the C=N bond (see Figure 4). This also explains why the [*trans–cis*]$_{equ}$ arrangement is favored over the other two equatorial arrangements.

In the following discussions, we focus on the two dominant conformers of **1** because the other four conformers have a negligible contribution at room temperature. For completion, simulated VA and VCD spectra of all conformers of **1** are depicted in Figure S2 in the Supporting Information. In Figure 5, VA and VCD spectra of the two most stable conformers of **1** and the population-weighted spectrum based on their relative Gibbs free energies are compared with the corresponding experimental data. All experimental VA bands with visible intensities in the $\tilde{\nu}=1700$–$1400\ cm^{-1}$ region have been predicted accordingly. The two closely spaced bands in the $\tilde{\nu}=1450$–$1400\ cm^{-1}$ region

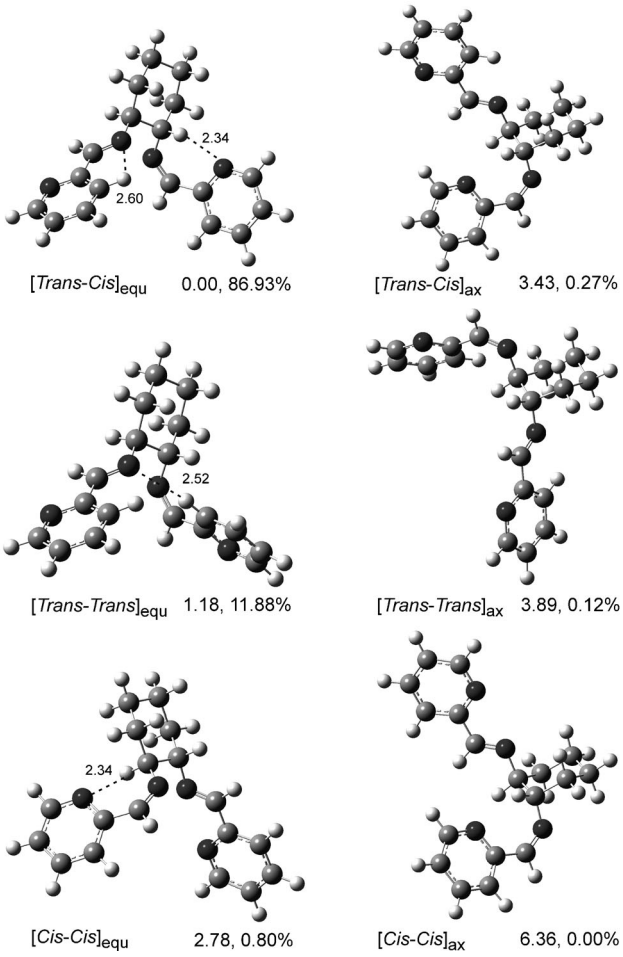


Figure 4. Conformations of compound *SS*-**1** at the PCM/B3PW91/cc-pVTZ level. The corresponding relative Gibbs free energies in kcal mol$^{-1}$ and the percentage Boltzmann factors at room temperature are also listed. Secondary intramolecular hydrogen bonds with bond lengths of $<2.8$ Å are indicated with dotted lines.

appear as one broader band in the calculation because the very small frequency shift is not accurately captured theoretically. Detailed comparisons between the experimental and calculated VA spectra in the region of $\tilde{\nu}=1400$–$970\ cm^{-1}$ are more challenging partly because the intensity is low and the density of peaks is high and some peaks are not well resolved experimentally. Nevertheless, it is straightforward to correlate most of the experimental VA bands in this region to the calculated ones. Notably, the VCD band intensity is strong in the $\tilde{\nu}=1400$–$970\ cm^{-1}$ region, where the VA intensity is low. One can confidently correlate all major VCD bands in this low-wavenumber region to the calculated ones. In the $\tilde{\nu}=1700$–$1400\ cm^{-1}$ region, on the other hand, the VCD intensity is generally weak, whereas the VA bands are strong. Although the calculated and experimental VCD patterns agree in general, some discrepancies are noted. For example, the bisignate +/− couplet in the $\tilde{\nu}=1600$–$1550\ cm^{-1}$ region was predicted to have a noticeably weaker positive feature than that observed experimentally. Overall, good agreement between the experimental and predicted VCD

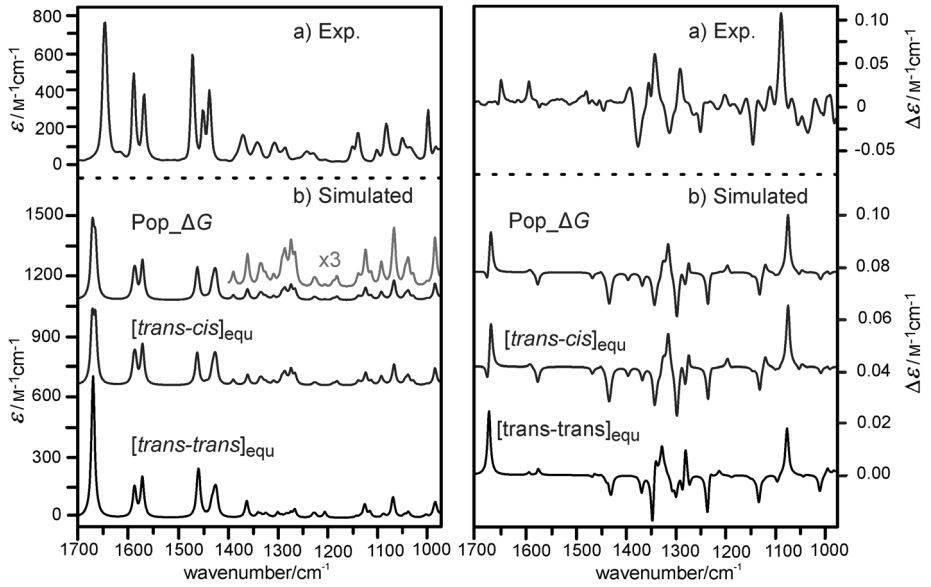


Figure 5. Comparison of the experimental and calculated VA (left) and VCD (right) spectra and the associated population-weighted spectra of *SS*-**1** at the PCM/B3PW91/cc-pVTZ level. The corresponding spectra of the two main conformers of **1** are also included.

spectra for **1** in the entire region of $\tilde{\nu}=1700$–$970\ cm^{-1}$ is achieved, despite the flexibility of the molecule.

### Compound 2

In compound **2**, the C=N bonds of **1** are hydrogenated by $NaBH_4$. Consequently, the degree of flexibility increases considerably from **1** to **2** because of the additional rotatable bonds. The rotatable bonds and four conformationally important dihedral angles are indicated in Figure 6. Preliminary searches suggest that conformers with intramolecular hydrogen-bonding interactions between the two NH groups are considerably more stable than those without. Keeping the aforementioned intramolecular hydrogen-bonding interactions intact, we varied the other four dihedral angles shown in Figure 6 to search for more conformers. This search resulted in 32 potential conformers. Although there are only 2 major conformers for compound **1**, there are 10

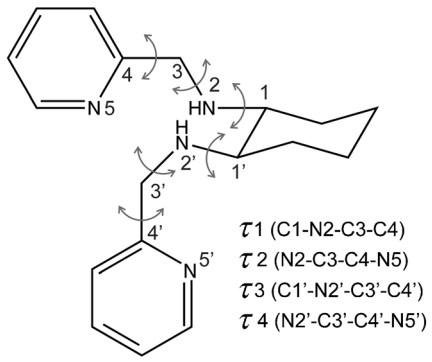


Figure 6. The rotatable bonds used in the conformational search are indicated with double arrows. The four conformationally important dihedral angels of **2** are also shown.

conformers of **2** with a percentage Boltzmann factor larger than 1% and they account for over 96% of the total population at room temperature in the initial search with the 6-311++G(d,p) basis set. The final optimized geometries of these ten conformers at the PCM/B3PW91/cc-pVTZ level are shown in Figure 7, as well as their relative Gibbs free energies and percentage Boltzmann factors at room temperature. Similar to compound **1**, the two pyridine substitutions prefer to adopt the equatorial orientation at the cyclohexane ring to retain the NH···N hydrogen-bonding interaction indicated in Figure 7. This portion of compound **2** remains essentially unchanged in all ten conformers shown in Figure 7. The values for the four conformationally important dihedral angles of these ten conformers are provided in Table 1.

Population-weighted VA and VCD spectra of these ten conformers are compared with the associated experimental data given in Figure 8. Because all of these conformers are relatively close in energy, the VA and VCD spectra of each individual conformer are also presented in Figures S3 and S4 in the Supporting Information, respectively, and compared with the experimental data. As seen in Figure S3 in the Supporting Information, the VA spectra of all ten conformers are similar. The two intense VA bands observed in panel B, corresponding to the C–C vibrational motions of the pyridine rings, are predicted for all ten conformers. On the other hand, in panel D, a group of fairly strong VA bands, associated with the cyclohexane C–H and pyridine C–H motions, are predicted for all conformers, but with somewhat different relative intensities. Closer examination reveals that the VA bands related to the cyclohexane C–H motions remain more or less the same among these conformers in panel D; this is consistent with the fact that the cyclohexane ring remains relatively unchanged among the conformers. The VA bands associated with the pyridine C–H motions, on the other hand, experience intensity changes from one conformer to the next, in which the pyridine rings take on different relative orientations. Although there are some small differences in the VA bands of different conformers in panel E, the predicted dominant VA bands are similar for all. Overall, the population-weighted VA spectrum is in good agreement with the experimental one (Figure 8).

A number of interesting points can be made for the VCD spectra of different conformers shown in Figure S4 in the Supporting Information. First, the VCD intensities are pre-

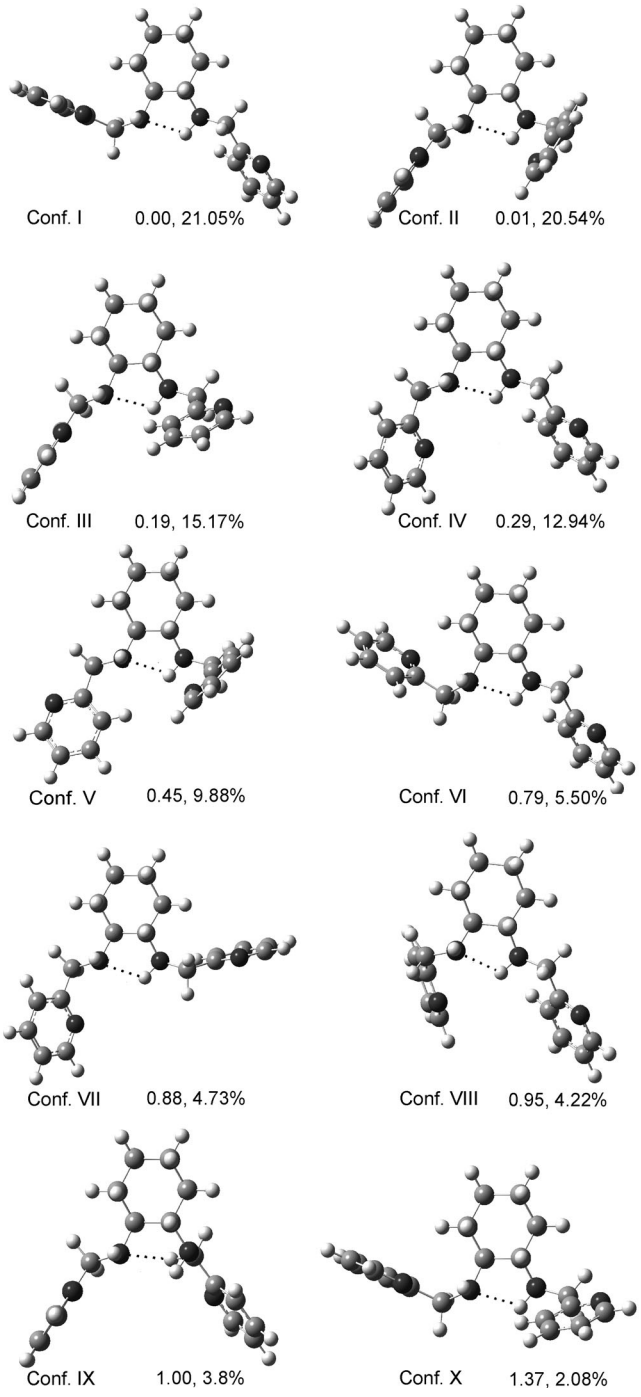


Figure 7. The ten most stable conformers of *SS*-**2**. The corresponding relative Gibbs free energies in kcal mol$^{-1}$ at the PCM/B3PW91/cc-pVTZ level and the corresponding Boltzmann factors at room temperature are also listed. The NH···N hydrogen bonds are indicated with dotted lines.

dicted to be weak for all conformers in the $\tilde{\nu}=1670$–$1560\,cm^{-1}$ region, that is, panel B. Although the VA patterns are similar in panel B, the VCD patterns are different for different conformers. Second, in the $\tilde{\nu}=1560$–$1500\,cm^{-1}$ region (panel D), strong VCD intensities are predicted for all conformers, but with drastically different patterns going from one conformer to the next. In the final population-weighted spectrum, accidental intensity cancelations result in much weaker VCD bands; this is consistent with somewhat weak and congested VCD signals observed experimentally. Agreement between the experimental and predicted VCD patterns is good, except that the negative band at $\tilde{\nu}\approx1470\,cm^{-1}$ is predicted to be much stronger than that observed experimentally; this highlights the challenges in dealing with flexible molecules with a large number of relevant conformers. Lastly, in the region below $\tilde{\nu}=1400\,cm^{-1}$ (panel E), all six most abundant conformers are predicted to show strong to medium negative VCD bands at $\tilde{\nu}\approx1360\,cm^{-1}$; this is consistent with the most intense VCD band observed in this vicinity experimentally. Considering that **2** is very flexible and has a significant number of relevant conformers with noticeably different VCD patterns, the overall agreement between the experimental VCD spectrum and the population-weighted spectrum is quite good. This in turn supports the conformers and conformational distributions identified.

Table 1. Dihedral angle values for the ten most stable conformers of *SS*-**2** at the PCM/B3PW91/cc-pVTZ level.

| Conformer[a] | $\tau1$ [°] | $\tau2$ [°] | $\tau3$ [°] | $\tau4$ [°] |
|---|---|---|---|---|
| I | −84.98 | −41.08 | −177.56 | −164.17 |
| II | −164.39 | 35.76 | 64.43 | 60.68 |
| III | −165.80 | 33.25 | 66.13 | −158.77 |
| IV | 175.03 | −78.18 | −178.16 | −166.83 |
| V | 168.86 | 164.69 | 62.27 | 53.83 |
| VI | −66.84 | 103.89 | −176.33 | −164.01 |
| VII | 173.89 | −76.61 | −98.33 | 156.07 |
| VIII | 75.65 | 66.79 | −176.31 | −165.55 |
| IX | −167.34 | 38.68 | 174.79 | 163.77 |
| X | −80.64 | −46.08 | 64.00 | −156.53 |

[a] Conformers are shown in Figure 7.

## Compound 3

In compound **3**, the subunit −NH−$CH_2$− in **2** is replaced with −NH−C(=O)−. The introduction of the two peptide bonds in **3** brings substantial rigidity to the structure. The lone electron pairs of the nitrogen atoms are involved in the resonance with the π electrons of the carbonyl groups. As a result, rotation around the N−$C_{carbonyl}$ bond is restricted, in contrast to free rotation around the N−C bond in **2**. As with the previous compounds, the equatorial position is much more favored than the axial orientation for **3**. In addition, the C=O group and the N atom of pyridine prefers to stay in the *trans* arrangement around the $C_{carbonyl}$–$C_{pyridine}$ bond, corresponding to the *cis* arrangement for the two N atoms shown in Figure 1. This results in a strong preference for the *cis–cis* configuration. One ends up with only one major conformer for **3** (Figure 9). The experimental VA and VCD data are summarized in Figure 10 and compared with spectra calculated at the PCM/B3PW91/cc-pVTZ level. For easier visual comparison, the simulated VA and VCD intensities are amplified by a factor of 5 and 8, respectively, in the region below $\tilde{\nu}=1450\,cm^{-1}$. The majority of experimental features are reasonably reproduced by the simulated

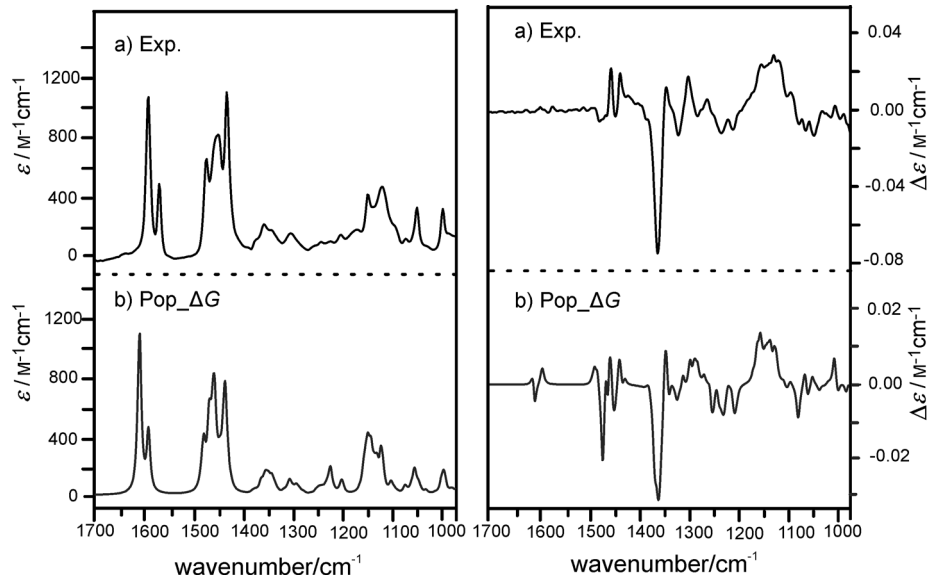


Figure 8. Comparison of the experimental and calculated VA (left) and VCD (right) spectra of the population-weighted spectra of *SS*-**2** calculated at the PCM/B3PW91/cc-pVTZ level.

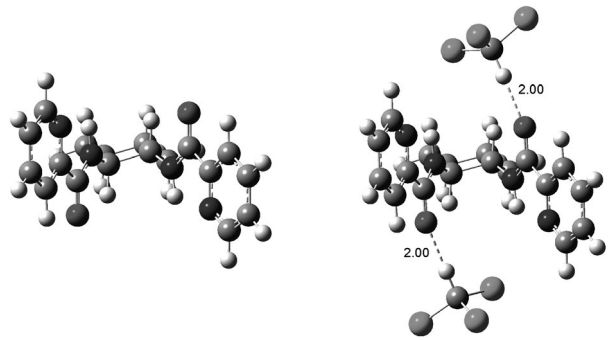


Figure 9. Geometries of the dominant conformer of *SS*-**3** (left) at the PCM/B3PW91/cc-pVTZ level and of the 1:2 explicit solvated complex of **3** with two molecules of $CDCl_3$ (right) at the B3PW91/cc-pVTZ level. The intermolecular hydrogen-bond lengths are given in Å.

ones, despite their low intensity in the $\tilde{\nu}=1400$–$970\,cm^{-1}$ region. The only noticeable exception is the VCD experimental features at $\tilde{\nu}\approx1650\,cm^{-1}$, corresponding to the amide I vibrational motions, which show a negative–positive doublet, in contrast to the prediction with PCM.

It has been demonstrated before that hydrogen-bonding interactions between a chiral solute and solvent may alter the appearance of the VCD spectral pattern noticeably in solution.[18–24] Such hydrogen-bonding interactions may be the cause for the disagreement between theory and experiment with regard to the amide I VCD signs. Such phenomena in the amide I region were investigated, for example, for *N*-acetylproline amide[25] and for the tryptophan zipper (trpzip) model hairpin in water.[26] Compound **3** has two carbonyl oxygen atoms that can serve as proton acceptors to the D atom of $CDCl_3$. We therefore constructed an explicit solvated complex of **3** with two molecules of $CDCl_3$, which is also depicted in Figure 9. The simulated VA and VCD spectra of this explicit solvated complex are also presented in Figure 10. The assignment for the bands in the $\tilde{\nu}=1700$–$1450\,cm^{-1}$ region is straightforward. In the $\tilde{\nu}=1450$–$1050\,cm^{-1}$ region, to aid a visual comparison, a number of experimental VA and VCD bands are labeled and have also been cross-checked for consistency in their VA and VCD band positions. The corresponding assignments for these bands are also provided in the calculated spectra. There are some minor changes to the VA and VCD features on going from **3** calculated with PCM to the explicitly solvated complex of **3** with two molecules of $CDCl_3$. For example, the calculated VA feature of the solvated complex at $\tilde{\nu}=1250\,cm^{-1}$ appears to be stronger owing to severe overlap of two VA bands, whereas these two VA bands of **3** calculated with PCM are well separated. The most noticeable change is that the signs for the bisignate VCD couplet at $\tilde{\nu}=1650\,cm^{-1}$ are reversed with the explicit solvation model and are now in agreement with experimental results. A similar sign-reversed phenomenon was reported for the carbonyl stretching band in the VCD study of pulegone in chloroform,[18,19] although the VCD carbonyl band was later identified as a non-robust mode.[19,24] Closer examination of the VCD amide I bands reveals that these modes are robust and the VCD signs associated with the symmetric and antisymmetric C=O bands have not changed upon hydrogen-bonding interactions with $CDCl_3$. Rather, the reversed VCD signs observed are due to switching of the frequency ordering of the symmetric and antisymmetric C=O bands caused by hydrogen-bonding interactions with $CDCl_3$. Detailed vibrational motion and robust mode analyses are provided in Table S1 in the Supporting Information. The above observations and discussion highlight the importance of explicit solvent–solute hydrogen-bonding interactions in interpreting VCD spectra.

## Conclusion

Three nitrogen-donor ligands, namely, *SS*-**1**, *SS*-**2**, and *SS*-**3**, with different conformational flexibility, have been synthesized and characterized. Their VA and VCD spectra have been measured in the fingerprint region in $CDCl_3$. Systematic searches were carried out to identify the lowest energy conformers in $CDCl_3$ by using the implicit solvent model. The explicit hydrogen-bonding solvation model was also evaluated for **3** in $CDCl_3$ to adequately explain the observed

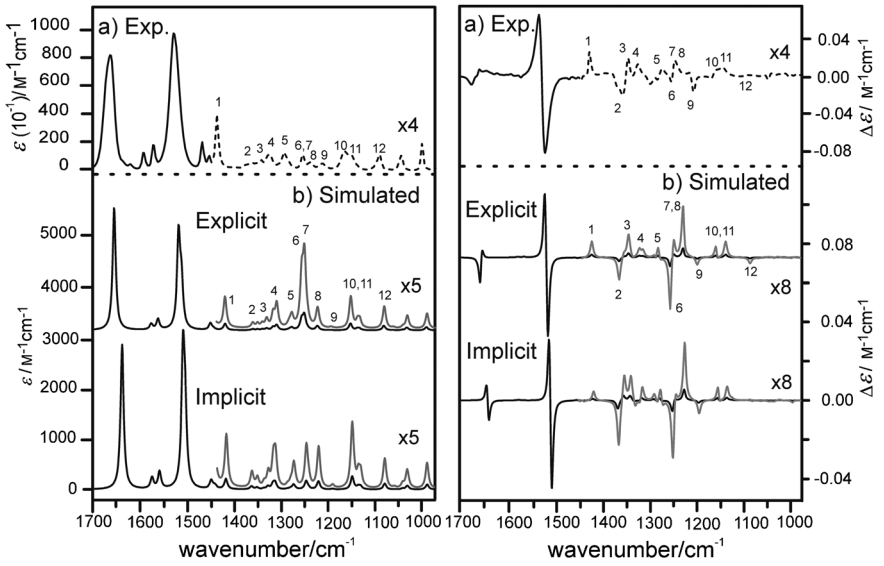


Figure 10. Comparison of the experimental and calculated VA (left) and VCD (right) spectra of implicit solvated **3** at the PCM/B3PW91/cc-pVTZ level and the explicit solvated complex of **3** with two molecules of $CDCl_3$ at the B3PW91/cc-pVTZ level. The dotted experimental spectra are taken from the insert in Figure 2. A number of bands are labeled to aid a visual comparison (see text for details).

reverse in sign in the VCD couplet in the amide I region. Good agreement between experimental and theoretical spectra was achieved for all three ligands, leading to the determination of the conformational distributions for all three compounds. This includes the highly flexible compound **2**, which has ten most stable conformers with Boltzmann factors ranging from about 2 to 20% at room temperature. Although detailed assignment of VA and VCD spectra becomes tougher with increasing flexibility of molecules, and thus, increasing number of conformers; this work demonstrates that conclusive assignment can nevertheless be achieved. In particular, although VA spectra of different conformers show only minor differences, the corresponding VCD spectra show exquisite sensitivity to chirality and are, at the same time, highly sensitive to even subtle conformational changes. Such high sensitivity of VCD spectroscopy to chirality and conformations makes it an attractive approach to investigate chirality and structural properties of multidentate nitrogen ligands and their metal complexes in solution.

## Experimental Section

*Experimental Details*

Compounds *SS*-**1** and *SS*-**2** and their opposite enantiomers were synthesized according to a reported experimental procedure.[27] Compound *SS*-**3** compound was purchased from Sigma Aldrich (purity 97%) and used without further purification. All compounds are air stable and unsusceptible to light. Both *SS*-**1** and *SS*-**2** are soluble in dichloromethane, chloroform, toluene, and benzene. These synthesized compounds were fully characterized by several spectroscopic techniques, such as $^1H$ and $^{13}C$ NMR spectroscopy and mass spectrometry, and shown to be pure. VA and VCD spectra of both enantiomers of these three compounds were recorded with an FTIR spectrometer (Bruker) equipped with a VCD optical bench (PMA 50). Different combinations of concentration and path length were used to optimize the absorbance of each sample to ensure reliable VCD measurements. Solutions with concentrations of about 0.38, 0.37, and 0.30 M were prepared for the enantiomeric pairs of *SS*-**1**, *SS*-**2**, and *SS*-**3** in $CDCl_3$ (purity 99.96%, Aldrich), respectively. The optimized path length was 0.1 mm for all compounds in the $\tilde{\nu}$= 1700–970 $cm^{-1}$ region, except for the enantiomeric pairs of *SS*-**3** for which the experiment was also performed with a shorter path length of 0.025 mm, owing to the strong absorbance in the amide I and amide II regions. All VCD spectra were recorded at 4 $cm^{-1}$ resolution and with a total data collection time of 3 h (3× 60 min). The $BaF_2$ cell windows were used. Final experimental VCD spectra were baseline corrected by using the difference between the *SS* and *RR* enantiomers under the same conditions.[6]

*Computational Details*

Geometry optimizations and harmonic calculations of vibrational frequencies of all conformers, as well as the VA and VCD intensities, were performed by using the Gaussian 09[28] program package. Lorentzian line shapes with a half width at half height (HWHH) of 4 $cm^{-1}$ were used to simulate the VA and VCD spectra calculated at the B3PW91/cc-pVTZ level. To evaluate the sensitivity of VA and VCD spectra to functionals and basis sets, calculations of the most stable conformer of *SS*-**1** were performed with several combinations of functionals and basis sets, namely, B3LYP/6-311++(d,p), B3LYP/cc-pVTZ, B3PW91/6-311++G(d,p), and B3PW91/cc-pVTZ. The results are summarized in Figure S5 in the Supporting Information. Theoretical VA and VCD spectra obtained were similar to each other, thus demonstrating good theoretical stability with different combinations of functionals and basis sets. The VCD spectra at the B3PW91/cc-pVTZ level showed slightly better agreement with the experimental data. This level of theory was therefore used for all calculations performed herein. The integral equation formalism (IEF) of PCM[29] with application of universal force field (UFF) radii was utilized to account for the implicit solvent effect of $CDCl_3$, for which a dielectric constant of 4.711 was used for chloroform.

## Acknowledgements

This research was funded by the University of Alberta and the Natural Sciences and Engineering Research Council of Canada. We thank Nargess Hosseini for her help with the syntheses. We also gratefully acknowledge access to the computing facilities provided by the Academic Information and Communication Technology group at the University of Alberta and by the Western Canada Research Grid (Westgrid). Y.X. holds a Tier I (Senior) Canada Research Chair in Chirality and Chirality Recognition.

[1] Y. Zhang, L. Xiang, Q. Wang, X. F. Duan, G. Zi, *Inorg. Chim. Acta* **2008**, *361*, 1246–1254.

[2] A. Ouali, M. Taillefer, J.-F. Spindler, A. Jutand, *Organometallics* **2007**, *26*, 65–74.
[3] H. Zhang, L. Chen, H. Song, G. Li, *Inorg. Chim. Acta* **2011**, *366*, 320–336.
[4] a) M. Livieri, F. Mancin, G. Saielli, J. Chin, U. Tonellato, *Chem. Eur. J.* **2007**, *13*, 2246–2256; b) Y. Murakami, J. I. Kikuchi, Y. Hisaeda, O. Hayashida, *Chem. Rev.* **1996**, *96*, 721–758.
[5] T. M. Kooistra, K. F. W. Hekking, Q. Knijnenburg, B. de Bruin, P. H. M. Budzelaar, R. De Gelder, J. M. M. Smits, A. W. Gal, *Eur. J. Inorg. Chem.* **2003**, 648–655.
[6] a) L. A. Nafie, *Vibrational Optical Activity: Principles and Applications*, Wiley, Chichester, **2011**; b) Y. He, B. Wang, R. K. Dukor, L. A. Nafie, *Appl. Spectrosc.* **2011**, *65*, 699–723; c) G. Yang, Y. Xu, "*Vibrational Circular Dichroism Spectroscopy of Chiral Molecules*", in *Top. Curr. Chem. Volume: Electronic and Magnetic Properties of Chiral Molecules and Supramolecular Architectures* (Eds.: R. Naaman, D. N.Beratan, D. H.Waldeck), Springer, Berlin, **2011**, *298*, 189–236.
[7] a) P. J. Stephens, F. J. Devlin, J. J. Pan, *Chirality* **2008**, *20*, 643–663; b) M. Gábor, T. György, V. Elemér, *Wiley Interdiscip. Rev.: Comput. Mol. Sci.* **2011**, *1*, 403–425.
[8] Y. He, X. Cao, L. A. Nafie, T. B. Freedman, *J. Am. Chem. Soc.* **2001**, *123*, 11320–11321.
[9] C. Johannessen, P. W. Thulstrup, *Dalton Trans.* **2007**, 1028–1033.
[10] W. Armstrong, F. A. Cotton, A. G. Petrovic, P. L. Polavarapu, M. M. Warnke, *Inorg. Chem.* **2007**, *46*, 1535–1537.
[11] T. Wu, X.-P. Zhang, C.-H. Li, P. Bouř, Y.-Z. Li, X.-Z. You, *Chirality* **2012**, *24*, 451–458.
[12] Z. Dezhahang, C. Merten, M. R. Poopari, Y. Xu, *Dalton Trans.* **2012**, *41*, 10817–10824.
[13] C. Merten, K. Hiller, Y. Xu, *Phys. Chem. Chem. Phys.* **2012**, *14*, 12884–12891.
[14] H. Sato, F. Sato, M. Taniguchi, A. Yamagishi, *Dalton Trans.* **2012**, *41*, 1709–1712.
[15] H. Sato, Y. Mori, T. Kitazawa, A. Yamagishi, *Dalton Trans.* **2013**, *42*, 232–237.
[16] H. Sato, A. Yamagishi, *Int. J. Mol. Sci.* **2013**, *14*, 964–978.
[17] Z. Dezhahang, M. R. Poopari, Y. Xu, *J. Mol. Struct.* **2012**, *1024*, 123–131.
[18] E. Debie, P. Bultinck, W. Herrebout, B. van der Veken, *Phys. Chem. Chem. Phys.* **2008**, *10*, 3498–3508.
[19] V. P. Nicu, E. Debie, W. Herrebout, B. Van der Veken, P. Bultinck, E. J. Baerends, *Chirality* **2009**, *21*, E287–E297.
[20] M. R. Poopari, Z. Dezhahang, Y. Xu, *Phys. Chem. Chem. Phys.* **2013**, *15*, 1655–1665.
[21] M. Losada, Y. Xu, *Phys. Chem. Chem. Phys.* **2007**, *9*, 3127–3135.
[22] M. R. Poopari, P. Zhu, Z. Dezhahang, Y. Xu, *J. Chem. Phys.* **2012**, *137*, 194308.
[23] G. Yang, Y. Xu, *J. Chem. Phys.* **2009**, *130*, 164506.
[24] a) V. P. Nicu, E. J. Baerends, *Phys. Chem. Chem. Phys.* **2009**, *11*, 6107–6118; b) V. P. Nicu, E. J. Baerends, *Phys. Chem. Chem. Phys.* **2011**, *13*, 16126–16129; c) S. Góbi, G. Magyarfalvi, *Phys. Chem. Chem. Phys.* **2011**, *13*, 16130–16133; d) V. P. Nicu, J. Neugebauer, E. J. Baerends, *J. Phys. Chem. A* **2008**, *112*, 6978–6991.
[25] K.-K. Lee, S. Hahn, K.-I. Oh, J. S. Choi, C. Joo, H. Lee, H. Han, M. Cho, *J. Phys. Chem. B* **2006**, *110*, 18834–18843.
[26] P. Bouř, T. A. Keiderling, *J. Phys. Chem. B* **2005**, *109*, 23687–23697.
[27] W. Park, M. H. Shim, J. H. Chung, J. Park, M. S. Lah, D. Lim, *Tetrahedron Lett.* **2006**, *47*, 8841–8845.
[28] Gaussian 09, Revision B.01, M. J. Frisch, G. W. Trucks, H. B. Schlegel, G. E. Scuseria, M. A. Robb, J. R. Cheeseman, G. Scalmani, V. Barone, B. Mennucci, G. A. Petersson, H. Nakatsuji, M. Caricato, X. Li, H. P. Hratchian, A. F. Izmaylov, J. Bloino, G. Zheng, J. L. Sonnenberg, M. Hada, M. Ehara, K. Toyota, R. Fukuda, J. Hasegawa, M. Ishida, T. Nakajima, Y. Honda, O. Kitao, H. Nakai, T. Vreven, J. A. Montgomery, Jr., J. E. Peralta, F. Ogliaro, M. Bearpark, J. J. Heyd, E. Brothers, K. N. Kudin, V. N. Staroverov, R. Kobayashi, J. Normand, K. Raghavachari, A. Rendell, J. C. Burant, S. S. Iyengar, J. Tomasi, M. Cossi, N. Rega, J. M. Millam, M. Klene, J. E. Knox, J. B. Cross, V. Bakken, C. Adamo, J. Jaramillo, R. Gomperts, R. E. Stratmann, O. Yazyev, A. J. Austin, R. Cammi, C. Pomelli, J. W. Ochterski, R. L. Martin, K. Morokuma, V. G. Zakrzewski, G. A. Voth, P. Salvador, J. J. Dannenberg, S. Dapprich, A. D. Daniels, Ö. Farkas, J. B. Foresman, J. V. Ortiz, J. Cioslowski, D. J. Fox, Gaussian, Inc., Wallingford CT, **2009**.
[29] J. Tomasi, B. Mennucci, R. Cammi, *Chem. Rev.* **2005**, *105*, 2999–3093.

Received: January 18, 2013
Published online: April 5, 2013